THE UNIVERSITY *of* EDINBURGH

Investigating the effect of oil-infusion on the icephobicity of elastomer coatings

Catherine Megregian

Doctor of Philosophy

The University of Edinburgh

January 2023

Declaration

I declare that this thesis has been composed solely by myself and that it has not been submitted, in whole or in part, in any previous application for a degree. Except where stated otherwise by reference or acknowledgment, the work presented is entirely my own.

Catherine Megregian

January 2023

Abstract

The hazards of ice accumulation include damage to infrastructure, disruption of transportation, and even major accidents. Historically, the solution has been to de-ice surfaces by chemical, mechanical or thermal means. Anti-icing coatings are a proposed alternative which passively prevent ice accumulation. The icephobicity of a coating is assessed via the ice adhesion strength and freezing delay. Elastomer coatings infused with miscible oil have shown particularly low ice adhesion. However, there has been little investigation of the effect on freezing delay. The aim of this work is to provide a comprehensive study of the icephobicity of oil-infused elastomers to better understand the effect of oil-infusion.

Seven elastomer coatings were investigated: two PDMS (polydimethylsiloxane) coatings, four silicone-oil/PDMS coatings (two molecular weights of oil, at two concentrations – 25% and 50%), and a commercial coating (NuSil R-2180).

Ice adhesion testing was performed via a push test method, in which ice frozen in acrylic cylinders on the coatings was displaced by a force probe. 100 repeat de-icing cycles were performed in a refrigerated laboratory at −10°C. Freezing delay was measured via visual observation of the time for a droplet of water to freeze, from deposition on the surface, and compared to a bare aluminium reference. The elastic modulus, contact angle, surface roughness and room temperature adhesion of the surfaces was characterised alongside the icephobicity testing.

Despite greater degradation over time, the oil-infused coatings exhibited consistently lower ice adhesion strengths than the non-oil infused coatings, less than 50% in most of the 100 de-icing cycles. De-icing did not cause significant damage or increase in ice adhesion strength of the oil-infused coatings, but the non-oil infused coatings exceeded the equipment load limit with increasing frequency, meaning they lose icephobicity. Fitting the data to models for interfacial cavitation and interfacial slippage showed a better correlation to interfacial slippage, and shear modulus had the strongest influence on adhesion strength. This understanding can assist future coating design. There was little difference in the freezing delay of the coatings, but all provided an improvement on bare aluminium. Measurements performed before and after adhesion testing showed a small decrease in freezing delay post-adhesion.

The effect of severe damage was investigated using specimens which were abraded with grit paper or cut by a scalpel. There was a slight increase in ice adhesion and small decrease in the freezing delay. Cryo-FIB/SEM showed a mixture of high and low conformation at the ice-coating interface. Recoating the surfaces restored the original performance of the coatings, which would allow for straightforward repair in practice.

To better understand the mechanism by which oil-infusion lowers ice adhesion strength, a new method for investigating interfacial slippage was developed. Using a microtribometer mounted under an optical microscope, de-icing tests were performed on ice droplets. Fluorescent microparticles embedded in the top of the coatings were tracked during de-icing to monitor for polymer flow. Results were inconclusive in determining the presence of interfacial slippage; however, suggestions for further work are made.

The oil-infused elastomer coatings are shown to have excellent icephobicity. Their use in anti-icing applications lowers the ice adhesion strength while maintaining freezing delay of non-oil infused coatings. Their use would reduce de-icing requirements and lessen the energy, time and resources spent on removing surface ice from, for example, bare metals. They would also reduce damage caused by accumulation and detachment of heavy ice loads. Durability of oil-infused elastomers is also shown not to be a major concern: de-icing causes minimal damage, good icephobicity is maintained even with moderate-to-severe damage, and recoating damaged surfaces is an effective method of repair.

Lay Summary

Ice build-up on a surface can be a blessing and a curse. It is the basis of winter sports like ice skating and curling, but it can also be a serious hazard to our daily lives: slippery pavements and roads can cause accidents, and damage to energy infrastructure can cause power outages at the coldest times of the year.

The ability to prevent ice from building up on a surface is called icephobicity and it can be broken down into two parts: 1) freezing delay – the ability to prevent water from freezing on a surface and 2) ice adhesion strength – the force required to remove ice once it has formed on a surface. An ideal icephobic coating would have a high freezing delay and a low ice adhesion strength.

Previous work has shown that silicone rubber has very low ice adhesion strength. This can be seen in the design of ice cube trays – it is much easier to remove ice from a soft, rubbery tray, than it is a stiff plastic or metal tray. Adding oil to the silicone rubber before processing it has been shown to lower the adhesion strength even more. However, the effect of adding oil on the freezing delay has not been studied.

In this work, seven silicone rubber coatings were made, three without oil and four with oil. The recipes with oil had varying viscosities and percentages of oil. The ice adhesion strength and freezing delay were measured and showed that the addition of oil did lower the ice adhesion strength considerably and did not affect the freezing delay of the coatings.

The way in which adding oil reduces adhesion strength is not well understood. Some believe that adding oil makes the coatings fluid enough that they can flow away from the ice during removal, like a liquid. A new technique was developed to observe this, by tracking the movement of fluorescent particles in the coating when the ice is removed. The results did not conclusively show flow of the particles.

A concern with silicone rubber coatings is that their softness means they are easily damaged, and this could make them less icephobic. However, this is shown not to be the case. The coatings were damaged by cutting and abrasion and then the icephobicity remeasured. Only when the coating is severely damaged, for example when large pieces are removed to expose the surface below, does it become an issue.

Applying another layer of the coating on top is shown to repair the coating well. A technique was also developed for imaging the cross-section of ice droplets on the damaged surfaces using a scanning electron microscope at sub-zero temperatures. Images of the contact between the damaged surface and the ice droplets are the first reported.

Silicone rubber coatings with added oil are shown to be excellent at preventing ice build-up.

Acknowledgements

Over the past four years I have had the pleasure to dedicate my time and attention to what can arguably be described as watching ice freeze. At times frustrating, difficult, and even absurd, it has also been one of the most rewarding and fulfilling periods of my life.

None of my work would have been possible without the contributions and support of so many other people. It really does take a village. I must first thank my supervisor Dr Jane Blackford for her immeasurable contribution to my work and life over the past four years and beyond. She provided me with guidance, encouragement, and inspiration during my project, whenever any hurdles arose. Throughout my PhD I have looked forward to our conversations, which ranged from the technical, to the deeply personal and even philosophical. I would also like to thank my second supervisor, Dr Vasileios Koutsos, who provided thoughtful discussions on all manner of polymer behaviours.

Working alone in a windowless laboratory at sub-zero temperatures could have been an isolating experience, but the staff, my fellow PhD students and post-docs never let it feel that way, always on hand for a chat and a cup of tea while I defrosted my fingers and toes.

I would like to express my gratitude for the assistance provided by the technical staff at the University, particularly Kevin Tierney, who made sure I wasn't trapped in the cold room at the end of every day; Chris Sturgeon, for believing that there's no stupid questions; and Eddie Monteith, who was never too busy to lend a hand. I would also like to thank Fraser Laidlaw for siting at the cryo-FIB/SEM with me for days on end.

I would like to thank my parents, sisters, and the rest of my family for their support during this time. Your pride in me has always been a galvanising force in my life, and this is as much your achievement as it is mine. To my friends in Edinburgh and beyond, you provided endless joy and laughter that kept me going and mobilised like a small army when asked to proof-read. Finally, I owe an unending debt to my partner, Rob, for being right beside me at every single step of this journey.

Table of Contents

List of Figures

List of Tables

List of Symbols

a	Segmental chain length
β	Rate at which an ice embryo of critical radius gains one water molecule
d	Freezing front height
d_s	Substrate thickness
d_0	Droplet height
E	Elastic modulus
f	Geometric and surface energy expression for nucleation
f_a	Force needed to detach a single chain of segmental length a
G	Shear modulus
g	Secondary geometric and surface energy expression for nucleation
ΔG^*	Free energy of formation for a critical ice embryo
ΔG_v	Volumetric free energy of phase-change for ice
γ	Water-air surface tension
γ_{lw}	Ice-water interfacial tension
γ_{lv}	Liquid surface tension
γ_{sl}	Solid-liquid interfacial energy
γ_{sv}	Solid surface energy
H	Enthalpy of ice formation
I_h	Hexagonal form of ice I
J	Heterogeneous nucleation rate
K	Kinetic constant for nucleation
k	Boltzmann constant
k_l	Ice thermal conductivity
k_s	Substrate thermal conductivity
l	Coating thickness
m	Contact angle/interfacial energy factor
N	Nucleation sites per unit area
P	Probability of nucleation in a droplet
R	Radius of surface features
R_a	Arithmetic average roughness
r	Ratio of true surface area to projected surface area
r_c	Critical ice embryo radius
φ_s	Fraction of droplet surface area in contact with solid

ρ^{CL}	Elastomer crosslink-density
ρ_I	Ice density
σ_A	Adhesion strength
T	Temperature
t	Time
$t_{freezing}$	Freezing delay
t_{growth}	ice growth time
ΔT	Temperature difference
θ	Static droplet contact angle
θ^*	Apparent contact angle
V	Volume
$V_f(z)$	Flow velocity
v	Poisson's ratio
W_A	Work of adhesion
x	Geometric factor for nucleation
Z	Zeldovich statistical probability factor
z	Depth of flow from wall

List of Acronyms

FIB	Focused ion beam
HMWSO	High molecular weight silicone oil
LLL	Liquid-like layer
LMWSO	Low molecular weight silicone oil
PDMS	Polydimethylsiloxane
PETG	Polyethylene terephthalate glycol
PTFE	Polytetrafluoroethylene
QLL	Quasi-liquid layer
SEM	Scanning electron microscopy
SHS	Superhydrophobic surface
SLIPS	Slippery liquid infused porous surface

1. Introduction

1.1. The challenges of ice accumulation

The accumulation of ice on surfaces is widespread (Kreder et al., 2016). Car windscreens need to be scraped clear on winter mornings, airplanes need to be de-iced before take-of and roads require gritting. De-icing airplanes increases downtime and accrues labour and equipment costs, as well as environmental impacts from groundwater contamination (Ramakrishna and Viraraghavan, 2005). Power lines can be damaged, causing power outages (Chang et al., 2007). Icy roads and pavements can lead to car accidents. Ice on boats, airplanes and cars can lead to higher fuel consumption and more expensive transport costs (Cooper et al., 1984, Cao et al., 2018). Surface icing affects everything from daily commutes to national infrastructure and international travel. While there are some solutions (for example, using chemicals like ethylene glycol in airplane de-icing, or salting roads and pavements; or mechanical or thermal removal of ice), most are active de-icing methods which can be costly, inefficient, or labour-intensive.

1.2. Passive anti-icing coatings as a solution

Recent work on preventing ice accumulation has led to passive anti-icing coatings. These coatings are assessed on their icephobicity (Brassard et al., 2018, Shen et al., 2019, Irajizad et al., 2019b), which is measured via two constituents:

i. **Ice adhesion strength**

   Defined as the peak ice detachment force divided by the contact area. It has previously been suggested that passive anti-icing can occur when ice adhesion strength is <100 kPa, but scientific improvements have revised this to 10-20 kPa (Golovin et al., 2016, Zhuo et al., 2021, Irajizad et al., 2019a, Jamil et al., 2019). The lower the ice adhesion strength, the better the icephobicity.

ii. **Freezing delay**

   Defined here as the time taken for water to freeze on a test surface. The greater the freezing delay, the better the icephobicity.

Together these describe the ability to mitigate ice formation and accumulation. Some studies use additional metrics, but most research recognises these two constituents of icephobicity.

An extensive number of surfaces have been examined over the past 25 years and there have been a few major advances. Both superhydrophobic surfaces (SHS) and slippery-liquid infused porous surfaces (SLIPS) have received significant attention for possible use as icephobic surfaces (Kreder et al., 2016). However, the findings of these studies have been inconsistent and lack agreement on their viability as icephobic surfaces (Maitra et al., 2015, Nosonovsky and Hejazi, 2012, Jung et al., 2011). More recent innovations have been made using elastomer coatings, especially those that are infused with miscible oils (Golovin et al., 2016, Wang et al., 2017, Urata et al., 2015, Beemer et al., 2016). Some of these materials have been shown to have incredibly low ice adhesion (<20 kPa) and don't suffer from some of the drawbacks associated with SHS and SLIPS.

Though they have shown promise, these oil-infused elastomer coatings are still poorly understood. Research has largely focused on measuring their ice adhesion strength and ignored freezing delay. Also, though they have shown incredibly low ice adhesion, the source of their low adhesion is not well understood. Some studies have suggested interfacial slippage (Golovin et al., 2016) as the mechanism of the icephobic behaviour of these coatings, but have not shown strong evidence for it. Generating a more complete understanding of the icephobicity of these coatings will help design improved coatings in the future.

1.3. Aim of PhD

The aim of this work can be split into three primary objectives:

i. **Characterise the icephobicity of oil-infused elastomer coatings.**

   This was carried out by measuring the ice adhesion and freezing delay, as defined in Section 1.2, but also included the additional methods of optical and SEM imaging, contact angle measurements and surface profilometry.

ii. **Observe the effect of damage on the coatings' icephobicity.**

   Via repeated de-icing cycles and imposed damage, the durability of the coatings was assessed. Imaging of the damage and its effect on the interface was carried out via optical microscopy, SEM and cryo-FIB/SEM.

iii. **Investigate the occurrence of interfacial slippage.**

This involved the development of an experimental method which allowed for visualisation of flow at the interface. To achieve this, a microtribometer was mounted under a microscope with fluorescent filters and the movement of fluorescent microparticles embedded at the interface was tracked during de-icing of a coating.

By combining the knowledge and understanding gained from these objectives, the chosen elastomer coatings are characterised with respect to their icephobicity, and interfacial slippage is shown (or otherwise) to be the fundamental source of the exceptional anti-icing behaviour.

The coatings studied are two polydimethylsiloxane (PDMS) coatings with different curing schedules; four PDMS/silicone oil infused coatings, made with oil of two different molecular weights and percentages; and a commercial coating, NuSil R-2180.

These findings will contribute to furthering the viability of elastomer coatings in real applications.

1.4. Structure of thesis

This thesis is split into nine chapters, including this introduction. Chapter 2 provides a literature review of past work on elastomer icephobic coatings. It reviews the metrics by which icephobicity can be quantified and presents analytical expressions for the fundamental science behind the two most common metrics, ice adhesion and freezing delay.

Chapter 3 introduces the first of the experimental sections, covering the selection and development of the elastomer coatings that were used in this study. This research focused primarily on PDMS, which was infused with silicone oil of two molecular weights, at two concentrations. A commercial icephobic polymer, NuSil R-2180, was also investigated. This section covers the reason for the choice of each coating as well as the development of the formulations and coating techniques used.

Chapter 4 presents the various characterisation techniques used. These include surface profilometry, contact angle measurements, elastic modulus, room temperature adhesion, optical microscopy and SEM. These additional techniques were employed

to better understand the icephobicity observations and identify any relationships between the variables.

Chapter 5 presents the first of the two icephobicity parameters: ice adhesion. The samples described in Chapter 3 were subjected to a push test to measure the adhesive strength of the ice-coating interface. The development of the testing method is discussed alongside data from the tests. The longevity of the coatings is also of considerable importance to commercial viability so 100 tests were carried out for each sample over the course of a year.

Chapter 6 presents the second of the icephobicity parameters: freezing delay. The coating samples were tested for freezing delay compared to aluminium. This chapter also includes a discussion of the development of the experimental procedure for these tests. Freezing delay tests were performed pre- and post-adhesion testing, to observe the effect of repeated de-icing cycles on the freezing delay of the different coatings. This is combined with theoretical calculations of the expected nucleation and growth rates for each coating.

Chapter 7 presents the results of specific damage testing on the icephobicity of the coatings. Each coating type was subjected to abrasive and cutting damage. The specimens were assessed for ice adhesion strength and freezing delay before and after the damage was applied. The specimens were then re-coated and re-assessed to determine if any performance degradation could be recovered. Cryo-FIB/SEM imaging was used to visualise the ice-coating interfaces and draw conclusions about the interfacial contact with damaged surfaces.

Chapter 8 presents the research carried into whether interfacial slippage is the source of the low ice adhesion strengths of these surfaces. This includes discussion of the extensive development of a new experimental method, which uses florescent microscopy to monitor surface layer movement of the polymer. The findings of this testing are presented and analysed.

Finally, Chapter 9, presents the conclusions drawn from the preceding chapters, and proposes possible future work.

2. Literature Review

Summary

A review is provided of the previous research carried out into the field of icephobic coatings, introducing hydrophobic, superhydrophobic and slippery liquid infused surfaces, before focusing on the study of oil-infused elastomer coatings, which are the subject of this study.

Methods for quantifying icephobicity are reviewed, with greatest emphasis placed on ice adhesion strength and freezing delay, although other metrics are discussed. The underlying science behind these metrics is presented. This includes analytical models for the prediction of ice adhesion strength and freezing delay.

2.1. Ice as a material

Ice is a crystalline solid, both found in nature and man-made. Though it is a common and familiar material, its properties and behaviour are in many ways unique. For example, ice is less dense than liquid water, allowing it to float. The low heat capacity of water and the high friction coefficient of ice mean that ice is susceptible to frictional heating, which allows for sliding and is leveraged in sports like ice skating (Hobbs, 1974).

This section reviews the structure of ice, as well as a selection of ice types relevant to this work.

2.1.1. The structure of ice

As stated, ice is a crystalline solid made from the regular arrangement of water molecules. In most natural conditions the molecules have a hexagonal arrangement, and this equilibrium phase is named ice I_h. This structure is presented in Figure 2.1 and is generally found when the pressure is greater than 0.2 GPa (2000 bar) and temperature is warmer than –200ºC. However, there are many other phases of ice possible, and a phase diagram of some ice phases is presented in Figure 2.2.

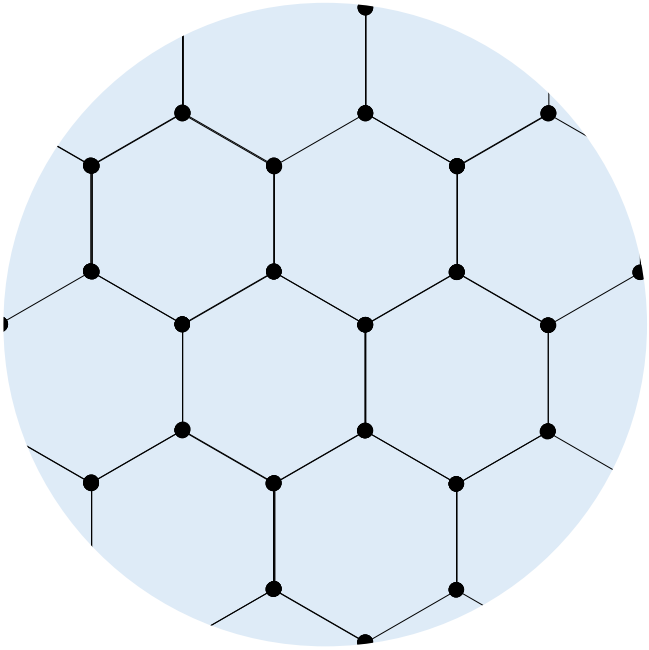

Figure 2.1 – Hexagonal arrangement of water. Each black dot represents an oxygen molecule, and the lines are the hydrogen bonds between the molecules.

The intermolecular bonding within ice is dominated by strong hydrogen bonds, the length of which is greater than the average spacing between amorphous liquid water molecules (Hobbs, 1974). For this reason, ice is, uncommonly, less dense than the liquid form of water.

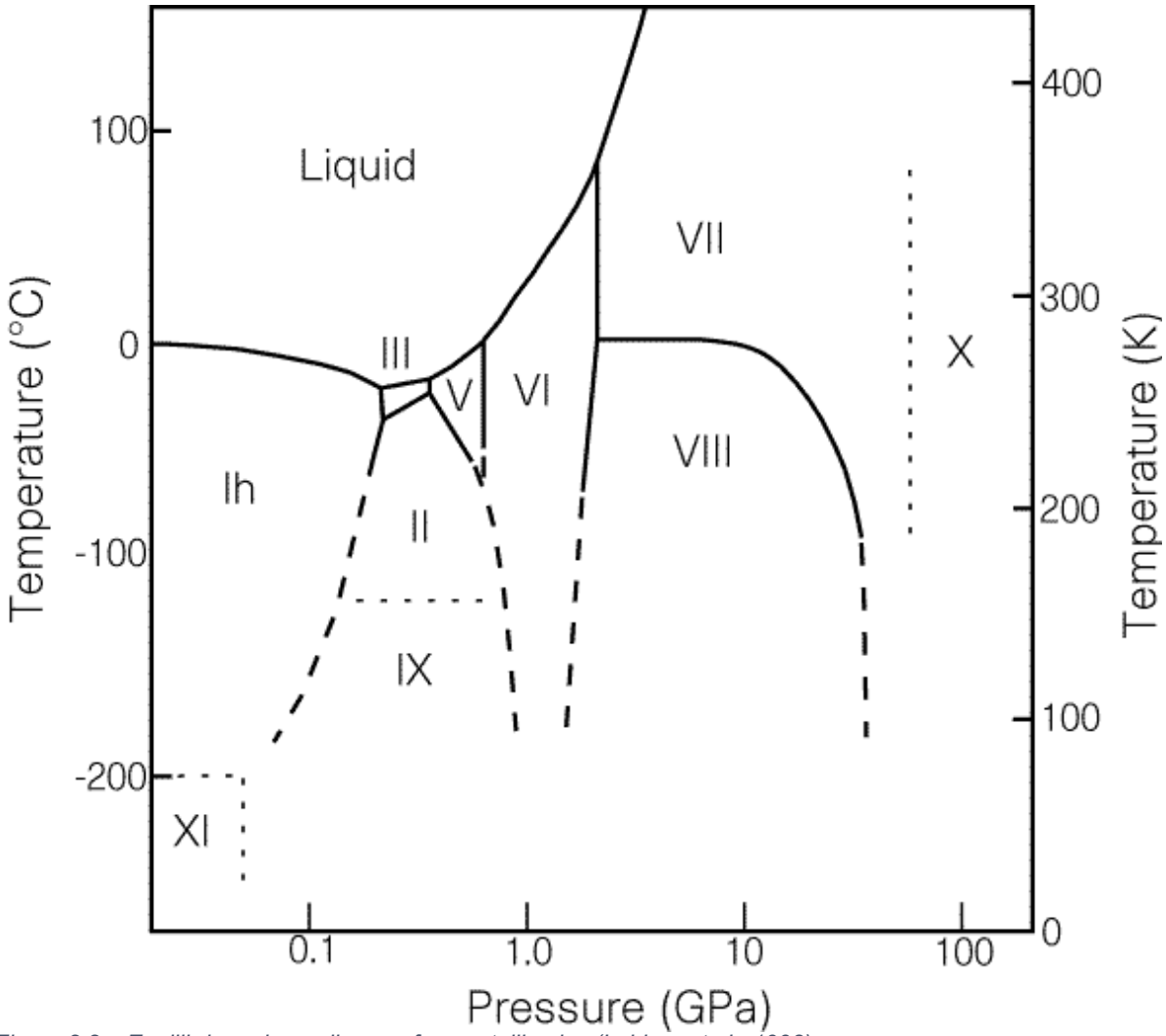

Figure 2.2 – Equilibrium phase diagram for crystalline ice (Lobban et al., 1998)

Ice also has a layer of liquid water at the surface at all times, called the quasi-liquid layer (QLL) or liquid-like layer (LLL), due to amorphousness of the outer molecules (Hobbs, 1974). An image of the QLL generated by molecular dynamics simulations is provided in Figure 2.3. This layer is around 10-100 nm thick, decreasing with increasing temperature, and complicates the interaction of ice with other surfaces. However, the layer is poorly understood, and further research would provide much needed knowledge on the interfacial properties and behaviour of ice.

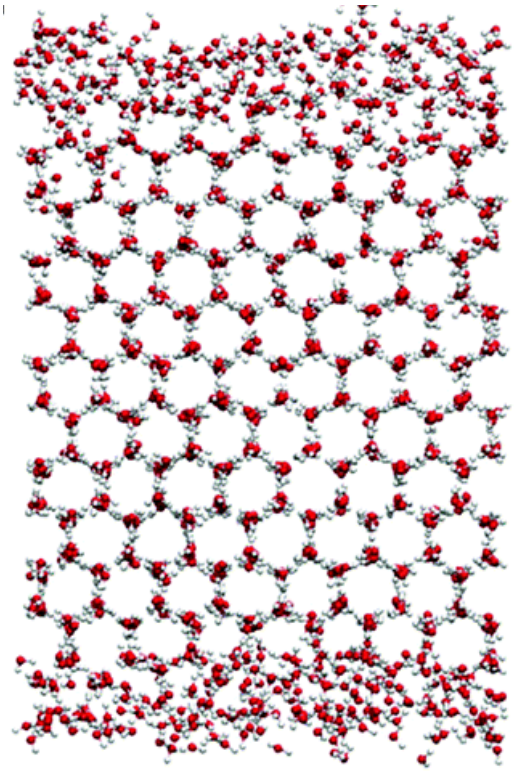

Figure 2.3 – Molecular dynamics simulation snapshot of the quasi-liquid layer formed at the outer surfaces of bulk ice I_h at T = 270 K. (Kim et al., 2020). The regular, hexagonal structure in the middle is the ice I_h, while the disordered molecules at top and bottom are the QLL.

2.1.2. Types of ice

2.1.2.1. Refrigerated ice

The ice exclusively used in this work is 'refrigerated' ice. This can be defined as ice formed from the slow cooling of warm, liquid water (>0ºC), which allows dense, bulk ice I_h to form. Ice cubes made in a freezer are an example of refrigerated ice. Refrigerated ice appears clear, though it may have some trapped air bubbles inside.

2.1.2.2. Environmental ice

Refrigerated ice is the most common type of man-made ice but is not often found in nature. Instead, most surface icing in the environment is formed from supercooled liquid water (<0ºC). This is normally possible in atmospheric phenomena, such as frost and clouds that produce freezing rain. Rime and glaze ice are the two types of ice most commonly formed in the environment and have structural differences that can make their physical properties and visual appearance quite different. Other types of ice can also form on surfaces, such as sea ice, but are less common than rime or glaze ice. It is also possible to get mixed glaze and rime icing.

2.1.2.2.1. Rime ice

Rime ice is formed when supercooled water droplets impact the surface and freeze on contact. This freezing is fast, in the order of microseconds, and normally occurs at lower temperatures (less than –10ºC) (Fortin and Perron, 2012).

Rime ice has lower density than refrigerated ice and glaze ice, because the droplets form discrete ice particles, with low packing density. The density has been measured as low as 200 kg/m^3 in some icing conditions (Macklin, 1962). The pockets of air within this form of ice make it appear white and textured. The poor packing density leads to lower contact area and weaker contact. Rime ice is weaker than glaze ice and is susceptible to cohesive fracture. An example image of rime ice is presented in Figure 2.4.

2.1.2.2.2. Glaze ice

Glaze is formed from the solidification of sheets of supercooled water, that may have formed from freezing rain. As the film of water is continuous, glaze ice has a higher density than rime ice, which is similar to refrigerated ice, up to 900 kg/m^3 (Poots and Makkonen, 2000). The freezing rate is in the order of milliseconds, and normally occurs at warmer temperatures (greater than –10ºC) (Fortin and Perron, 2012). Droplets are generally larger than in rime ice (Poots and Makkonen, 2000).

Glaze ice appears very clear, though there may be some trapped bubbles of air which make it appear white in places. Glaze ice generally has good contact with the surface. An example of glaze ice is presented in Figure 2.4. Icicles are another example of glaze ice.

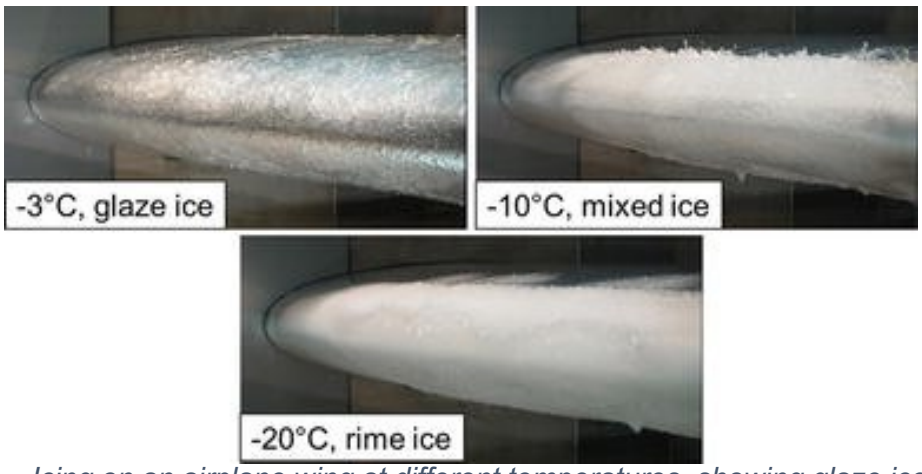

Figure 2.4 – Icing on an airplane wing at different temperatures, showing glaze ice formed at –3ºC, rime ice formed at –20ºC and mixed icing at –10ºC (Endres et al., 2017).

2.2. Definition of icephobicity

The term icephobicity has become commonly used in the field recently. Though there is no formalised definition of the word amongst the field, the definition that is adopted here is 'resistance to accumulation of ice'.

2.3. Development of icephobic coatings

Ice accumulation has been an issue throughout human history. From the very mundane – making pavements slippery, to the catastrophic – causing airplane crashes. Active de-icing, in which ice is removed by human intervention, has long been the most common solution. However, as wider technological progress has been made, there has been a desire to prevent ice accumulation in a more efficient way, using passive coatings. Passive coatings could reduce, or eliminate, the requirement for active de-icing, saving time, money, labour, and other resources. They would also be preventative rather than reactive, considerably reducing the risks of ice accumulation.

The development of anti-icing coatings has seen successive improvements over the past 100 years, with acceleration especially in the last 30 years (Kreder et al., 2016). This section will review the major milestones in the field.

2.3.1. Hydrophobicity and the Young-Dupré equation

Much of the development of icephobic coatings originated from a basic fact: ice is the solid form water. It should therefore follow that if a coating is water resistant it will be ice resistant. Resistance to wetting by water is hydrophobicity and has seen much more extensive study, dating back to early, fundamental studies on solid-liquid interactions. Young's observations of equilibrium droplet wetting on solid surfaces was first published in 1805 (Young, 1805). Described mathematically, it gives the following relationship:

$$\gamma_{sv} = \gamma_{sl} + \gamma_{lv} \cos\theta \tag{2.1}$$

Where γ_{sv} is the surface energy of the solid, γ_{sl} is the interfacial energy between the solid and the liquid, γ_{lv} is the surface tension of the liquid and θ is the contact angle of the droplet. This relationship is presented graphically in Figure 2.5.

The Young equation implies that if attraction of water molecules to the surface is high the droplet will spread, leading to a contact angle < 90°. Conversely, if the water droplets are weakly attracted to the surface, it will act to minimise the contact area and

the contact angle will be > 90°. When the contact angle is greater than 90° the surface is hydrophobic, and hydrophilic when it is less than 90°.

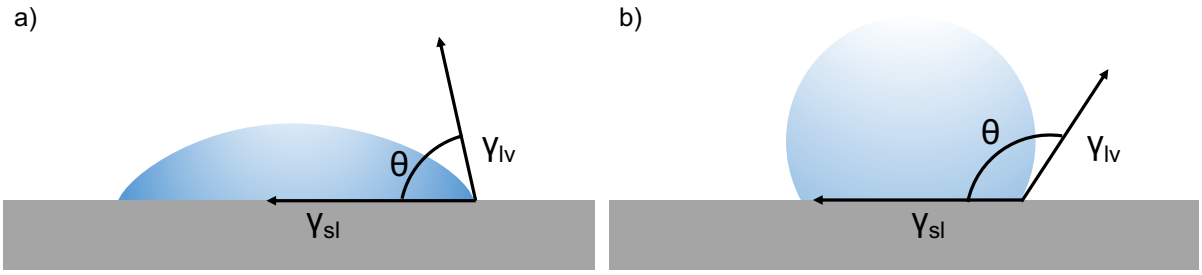

Figure 2.5 – The water contact angle, θ, gives an indication of the hydrophobicity of the surface. When θ < 90° the surface is hydrophilic, as shown in panel a). In panel b) θ > 90° and the surface is hydrophobic. In the system shown here, γ_{lv} and γ_{sl} are the liquid-vapour and solid-liquid interfacial energy, respectively.

Hydrophobicity is widely found in nature, and this has inspired many of the original hydrophobic coatings utilised by society. For example, beeswax has long been used as a water repellent surface treatment on textiles.

Building on Young's work, the Young-Dupré equation was derived to determine the work of adhesion, W_A, between the droplet and the solid. Work of adhesion is a measurement of the energy required to separate two surfaces. It was described by Adam (1957) as:

$$W_A = \gamma_{lv}(1 + \cos\theta) \tag{2.2}$$

As the work of adhesion is a measure of the energy required to separate two surfaces, reducing it will decrease the wetting of a surface. Hydrophobicity is therefore dependent on the surface chemistry of a material, as the molecular attraction is governed by the chemical structure of the solid. Hydrogen bonding, van der Waals and electrostatic forces can all contribute to the interfacial energy.

The energy required to remove a droplet on a surface can therefore be lowered by lowering the surface energy of the solid substrate. Significant research has been carried out in the aim of reducing surface energy as much as possible. Low surface energy coatings boomed with the dawn of polymer synthesis and have become some of the most widely used polymer coatings. The most notable example of this is Teflon, or polytetrafluoroethylene (PTFE) which has an exceptionally low surface energy and has become a ubiquitous non-stick coating.

Fluorinated hydrocarbons like PTFE and others, have shown excellent hydrophobicity and were some of the first coatings examined for icephobicity, on the assumption of their similarity. However, most studies have found that Teflon based coatings only reduce the adhesion strength to around 300 kPa, down from approximately 1600 kPa on bare aluminium (Susoff et al., 2013). Additionally, the use of fluoropolymers is often considered unfavourable due to the concerns over the environmental and health effects of fluoropolymer production and use. Icephobicity test results for PTFE have been mixed, showing some improvement compared to high surface energy materials like metals, but not a significant reduction in ice accumulation (Cao et al., 2020, Jafari et al., 2016).

As there is a limit to which the surface energy of a solid can be lowered by adjusting the chemistry, further strategies for anti-icing have been explored.

2.3.2. Superhydrophobicity

With improvements in polymer synthesis and processing technology, as well as high resolution microscopy, SEM, TEM, etc., the next development in icephobicity came again from natural inspiration. Continuing in the assumption that hydrophobicity provides a route to icephobicity, research focused on surfaces with exceptional water resistance, such as lotus leaves (Koch et al., 2009), butterfly wings (Bixler and Bhushan, 2013) and shark skin (Liu and Li, 2012).

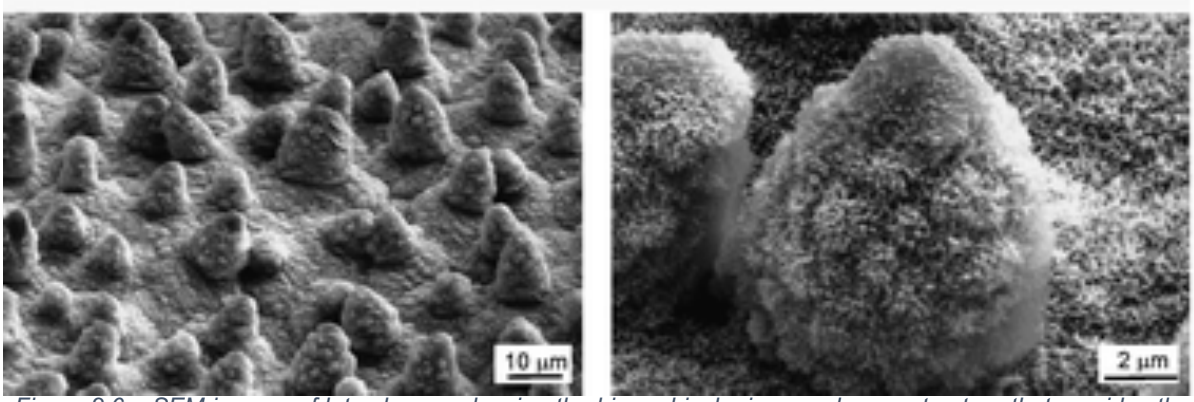

Figure 2.6 – SEM images of lotus leaves showing the hierarchical micro- and nano-structure that provides the hydrophobic behaviour which has inspired the design of synthetic superhydrophobic surfaces (Koch et al., 2009).

Examination of these surfaces through SEM imaging, such as in Figure 2.6, revealed that they have very particular surface morphology. The image in Figure 2.6 shows the surface of a lotus leaf. The leaf is covered in micropillars, which themselves have a secondary, nano-scale roughness. These surfaces are far from the ideal, smooth

surfaces of Young's equation and it is this hierarchical roughness that is the source of the exceptional water resistance. Rather than increasing the real area of contact, the pillars hold the droplets above the surface. The air below the droplets provides a low energy buffer layer and the interfacial contact between the droplet and the solid surface is limited to the small area of the tips of the hierarchical structures. Reducing the interfacial contact area in turn reduces the energy required to remove a water droplet.

2.3.2.1. Complex wetting states

When droplets sit suspended above a surface they are said to be in the Cassie-Baxter wetting state. This ability is dependent on the surface tension of the droplet, interfacial energy between the droplet and the solid, the precise geometry of the pillars and their spacing on the surface (Bonn et al., 2009). Extensive studies have been carried out to optimise these factors. The use of hierarchical roughness has allowed for the development of surfaces with contact angles > 150° (Kreder et al., 2016). Surfaces that meet this requirement have since been labelled superhydrophobic surfaces (SHS). SEM images of water droplets in the Cassie-Baxter wetting state on a superhydrophobic surface are presented in Figure 2.7.

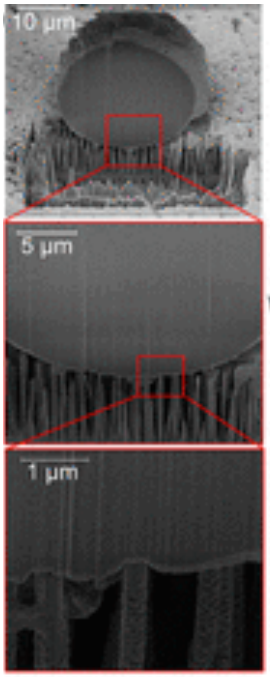

Figure 2.7 – SEM imaging of a water droplet on a silicone nano-wire superhydrophobic surface, exhibiting Cassie-Baxter wetting (Rykaczewski et al., 2012).

However, Cassie-Baxter wetting is a meta-stable state, and is liable to transition to the stable Wenzel wetting state under external force, such as impact or pressure changes (Murakami et al., 2014). The Wenzel state describes full or partial penetration of the droplet and the surface, leading to an increase in the real area of contact and the energy for removal. Graphical representation of both wetting states is provided in Figure 2.8, but both states are summarised briefly here:

i. **Cassie-Baxter wetting:** The water droplet sits on top of the surface textures and does not penetrate the features. There is reduced real contact area between the coating and the droplet, which will lessen the force required for removal. Cassie-Baxter wetting is described by (Cassie and Baxter, 1944):

$$\cos\theta^* = -1 + \phi_s\,(\cos\theta + 1) \tag{2.3}$$

Where θ^* is the apparent contact angle and φ_s is the fraction of the droplet's surface area in contact with the solid.

ii. **Wenzel wetting:** The water droplet penetrates partially or completely into the surface texture. This will increase the real contact area between the coating and droplet, increasing the required force for detachment. Wenzel wetting is described by (Wenzel, 1936):

$$\cos\theta^* = r\cos\theta \tag{2.4}$$

Where r is the ratio of the true surface area to the projected surface area (Kreder et al., 2016).

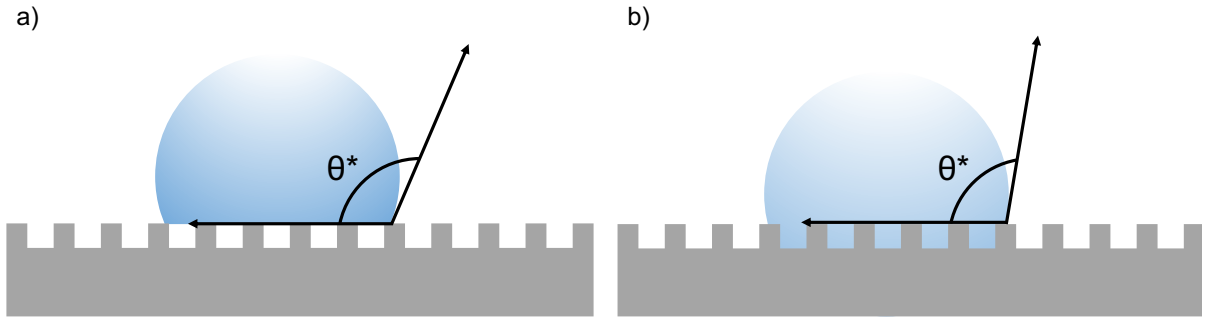

Figure 2.8 – Wetting states of a water droplet on textured, superhydrophobic surfaces. The water droplet can either be in a) Cassie-Baxter, or b) Wenzel wetting states. The apparent contact angle, θ, is greater in Cassie-Baxter wetting for a surface of the same chemical composition.*

2.3.2.2. Superhydrophobic coatings

SHS can be produced either by applying a coating on top of a substrate or removing some of the surface material to create a hierarchical texture, for example by chemical etching (Saleema et al., 2011a) or laser processing (Guo et al., 2021). They can have well defined geometries or irregular structures, depending on the fabrication method.

The fabrication technique is itself dependent on the material choice and application. Hundreds of SHS have been fabricated in many materials, as the only requirement is a morphology that can support the Cassie-Baxter wetting state. Some success has been achieved in making superhydrophobic surfaces in metals (Saleema et al., 2011b) which have the added benefit of being durable and wear-resistant compared to polymer coatings. They can also be used in situ on pipework and on other metal surfaces without requiring an additional coating that may hinder other performance factors, for example by increasing the weight of a system. This also removes other considerations when applying a coating, such as adhesion to the substrate and some environmental concerns.

Hierarchical roughness of metallic surfaces has shown improvement to their hydrophobicity, but due to their high surface energies and wetting affinity, the transition from the Cassie-Baxter to Wenzel wetting states is favoured and their superhydrophobicity is less stable than in low surface energy materials.

Excellent superhydrophobicity has been achieved when combining low surface energy materials, like fluorocarbons and silicone polymers, and hierarchical roughness (Farhadi et al., 2011). These materials have water contact angles of > 150°, and very low droplet roll-off angles (Kreder et al., 2016) The energy required to remove water droplets from these surfaces is negligible and wetting is virtually non-existent.

One issue with the use of SHS is their poor durability. The roughness can be very delicate and susceptible to wear. As damage to the surfaces progresses, the efficacy of the coatings deteriorates, and the wetting is likely to transition to Wenzel wetting. This is made worse when the superhydrophobic surface is made from a soft system with little wear resistance, like soft polymer coatings. Depending on the real contact area that may arise, damaged superhydrophobic surfaces can have higher contact areas than smooth surfaces. Furthermore, the surfaces are often difficult to repair due to the specificity of their morphology and fabrication methods.

2.3.2.3. False equivalence of hydrophobicity and icephobicity

The other issue with using superhydrophobic surfaces is the underlying assumption that icephobicity and hydrophobicity are analogous. Hejazi et al. demonstrated that, as the fundamental mechanical responses of solids and liquids are different, icephobicity and hydrophobicity cannot be considered equivalent. Liquids are completely viscous and cannot resist shear stresses (Hejazi et al., 2013), so will roll off surfaces under much less force than solid ice droplets. The mechanical removal of ice will thus accelerate damage to SHS compared to the removal of liquid droplets.

SHS have shown mixed ability to lower ice adhesion strength (Kreder et al., 2016). Some studies have reported very low ice adhesion strength, but others have shown an increase in the ice adhesion strength. It has been posited this is due to a change in wetting states. There is some suggestion that, even if a water droplet maintains Cassie-Baxter wetting until freezing, there may be local expansion of the ice into the features during freezing, or frost formation from humid air inside the surface texture. There is much contrasting evidence in the field that is yet to be resolved.

It has also been demonstrated that ice nucleation can be promoted on surfaces with certain morphologies (Campbell et al., 2017). For example, microgrooves, that support Cassie-Baxter wetting, can encourage ice formation (Bi et al., 2017, Lo et al., 2017, Li et al., 2018). Combined with the possibility of interlocking or increased interfacial contact in the Wenzel state, the use of SHS can actually be detrimental to the icephobicity of a surface, compared to the chemically equivalent flat surface.

2.3.3. Slippery Liquid Infused Porous Surfaces

Building on the research into SHS, the next development in icephobic coatings was the creation of slippery liquid infused porous surfaces (SLIPS). SLIPS were designed to address a primary weakness of SHS – the instability of the vapour within the textured surfaces, which can lead to Wenzel wetting when disturbed (Wong et al., 2011). Like SHS, they utilise micro/nano-textured surfaces with a fluid in between the structures to reduce the contact area between the solid surface and the water. In SLIPS, the fluid used is a lubricating liquid, which typically has better stability than air (Kreder et al., 2016).

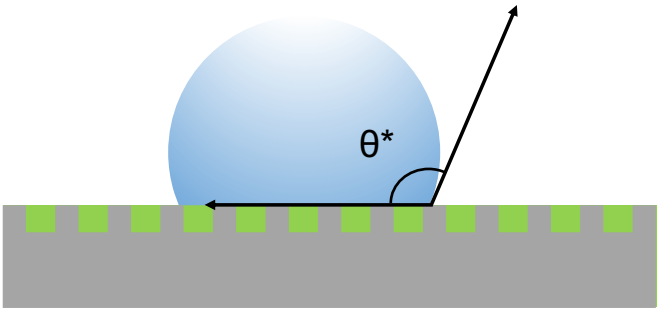

Figure 2.9 – Water droplet on a SLIP surface, in Cassie-Baxter wetting state.

SLIPS have shown remarkable improvements to hydrophobicity and in some cases have also shown incredibly low ice adhesion strengths, frequently < 20 kPa, allowing the ice to slide off under very low shear forces. In the ideal case, the ice can be removed under its own weight, wind, or vibration. A schematic of a water droplet on SLIPS is presented in Figure 2.9 and SEM images of water and ice on SLIPS are presented in Figure 2.10.

In addition to requiring a higher displacement pressure than air, the lubricating liquid may coat the surface features themselves, promoting the sliding of droplets over the surface.

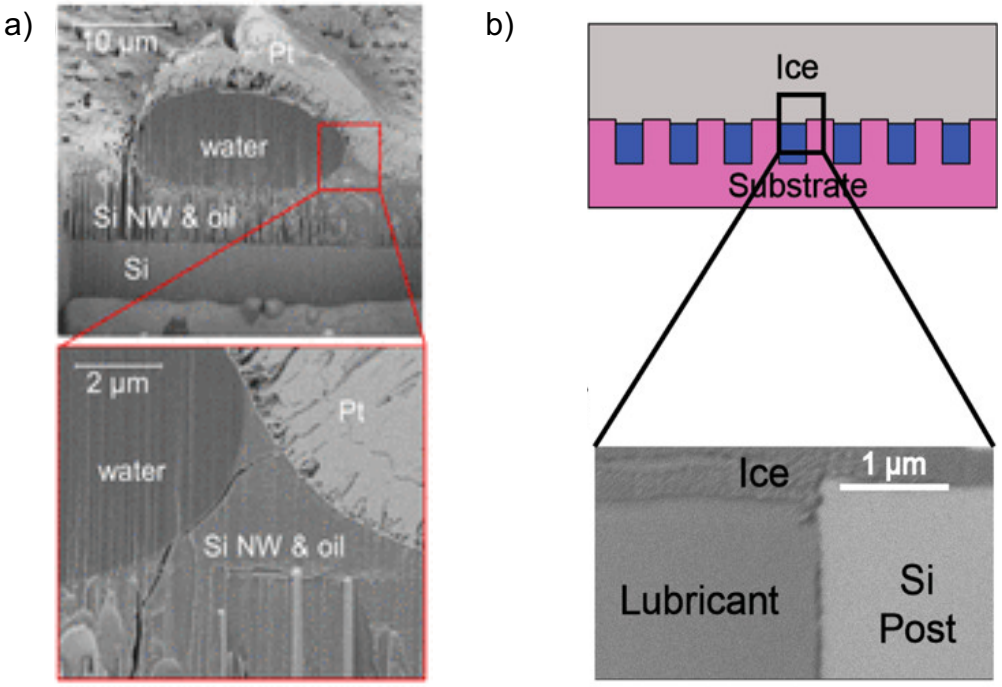

Figure 2.10 – SEM images of a) a water droplet (Rykaczewski et al., 2012) and b) an ice layer (Subramanyam et al., 2013), sitting on a SLIP surface.

Despite having better icephobicity than SHS, SLIPS still have some drawbacks:

- SLIPS require complex, specifically designed surface textures to retain the liquid on the surface. This requires more complicated fabrication techniques, whereas some SHS can be spray coated.
- Eventually the liquid will leach from the surface, either from being wicked away during droplet removal, or by passive leaking from the textures. Liquid replenishment from subsurface reservoirs will lengthen their usefulness, but eventually they will require lubricant reapplication to maintain icephobicity.
- Like SHS, the hierarchical roughness can be very delicate. Damage can lead to reduction in hydrophobicity/icephobicity.
- The lubricating liquid must be carefully chosen. The priority is hydrophobicity of the liquid, but as it will slowly drain from the surface, the environmental impact of the liquid must be considered alongside any chemical interactions it may have with the surface and the ice.

2.3.4. Smooth oil-infused elastomers

In response to the disadvantages of SHS and SLIPS, and in an effort to improve icephobicity rather than the hydrophobicity, alternative approaches have been investigated. Recognising that the hierarchical structures have inherent drawbacks, a return to smooth surfaces was sought. Smooth surfaces are defined here as having no engineered surface roughness. As previously discussed, fluoropolymers are one such example, but have limited effectiveness in reducing ice adhesion.

Subsequent research has focused on the use of silicone polymers, which have similarly low surface energy. Polydimethylsiloxane (PDMS) is the simplest of the silicone polymers, with two methyl groups on the silicone-oxygen backbone, as presented in Figure 2.11.

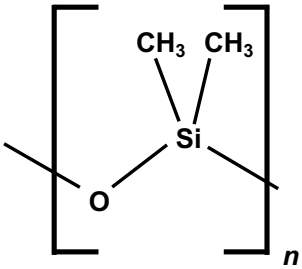

Figure 2.11 – PDMS monomer.

Though a benefit of polymer coatings is the ability to tailor the functional groups on the polymer chain, much of the research into silicone polymers for icephobic purposes has used PDMS as the focus, for its simplicity and widespread availability. PDMS is widely used in both consumer and industrial applications as a rubber and is popular for its resistance to heat, UV, and chemical attack. PDMS coatings are elastomers formed from cross-linking of polymer chains. Without adjusting the chemical formulation of an elastomer, the physical properties can be adjusted by varying the cross-link density.

The findings from early icephobicity studies on PDMS showed a minor improvement on Teflon, showing an average adhesion strength of 200 kPa (Susoff et al., 2013). However, PDMS is very soft and is not often considered viable for long term coatings due to issues of durability and wear. To combat this, attempts have been made to strengthen the material, such as mixing it with a tougher polymer (Zhuo et al., 2018); or making a composite with a harder material to increase abrasion resistance (Huovinen et al., 2014), introducing self-reparability (Cui and Pakkanen, 2020) or increasing the cross-linking density of the PDMS (Galliano et al., 2003).

Despite improving the durability of PDMS, all these methods of toughening the polymer typically result in a decrease in icephobicity. For this reason, some studies have investigated the effect of reducing the cross-linking density of PDMS to improve icephobicity. Though different methods have been utilised, the findings of Golovin et al. (2016) are perhaps the most exceptional. They utilised PDMS infused with silicone oil to achieve ice adhesion strengths < 20 kPa. Other groups have since found similar results when investigating other oil-infused silicone coatings (Beemer et al., 2016, Wang et al., 2017, Urata et al., 2015, Irajizad et al., 2019a, Gao et al., 2019). However, this behaviour is not limited to silicone-based polymers and has also been demonstrated in polyurethane coatings (Sivakumar et al., 2019, Golovin and Tuteja, 2017).

Oil-infusion is achieved by mixing an unreactive, miscible oil into the elastomer mixture before curing. This inhibits cross-linking, a diagrammatic representation of which is presented in Figure 2.12.

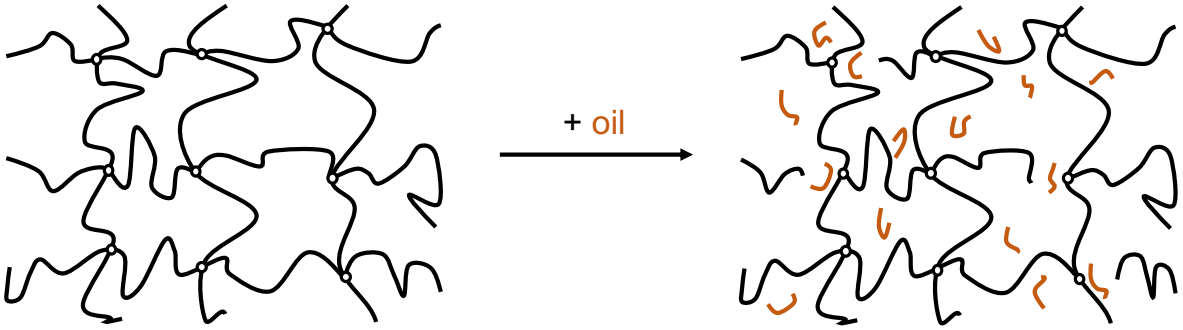

Figure 2.12 – Simplified diagram of the effect of adding oil (in brown) to the pre-polymer mixture (in black) before curing. Instead of a very complete cross-linked network, the oil molecules interrupt the cross-linking and are also available as free chains. Cross-link sites are indicated by circles.

The density of the cross-links has been shown to directly relate to the toughness of a polymer – the more cross-links, the better the elastomer is at distributing energy throughout the polymer, and the more bonds which must be broken to deform the material. When cross-linking is reduced the elastomer becomes softer, weaker, and more viscous. In effect, as cross-linking falls, the elastomer becomes closer in properties and behaviour to a liquid polymer melt. Irajizad et al. showed the extent of this in creating an elastomer gel with high weight percentage of oil that was incapable of withstanding abrading forces of 1 N (Irajizad et al., 2019a).

Despite their poor mechanical durability, smooth oil-infused elastomers have shown some of the most promising icephobicity. They are much easier to produce than SHS and SLIPS, and as they are of uniform composition throughout, the consequences of wear are lessened. They provide similar ice adhesion strengths to SLIPS and better long-term viability (Kreder et al., 2016).

2.3.5. Other coating strategies

Other, more chemically complex coatings have also been investigated for anti-icing solution, a selection of which are briefly summarised here. These technologies all show promising icephobicity but have disadvantages when compared to smooth oil-infused elastomers that have been incompletely addressed.

i. Antifreeze coatings

Based on the ability of biological organisms such as fish to survive in freezing environments by generating anti-freeze proteins in their blood, the application of anti-freeze chemistries on a surface has shown some success in suppressing ice formation (He et al., 2018a). The benefit is two-fold. The anti-freeze molecules bind to ice nuclei

and prevent them from growing (Liu et al., 2016) and the liquid water trapped on the surface then provides a lubricating layer that inhibits adhesion of any ice droplets.

However, both biological anti-freeze proteins (Voets, 2017) and synthetic analogues (Hederos et al., 2005) are more complicated to synthesise and apply, and anti-freeze proteins are susceptible to denaturing (Eskandari et al., 2020). As the temperature falls and the thermodynamic driving forces for nucleation become greater, their efficacy will decrease (Griffith and Yaish, 2004), reaching a theoretical limit at the homogenous nucleation threshold of approximately –40°C (Hobbs, 1974).

ii. Photothermal coatings

Photothermal coatings present a slight departure from the other approaches to reducing formation. By combining insulating, low surface energy materials with photothermal compounds, such as carbon nanotubes (Zhou et al., 2022, Liu et al., 2020, He et al., 2022, Jiang et al., 2018), candle soot (Wu et al., 2020) or iron oxide particles (Jamil et al., 2021, Wu et al., 2019, Yin et al., 2015), thermal energy from the sun is absorbed, trapped and redirected to any ice that has accumulated on the surface, promoting melting and easier removal of ice.

Though this is a very promising technology it is limited by the efficiency of the thermal transfer and must ensure thermal losses into the surroundings are not too great. It is also hindered by the simple fact that snow and ice arise mostly in winter when climates suffer from lack of sunlight. The coatings are therefore limited in their usefulness at night, or in days with weaker solar radiation at ground level. Therefore, they are perhaps best used in combination with other anti-icing strategies that are not sunlight dependent.

iii. Brush-like surfaces

Taking further inspiration from the view that the closer a surface is to a liquid the lower the ice adhesion strength, brush-like surfaces have received some interest. These surfaces chemically graft macromolecules at one end to the desired surface, leaving the other end free to move. These macromolecules can be chemically complex, but very low ice adhesion strengths have also been achieved when using simple PDMS-based brushes (Zhao et al., 2021, Zheng et al., 2022, Zhao et al., 2022, Li et al., 2022).

Brush-like coatings can also demonstrate higher contact angles and lower roll-off angles of liquid droplets compared to oil-infused elastomers.

However, their long-term durability has been under-researched, and their primary disadvantage is their application methods. Most brushes require multiple synthetic steps and more complex surface preparation to graft the coatings. This makes them more expensive to generate than oil-infused elastomers and leads to unanswered questions about their repairability. However, they remain promising solutions for the future, and have shown added functionality in the ability to incorporate end-groups with anti-freeze properties (He et al., 2020a, He et al., 2016).

2.4. Icephobicity metrics

A standardised method of quantifying icephobicity has not been developed. Icephobicity, as described in Section 2.1, describes a material's resistance to ice accumulation. The methods by which it can be quantified are varied. The most commonly used metrics are described here.

2.4.1. Ice adhesion

Ice adhesion can be defined as the force required to remove ice from a surface. The lower the ice adhesion strength the less force required to remove the ice. This is the most used method of measuring icephobicity and there is a broad consensus that for a coating to be classified as icephobic, ice adhesion strength must measure < 100 kPa (Hejazi et al., 2013, Golovin et al., 2016, Janjua et al., 2017). Some take this further and state that true passive de-icing is only possible below 20 kPa (Kreder et al., 2016, Dou et al., 2014, Jamil et al., 2019) or 10 kPa (Beemer et al., 2016, He et al., 2017b). At these values of ice adhesion, ice can be removed by its own weight, wind, or vibration.

This section will review the methods for measuring ice adhesion strength, and the detachment models which are mostly commonly used to describe ice adhesion strength.

2.4.2. Measurement methods

Despite extensive research on the topic, ice adhesion testing lacks standardisation, affecting the ability to compare between research groups and studies. Arguments have been made for standardisation (Bleszynski and Clark, 2021, Hakimian et al., 2020, Mulherin et al., 1998, Rønneberg et al., 2019a), or adoption of a unifying framework

(Irajizad et al., 2019b). In the meantime, a range of test methodologies continues to be employed, which offers a broader, more inclusive perspective.

The most significant difference between studies is the test geometry. The most common methods include the 'push' test, 'zero-degree cone' test, lap shear test and centrifugal test. These geometries are reviewed below and more comprehensively in the literature (Bleszynski and Clark, 2021, Kasaai and Farzaneh, 2004, Tetteh et al., Rønneberg et al., 2019a, Work and Lian, 2018).

As will be discussed in Chapter 5, the geometry adopted in this study is the 'push' test.

i. Push test

In the push test geometry, demonstrated in Figure 2.13, ice is frozen in a mould on the coating surface. A probe arm is then brought into contact with the ice and mould, moving at a constant speed. Upon contact, the force exerted on the ice by the probe rises to maintain the speed. When the force applied to the ice exceeds the adhesion strength, the ice is detached from the coating.

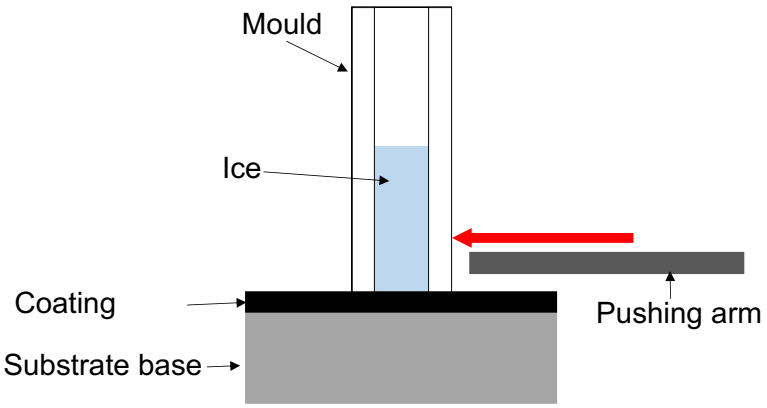

Figure 2.13 – Ice adhesion push test geometry, showing ice frozen in a mould on the coating surface and displaced by a probe arm.

This is the most commonly adopted ice adhesion test methodology (Meuler et al., 2010), as it only requires a force probe. However, the specifics of the geometry lead to torque on the specimen and unequal stress distributions across the surface (Work and Lian, 2018). The stress concentration at the front edge of the interface means the measured detachment force is smaller than would be expected in a purely shear (Mode 2) fracture.

ii. Zero-degree cone test

The zero-degree cone method (Figure 2.14) utilises a coated pin placed inside a hollow cylindrical substrate. Ice is frozen around the pin, the pin is pulled out of the mould at constant speed and the peak detachment force is measured (Haehnel and Mulherin, 1998).

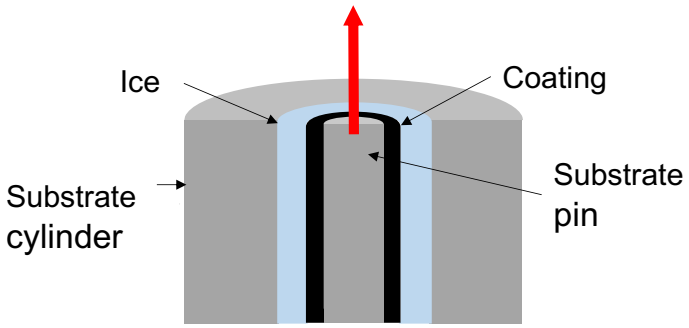

Figure 2.14 – Zero-degree cone test, in which ice is frozen around a coated pin within a larger, uncoated substrate cylinder. The pin is pulled out of the ice, generating shear stress.

Unlike the push test geometry, the shear force is applied over the interfacial contact area and generates purely shear detachment. However, the geometry requires more specialised testing equipment, and there is concern that the constrained expansion of ice within the mould during freezing may influence the required detachment force by introducing stress concentrations within the ice (Makkonen, 2012, Yavas et al., 2019). Strong ice adhesion on the uncoated substrate is also required to ensure the ice detaches from the coated pin.

iii. Lap shear

The lap shear adhesion test uses a standard lap test geometry (Figure 2.15), in which the ice in a mould is frozen between a coated lap joint and an uncoated lap joint. One of the joints is then pulled, applying shear stress across the interface. When the shear force exceeds the adhesion strength at the more weakly adhered joint (the coated joint), it will preferentially detach at that interface. Double lap shear joints have also been utilised (Ferrick et al., 2006).

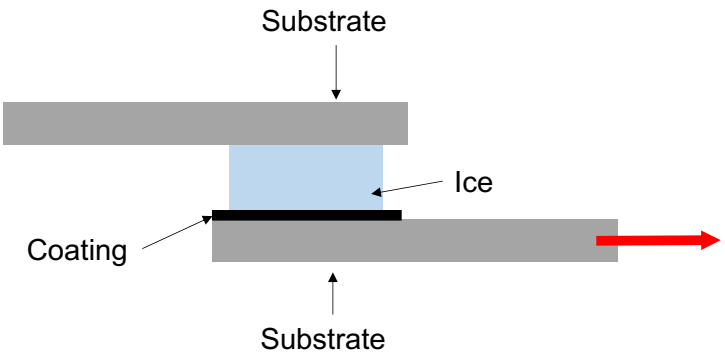

Figure 2.15 – Lap shear ice adhesion test geometry, with the ice frozen in a mould between one coated and one uncoated substrate. The coated lap shear joint is pulled away to detach the ice from the surface.

The lap shear test geometry has many similarities to the zero-degree cone method: pure shear stress, specialised testing equipment and a requirement for good adhesion to the uncoated substrate. There is the additional consideration of how to freeze the ice in place. This normally involves filling the mould completely with water on one of the lap joints, allowing it to freeze, removing the mould and then melting the ice onto the other lap joint (Laroche et al., 2020, Work et al., 2018).

iv. Centrifugal

In centrifugal ice adhesion testing (Figure 2.16), supercooled water is sprayed onto a coated arm and allowed to freeze. The coated arm is then spun at increasing speed, until the shear force on the ice overcomes the adhesion strength and the ice slides off.

Centrifugal testing is the second most commonly used test geometry. Researchers at the Anti-icing Materials International Laboratory (AMIL) have carried out centrifugal tests on hundreds of specimens (Guerin et al., 2016, Laforte and Beisswenger, 2005, Laforte et al., 2015).

The primary benefit of this method is that it provides the greatest similarity to real icing and de-icing processes. Rather than using refrigerated ice, environmental ices such as glaze and rime ice (Rønneberg et al., 2019b) can be generated when the centrifuge is combined with methods for generating supercooled water, like a wind tunnel.

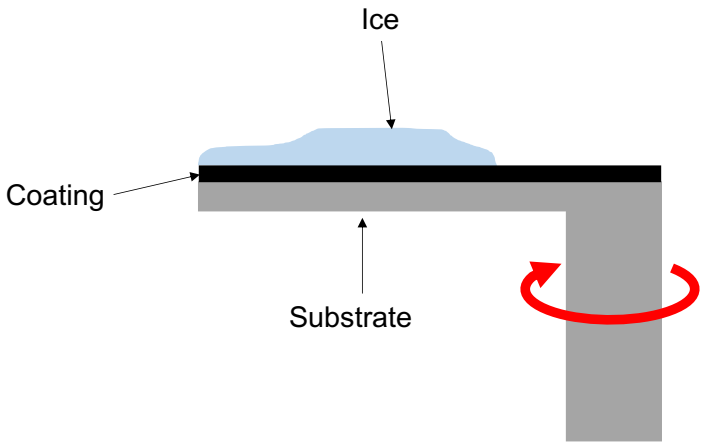

Figure 2.16 – Centrifugal ice adhesion geometry, in which ice is frozen on top of a coated arm which is then spun at increasing speed to detach the ice.

However, this equipment is not widely available, so comparison to results from other laboratories is difficult (Rønneberg et al., 2019c). The calculation of the adhesion strength is also complicated by the irregular contact area that arises during deposition of the ice, requiring accurate visualisation and measurement of the interfacial area.

2.4.2.1. Adhesion models for ice push tests on elastomer coatings

Adhesion theory is based on the fundamental observation that when the external force bringing two surfaces into contact is removed, the surfaces may stay in contact until force is applied to separate them. This is particularly true on soft, deformable surfaces which demonstrate high surface conformation, such as elastomer coatings.

Beyond the mechanical and chemical properties of the interacting surfaces, macroscale ice adhesion is further complicated by interdisciplinary considerations and non-ideal surfaces, such as the interfacial geometry (Memon et al., 2020), fracture mode (Work and Lian, 2018), strain rates (Kim et al., 2007b, Wang et al., 2014a), temperature (Emelyanenko et al., 2020, Andrews et al., 1984) and the freezing conditions (Rønneberg et al., 2019b). Though the interplay of some of these factors has been investigated (Wang et al., 2018a, Makkonen, 2012, Fortin and Perron, 2012), there remains no unifying equation describing ice adhesion.

Instead, more specific adhesion models are often used. For ice adhesion on oil-infused elastomer coatings, measured by push tests, two detachment models are commonly proposed, interfacial cavitation and interfacial slippage, which are discussed here.

2.4.2.1.1. Interfacial cavitation

Building on Kendall's work for adhesion to elastic solids (1971), Chaudhury and Kim (2007) proposed that the detachment for a rigid slab in contact with an elastic solid under shear is achieved through cavitation at the interface.

The relationship is described by:

$$\sigma_A \propto \sqrt{\frac{W_A G}{l}} \tag{2.5}$$

Where σ_A is adhesion strength, W_A is the work of adhesion, G is the shear modulus and l is the coating thickness. W_A is defined via the Young-Dupré equation (Adam, 1957) as:

$$W_A = \gamma(1 + \cos\theta) \tag{2.6}$$

Where γ is the water-air surface tension and θ is the water-coating static contact angle.

Shear modulus, G, can be determined from the elastic modulus, E, and Poisson's ratio, ν, via the relationship for a homogeneous, isotropic material:

$$G = \frac{E}{2(1+\nu)} \tag{2.7}$$

The model supposes the shear force applied parallel to and above the interface causes the front edge to lift, and the adhesive forces bring the soft coating up with it. The front edge of the coating is then under tension, which is released when the adhesive forces are overcome. The mismatched shear moduli cause instability, and a wave of trapped air cavities is formed along the interface, detaching the ice from the surface (Kendall, 1971, Ghatak et al., 2005, Chaudhury and Kim, 2007, Beemer et al., 2016). A graphical representation of this behaviour is presented in Figure 2.17.

This model has been applied by many in the field of ice adhesion to smooth elastomer coatings with good agreement (Beemer et al., 2016, He et al., 2018b, Wang et al., 2014a, Urata et al., 2021, Xie et al., 2021)

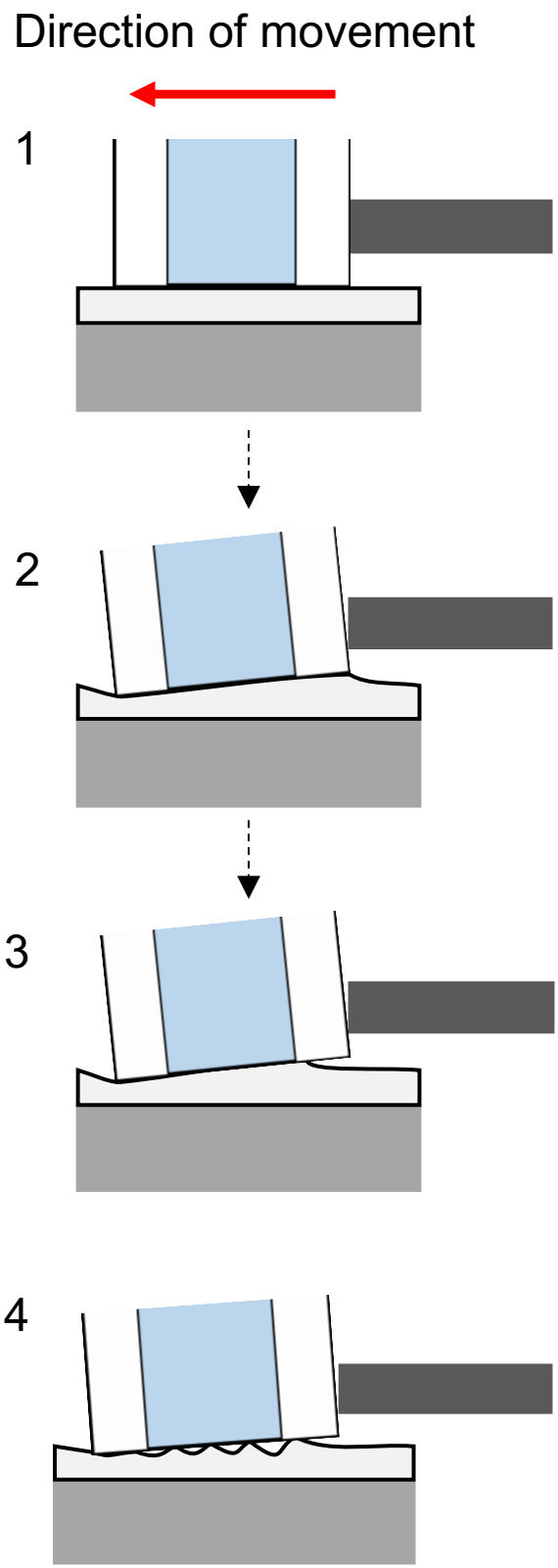

Figure 2.17 – Visualisation of interfacial cavitation process 1) probe contact causes initial lateral elastic deformation; 2) torque on the ice cylinder causes it to tilt and peel off, with the front of the coating interface under tension and the back under compression; 3) the adhesion between the coating and the ice is overcome at the front of the interface and a crack forms; and 4) cavitation occurs – the collapse of the coating when the crack forms generates a wave across the coating surface, which separates the ice from the coating.

2.4.2.1.2. Interfacial slippage

Interfacial slippage can be defined as the suspension of the no-slip boundary condition at an interface under shear, allowing viscous flow and a non-zero fluid velocity at the interface. It was suggested from a theoretical basis by Brochard and de Gennes (1992) at liquid-solid and liquid-liquid interfaces and was observed analytically and empirically in polymer melts (Hénot et al., 2018, Migler et al., 1993) and adhesives (Newby et al., 1995, Zhang Newby and Chaudhury, 1997). A simplified flow profile displaying interfacial slippage in a liquid at a liquid-solid interface is provided in Figure 2.18.

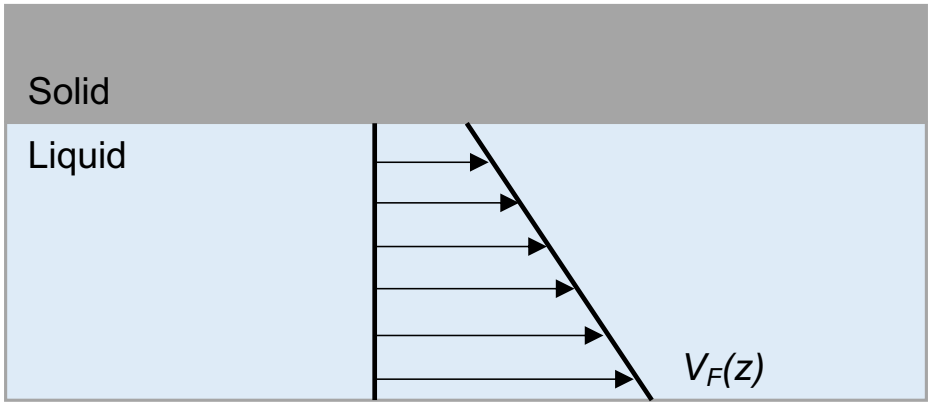

Figure 2.18 – Simplified representative flow profile showing non-zero flow velocity, $V_f(z)$, at a liquid-solid interface. In this example velocity scales linearly with depth, d, from the interface, but this is likely to be very different in real flows.

The proposition that interfacial slippage occurs at ice-elastomer interfaces has been most notably attributed to the work by Golovin et al. (2016), though Andrews posited its presence at ice-rubber interfaces 30 years earlier (1984). Wang et al. also suggested it was the source of adhesion decay during detachment of ice from PDMS surfaces they had observed (2014a). However, since 2016, others have also claimed its presence at ice-elastomer interfaces without direct observation (Ibáñez-Ibáñez et al., 2021a, Sivakumar et al., 2019, Gao et al., 2019, Shen et al., 2018).

The proposed mechanism by which interfacial slippage occurs at elastomer-ice interfaces is that, as the elastomer is brought under shear stress and elastically deforms, the polymer chains at the coating surface have sufficient mobility to flow past each other, making it easier for the ice to be detached from the surface. The chains adhered to the ice at the surface detach and slide along the interface to release the shear stress. Detachment becomes similar to the de-wetting process of a liquid (Ghatak et al., 2000, Vorvolakos and Chaudhury, 2003, Newby et al., 1995, Golovin

et al., 2016, Zhang Newby and Chaudhury, 1997, Zhang Newby and Chaudhury, 1998, Migler et al., 1994, Chernyak and Leonov, 1986)

Oil-infusion, which reduces the cross-linking density and provides free chains, has been purported to generate sufficient mobility to allow such flow (Golovin et al., 2016).

The detachment steps of a single polymer chain are modelled by Vorvolakos and Chaudhury (2003) in Figure 2.19. A graphical representation of this behaviour in ice-elastomer push tests is presented in Figure 2.20.

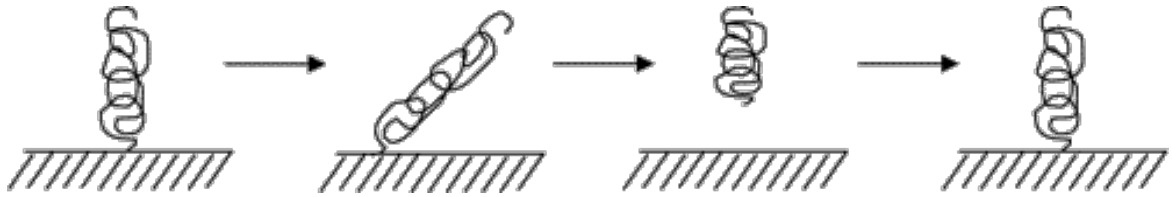

Figure 2.19 – Detachment and reattachment of a polymer chain as a surface slides beneath it. The chain is stretched by a shearing force, then detaches from the surface, before relaxing and reattaching in a new location (Vorvolakos and Chaudhury, 2003).

The mathematical model describing interfacial slippage is given by (Golovin et al., 2016):

$$\sigma_A = \frac{G f_a a}{kT} \tag{2.8}$$

Where σ_A is the adhesion strength, G is the shear modulus, f_a is the force needed to detach a single chain of segmental length a, k is the Boltzmann constant, and T is temperature.

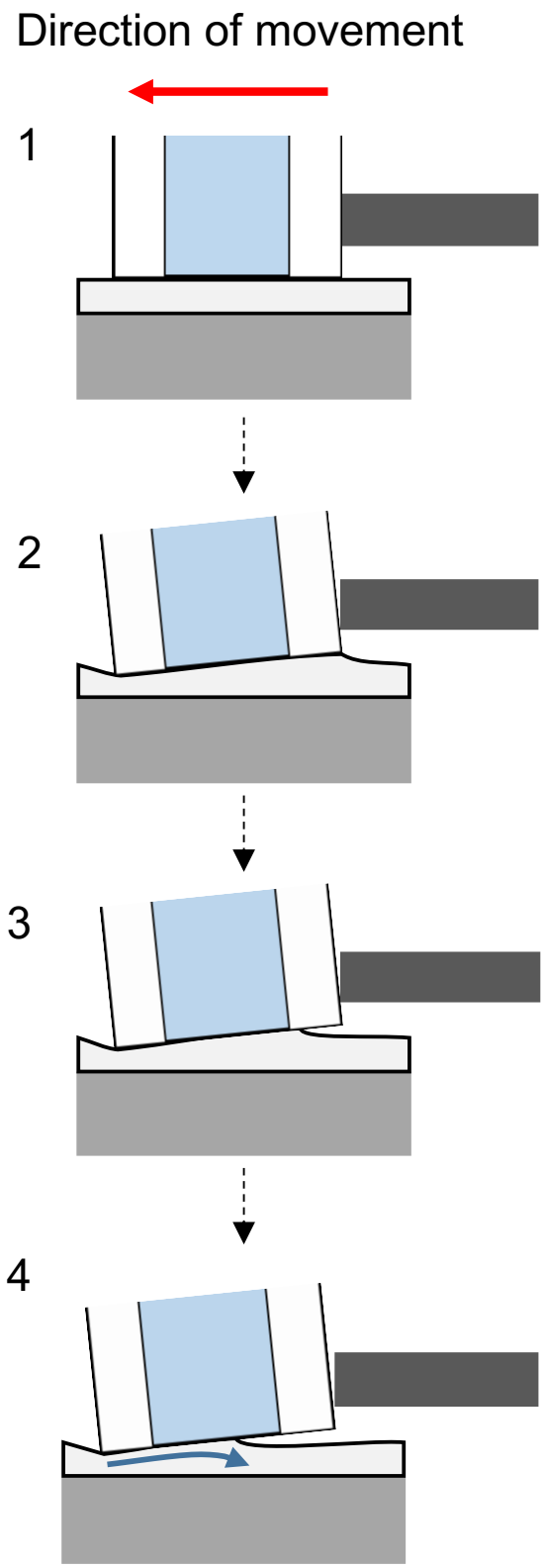

Figure 2.20 – Visualisation of interfacial slippage process. The initial stages are the same as interfacial cavitation: 1) probe contact causes initial lateral elastic deformation; 2) torque on the ice cylinder causes it to tilt and peel off, with the front of the coating interface under tension and the back under compression and 3) the adhesion between the coating and the ice is overcome at the front of the interface and a crack forms. However, the detachment mechanism occurs via step 4) slippage – the polymer chains detach from the surface of the ice and flow backwards along the interface to release the shear stress.

2.4.3. Freezing delay

2.4.3.1. The freezing process

Ice is formed from liquid water via two stages, which will be discussed separately:

i. **Nucleation**
ii. **Ice growth**

2.4.3.1.1. Nucleation

Nucleation is the process by which water begins to form ice. As water cools down to 0°C and below, the thermal energy of the water molecules falls, until the hydrogen bonding becomes dominant and hexagonal ice I_h is formed (Figure 2.1). However, this process of forming hexagonal crystal structures is initially unstable. Ice embryos are formed within the liquid water – effectively small pieces of crystalline ice – but if they are below a critical size, it is thermodynamically unfavourable to propagate, and they will dissolve back into the liquid. This cycle happens continuously until an embryo of critical size is formed and the ice nucleus propagates (Figure 2.21).

Nucleation is often promoted by the presence of foreign particles and asperities, and as such when water is freezing on top of a surface, nucleation preferentially occurs at the interface. This is heterogeneous nucleation and occurs because the surface imperfections act as nucleation sites (Hobbs, 1974).

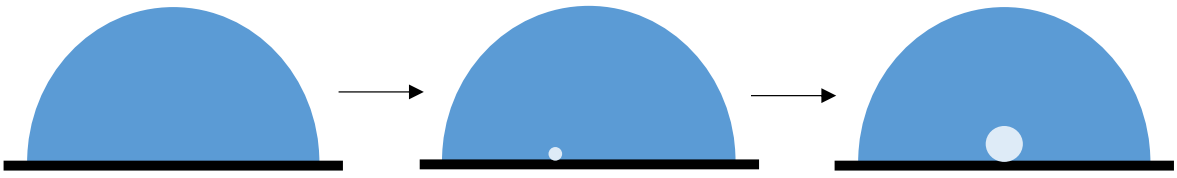

Figure 2.21 – Heterogeneous ice nucleation process of a droplet on a surface, showing the formation of unstable ice embryos and then ice nuclei of a critical diameter for stable growth.

Based on classical nucleation theory, the heterogeneous nucleation rate, *J*, on a surface for a given temperature is (Fletcher, 1958):

$$J(T) = K \exp\left(-\frac{\Delta G^*}{kT}\right) \tag{2.9}$$

Where K is a kinetic constant equivalent to:

$$K = Z\beta N \tag{2.10}$$

Z is the Zeldovich statistical probability factor (Irajizad et al., 2019b), while *β* is the rate at which an ice embryo of critical radius gains one water molecule, and *N* is the number of nucleation sites per unit area. *T* is temperature and k is the Boltzmann constant. *ΔG** is the free energy of formation for a critical ice embryo, which, for nucleation on a foreign, non-planar surface, is given by:

$$\Delta G^* = \frac{16\pi {\gamma_{IW}}^3}{3{\Delta G_v}^2} f(m,x) \tag{2.11}$$

Where γ_{IW} is the interfacial tension of ice and water, ΔG_v is the volumetric free energy of phase-change for ice and *f(m,x)* is a function of the surface energy and geometry of the system for a nucleating surface. For a convex nucleation site, *f(m,x)* is described by:

$$\begin{aligned} f(m,x) = 1 + \left(\frac{1-mx}{g}\right)^2 + x^2 \left\{2 - 3\left(\frac{x-m}{g}\right) + \left(\frac{x-m}{g}\right)^3\right\} \\ + 3mx^2\left(\frac{x-m}{g} - 1\right) \end{aligned} \tag{2.12}$$

With *g* further defined as:

$$g = (1 + x^2 - 2mx)^{\frac{1}{2}} \tag{2.13}$$

For a concave nucleation site, *f(m,x)* is:

$$\begin{aligned} f(m,x) = 1 - \left(\frac{1+mx}{g}\right)^2 - x^2 \left\{2 - 3\left(\frac{x+m}{g}\right) + \left(\frac{x+m}{g}\right)^3\right\} \\ + 3mx^2\left(\frac{x+m}{g} - 1\right) \end{aligned} \tag{2.14}$$

And *g* is instead:

$$g = (1 + x^2 + 2mx)^{\frac{1}{2}} \tag{2.15}$$

In both cases *m* is described using the contact angle of the surface, *θ*, via:

$$m = \cos(\theta) \tag{2.16}$$

The term *x* is a geometric factor dependent on the radius of surface features, *R*, and the critical ice embryo radius, r_c, and is defined as:

$$x = \frac{R}{r_c} \tag{2.17}$$

Further, r_c is given by:

$$r_c = \frac{2\gamma_{IW}}{\Delta G_v} \tag{2.18}$$

The equations above can also be expressed via statistical models to predict the probability of heterogeneous nucleation:

$$\ln\left[1 - P(V,t)\right] = -\int_0^t V * J dt \tag{2.19}$$

Where *P(V,t)* is the probability of nucleation in a droplet of given droplet volume *V,* within time*, t.*

2.4.3.1.2. Ice growth

After nucleation occurs the ice nucleus will grow, preferentially propagating along the other nucleating sites on the interface. When a layer of ice has formed at the interface, it will progress upwards through the water, solidifying the remaining liquid. This process is the growth stage, represented visually in Figure 2.22.

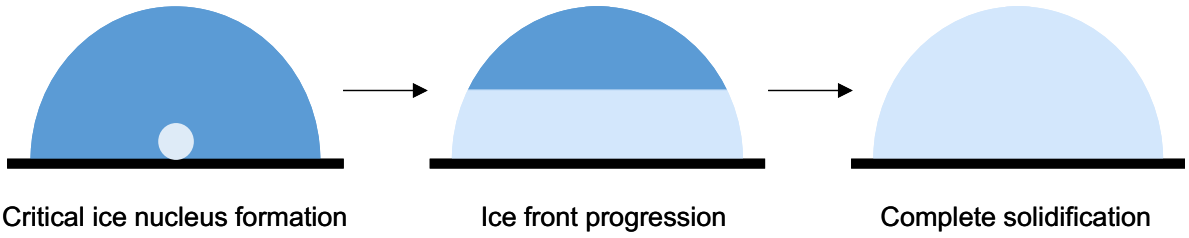

Figure 2.22 – Ice growth process, starting from the formation of an ice nucleus of critical diameter at the substrate before upwards progression of the freezing front. Freezing is complete when the freezing front reaches the top of the droplet.

The ice growth time on a freezing water droplet, t_{growth}, as observed visually by progression of the freezing front (ice-water interface), can be determined via (Irajizad et al., 2019b):

$$t_{growth} = \frac{\rho_I H}{\Delta T} l \left(\frac{2d_0 - d}{2k_I} + \frac{d_s}{k_s} \right) \quad (2.20)$$

Where ρ_I is the ice density, H is the enthalpy of ice formation, ΔT is the temperature difference at the ice-water interface, d_0 is the droplet height, d is the freezing front height, k_I is the thermal conductivity of ice, d_s is the thickness of the substrate and k_s is the thermal conductivity of the substrate.

This is a simplified heat transfer model, assuming conductive heat transfer greatly exceeds convective heat transfer. Equation (2.20) assumes quasi-steady state heat transfer based on fast thermal diffusion through the ice compared to the time scale for growth (Irajizad et al., 2019b).

2.4.3.2. Measuring freezing delay

Freezing delay is the second most common metric used to characterise the icephobicity of a surface. There is no precise definition of freezing delay, and it can vary between studies. Measurement methods are split into two primary categories, time-based and temperature-based. A time-based method is used in this study. Both approaches involve depositing a droplet of water on the surface and allowing it to freeze. They are summarised here:

i. Time-based

In a time-based approach, the droplet is placed on a supercooled surface and the temperature of the system is fixed at a given value. Then the time for the droplet to nucleate or completely freeze is measured by visually observing the progression of freezing (Barthwal et al., 2019, Lin et al., 2018, Gao et al., 2019).

ii. Temperature-based

In a temperature-based method, a droplet is deposited on a surface that is warmer than 0°C, and then the temperature of the surface is reduced at a constant rate (Chen et al., 2017). The temperature at which nucleation or complete freezing occurs is then noted (Shamshiri et al., 2021).

The endpoint of freezing delay can also vary across studies. Within the literature some will stop measuring at nucleation (Irajizad et al., 2019b, Alizadeh et al., 2012). However, most assume the same definition: complete solidification as indicated by the

freezing front reaching the top of the droplet (Hong et al., 2019, Wang et al., 2019, Guo et al., 2020).

2.4.4. Other metrics

It can be argued that icephobicity – the resistance to ice accumulation – is best described by the ability to prevent ice formation (freezing delay), and to remove ice once formed (ice adhesion). However, some research has utilised other metrics, which are discussed here.

i. Retraction of impacting droplets

The retraction rate of droplets impacting a surface has been considered by many as a useful way to quantify icephobicity. By designing surfaces which minimise the contact between droplet and surface the hope is that there will be a lower likelihood of freezing (Jamil et al., 2018). In these experiments water droplets, which may or may not be supercooled, are dropped from height above the surface. Their impact is recorded, and contact time (Jin et al., 2017, Qian et al., 2020) or the droplet diameter (Mishchenko et al., 2010, Richard et al., 2002) are noted as the droplet spreads from the force of the impact and then retracts to the equilibrium droplet diameter based on the interfacial energy between the water and the coating. Visual examples of droplet spreading and retraction are presented in Figure 2.23 (Mishchenko et al., 2010).

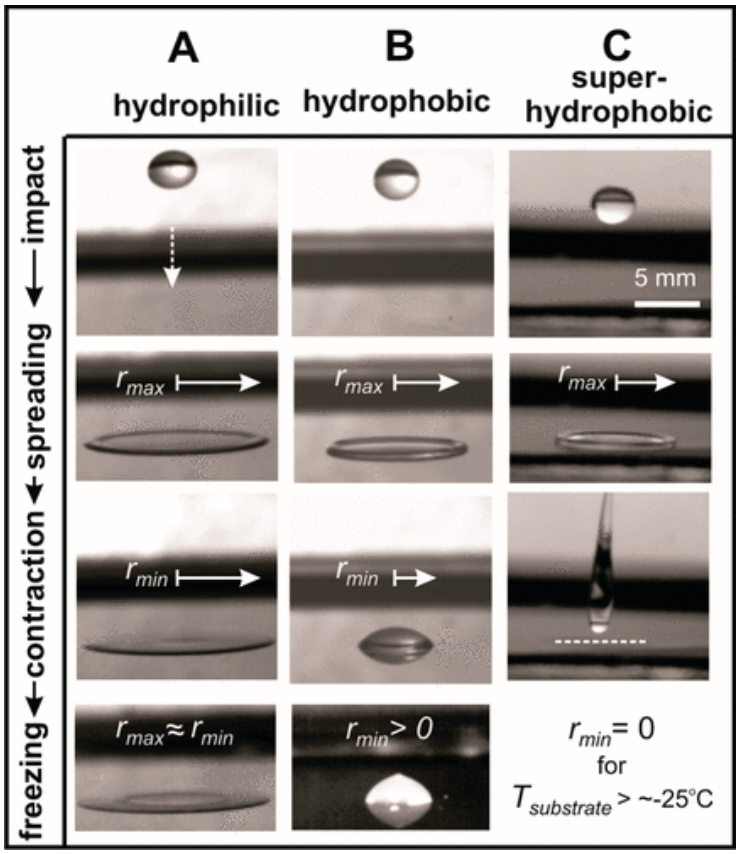

Figure 2.23 – Images of droplet impact and retraction on a hydrophilic, hydrophobic and superhydrophobic coating. The maximum and minimum droplet radii are noted after impact. The superhydrophobic coating allowed for complete retraction of the droplet and the droplet bounced off the surface, while the hydrophilic coating had negligible retraction. (Mishchenko et al., 2010).

ii. Frost formation rate

Frost formation rate is occasionally used as an icephobicity metric. While there is validity in considering this metric based on real icing scenarios, it is difficult to create reliable test methods and quantify the result. Frost formation is highly dependent on the environmental conditions, particularly the humidity of the air above a surface (Kulinich et al., 2011).

Most commonly, it is measured by observing the rate of surface coverage by frost (Cai et al., 2011, Liu et al., 2008, Zhang et al., 2017, Kim et al., 2012). This is achieved by supplying a stream of warm, humid air over a supercooled surface, and then calculating the percentage of the area covered by frost at set time steps. An example of frost formation measurements on surfaces is presented in Figure 2.24, in which frost coverage is observed on a series of surfaces over 100 minutes (Wei et al., 2018).

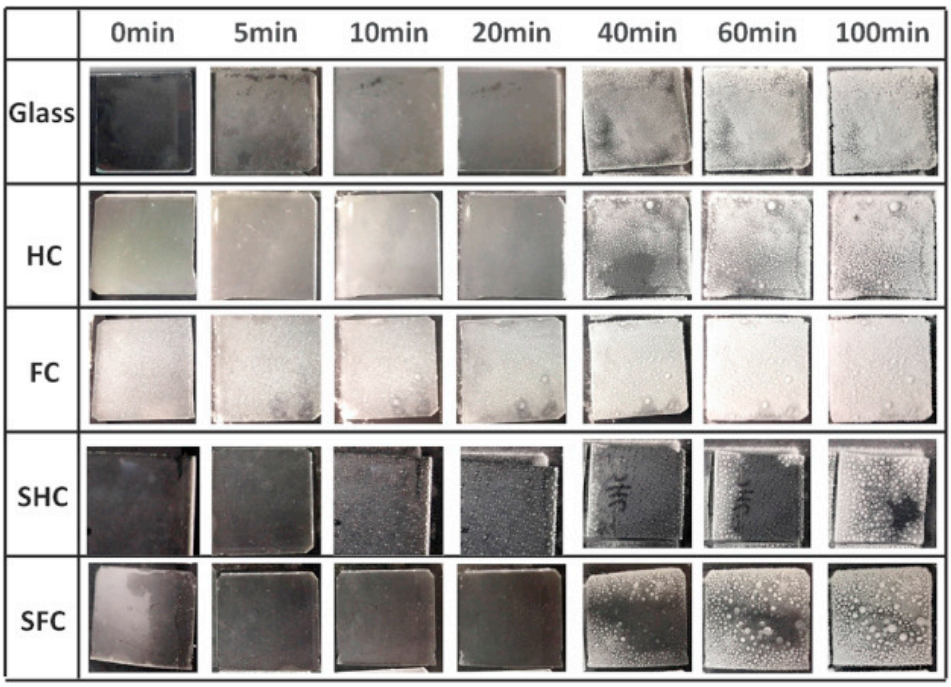

Figure 2.24 – Frost formation observations carried out on a series of surfaces: glass, a nano-textured hydrophobic coating (HC), a superhydrophobic fluorinated coating (FC), a lubricated nano-textured hydrophobic coating (SHC) and a lubricated superhydrophobic fluorinated coating (SFC). Complete frost coverage is significantly delayed on the coatings with a lubricating surface layer. (Wei et al., 2018)

2.5. Conclusion

This review introduces the complexity involved in the study of icephobic coatings. By charting the development stages from hydrophobic coatings to SHS and SLIPS, before returning to smooth, low surface energy oil-infused elastomers, we can see the changing design rationale as people better understood the underlying differences between ice and water repellence.

The study of icephobicity is complicated by the variety of metrics and test methods used to quantify it. The two most common metrics, and those that are utilised in this study, are ice adhesion and freezing delay. Measurement methods for both of these metrics were reviewed.

The technological improvements in coatings were accompanied by a better understanding of the factors that contribute to the icephobicity and the development of expressions for adhesion strength and freezing delay of a surface. Ice detachment models of interfacial cavitation and slippage are two such expressions, which were presented as possible explanations for the ice release mechanism. Classical nucleation and ice growth equations were provided to describe the freezing delay time.

3. Polymer Selection and Fabrication

Summary

The precise coatings studied in this work are introduced. They are: two polydimethylsiloxane (PDMS) coatings, cured at 80°C for 2 hours or 100°C for 45 minutes; four silicone-oil/PDMS coatings, with a low and high molecular weight oil, at 25% and 50% by volume; and a commercial anti-icing coating (NuSil R-2180). These coatings were selected for their simple silicone chemistry, straightforward fabrication methods, low ice adhesion strengths and because they have been reported to exhibit interfacial slippage. The coatings were fabricated by casting in moulds on primed substrates and heat curing.

3.1. Introduction

Most research on icephobic elastomer coatings has been carried out on silicone-based or polyurethane-based formulations. Purchasable, ready-made pre-polymer kits, which only require activation and curing, are often used. Some research groups create their own formulations from pure base chemicals, eliminating the filler chemicals and proprietary additives that are present in many commercial formulations. This allows for more precise control and knowledge of the chemistry but can be time-consuming to develop. More advanced elastomer coatings with specific functionalization, for example: polyhedral oligomeric silsesquioxane (POSS) modified polymers (Gao et al., 2019), interpenetrating polymer phases (Zhuo et al., 2018), carbon nanotubes (Wang et al., 2021) and composites (Arianpour et al., 2013, Memon et al., 2021), have been investigated for their specialised abilities.

The primary objectives of this work are to comprehensively investigate the effect that oil-infusion has on the icephobicity of elastomer coatings, and to identify whether interfacial slippage occurs in these coatings. Most of the studies that have reported or suggested the occurrence of interfacial slippage have used silicone elastomers. With the aim to examine these claims, and the benefit of studying a simple chemistry, a silicone base was chosen. Other than infusing oil, no functional additives were used, to build a clearer picture, unobscured by competing contributions.

Oil-infusion is achieved by mixing an unreactive, miscible oil into the elastomer mixture before curing. This inhibits cross-linking, a diagrammatic representation of which is presented in Figure 2.12.

There has been some examination of commercial coatings, whether marketed as being anti-icing or not, such as NuSil R-2180 and R-1009, Teflon™ or NeverWet. Some are elastomers and have shown promising ability to reduce ice adhesion.

This chapter details the specific elastomer formulations, and why each component was selected. The fabrication methods are described.

3.2. Elastomer selections and formulations

3.2.1. Base elastomer: Sylgard™ 184 Polydimethylsiloxane

The basic elastomer selected was polydimethylsiloxane (PDMS). It has a simple chemical structure, is relatively cheap and poses a low risk of harm to health or the environment. This makes it more easily scalable to a wide variety of applications. It is the most commonly selected base material for other research on the topic, which allows for better comparison of results.

A pre-prepared formulation was used: Sylgard™ 184, manufactured by Dow, which is the predominant choice for off-the-shelf PDMS formulations among the field. Sylgard™ 184 is supplied as a two-part kit, comprising a base and curing agent which combine at a recommended ratio of 10:1. The primary component in the base, and backbone of the resulting polymer network, is dimethylvinyl-terminated PDMS. The chemical structure is detailed in Figure 3.1.

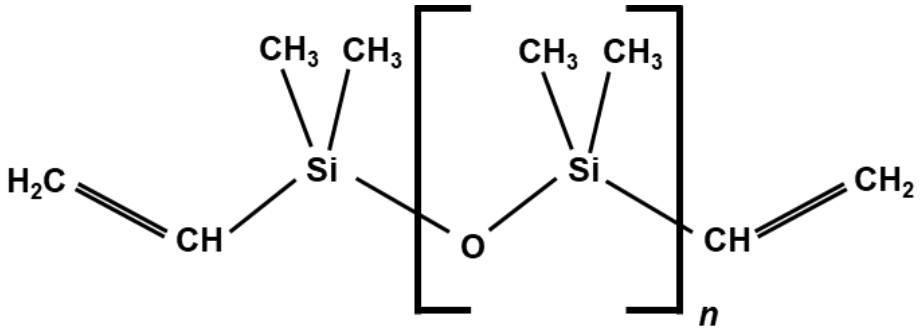

Dimethylvinyl-terminated PDMS

Figure 3.1 – Structure of dimethylvinyl-terminated PDMS showing the repeating monomer unit and dimethylvinyl end groups.

Dimethylvinyl-terminated PDMS is made up of a linear oxygen-silicone backbone with dimethyl functional groups on the silicone atoms and vinyl end-groups. The vinyl end-groups are susceptible to attack by a cross-linker in the presence of a platinum catalyst, forming the cross-linked network (Ortiz-Acosta, 2012).

The uncross-linked chains and the cross-linker are found in the base, while the platinum catalyst is in the curing agent (Brounstein et al., 2021). Upon mixing of the two, un-reversible cross-linking (curing) begins.

The polymer chains between the cross-links are linear. The molecular weight of the chains is not publicised, but has been reported as 27,000 g/mol with a viscosity of 500 cSt (Santiago-Alvarado et al., 2014).

Dow provides a selection of recommended curing schedules:

- 48 hours at room temperature (25°C)
- 45 minutes at 100°C
- 20 minutes at 125°C
- 10 minutes at 150°C

The effect of the curing temperature on the physical properties of the Sylgard ™ 184 has been documented (Johnston et al., 2014), with higher curing temperatures corresponding to stronger, less elastic PDMS, with more cross-links.

Additional curing schedules have been used in other studies (Ibáñez-Ibáñez et al., 2021a, Meuler et al., 2010, Wang et al., 2018a). Significantly, Golovin et al. (2016), reporting interfacial slippage in their plain Sylgard™ 184 coatings cured at 80°C for 2 hours.

In this work, two curing schedules for plain PDMS were used: 45 minutes at 100°C and 2 hours at 80°C. The manufacturer recommended cure (100°C) was selected to provide a reference; it is not believed to demonstrate interfacial slippage. The 80°C curing schedule was adopted based on the approach by Golovin et al., to investigate the proposal of interfacial slippage as the detachment mechanism.

3.2.2. Infusing oil

Previous studies have examined a wide range of infusing oils, such as (vegetable oil) (Golovin et al., 2016), isocetane (Urata et al., 2015) and polymethylphenylsiloxane (Urata et al., 2021). Silicone oil (trimethylsiloxy-terminated PDMS) was selected as the infusing oil for this work because it has good miscibility with the Sylgard™ 184 components. It is also unreactive with Sylgard 184™. As the monomer is the exact same as the Sylgard™ 184 base, there is no concern about chemical contributions affecting the properties, and effectively no change to the surface energy (Galliano et al., 2003). The only difference between silicone oil and the Sylgard™ 184 elastomer base is the end-groups. As seen in Figure 3.2, the silicone oil has three methyl end-groups. These end-groups are not receptive to the cross-linker and the molecules

remain as free chains when combined with the Sylgard™ 184 components, as depicted in Figure 2.12.

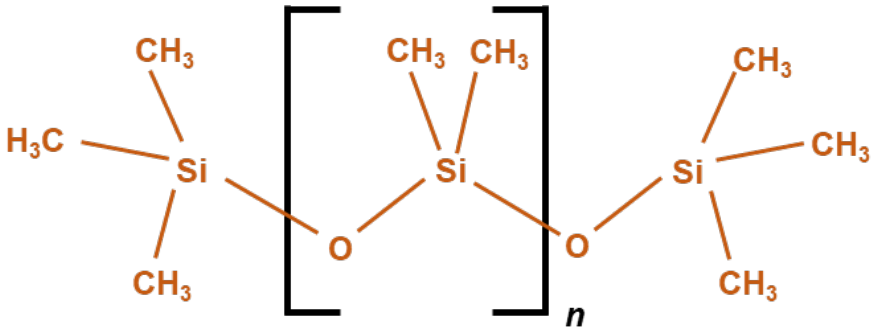

Figure 3.2 – Structure of trimethyl-terminated PDMS showing the repeating monomer unit and trimethyl end groups.

Two different molecular weights and concentrations of silicone oil were used, to determine the influence of these factors on the icephobicity and possible occurrence of interfacial slippage. They were: a low molecular weight silicone oil (LMWSO – 6,000 g/mol) and a high molecular weight silicone oil (HMWSO – 28,000 g/mol), each added at 25% and 50% by volume. Using silicone oil of two very different weights should provide clearer trends in the results where molecular weight is a factor. The density and viscosity of the two weights of oil used are given in Table 3.1.

The oil-infused coatings were cured at 80°C, to maintain consistency with the PDMS 80°C specimen. Golovin et al. (2016) reported interfacial slippage on coatings similar to the 25% LMWSO, 50% LMWSO and 25% HMWSO coatings, cured at 80°C. Though there is ice adhesion data for simliar coatings, the precise collection of formulations adopted here has not been documented in the literature before.

Table 3.1 - Selected properties of silicone oil. Data provided by supplier

Silicone oil	Weight-average molecular weight, M_W (g/mol)	Density (kg/m^3)	Viscosity (cSt)
Low molecular weight	6,000	950	100
High molecular weight	28,000	971	1000

3.2.3. Commercial anti-icing coating

Though not widely adopted, there are some commercially available industrial anti-icing coatings. One such coating that has shown promising icephobicity is NuSil R-2180, manufactured by Avantor. NuSil R-2180 is a proprietary silicone elastomer that has been marketed as an icephobic, anti-icing coating, with aerospace applications (Sivas et al., 2007). It has the same silicone-oxygen backbone as Sylgard™ 184, with different functional groups bonded to the silicone atoms, rather than the methyl groups of PDMS.

It has been suggested that NuSil R-2180 utilises interfacial slippage as the mechanism for its low ice adhesions strength (Golovin et al., 2016). This, combined with assessing its freezing delay, was the reason for investigating it alongside the PDMS-based specimens in this study. It is also of interest to compare the icephobicity of a coating currently on the market with the coatings designed and fabricated here.

Like Sylgard™ 184, NuSil R-2180 is supplied as a two-part mixture, combined at a ratio of 1:1. Part A contains the pre-polymer chains and cross-linker, while Part B contains the catalyst.

It should be noted that, despite being made of up to 90% solvent, the pre-polymer has a high viscosity and is shear-thickening, making it more difficult to work with in some ways than the Sylgard™ 184 PDMS formulations. The molecular weight of the NuSil R-2180 pre-polymer chains is not reported. The curing schedule used is a ramped schedule recommended by the manufacturer to facilitate evaporation of the large amount of carrier solvent (xylene).

3.3. Fabrication

The seven coatings selected for study were:

- **PDMS 80°C** (plain PDMS cured at 80°C for 2 hours)
- **PDMS 100°C** (plain PDMS cured at 100°C for 45 minutes)
- **25% LMWSO** (25% low molecular weight silicone oil + 75% plain PDMS cured at 80°C for 2 hours)
- **50% LMWSO** (50% low molecular weight silicone oil + 50% plain PDMS cured at 80°C for 2 hours)

- **25% HMWSO** (25% high molecular weight silicone oil + 75% plain PDMS cured at 80°C for 2 hours)
- **50% HMWSO** (50% high molecular weight silicone oil + 50% plain PDMS cured at 80°C for 2 hours)
- **NuSil R-2180**

A few different fabrication methods were initially considered, including spray coating, manual dip coating and mould casting. Manual dip coating was quickly rejected for lack of control over the coatings thickness. The pre-polymer mixture spilled off the sample, and the thickness was solely dictated by the surface tension of the liquid. Spray casting allowed for good control of the thickness but took a very long time to build up coatings in the thickness of interest in this study. This will be discussed more in Chapter 5 but was approximately 200 μm. Casting allowed for adequate control of thickness, and a reasonable time for application.

The oil percentages were chosen to be 25% and 50%. This was to ensure any effect on results by the percentage of oil was more pronounced. Initial specimens were also made with 75% oil, but for both LMWSO and HMWSO, this resulted in inhibiting cross-linking to such an extent that the coatings did not cure sufficiently and were mechanically unviable.

To improve adhesion of the coatings to the substrates (aluminium and PETG slides, steel stubs), primers recommended by the manufacturers were applied before the coating. Without the primer, adhesion to some substrates was poor – in the case of the aluminium slides, the coatings could easily be peeled off by hand after curing.

Ultimately two specimens were produced for each coating type. The finalised fabrication steps are outlined in the following sections.

3.3.1. PDMS and silicone-oil/PDMS formulations

The PDMS and silicone-oil/PDMS coatings were prepared as follows:

i. The substrates were cleaned with hexane and isopropanol then primed using DOWSIL 1200 OS, which was cured for 30 minutes at room temperature.
ii. The Sylgard™ 184 base and curing agent were mixed in a ratio of 10:1, as directed by the manufacturer.

iii. For the silicone-oil/PDMS mixtures, silicone oil was added before the curing agent and mixed into the base at 25% or 50% of the total volume of the final mixture.
iv. The total volume of each mixture was 5.5 ml.
v. The components were mixed manually for 1 minute.
vi. The mixture was left for 30 minutes to disperse any bubbles that had been created during mixing.
vii. A square mould measuring 20 mm x 20 mm was taped to the substrate, into which the pre-polymer mixture was dispensed by syringe. For the icephobicity specimens the dispensed volume was 0.2 ml.
viii. The coated specimens were heat-cured in an oven. There were two curing schedules employed: 100°C for 45 minutes, as directed by the manufacturer, or 80°C for 2 hours. PDMS specimens were made using each of the two curing schedules. All the silicone-oil/PDMS specimens were cured at 80°C for 2 hours.

3.3.2. NuSil R-2180

The NuSil R-2180 specimens were made according to the manufacturer's direction:

i. The substrate was cleaned with hexane and isopropanol then primed with NuSil SP-270, which was cured for 30 minutes at room temperature.
ii. Then NuSil R-2180 Part A and Part B were mixed in a ratio of 1:1. The total volume was 10 ml.
iii. A square mould measuring 20 mm x 20 mm was taped to the substrate, into which the pre-polymer mixture was dispensed by syringe. For the icephobicity specimens the dispensed volume was 0.7 ml.
iv. The specimens were vacuum degassed for 30 minutes at room temperature to remove the xylene solvent.
v. The specimens were heat cured at 75°C for 45 minutes and then 150°C for 135 minutes.

3.4. Conclusion

The seven coatings studied in this work were:

- PDMS 80°C
- PDMS 100°C
- 25% LMWSO

- 50% LMWSO
- 25% HMWSO
- 50% HMWSO
- NuSil R-2180

PDMS (specifically Sylgard™ 184) was selected as the basic elastomer as it has a simple chemistry, is easy to handle, cheap, safe and has demonstrated relatively low ice adhesion. Two curing schedules were used: 80°C for 2 hours, which reportedly exhibits interfacial slippage, and 100°C for 45 minutes, as a non-slippage reference.

The infusing oil was silicone oil, which is, in essence, chemically identical to the Sylgard™ 184. It has excellent miscibility with the Sylgard™ 184 and is unreactive. Two molecular weights (low and high) were used, at 25% and 50% volume, to examine the influence of these factors on icephobicity. Furthermore, interfacial slippage has been reported in the literature on the 25% LMWSO, 50% LMWSO and 25% HMWSO coatings.

A commercially available silicone elastomer coating marketed as icephobic, NuSil R-2180, has also been suggested to demonstrate interfacial slippage, and is investigated as well.

The coatings were fabricated by casting in moulds on primed substrates and heat curing. The infusing oil was mixed into the pre-polymer base before the curing agent/catalyst was added, to inhibit cross-linking of the elastomer network.

4. Room Temperature Characterisation

Summary

The elastic modulus, contact angle, coating thickness, surface roughness, and room temperature adhesion are measured before and after ice adhesion testing to investigate their influence on icephobicity. The static water contact angle provides a measure of the surface energy, of which there is negligible difference between the coatings because of their similar chemistry. All coating types have contact angles between 100-107° pre- and post-adhesion testing.

Stylus profilometry is used to measure surface roughness, with the values shown to be artificially high via optical microscopy and SEM imaging. This is likely caused by interference of the stylus by surface-oil capillary forces and large elastic deformations in the coatings. Compression testing reveals the very low elastic moduli of the coatings, particularly the 50% LMWSO and 50% HMWSO which have moduli around 0.3 MPa. All the oil-infused coatings have lower moduli than the non-oil infused coatings. Stylus profilometry is, however, able detect moderate-to-severe damage.

Generally, there is little damage to the surfaces from de-icing, but SEM imaging shows examples of gouging and abrasive wear on the coatings. Optical microscopy confirms the presence of surface oil on the HMWSO coatings.

Room temperature adhesion tests show that the 50% LMWSO and 50% HMWSO coatings have the greatest peak adhesive forces upon retraction of a compressive load. This suggests the oil percentage and/or elastic modulus have greater influence on the adhesive force than the presence of surface oil or the molecular weight of the oil itself.

4.1. Introduction

To develop a clearer picture of the icephobic behaviour of the coatings, bulk and surface characterisation of the coatings is a key requirement. In this chapter the properties of the coating specimens are evaluated via elastic moduli and contact angle measurements, profilometry, room temperature adhesion testing, SEM and optical microscopy. These findings will subsequently be combined with icephobicity testing in Chapter 5 and Chapter 6 to develop a better understanding of the anti-icing performance of the coatings.

Unless otherwise specified, the specimens examined in this chapter were the same specimens used in the ice adhesion strength (Chapter 5) and freezing delay testing (Chapter 6). The fabrication of the specimens is described in greater detail in the indicated chapters. Briefly, films of each coating were cast on two aluminium substrates, generating two specimens per coating type. Coating preparation is described in Chapter 3.

The rationale for using the same specimens is that it allowed for the surfaces to be re-characterised after the full ice adhesion testing regimen. The ice adhesion testing is detailed in Chapter 5, and involves placing an acrylic cylinder on the specimen, filling it with water, and then freezing it. Once frozen the ice-cylinder is pushed off the coating surface by a probe. This process of freezing and then detaching an ice cylinder is a ‘de-icing cycle’. Over the course of the ice adhesion testing regimen, the specimens were subjected to 100 de-icing cycles. This allowed the effect of surface wear on the ice adhesion strength, from repeated ice detachment, to be investigated.

The effect of wear on the surface properties is studied by characterising the surfaces of the specimens before and after the adhesion testing. This can then be compared to any changes in the ice adhesion strength and freezing delay to determine whether there is any connection between these surface properties and the icephobicity of the coatings.

4.2. Elastic modulus

As demonstrated in Chapter 2, one of the properties shown to be significant to the ice adhesion strength of elastomers is their elastic modulus. This section describes the characterisation of the coatings’ elastic moduli.

4.2.1. Experimental method

Elastic modulus tests were performed using a 50 N Instron mechanical tester in compression. A photograph of the equipment is provided Figure 4.1.

To make the test specimens, a thick film of each coating was cast in a dish. The elastomers were prepared using the standard methods detailed in Section 3.3. The thickness of the films was between 1.5-3 mm.

From the thick films, 4 mm-diameter cylinders were punched out using a biopsy punch.

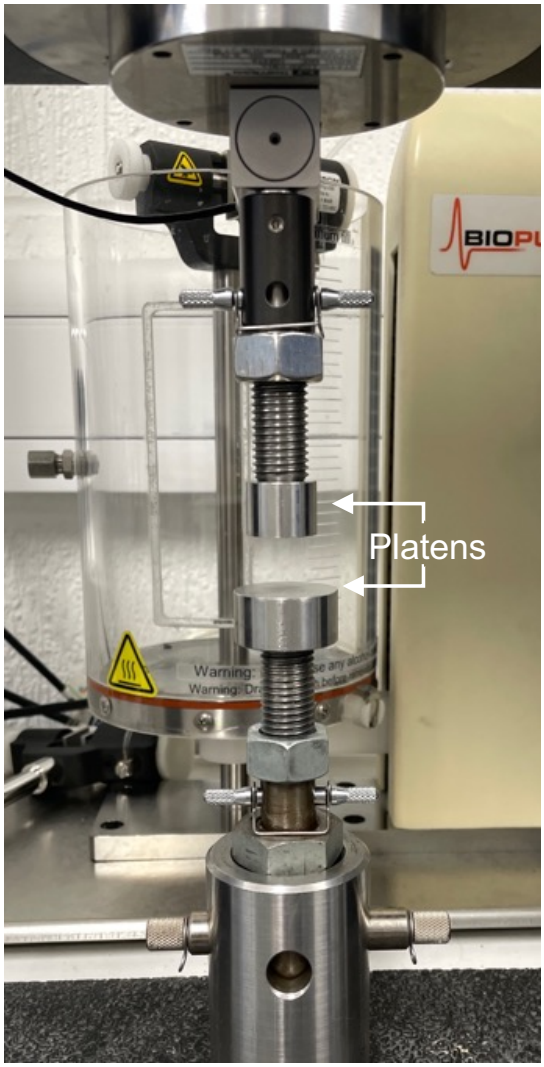

Figure 4.1 – Compression testing apparatus, highlighting the upper and lower platens, between which a test specimen would be placed.

The thickness of the cylinders was then measured using a digital calliper. Three specimens were prepared for each coating type.

The specimen was then compressed at a rate of 20% strain/minute, up to 50% strain. Force-displacement curves were generated during testing, and then converted to stress-strain curves. An example stress-strain curve is provided in Figure 4.2. The modulus was taken as the gradient of the initial linear elastic region of the curve. The values reported in Figure 4.3 are the average of a minimum of three specimens for each coating type.

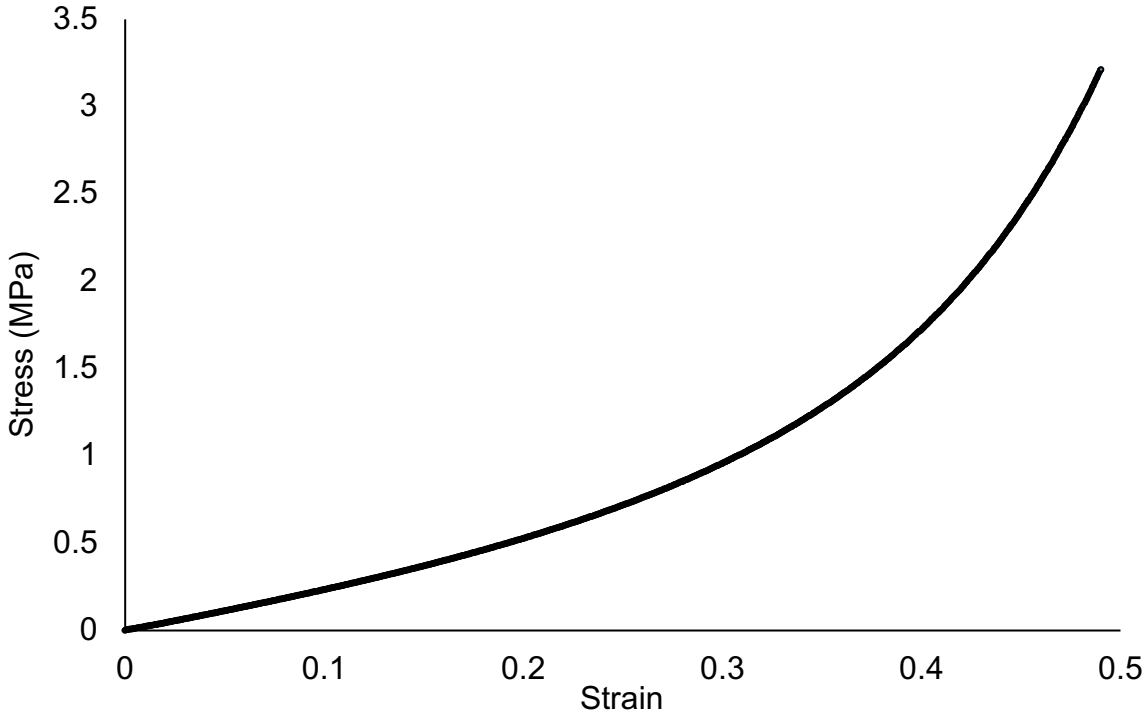

Figure 4.2 – Example stress-strain curve from compression testing to determine elastic modulus.

4.2.2. Results

The findings from the modulus testing is presented in Figure 4.3. The average value for the PDMS 100°C is 2.62 MPa. This is in good agreement with similar studies, which reported values of 2.4-2.9 MPa (Ibáñez-Ibáñez et al., 2021a, He et al., 2018b, Ibáñez-Ibáñez et al., 2021b, Ibáñez-Ibáñez et al., 2022).

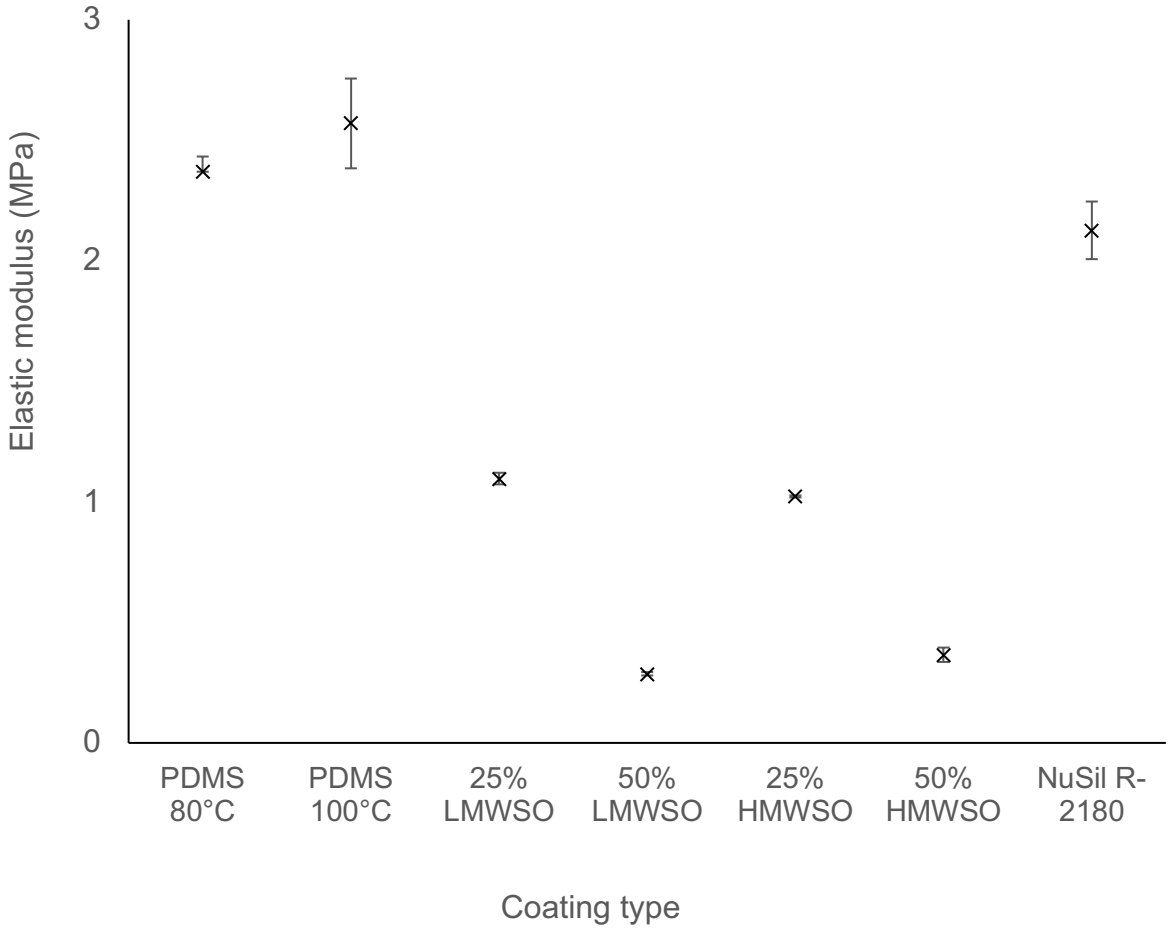

Figure 4.3 – Elastic moduli of the different coating types, as measured by compression tests, with range bars.

The oil-infused coatings all had lower moduli than the non-oil infused coatings, with a range of 0.29-1.10 MPa. The non-oil infused coatings have a range of 2.12-2.62 MPa. The non-oil infused coatings had similar moduli, with the PDMS 80°C slightly lower than PDMS 100°C and the NuSil R-2180 slightly lower than both PDMS types. The percentage of oil has a much stronger influence on the elastic modulus than the molecular weight of the oil, with similar elastic moduli across the two 25% coatings, and the two 50% coatings. The coating with the lowest modulus was the 50% LMWSO coating. The influence of this property on the ice adhesion strength will be examined more in Chapter 5.

4.3. Contact angle

The water contact angle is commonly used as a predictor for ice adhesion strength of a coating, as it is indicative of the chemical attraction between the two. Hydrophobic (contact angle >90°) and superhydrophobic surfaces (contact angle >150°) have shown some correlation between contact angle and ice adhesion strength (Kreder et

al., 2016), although this is not a universal finding, and is the topic of much debate within the field (Nosonovsky and Hejazi, 2012).

4.3.1. Experimental method

A facile method was adopted for measuring the static contact angle of water droplets. This involved placing a droplet of deionised water on the surface using a 1.00 ml pipette. The droplets measured 0.05 ml. This was the minimum volume possible based on the syringe tip diameter and water surface tension. This droplet volume was the same as the droplet volume used in the freezing delay tests in Chapter 6, which should provide phenomenological consistency when assessing the two properties together.

A picture of the droplet was taken with a Canon 6D DSLR. Three droplets were placed one at a time on a specimen, and a picture was taken of each droplet. Between tests, the specimens were tilted so the droplet rolled off. Any remaining water was gently blotted off using a paper towel.

Water droplets have been shown to relax and spread on elastomer surfaces, ostensibly due to the viscoelasticity of the polymers (Ibáñez-Ibáñez et al., 2021b). Therefore, the pictures were taken immediately after deposition. The droplets were backlit with LED lights to provide better contrast for subsequent image analysis.

The pictures of the droplets were analysed using the contact angle plug-in on the ImageJ software. Due to the droplet size, an elliptical fit was used to determine the contact angle. Both specimens of each coating had three droplet photos taken. These six photos were then analysed using the ImageJ software three times each, generating 18 measurements from which the contact angle was then taken as the average value. An example photo of the droplet and the image processing methods are provided in Figure 4.4.

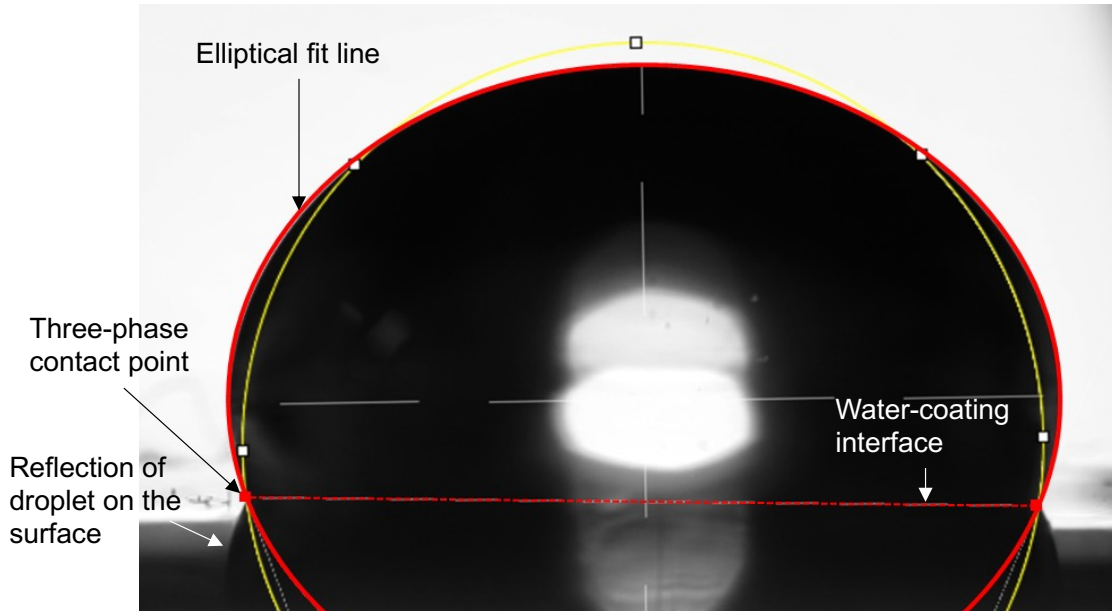

Figure 4.4 – Water droplet photo showing image processing for contact angle measurement. ImageJ software used an elliptical fit (highlighted in red) and the two three-phase contact points at the edges of the water-coating interface to calculate the contact angle. The yellow line assumes a circular fit, which is not appropriate in this study, as it is exhibited by smaller droplets than those used here.

The contact angles were measured before and after the adhesion testing regimen to observe any effects from wear and dust accumulation on the surfaces. Example images of droplets on a specimen before and after adhesion testing are provided in Figure 4.5.

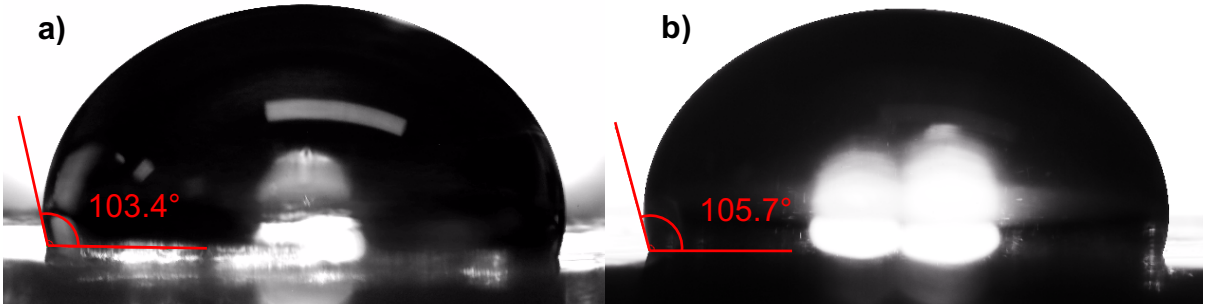

Figure 4.5 – Photos of water droplets on a 50% LMWSO specimen a) pre-adhesion and b) post-adhesion. Contact angles as measured using the ImageJ software are denoted on each image.

4.3.2. Results

The results from the contact angle testing are presented in Figure 4.6. The average contact angles for the coatings range from 100° to 107°. There is little difference between the coatings, which is expected as the contact angle is dependent on the surface energy of the system, which is itself dependent on the chemical attraction

between the water and the coating. The coatings have very similar chemistry, so little difference in contact angles was expected.

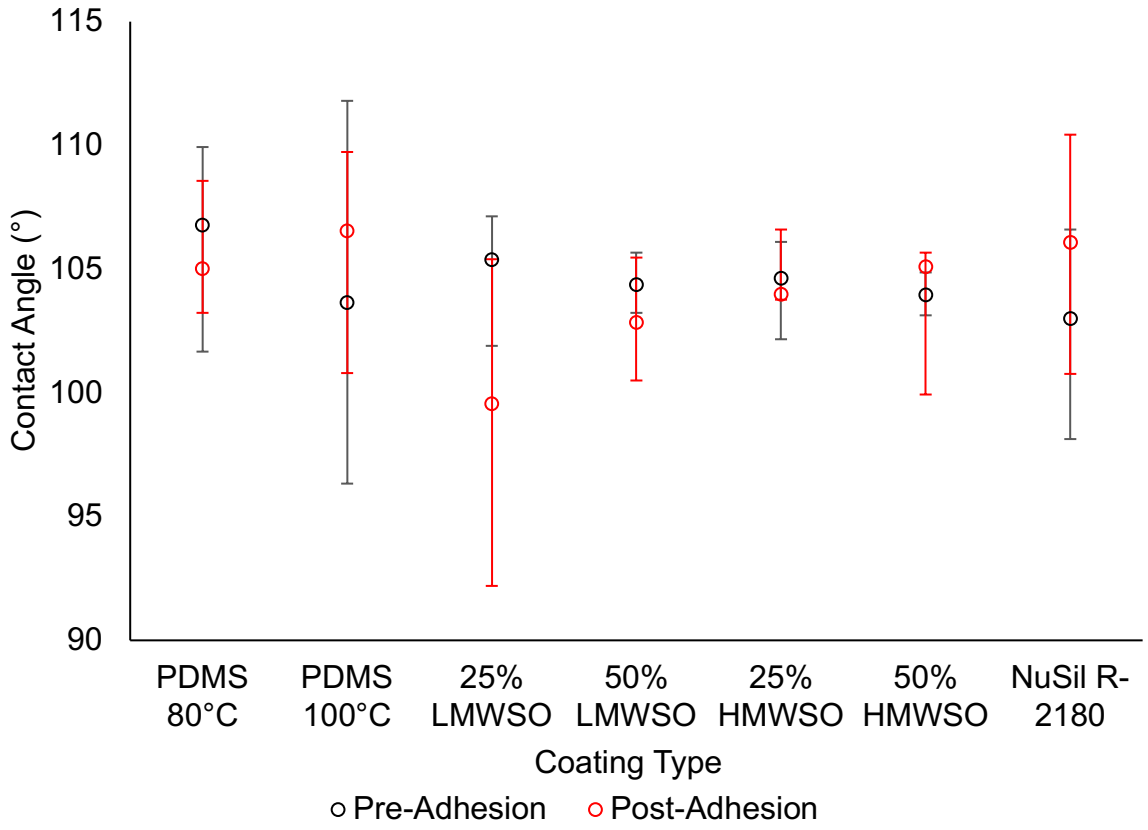

Figure 4.6 – Contact angles on the different coating types pre- and post-adhesion, with range bars. Average values are calculated from two specimens per coating type, on which three droplets were placed and photographed. Each photograph was analysed three times using the contact angle plug-in on ImageJ.

The contact angles show no trends when comparing pre-adhesion results and post-adhesion results. There is a 4-3 split across the coatings when looking at whether they increased or decreased after the adhesion regimen. The range bars for both sets of data have considerable overlap, showing little significant difference between the pre- and post-adhesion data. These results indicate that the effects of surface wear and dust accumulation that occurred during the adhesion regimen were insufficient to meaningfully change the contact angle.

4.4. Coating thickness

The thickness of the specimens is understood to contribute to the measured ice adhesion. The thinner the coating the more closely its behaviour to that of the underlying substrate. As the coating becomes thicker, the thickness becomes less important, and ice adhesion has been shown to become independent of thickness as

the coating approaches a ‘bulk’ thickness – in the range of 0.5-2 mm (Wang et al., 2014a, Kim et al., 2007a). The role of thickness in ice adhesion strength is examined in greater detail in Chapter 5.

The coating thickness will also affect the thermal behaviour of the system and the heat transfer from the droplet during the freezing process. The coatings all have lower thermal conductivities than the aluminium substrate, so will act as an insulator and slow the droplet cooling. As discussed in Chapter 6, this will not only slow droplet cooling, but also retard the ice growth process. Because of this influence on both ice adhesion and freezing delay, the two icephobicity metrics, determination of coating thickness is important for understanding the icephobicity behaviour of the different coatings.

4.4.1. Experimental method

A Mitutoyo SJ-410 stylus profilometer was used to measure the thickness. Stylus profilometry has been used previously for determining soft film thickness (Wang et al., 2018b, Samel et al., 2007). The coatings had been designed to be approximately 200 μm thick. This is near the upper end of the range in which ice adhesion is dependent on thickness, so would minimise the effect of small differences in thickness contributing to the measured ice adhesion strength.

The stylus had a tip diameter of 4 μm and an angle of 60° and applied a force on the surface of 0.75 mN when performing the traces. The real error of the profilometer measurements is 0.02 μm vertically, and 4 μm (the tip diameter) horizontally. Five evenly spaced profile traces were performed along the length of each coating specimen, starting and ending on the aluminium substrate. The probe speed was 0.5 mm/s. The data was then processed by the profilometer to calculate the average thickness of the coating. This method involved manually identifying the substrate base, and the lowest point on the surface of the coating (minimum coating thickness). The coating thickness for the specimen is then the difference between the substrate base depth, and the average height of the points above the minimum coating thickness. An image of the processing method is provided in Figure 4.7. The average thickness of a coating was then calculated from the measured thickness of all 10 traces across the two specimens.

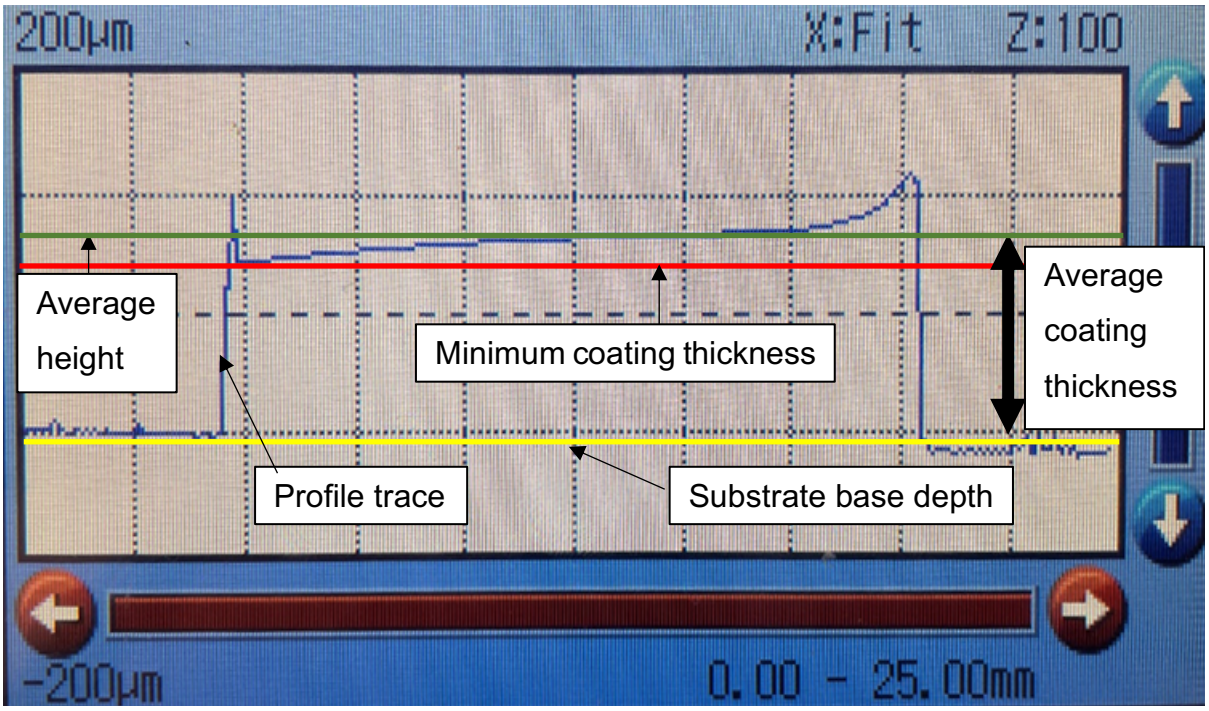

Figure 4.7 – Determination of coating thickness from a specimen profile trace. The substrate base depth and minimum coating thickness are manually identified. The coating thickness is the difference between the substrate base depth and the average height of the points above the minimum coating thickness line.

4.4.2. Results

The results of the thickness measurements are presented in Figure 4.8. The specimens have thickness of 200 µm ± 11%. The values presented on the figure are the average for both specimens for each coating type. The 11% variability between all the specimens was deemed acceptably low. It can be noted that there is greater spread in the thicknesses of the oil-infused coatings. This can be attributed to their lowered viscosity by addition of the oil pre-curing, which can lead to leaking from the casting moulds and greater variability in the final coating thickness. The results were corroborated by measurements with a micrometer.

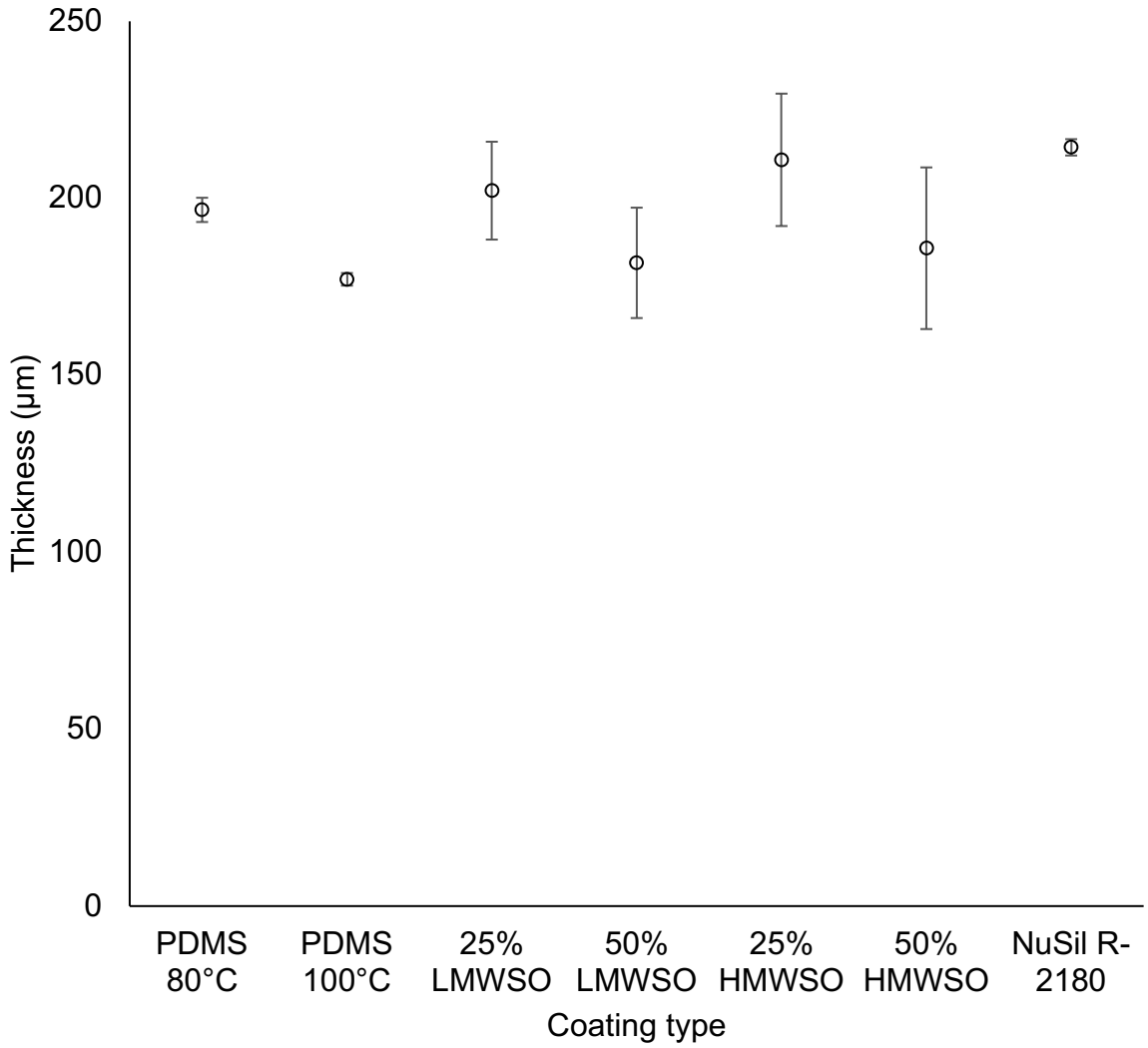

Figure 4.8 – Thicknesses of the coating types. Values are the average of two specimens for each coating type. The spread between the two specimens is indicated by range bars. Thickness of each specimen was calculated as the average of 5 evenly spaced profiles.

4.5. Roughness

The roughness of the specimens has been suggested to be an influencing factor for the ice adhesion strength and the freezing delay, though without a clear consensus on the role it plays in improving or weakening the icephobicity (Nosonovsky and Hejazi, 2012, Kreder et al., 2016).

With respect to the ice adhesion strength, the extent to which roughness is significant may be determined by the wetting state associated with that roughness. As discussed in Chapter 2, liquid droplets on rough surfaces are generally found in one of two states: the metastable Cassie-Baxter wetting state, or the stable Wenzel state (Murakami et al., 2014, Heydari et al., 2013, Jung, 2019). It is therefore useful to characterise the

roughness ahead of the ice adhesion measurements to determine if any trends are visible within the coatings studied here.

With respect to the nucleation and freezing delay that will be examined in Chapter 6, there are similarly mixed theories on the role of surface roughness. Surface roughness is used in the literature as a method for limiting ice nucleation by controlling the size of asperities (Montes Ruiz-Cabello et al., 2021, Oberli et al., 2014). However, this requires precise control of the surface texture, which is difficult and often unsustainable over repeated de-icing cycles. Additionally, most research into this has been carried out with microdroplets of water, with limited examination of larger droplets.

The softness of the coatings, and hence their susceptibility to wear, is often a major criticism of these coatings, with the suggestion that high wear rates from de-icing will cause fast degradation. Roughness measurements can provide an assessment of the extent of surface wear of the coatings with repeated de-icing cycles. This can then be considered against the ice adhesion strengths and freezing delay over repeated testing, to see if any wear accumulation does generate a loss of icephobicity.

4.5.1. Experimental method

The roughness was measured using the same Mitutoyo SJ-410 stylus profilometer as the thickness measurements. The specimens characterised were the same as in the ice adhesion and freezing delay testing.

10 evenly spaced traces were performed on each specimen, 5 along the length and 5 along the width of a coating specimen. The probe speed was 0.5 mm/s. The measurement length was 15 mm.

Arithmetic average roughness, R_a, was then calculated by the profilometer. The roughness of a coating type was then the average of 20 traces, 10 on each specimen. R_a was used as it is the most commonly reported metric in the literature, which allows for better comparison to other studies. Measurements on the specimens were performed before and after the adhesion testing regime.

The suitability of stylus profilometry to the measurement of roughness of soft coatings will be discussed in Section 4.5.3.

4.5.2. Results

The results of the roughness testing are presented in Figure 4.9. In terms of the pre-adhesion roughness, the values for the PDMS 80°C, PDMS 100°C, 25% LMWSO, 50% LMWSO and NuSil R-2180 specimens were consistent with each other, with R_a in the region of 0.05-0.15 µm and very little scatter in the results. This was expected, as the polymer coatings have no engineered surface texture, and should form a fairly smooth surface during the curing process.

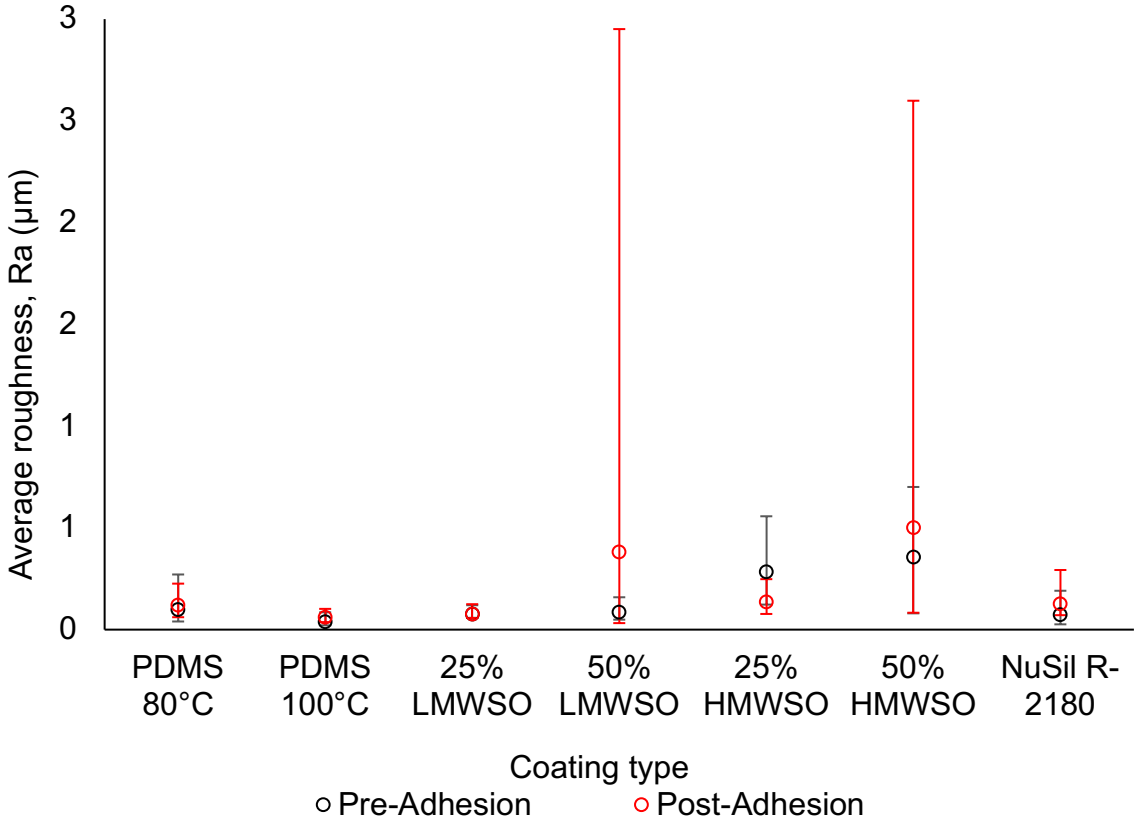

Figure 4.9 – Average surface roughness over 20 measurements of each coating type, with range bars.

The two HMWSO specimens (25% and 50%) presented notably higher initial roughness, at 0.30 µm and 0.36 µm respectively. This magnitude of roughness was unexpected; as already stated, there was no designed roughness, and the coating forms from the slow curing and solidification from the liquid state. It is likely that this result is not an accurate representation of the real surface roughness, but error from some other surface phenomenon. This will be explored further in the following sections, but two initial possibilities were present. Firstly, it is possible the increased softness and weakening of these coatings by the addition of the oil caused high

surface deformation under the force of the profilometer, which was incorrectly interpreted as roughness. Alternatively, capillary effects from surface oil could be providing instability as the stylus traverses the surface, or a combination of both capillary effects and large elastic deformations. The presence of surface oil when infusing with high molecular weight oils was observed by Golovin et al. (Golovin et al., 2016), and oil is clearly visible by eye on the 50% HMWSO coating, but not on the 25% HMWSO. The presence of surface oil is examined in Section 4.7.

When examining the effect of the 100 repeated de-icing cycles that were carried out during the adhesion testing regimen, we can see that for the PDMS 80°C, PDMS 100°C, 25% LMWSO and NuSil R-2180 specimens, there was very little change in the measured roughness post-adhesion. This indicates little change to the surface from wear. The 50% LMWSO coating had a fairly large increase, to 0.38 µm; however, this can be attributed to incidental (not caused by de-icing) damage that occurred to a specimen during adhesion testing, which caused a gouge in the surface. As shown by the size of the range bar, the spread in the data is large – the roughness was high where the gouge was, but in the order of 0.05-0.15 µm elsewhere. These observations are confirmed with imaging in Section 4.7. The roughness traces for the specimen pre- and post-adhesion are provided in Figure 4.10, with detection of the gouge in the orange and black traces of panel b).

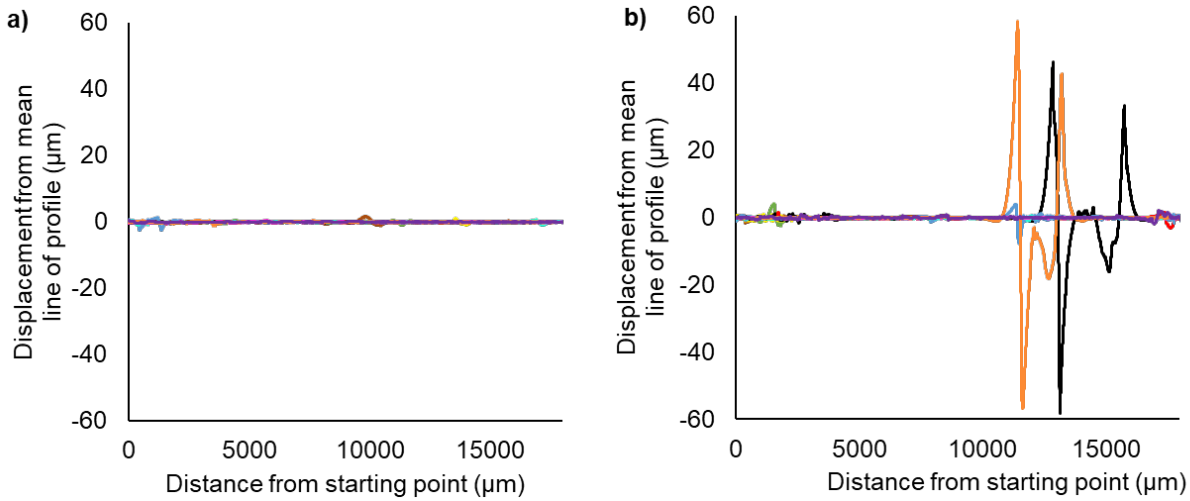

Figure 4.10 – The surface roughness traces for the 50% LMWSO specimen a) pre-adhesion and b) post-adhesion. The specimen was impacted by a screwdriver tip during adhesion testing, causing incidental damage. The gouge in the surface is detected in the orange and black traces on panel b), which have the same morphology.

Interestingly, the 25% HMWSO coating showed a decrease in roughness, to 0.14 μm, despite the wear experienced. The 50% HMWSO saw an increase, to 0.50 μm, as well as a wide spread in the range of measurements, again from some incidental damage to the surface. Without the skew in the data caused by the incidental damage, the results would be similar to the pre-adhesion test data.

Further examination of the shape of the roughness traces also helps in understanding the surface phenomena. Example traces are presented in Figure 4.11, for three of the surfaces: 25% LMWSO, 25% HMWSO and 50% HMWSO. They show that the 25% LMWSO specimen was relatively smooth prior to the adhesion testing regimen. The post-adhesion traces show there is a small increase in roughness, possibly as a result of surface wear. This behaviour was seen in all four coating types which exhibited low roughness pre-adhesion (PDMS 80°C, PDMS 100°C, 25% LMWSO and 50% LMWSO). The 25% HMWSO had high roughness prior to adhesion testing, which appeared to fall drastically after adhesion testing. The 50% HMWSO specimen had high roughness both pre- and post-adhesion testing.

This divergent behaviour of the two HMWSO coatings post-adhesion could be explained by the different oil percentage in each coating: if there was oil present on both surfaces pre-adhesion, it is likely the de-icing cycles removed it. It is then possible that the 25% HMWSO coatings did not have sufficient internal oil to replenish the surface oil, but that the higher percentage 50% HMWSO was able to replenish the surface oil. This replenishment via supply from the bulk has been observed in the literature in other organogel coatings (Urata et al., 2015), and proposed in these oil-infused PDMS coatings (Golovin et al., 2016). The 50% HMWSO not only has greater oil reserves within the coating, but also has higher osmotic pressure for replenishment. It is therefore possible that the 50% HMWSO specimens were able to replenish the oil upon removal by de-icing, while the 25% HMWSO coatings were not. This would result in the 25% HMWSO coating falling back to the expected range (0.05-0.15 μm) from removal of oil-generated capillary effects, post-adhesion. The continuation of capillary effects, combined with the incidental damage, could explain why there is an increase in measured roughness of the 50% HMWSO post-adhesion.

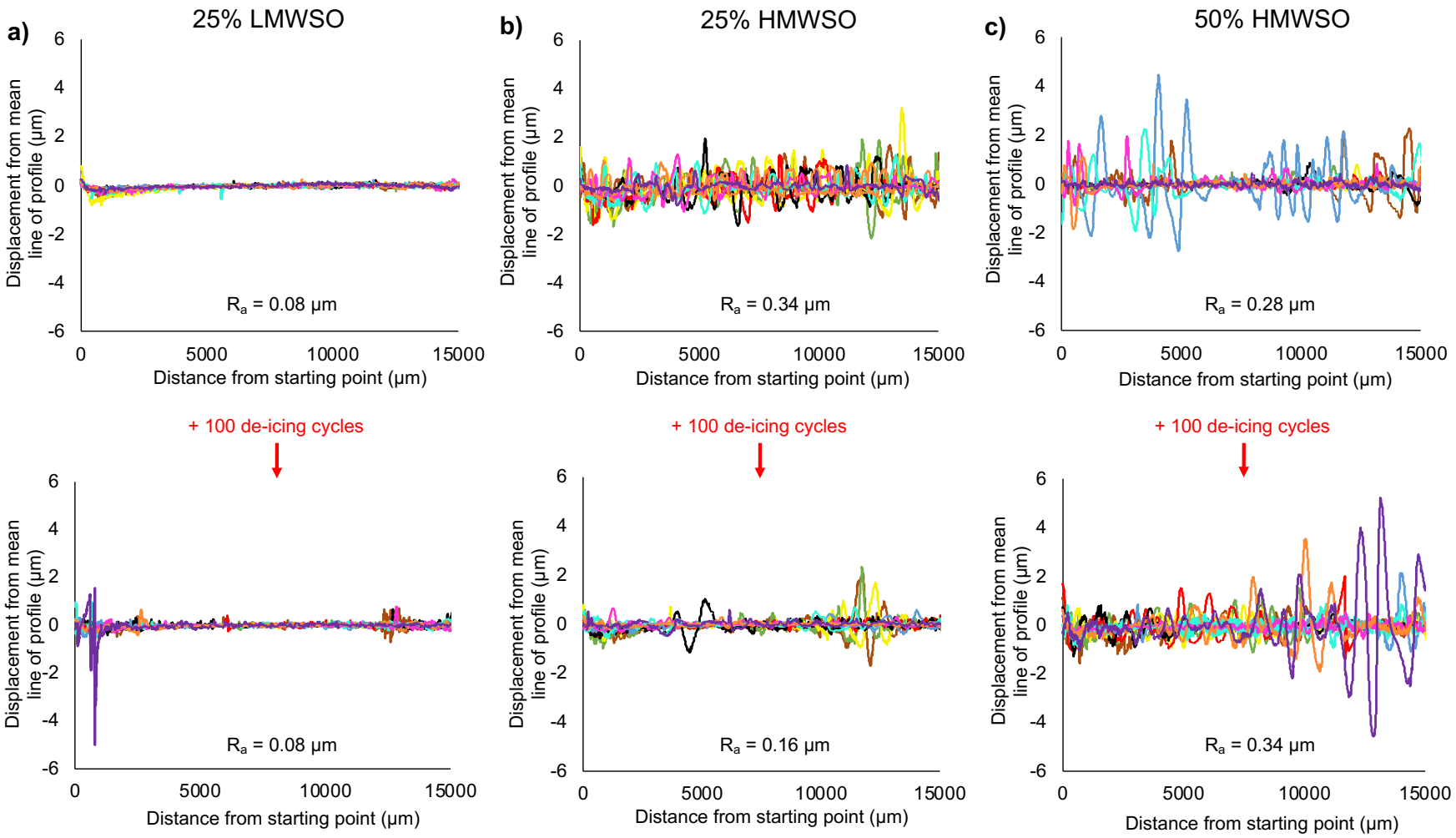

Figure 4.11 – Roughness profiles pre- and post-adhesion testing for a) 25% LMWSO specimen, b) 25% HMWSO specimen, and c) 50% HMWSO specimen. The 25% LMWSO specimen is fairly smooth pre-adhesion testing and sees a small increase in roughness post-adhesion testing. The 25% HMWSO specimen has high roughness pre-adhesion, but the roughness appears to fall after the adhesion testing. The 50% HMWSO specimen has similarly high roughness pre- and post-adhesion testing. Each colour corresponds to one of the 10 roughness traces performed on the specimens. The average values of R_a for the 10 traces are indicated on each plot.

4.5.3. Stylus profilometry for detecting large-scale surface roughness

The softness of elastomer coatings leads to concerns of surface deformation from the force of the stylus and uncertainty in the data. The most common methods for measuring roughness of elastomers are AFM and 3D confocal microscopy. However, the elastomers investigated in this work are transparent, making 3D confocal microscopy impractical. Though stylus profilometry is not a common method, there is some support for its use in the literature, in which other studies have also used it for both roughness measurements (Gevaux et al., 2018, Lucas et al., 2008) and profile traces (Dahlberg et al., 2018, Trantidou et al., 2017). Most commonly this is in the field of microfluidic devices fabricated from elastomers, which have micron-scale surface features.

While less precision is available, it has been shown in this work that stylus profilometry is able to detect moderate-to-severe damage caused by wear. The profilometer was able to detect incidental damage to one of the 50% LMWSO specimens in Figure 4.10. Additionally, all but the 25% HMWSO specimen (for reasons discussed) showed a small increase in measured roughness after the ice adhesion testing regimen, likely from surface wear. Visualisation of the surface wear is provided in Section 4.7. The profilometer was also able to detect deliberate damage on the specimens. This will be discussed fully in Chapter 7 but is mentioned here as evidence to support the proposal that that the stylus profilometer has adequate sensitivity for some scenarios.

4.6. Room temperature adhesion

To give additional context for the unexpected roughness measurements and the surface properties of the coatings in general, room temperature adhesion measurements were performed. For example, if there are capillary forces interfering with the roughness measurements, this may be revealed by the adhesion measurements.

A straightforward compressive/tensile test method was utilised to determine the room temperature adhesion. This is described below.

4.6.1. Experimental method

For measuring the room temperature surface adhesion, tests were performed using a 50 N Instron mechanical tester. Each coating type was cast as a thick film in a dish and prepared as normal, described in Chapter 3. The thickness of the films was

between 1.5-3 mm. The same films and apparatus were used in the determination of elastic modulus, also described in Section 4.2.

From the thick films, 6 mm diameter cylinders were punched out using a biopsy punch. The thickness of the cylinders was then measured using a digital calliper. The cylinders were roughened with 400 grit sandpaper to improve adhesion and then cylinders glued to a 1 mm diameter steel disc. The glue was left to cure for 30 minutes before testing. The steel discs were backed with a strong adhesive glue. The specimens were not subjected to de-icing and were used as-made.

After the cyanoacrylate glue had cured, the discs were stuck down to the bottom compression platen of the mechanical tester. The top platen was then brought down to the surface of the specimen. The specimen was then subjected to compression, at a speed of 50 μm/s, up to 3% strain. Once this was achieved the top platen was retracted at the same speed, until the force fell to 0 N and the platen detached from the specimen.

Force-displacement curves were generated during testing, and then converted to stress-strain curves.

4.6.2. Results

An example stress-strain curve is presented in Figure 4.12. It shows that the stress remains non-zero even when displacement is negative, i.e., adhesive force between the platen and specimen creates tensile strain in the specimen, stretching it. The peak adhesive stress is determined as the lowest point on the curve. The average value for peak adhesive stress was then calculated from the three specimens. The results for each coating are presented in Figure 4.13.

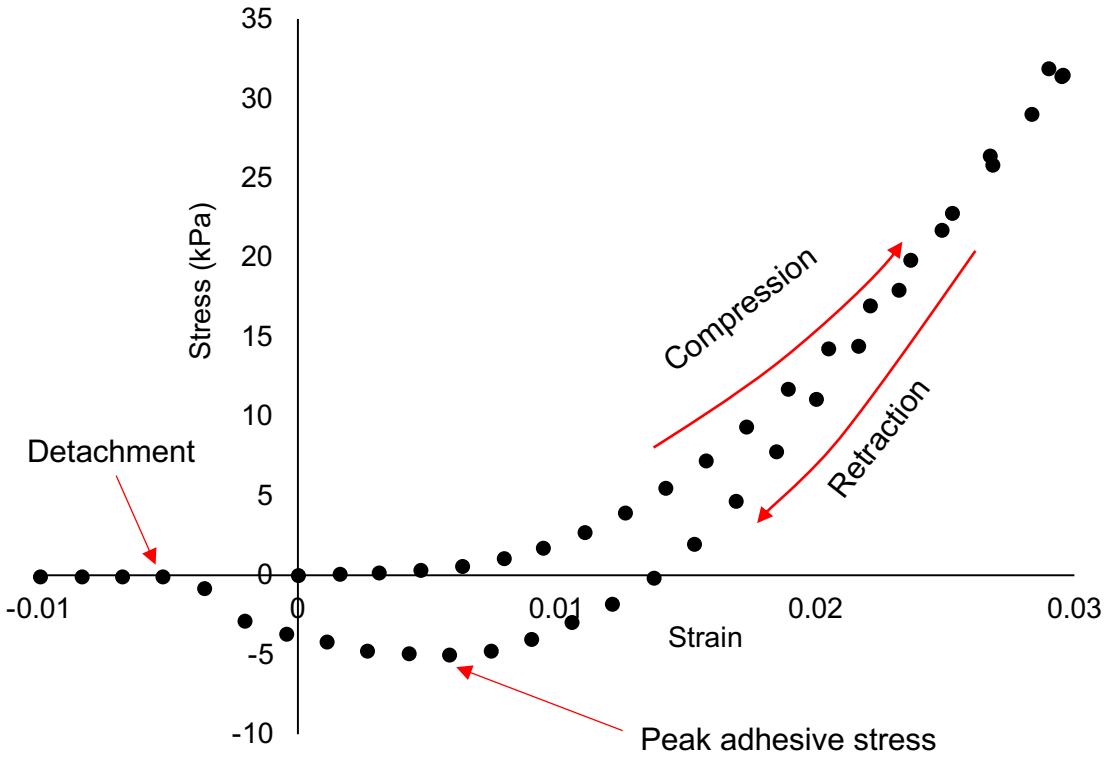

Figure 4.12 – Stress-strain curve for a PDMS 80°C specimen placed under a compressive load. The load is applied up to 3% strain and then removed. During retraction, there is an adhesive force between the upper compression platen and the specimen surface. As the platen rises above the initial height of contact (at compressive strain = 0), there is still adhesion between the surfaces and stress on the specimen. The specimen is briefly loaded in tension, until the adhesion forces are overcome, and the detachment occurs.

Most of the coatings have very similar peak adhesion stress, around 1-3 kPa. However, the 50% LMWSO and 50% HMWSO coatings show higher peak adhesion stress. This suggests that the peak adhesion stress is most influenced by the percentage of oil and softness of the coating and less so by the molecular weight of the oil or presence of oil.

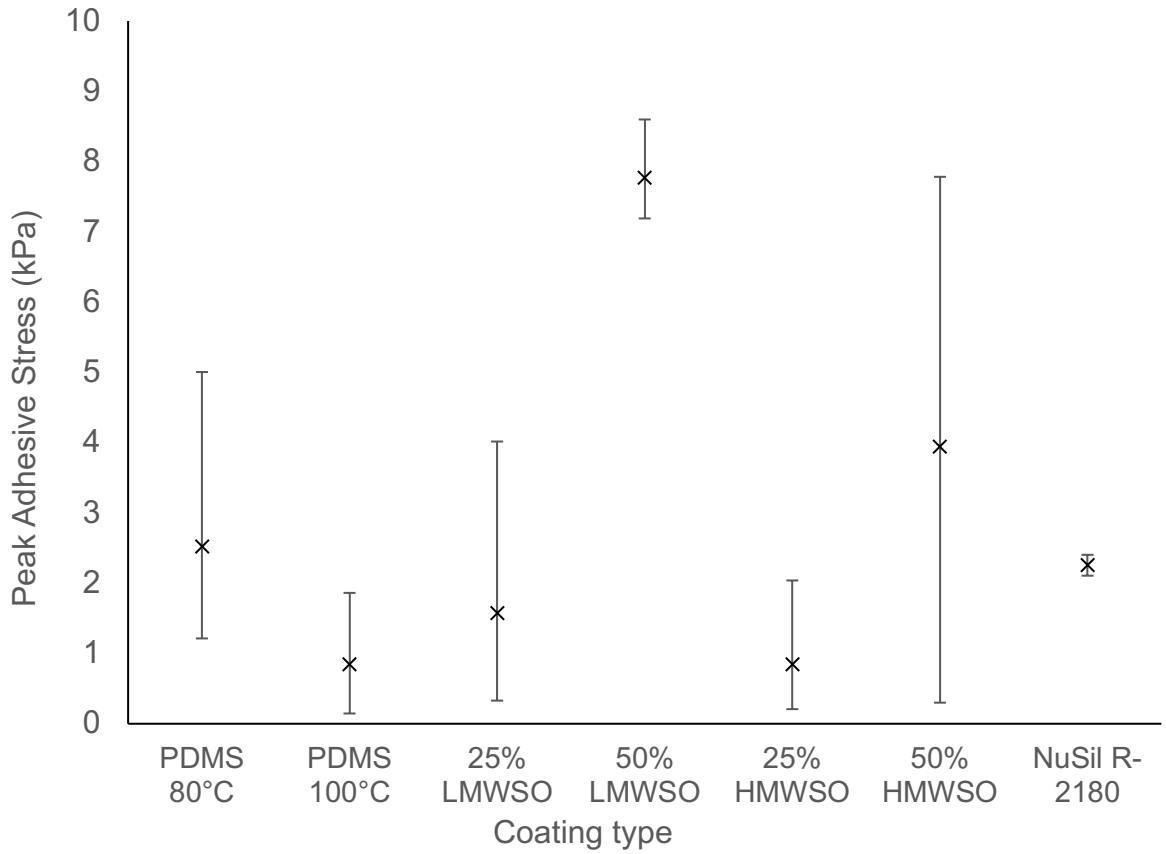

Figure 4.13 – Peak adhesive stress of the coatings calculated from three specimens. Most of the specimens have similar adhesion, with the 50% LMWSO and 50% HMWSO specimens being notably higher.

When comparing the peak adhesive stress with the elastic modulus results, there is the complementary observation that the 50% LMWSO and 50% HMWSO coatings have the lowest moduli. This indicates that the softer and more elastic the coating, the higher the conformation and contact between the platen and coating, and the higher the adhesive forces. The greater elasticity also allows for higher strain in the coating, so it can remain in contact with the platen at greater tensile displacements. This is supported by plotting the peak adhesive stress against the elastic modulus in Figure 4.14, which shows a moderate negative correlation.

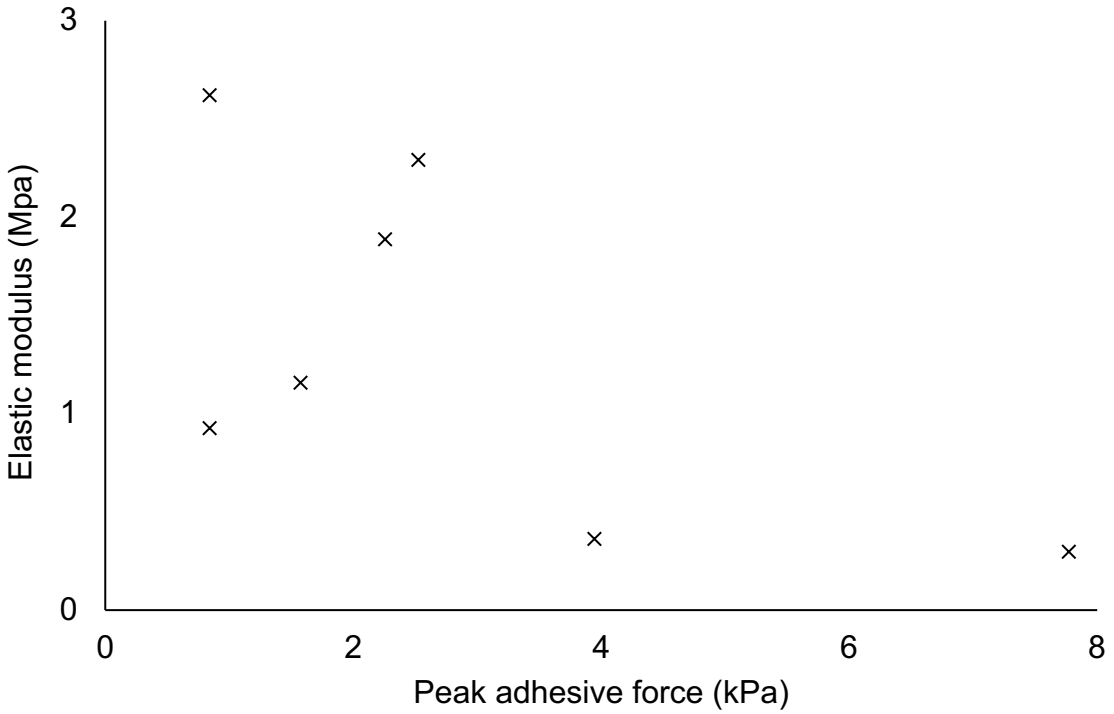

Figure 4.14 – Peak adhesive force and elastic modulus of the coatings, showing a moderate negative correlation.

4.7. SEM and optical microscopy

Microscopy of the specimens allows for improved visual assessment of the coatings. This is useful in many ways, including for visual corroboration of the surface roughness, and identification of any other relevant surface features. If there is oil on the surface of the coatings, for example, microscopy may reveal that.

4.7.1. Experimental method

Room temperature SEM and optical microscopy were used for visualising the surfaces. A Zeiss Axioscope 2 was used for the optical microscopy. A TM4000 plus was used for the SEM imaging. Secondary electron imaging was carried out using a 5 kV accelerating voltage under a moderate vacuum, which allowed the surfaces to be imaged without sputter coating.

The specimens were imaged before and after the ice adhesion testing, visualising any wear-related damage and dust accumulation from the ice adhesion testing process. As there was the possibility of oil on the 25% HMWSO and 50% HMWSO coatings, it was decided to first look at these under the optical microscope, so as not to remove any oil under the vacuum of the SEM.

4.7.2. Results and discussion

4.7.2.1. Optical microscopy

To check for the presence of surface oil on the HMWSO, optical microscopy was used (there is no vacuum to potentially remove the oil, as in SEM). Selected images of the specimens before adhesion testing are presented in Figure 4.15. The 25% HMWSO and 50% HMWSO specimens show distinct differences. On the 25% HMWSO specimens there are clearly discrete droplets of oil across the surface. The presence of oil on the surface of the 50% HMWSO coating is less obvious. This is because it is a continuous layer on the surface and is most easily identified by the interaction of dust and dirt on the surface which interrupts the surface tension of the oil layer. This appears almost as a halo around the particles/fibres, where they are in contact with the oil. This confirms the presence of oil on the specimens.

The specimens were also imaged after the adhesion testing regimen, presented in Figure 4.16. The images are within the ice-cylinder contact area. The 25% HMWSO specimen has no surface oil visible, as droplets or a continuous layer, within the contact area. However, outside of the contact area, there were still droplets of oil, which had not been removed from the surface by the ice detachment process. The 50% HMWSO specimen showed some evidence of an oil layer via the halo effect around the dust particle contact points. However, the layer does not cover the whole surface – there are some fibres/particles which do not have a halo around them.

This evidence supports the hypothesis that there is oil on both surfaces before ice adhesion, with more oil on the 50% HMWSO, and that the de-icing cycles removed the oil from the surfaces. The 25% HMWSO did not replenish the surface oil after testing had finished, while the 50% HMWSO was at least able to partially replenish the surface oil.

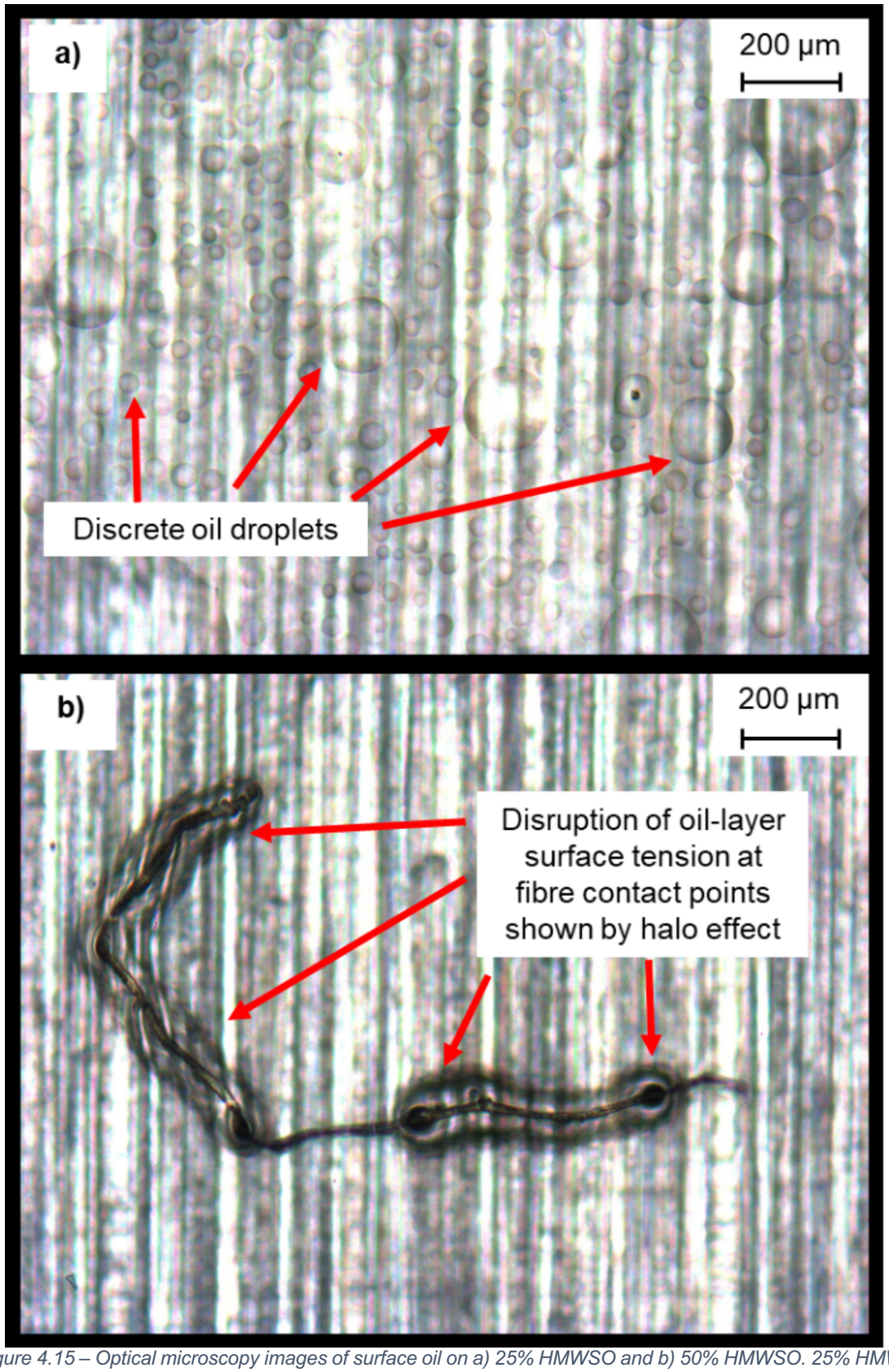

Figure 4.15 – Optical microscopy images of surface oil on a) 25% HMWSO and b) 50% HMWSO. 25% HMWSO surface has discrete surface oil visible as droplets on the surface pre-adhesion. 50% HMWSO surface has a continuous layer of oil, visible by the interaction of the dust-fibre contact points with the oil.

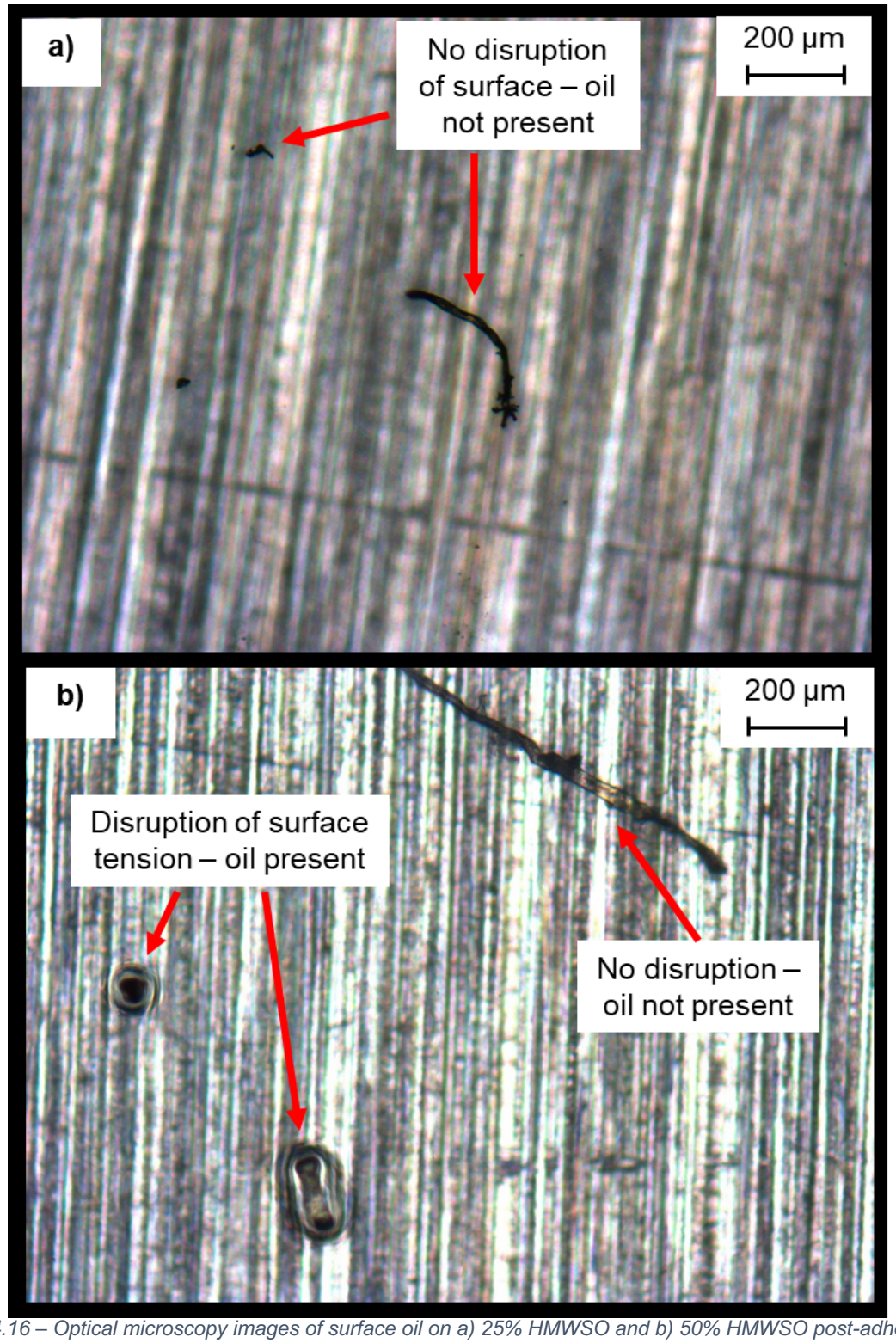

Figure 4.16 – Optical microscopy images of surface oil on a) 25% HMWSO and b) 50% HMWSO post-adhesion. 25% HMWSO specimen has no surface oil visible as droplets, within the ice cylinder contact area (where testing occurred). But outside of the detachment area, there were still droplets of oil, which had not been removed from the surface (not shown here but appears same as in Figure 4.15a). 50% HMWSO specimen has some areas where an oil layer remains, again shown by the halo effect around the dust contact points where the oil layer surface tension has been disrupted. However, it does not cover the whole surface – there are some fibres/particles which do not have a halo around the contact points.

4.7.2.2. SEM

A selection of SEM images are presented in Figure 4.17. These images are representative of the findings on the coatings without surface oil (PDMS 80°C, PDMS 100°C, 25% LMWSO, 50% LMWSO and NuSil R-2180). All the surfaces have minimal texture pre-adhesion, with no obvious roughness. The only features of note are dust and dirt on the surface. This agrees with the pre-adhesion roughness measurements, which showed minimal roughness. Images of the specimens after adhesion testing show little damage to the surfaces. Some instances of damage were identified and are presented in further detail in Figure 4.18 and Figure 4.19.

It can be observed on the images that the dust present on the specimens pre-adhesion is generally spread uniformly across the surface. After adhesion, the dust lays primarily around the edges of the images in Figure 4.17 and Figure 4.18. This occurs because any dust that settles within the bounds of the ice cylinder contact area between tests is removed by detachment of the ice cylinder. The ice detachment arguably 'cleans' the surface of dust. From the images in Figure 4.17, it can be seen that significant dust build-up occurred around the outside of the ice cylinder contact area over the 100 tests (approximately 9 months exposed to the cold lab atmosphere – see Chapter 5 for details).

Figure 4.18 shows pre- and post-adhesion SEM imaging of a PDMS 80°C specimen. The initial imaging displays similar features to the other coating types, and the post-adhesion images highlight the two types of damage that were identified. There is characteristic elastomer abrasive wear, as well as evidence for cohesive damage that caused gouging in the surface (in cohesive fracture, fracture occurs within a specimen, not at the interface). There is a gouge in the surface with a tear-drop shape, as well as single tracks made from abrasion by debris at the left of the image. Crack networks have formed at the tip of the gouge in the surface. These cracks were only present in the pure PDMS surfaces, indicating reduction in brittleness by the addition of oil. Gouging damage was the most commonly seen damage type across all the specimens post-adhesion.

Further examples of damage to the LMWSO specimens are presented in Figure 4.19. These images show higher magnification views of some of the different damage types - mostly cohesive gouging (a, b, c, d,), but with some abrasive wear (b, c, e and f). It

should be noted that though there is large crack formation in the surface (a, d), the cracks are stable and not forming networks. This may suggest that, though these surfaces are more susceptible to damage from their softness, catastrophic brittle failure is better prevented by the addition of the oil.

Images (a) and (d) are of a 50% LMWSO specimen, which experienced incidental damage during adhesion testing when impacted by a screwdriver tip. This caused relatively large-scale damage to the surface when compared to the other damage events. The gouges created by this impact are significantly larger and deeper than the gouges created by ice detachment. It is likely that the damage changed the results of the icephobicity testing on this specimen, at the very least by changing the contact area of the ice on the surface for adhesion testing.

The imaging, combined with the roughness measurements, demonstrates that the ice detachment process generates minimal damage to any of the surfaces. The scale of damage is therefore unlikely to be the source of any significant increases in adhesion strength over time but is possibly the cause for the decreases in indefinite nucleation suppression exhibited by the coatings post-adhesion – this will be discussed further in Chapter 6.

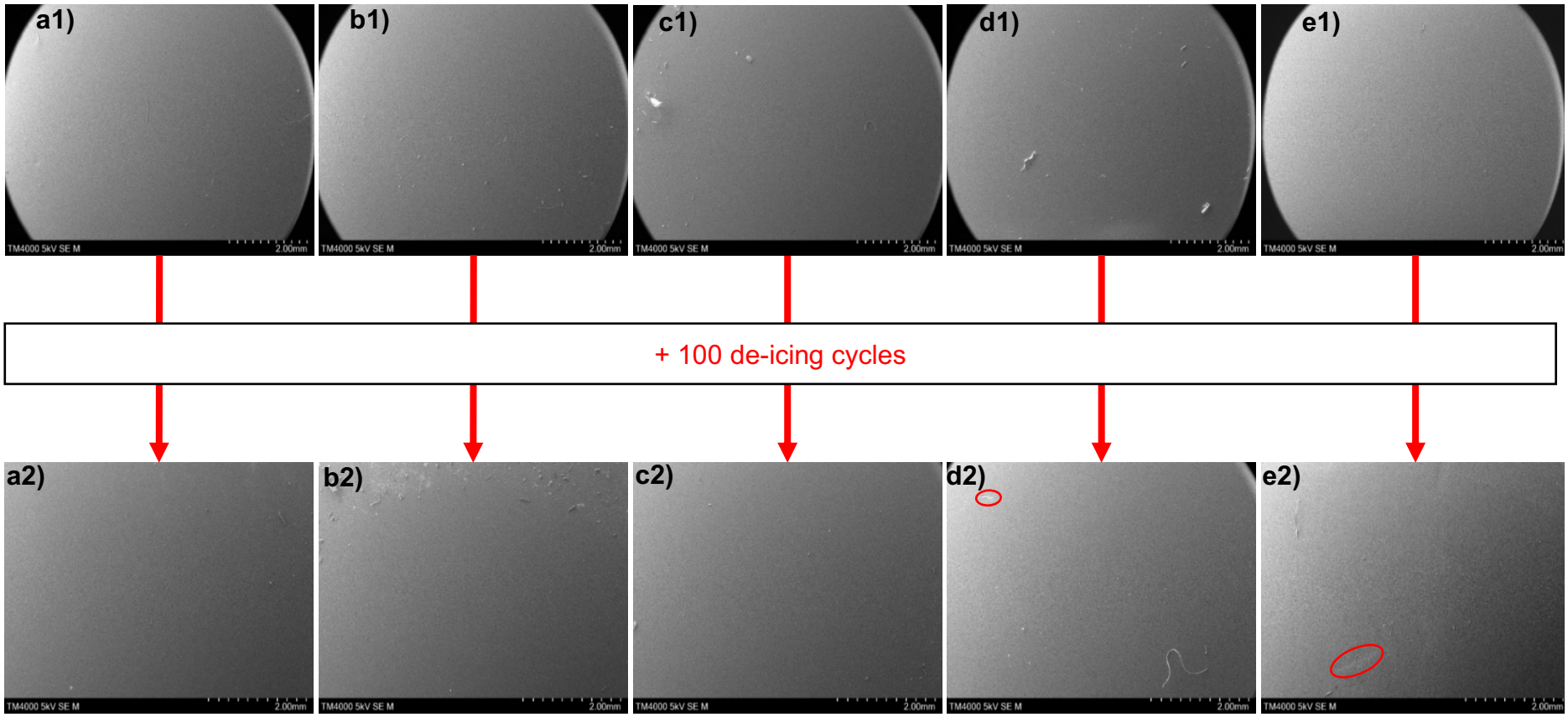

Figure 4.17 – SEM images of coating surfaces pre- and post-adhesion. Each of the coatings without surface oil are presented and are: a) PDMS 80°C, b) PDMS 100°C, c) 25% LMWSO, d) 50% LMWSO, and e) NuSil R-2180. Only visible features on pre-adhesion surfaces are dust and fibres. Post-adhesion surfaces show minimal damage, circled in red on (d2) and (e2) and shown in greater detail in Figure 4.19 (b) and (e), respectively. The ice cylinder's circular contact area can be seen surrounded by dust at the top of (b2).

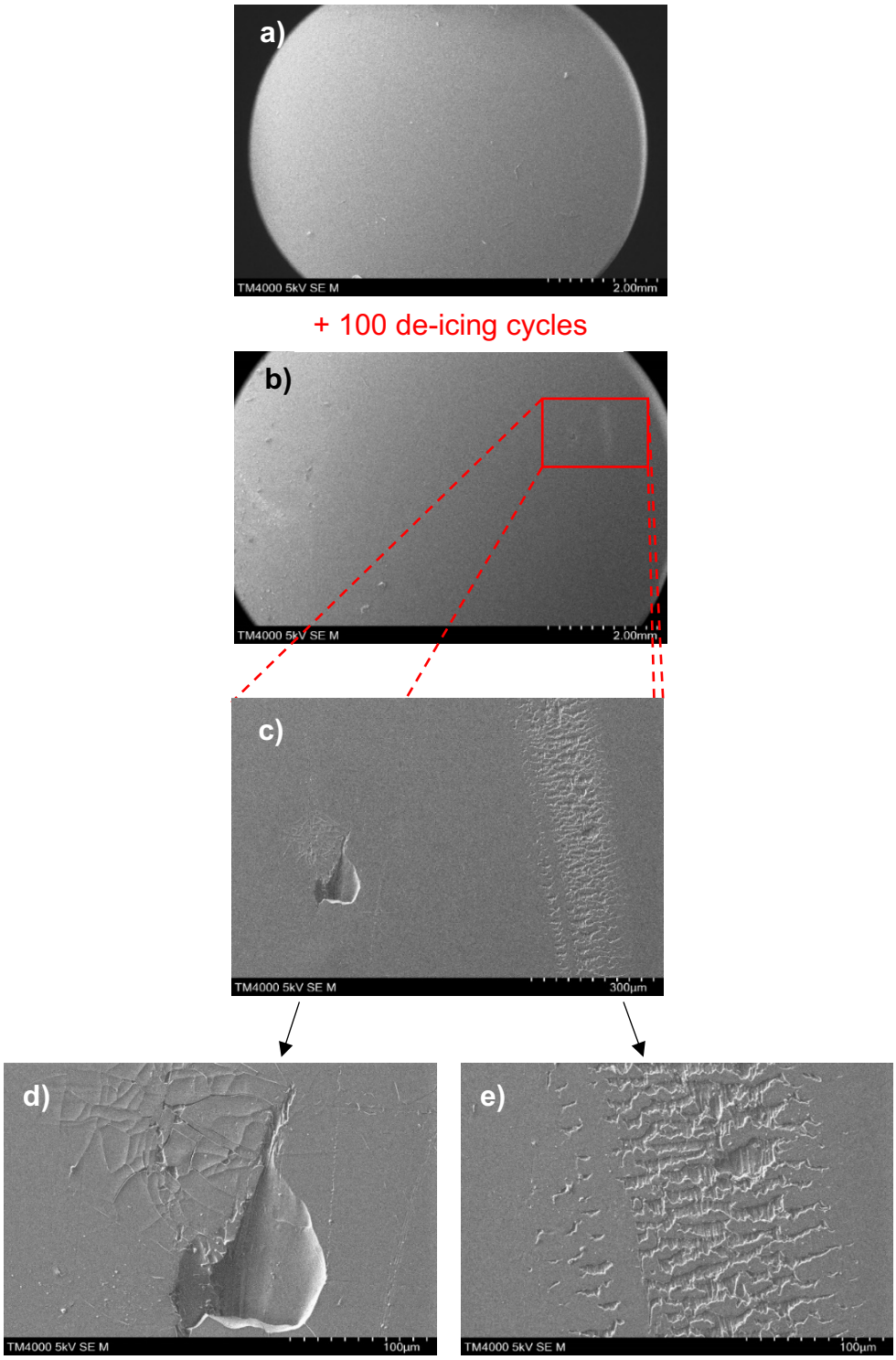

Figure 4.18 – SEM images of a PDMS 80°C specimen (a) pre-adhesion and (b-e) post-adhesion. Panels (a) and (b) present representative view over a wider area of the specimen. The primary features visible are of dust and dirt on the surfaces. Panel (b) has significant dust build up on the left side of the image, and almost no dust in the centre of the image, where the ice cylinder was placed for each adhesion test. Panel (c), (d) and (e) show higher magnification images of the surface, where damage has occurred. Panel (d) shows gouging damage that was common across many of the surfaces. It also shows cracking at the tip of the divot. Figure (e) shows sliding wear damage in keeping with patterns observed in other elastomer wear experiments.

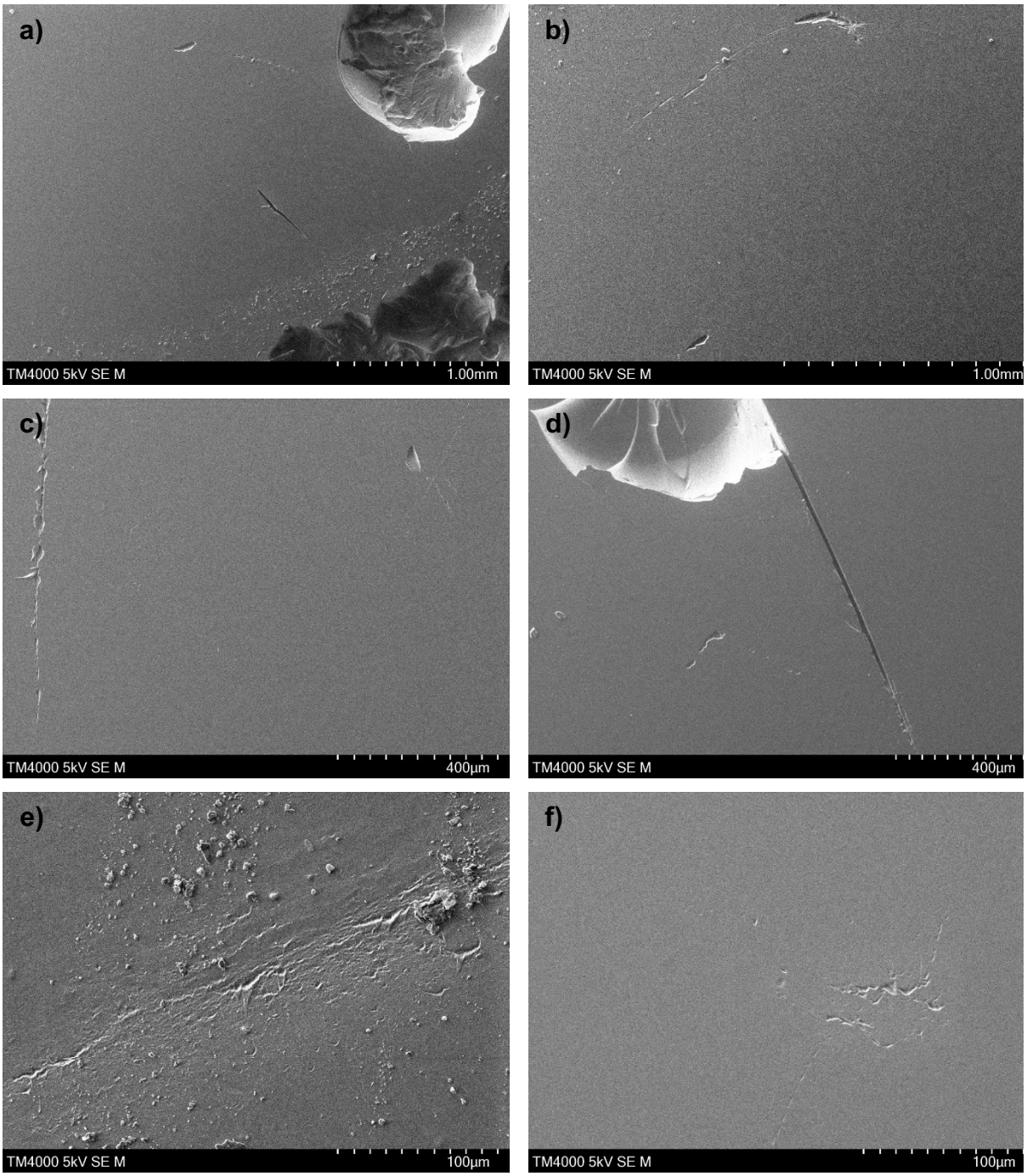

Figure 4.19 – Examples of damage to LMWSO coatings after adhesion testing, at increasing magnification. Images show a mixture of cohesive gouging (a, b, c, d,) and abrasive wear (b, c, e and f). Cracks in the surface (a, d), are stable and not forming networks. The incidental damage from impact by a screwdriver tip on one of the 50% LMWSO specimens is visible in figures (a) and (d).

4.8. Conclusion

The elastic modulus, contact angle, coating thickness, surface roughness, and room temperature adhesion were measured for each coating type. The numerical characterisation was combined with optical microscopy and SEM imaging of the surfaces for visualisation. Measurements and imaging were performed before and after the ice adhesion testing regimen, to observe whether wear from the de-icing cycles damaged the surfaces. This will help in making links between wear damage, the surface properties, and changes in icephobicity in future chapters.

The elastic modulus of the coatings was characterised because of its influence on ice adhesion strength. There was good agreement between the PDMS 100°C modulus measured in this work (2.62 MPa) and other studies. All the moduli were within the range of 0.29-2.62 MPa. The oil-infused coatings had lower elastic modulus than the non-oil infused coatings and the molecular weight of the oil had little influence on the elastic modulus. The 50% oil coatings had lower modulus than the 25% coatings, and the 50% LMWSO had the lowest elastic modulus of all the coatings.

In the contact angle measurements, there was little difference between the coatings, with all coatings measuring between 100-107°. This was expected, as the contact angle is mostly determined by the surface chemistry, which is very similar between the coatings.

Measured by stylus profilometer, the coating specimens were 200 μm ± 11% thick. Roughness measurements were also performed via stylus profilometer, and the coatings displayed a small increase in roughness post-adhesion testing, which could correspond to small amounts of damage from surface wear. However, these measurements are likely erroneous and exaggerate the roughness values due to high surface deformations in the soft coatings, or the presence of surface oil that can cause capillary forces. The stylus profilometer was able to identify incidental damage on a 50% LMWSO specimens, suggesting it has some utility in detecting severe damage.

The presence of oil droplets on the 25% HMWSO coating and a continuous oil layer on the 50% HMWSO coating, was confirmed by optical microscopy before adhesion. After adhesion testing, there were no droplets on the 25% HMWSO coating within the ice-cylinder contact area. Oil puddles remained in areas on the 50% HMWSO coating. These findings suggest that de-icing cycles removed the oil from both surfaces, and

that it was able to be replenished from the bulk in the 50% HMWSO coating but not in the 25% HMWSO.

The SEM imaging showed no intrinsic roughness pre-adhesion. De-icing generated minimal damage to the coatings, though slightly more on the softer, oil-infused coatings. Gouging and abrasive wear were the most common forms of damage.

Room temperature adhesion tests show the 50% LMWSO and 50% HMWSO have the greatest peak adhesive forces upon retraction of a compressive load, at 8 kPa and 4 kPa respectively. The results indicate the oil percentage and elastic modulus of the coatings have the greatest influence on the adhesive force but the presence of surface oil is likely the biggest contributor to the erroneous roughness measurements.

5. Ice Adhesion

Summary

Ice adhesion strength of the coatings is assessed via push tests carried out at –10°C. The findings of 100 repeat de-icing cycles show a notable difference between oil-infused and non-oil infused coatings. Ice adhesion of oil-infused coatings was less than 50% of the non-oil infused coatings in most tests. The 50% LMWSO performed best, with average adhesion strength of 16.5 kPa over all 100 tests, and 17.8 kPa in the final 10 tests. The worst coating was the PDMS 80°C, with 99.3 kPa over all 100, and 103.6 kPa in the final 10. Degradation from surface wear is shown not to be a particular concern on the oil-infused coatings. The non-oil infused coatings exhibited tests that exceeded the load limit (at least >650 kPa, strain gauge measurements indicate >1000 kPa), with increasing frequency over time. This renders the non-oil infused coatings not icephobic over time, and heavily recommends the use of oil-infused coatings over non-oil infused coatings in anti-icing applications. They would provide an improvement on bare metal surfaces.

The ice adhesion results are compared to values from literature, which show remarkably good agreement, despite differences in experimental details. This suggests a hierarchy in the influence of the properties, which is examined by the application of two ice adhesion models: 1) interfacial cavitation and 2) interfacial slippage. This analysis shows shear modulus has the strongest influence on adhesion strength, compared to coating thickness, work of adhesion and contact angle. The correlation between ice adhesion and shear modulus is shown to be better described by a linear dependency than a square root relationship, which suggests the presence of interfacial slippage.

5.1. Introduction

Of the two icephobicity constituents, **i)** ice adhesion strength and **ii)** freezing delay, ice adhesion strength is more commonly studied. A wealth of knowledge exists within the literature on the ice adhesion strength of many surfaces and coatings. Measuring the ice adhesion strength helps quantify the energy requirement for de-icing a surface. The lower the ice adhesion strength of a surface the less energy required for de-icing, which saves time and resources. Characterising ice adhesion of a surface can also help predict the performance, and improve the design, of future coatings.

Ice adhesion testing lacks standardisation, and a range of test geometries, such as the 'push' test, 'zero-degree cone' test, lap shear test and centrifugal test are used. These are discussed thoroughly in Chapter 3 but are reviewed briefly in Figure 5.1.

The artificiality of ice formation is often a major criticism of these tests. Most studies do not test naturally formed ice, but 'refrigerated' ice. However, their practicality makes them useful in providing a first screening or comparison of surfaces (Laroche et al., 2020). Within a given test geometry, finer details such as water purity, freezing conditions, temperature, humidity, strain rate and specimen geometries can affect the measured adhesion strength (Makkonen, 2012).

Another important consideration in ice adhesion measurements is the physical and environmental history of a specimen. Many of the most promising anti-ice coatings have poor mechanical durability, as they rely on delicate surface textures, lubricating fluids, soft materials, or a combination of these (Kreder et al., 2016). These surfaces can be highly susceptible to wear from repeated de-icing cycles, which is normally associated with an increase in ice adhesion strength and a loss in performance over time. This can also be worsened by UV, thermal and chemical exposure. Evaluation of coating durability is therefore important when considering the viability of their use in real applications. This often involves repeat icing and de-icing cycles, or artificially-accelerated ageing via abrasion, UV, thermal or chemical exposure (Golovin et al., 2016, Ibáñez-Ibáñez et al., 2022, Maghsoudi et al., 2021, Beemer et al., 2016).

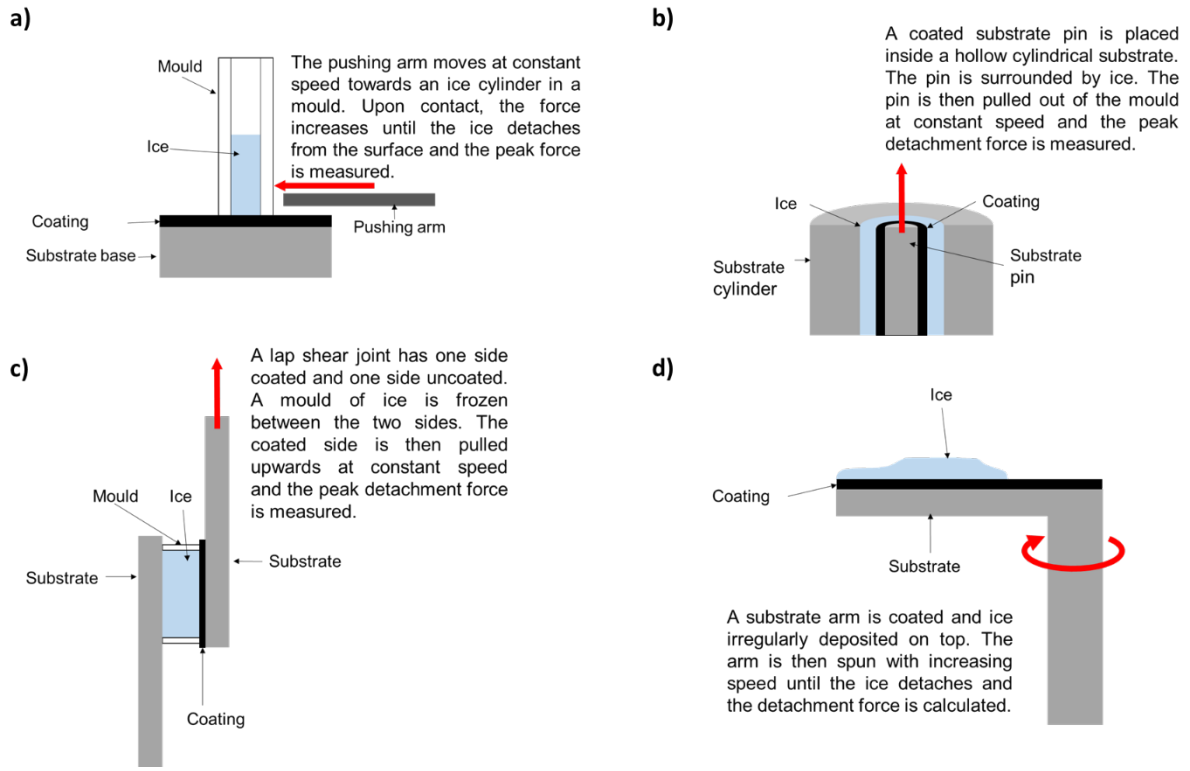

Figure 5.1 – Schematics of common ice adhesion test geometries a) push test, b) zero-degree cone, c) lap shear joint and d) centrifugal test

The minimum acceptable adhesion strength for a coating to be considered icephobic is <100 kPa (Hejazi et al., 2013, Golovin et al., 2016, Janjua et al., 2017). However it has been argued that true passive de-icing is only possible below 20 (Kreder et al., 2016, Dou et al., 2014, Jamil et al., 2019) or 10 kPa (Beemer et al., 2016, He et al., 2017b). For context, bare metals such as aluminium and steel display ice adhesion strengths in the range of 200-2000 kPa (Kreder et al., 2016).

In this work, 100 repeat de-icing cycles were performed via push tests on the coatings. 100 tests is a significant number of de-icing cycles, which helps expose the effects of wear. Many other studies use multiple de-icing cycles to investigate surface wear. These range from 3 (Yeong et al., 2018) to 100 (Beemer et al., 2016, Golovin et al., 2016) de-icing cycles. The more tests that are performed, the better the understanding of the long-term performance of the coatings.

Ice adhesion is measured during each de-icing cycle to monitor the effect of wear. The full adhesion testing results are presented, alongside analysis and observations. The results are compared to findings from other studies for corroboration, and two models

for ice adhesion are applied to the data to assess the suitability of the models in describing the physical phenomena.

5.2. Experimental methods

5.2.1. Test set up and apparatus

The 'push' test geometry was chosen for these experiments, as it is straightforward to set up and operate. It is the most commonly used method and allows for more extensive comparison with literature data. The geometry of the test and specimens themselves makes the specimens easier to fabricate. Compared to the centrifugal method, the determination of contact area is also more straightforward. The specific apparatus used was a ForceBoard™ measurement system. A schematic of the set-up is shown in Figure 5.2 and a photo in Figure 5.3. Schematics and photos of the testing process are provided in Figure 5.4.

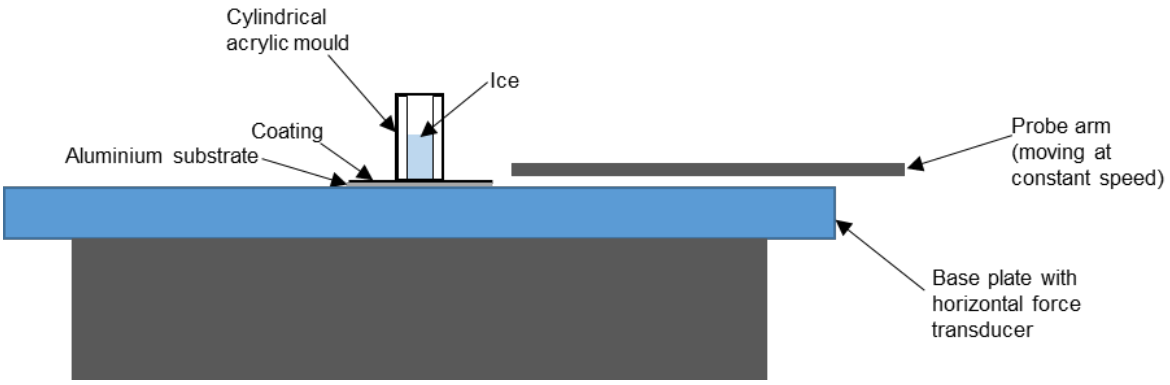

Figure 5.2 – Schematic of ice adhesion push test set up.

The test comprises a cylindrical acrylic mould placed on top of the coated specimen, which is bolted to the ForceBoard™ base plate. The mould had dimensions of 10 mm internal diameter and wall thickness of 1 mm; the height measured 25 mm.

The ice adhesion force is measured by displacing the ice (frozen in the mould) from the specimen surface and recording the force required for detachment. The ice is displaced by a metal probe arm moving at constant speed and the horizontal force is measured via transducers in the base plate.

The adhesion strength, σ_A, is then calculated using:

$$\sigma_A = \frac{peak\ detachment\ force\ (N)}{interfacial\ contact\ area\ (m^2)} \tag{5.1}$$

One of the important characteristics of the push test method is that the force is applied parallel to and above the actual interface. This creates torque on the specimen and a stress concentration at the front of the interface. The measured detachment force is therefore smaller than would be expected in a purely shear (Mode 2) fracture. To minimise the torque effect and approach the true shear stress as best as possible, the probe height was set at 1 mm, as is common in the literature (Golovin et al., 2016, Ibáñez-Ibáñez et al., 2021a, Cui and Pakkanen, 2020). Pilot tests to confirm this effect are discussed further in Section 5.2.4.2.

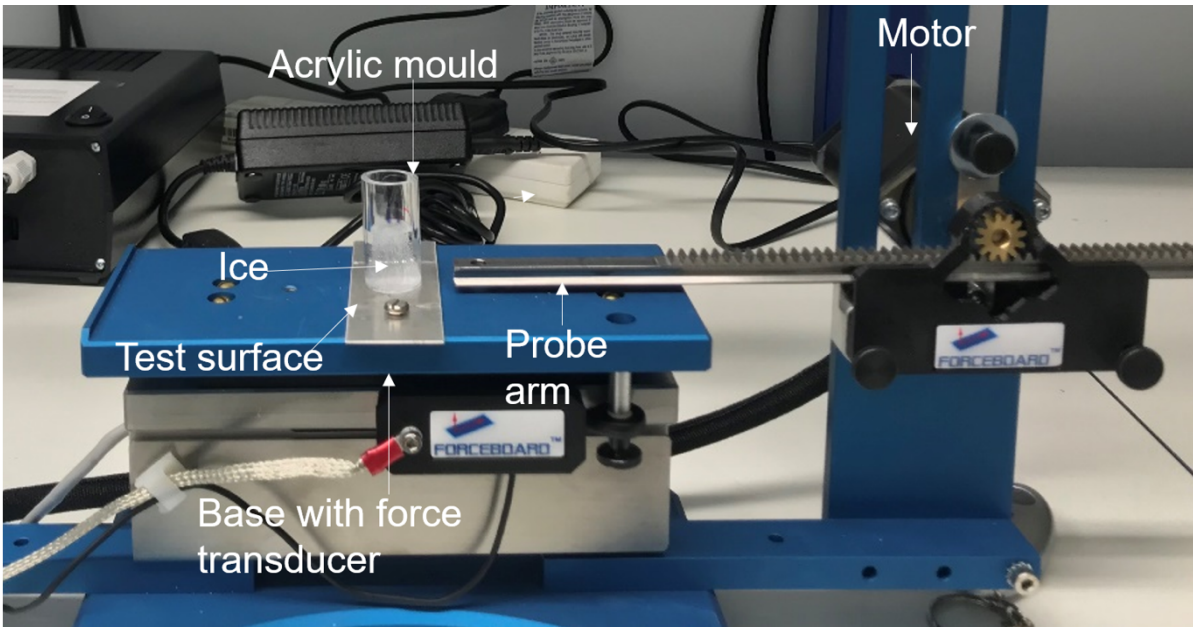

Figure 5.3 – Ice adhesion test set up. A ForceBoard™ is used to perform a push test on an ice cylinder frozen to the test surface.

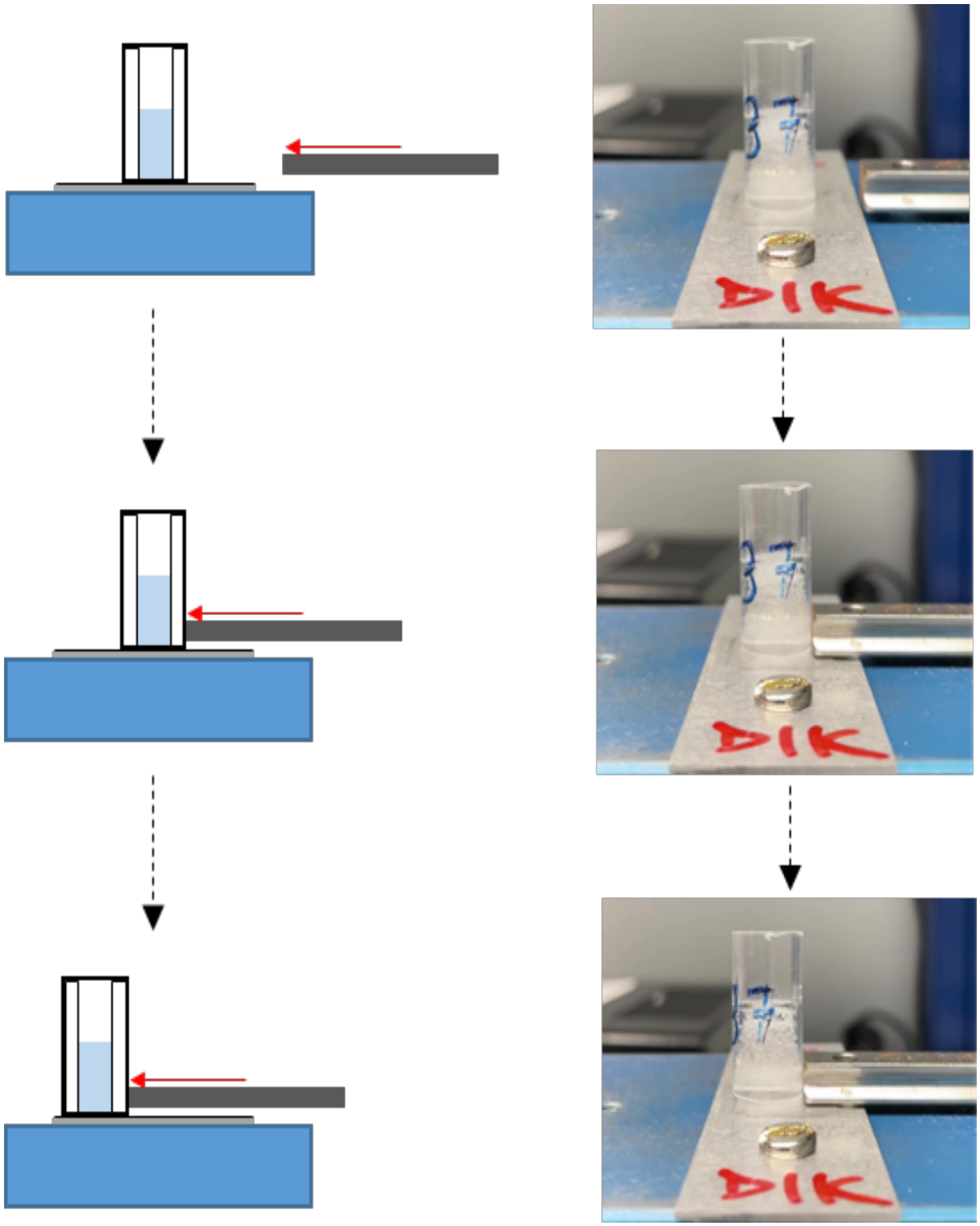

Figure 5.4 – Schematic and photos showing the push test process. The probe arm moves at a constant speed towards the cylinder of ice frozen to the coated substrate. The probe then makes contact with the ice cylinder, increasing the applied force until the ice detaches and slides along the surface.

A computer generated image of the stresses in the push test specimen is provided in Figure 5.5, as modelled by Makkonen (2012), with similar results in other studies (Woll, 2018). The stress concentration at the front of the interface is visible in red.

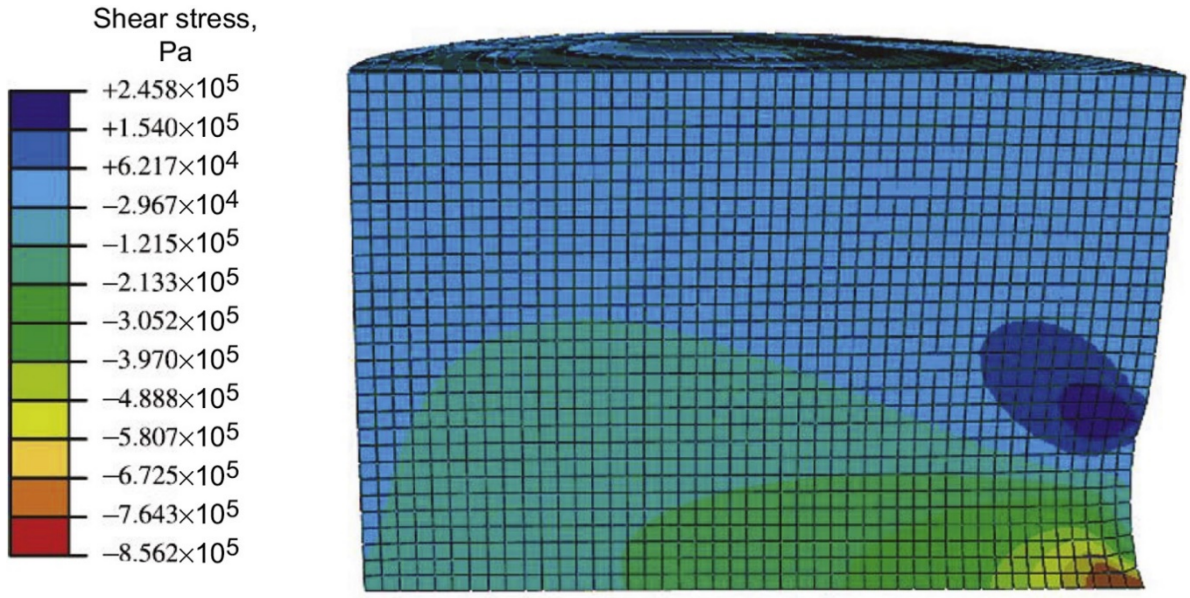

Figure 5.5 – Stress mapping of an ice cylinder cross-section undergoing a push test. A stress concentration is identified at the front of the interface (bottom right corner), below the probe contact point (Makkonen, 2012).

5.2.2. Specimen dimensions and preparation

The coating surface area measured approximately 20 mm x 20 mm, with thicknesses of 200 µm ± 11%, as measured by profilometer (Mitutoyo SJ-410) and described in Chapter 4. It has been shown that the bulk mechanical properties of PDMS are thickness dependent, and that 200 µm is around the critical threshold above which the mechanical properties are independent of thickness (Liu et al., 2009). The elastomers were prepared as described in Chapter 3. The specimens were cast in square silicone moulds with 20 mm x 20 mm internal dimensions, onto aluminium substrates of 1 mm thickness. For each coating type two specimens were made and tested. Photos of ice adhesion test specimens are provided in Figure 5.6.

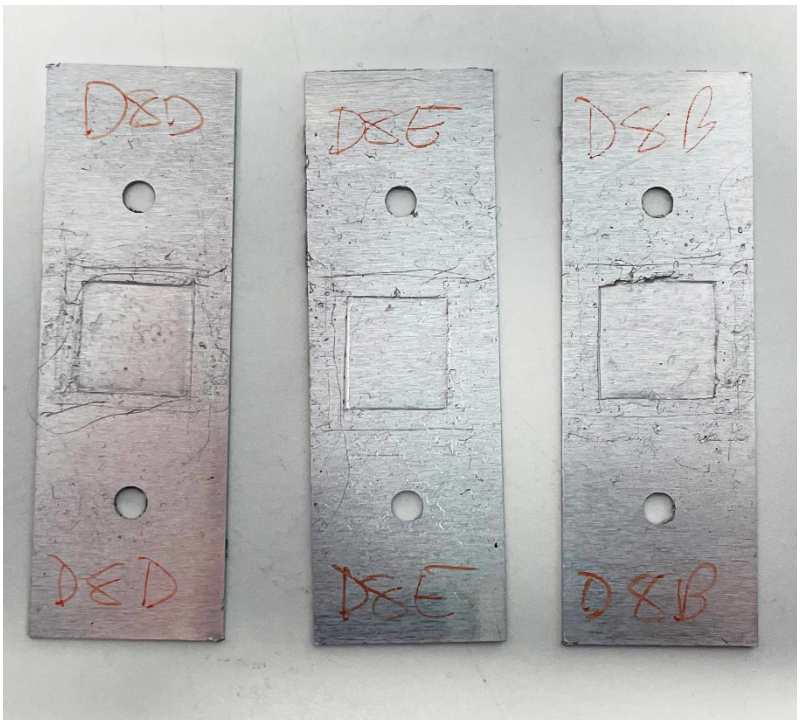

Figure 5.6 – Examples of ice adhesion test specimens – elastomer coatings cast on aluminium substrates. Specimens have undergone repeated de-icing cycles.

5.2.3. Freezing and test conditions

The entire testing process was carried out in a cold laboratory environment. The laboratory was previously developed for sub-zero experimentation and is comprised of a series of rooms which house the equipment used in this work (Skouvaklis, 2010). An antechamber limits the impact of sudden ingress of warm air when entering or leaving the laboratory. The laboratory's temperature can be controlled to be between 0°C and –18°C.

The temperature in the laboratory was maintained at –10°C ± 1°C by supply of refrigerated air. The humidity of the room was approximately 80% ± 10%. This was measured via Extech RH520A humidity and temperature chart recorder over three days. Temperature was verified by thermocouple measurements and internal thermometers in the chamber. Temperature and humidity traces are provided in Figure 5.7. An automatic defrost occurs every 6 hours and causes periodic fluctuations in the temperature and humidity as chilled air supply is temporarily halted.

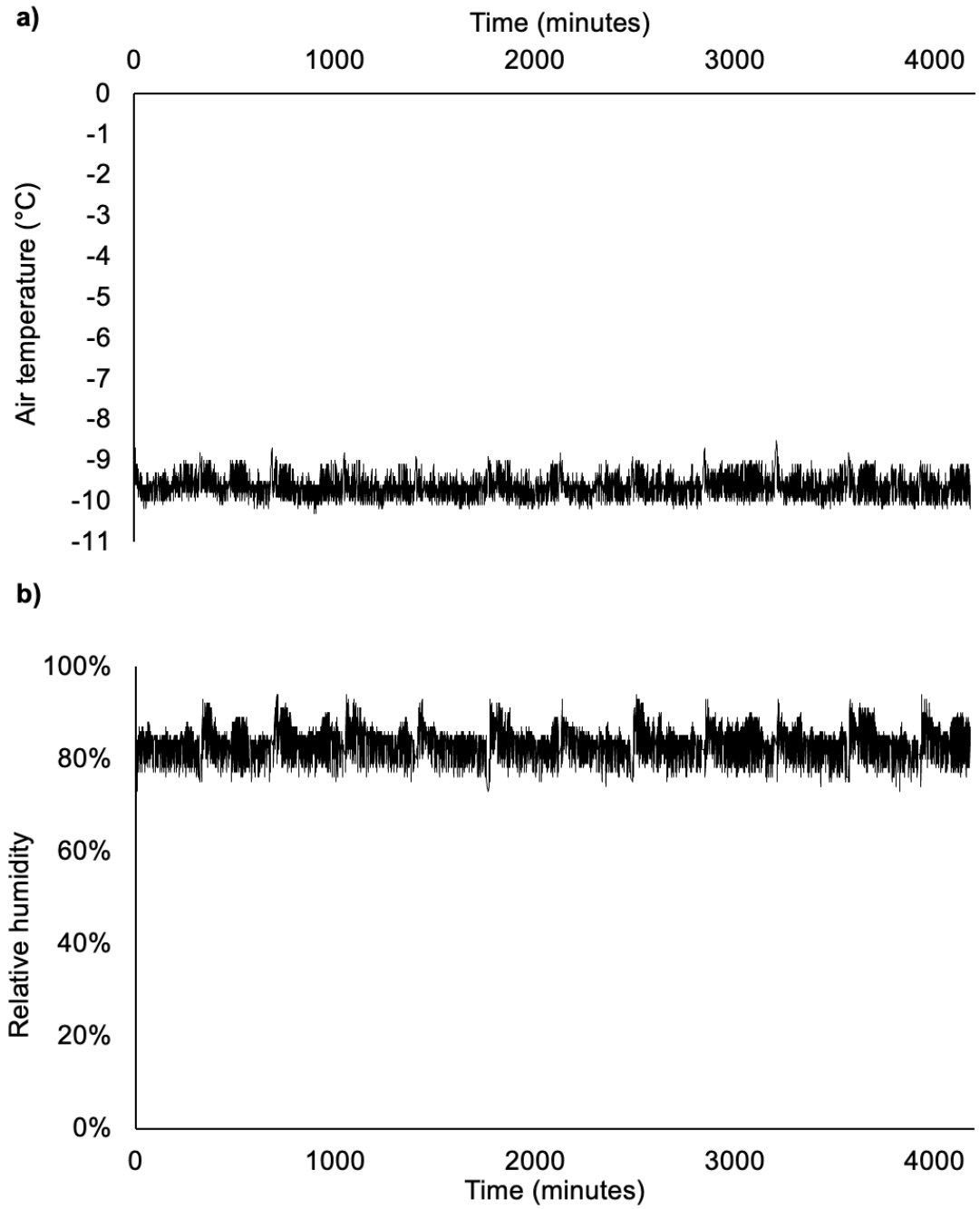

Figure 5.7 – Traces of a) temperature and b) humidity of the cold laboratory environment over three days. Periodic behaviour stems from the automatic defrost cycle that occurs every 6 hours.

To prepare the push test specimens, distilled water was allowed to cool to 1°C in a beaker and then 1 ml of chilled water was dispensed into the mould by syringe. The water was then left to freeze and cool to –10°C. The specimens were left at –10°C overnight in agreement with other studies (Susoff et al., 2013, Meuler et al., 2010). The push test was then carried out the following day. Tests were repeated, for a total of 100 tests, over nine months. This long-term exposure to the air and sub-zero

temperatures may also affect coating performance over time and is arguably a better reflection of real icing than room temperature storage.

5.2.3.1. Expansion of ice

Constrained expansion of the ice in the mould has been noted in other studies to cause the mould to lift off the coating prior to adhesion testing (Woll, 2018). An image of this is provided in Figure 5.8.

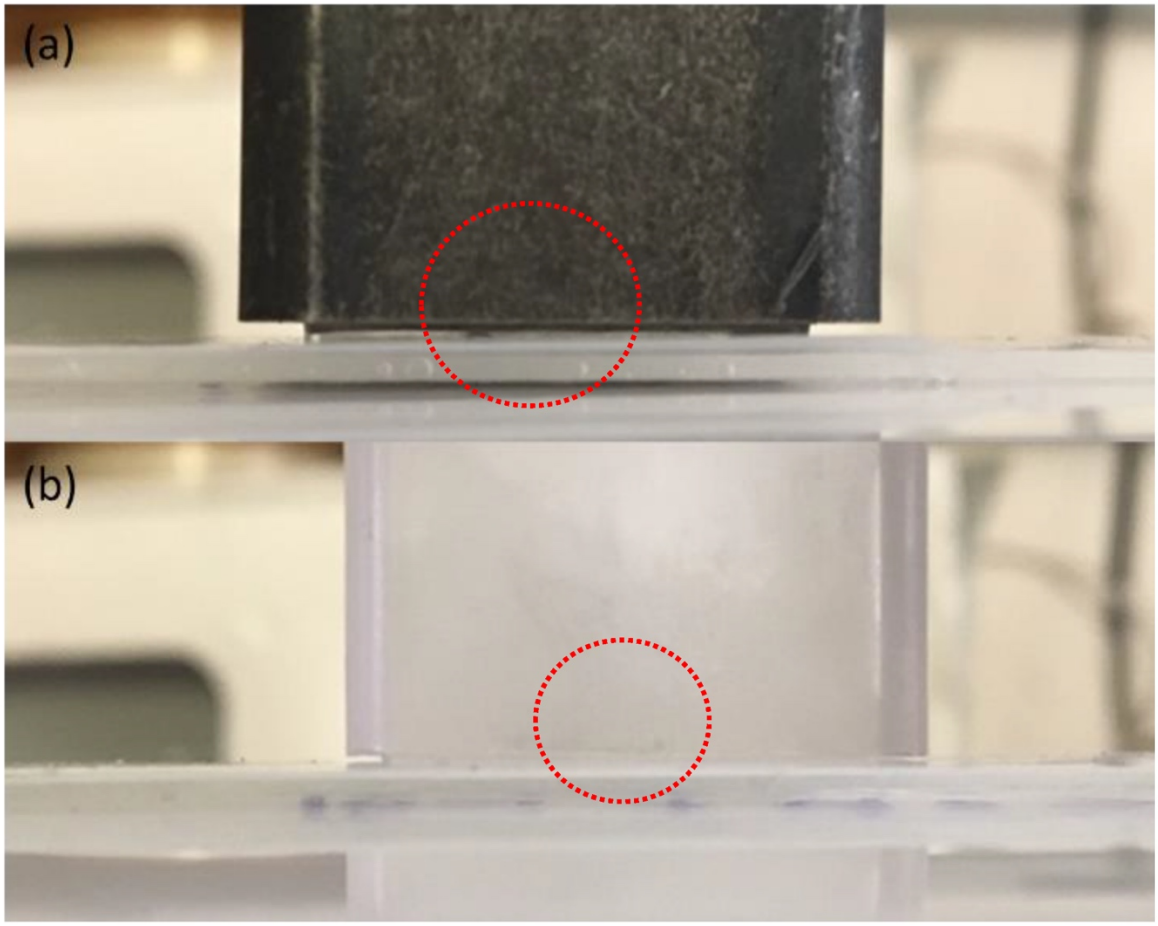

Figure 5.8 – In situ photos of ice in rectangular moulds made of a) steel and b) polycarbonate, with the gap between the mould and the coating surface circled (Woll, 2018).

While this was not directly observed in situ in this work, the same effect was revealed in a test in which an ice cylinder was left in place for one week before testing. Upon removal, examination of the fracture surface showed that sublimation of the ice had occurred around the bottom edge, indicating the presence of a gap between the mould and coating. This can be viewed in Figure 5.9 and compared to the ice fracture surface in Figure 5.16, which shows no sublimation, and has a very small ice lip which is just visible on the left of the image.

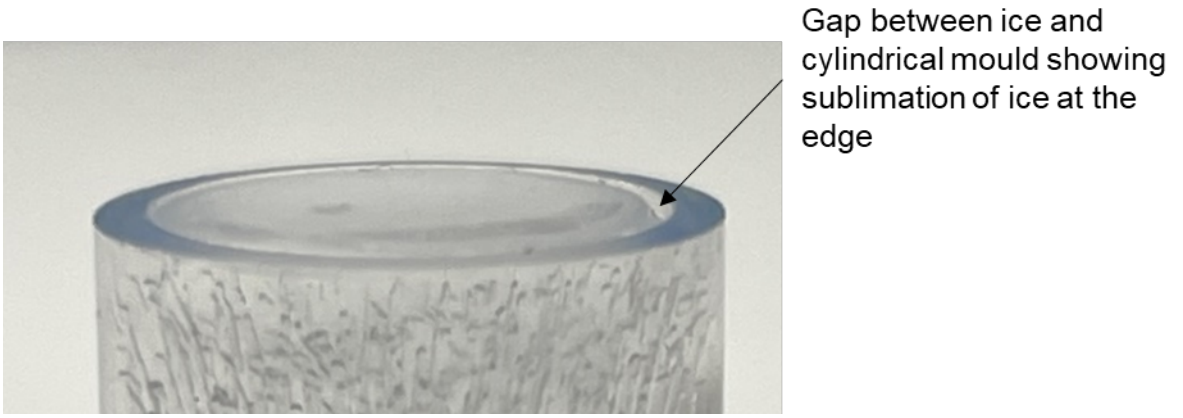

Figure 5.9 – Photo of ice fracture surface after leaving ice cylinder on coating for one week before performing push test. A gap has formed between the edge of the ice and the cylinder at the fracture surface. This was formed by sublimation of the ice at this edge, and indicates the edge was exposed to the air by expansion of the ice which lifted the mould off the coating surface.

The effect of this expansion and mould lift-off is poorly documented or understood. On one hand, it suggests that adhesion between the mould and the surface contributes minimally to the measured adhesion values, but it might also lead to crack initiation at the bottom edge of the mould-ice interface and greater normal stress (Bleszynski and Clark, 2021, Woll, 2018). While this is an interesting complexity that has received little attention in the literature, it will not be considered further in this work, beyond an argument that the ice should not be left on the coating for more than a day before sublimation of the surface generates uncertainty in, and an overestimation of, the ice-coating contact area.

5.2.4. Pilot tests

After initial set up of the testing equipment and specimens, brief pilot tests were carried out to determine the influence of probe speed and probe height on the measured adhesion. This informed the final testing procedure. The procedure as described in Section 5.2.1 and 5.2.3 was used in the pilot testing.

5.2.4.1. Probe speed

Three probe speeds were investigated. The probe speeds were: 5 mm/s, 10 mm/s and 15 mm/s. The tests on probe speed were carried out on two PDMS 80°C specimens. The results are presented in Figure 5.10. There appears to be a negative correlation between probe speed and adhesion strength. Other tests which have examined probe speed effect have shown no correlation (Meuler et al., 2010) or a weakly positive correlation (Mirshahidi, 2021, Wang et al., 2014a). Few conclusions have been drawn,

beyond most noting that strain rate does not seem to strongly affect the ice adhesion strength. Generally though, the probe speeds were much lower than those examined here, so it is possible there are different trends in different speed ranges.

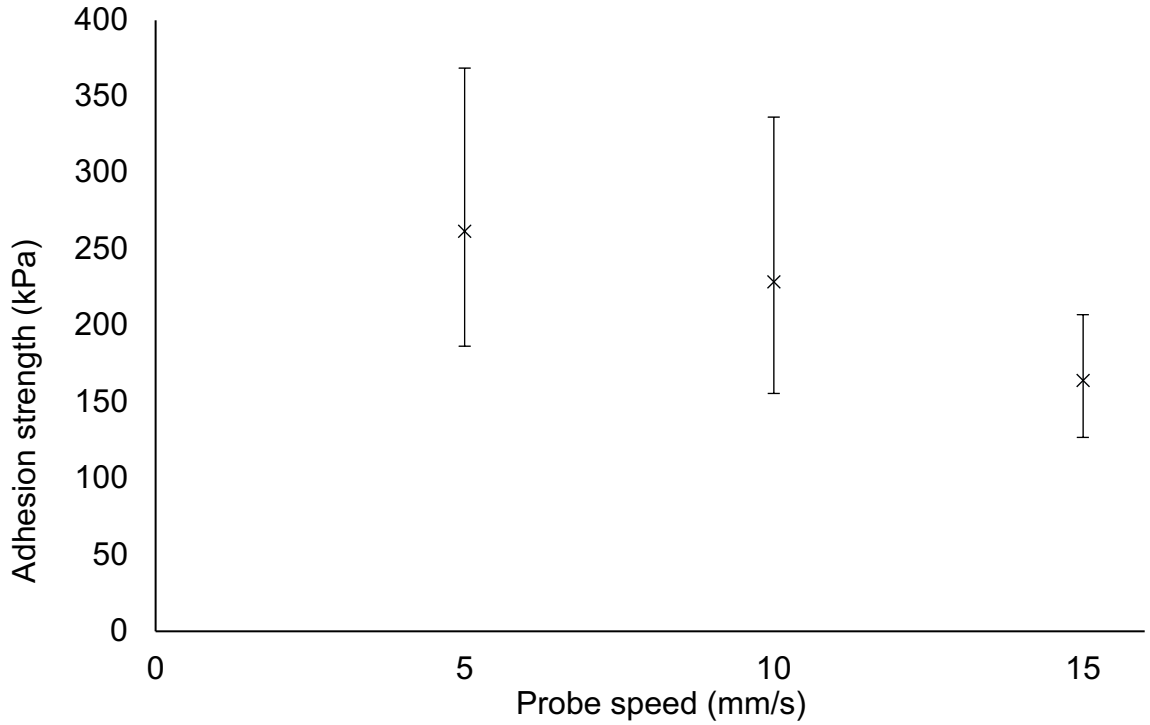

Figure 5.10 – Results from pilot tests on impact of probe speed, showing a decline in adhesion strength with increasing probe speed. Tests were performed on two PDMS 80°C specimens.

There has been little report in the literature of what the real strain rates experienced in icing situations are. This is understandable as the strain rates depend on the application. However, understanding in the field and future design would be improved if appropriate strain rate ranges for different applications were more widely considered in experimental design.

Based on these findings, the slowest of the three probe speeds was selected. The benefit of this is that it allows for better resolution of force curves, which have a data sampling rate of 40 Hz.

5.2.4.2. Probe height

Three probe heights were investigated. The probe heights (as measured from the top of the coating to the bottom of the probe) were: 1 mm, 8 mm and 15 mm. The tests on probe height were performed on two 50% LMWSO specimens.

The results for the study into probe height are presented in Figure 5.11. As probe height increased, there was a decline in the adhesion strength. This was expected, as the torque experienced by the ice cylinder will increase and reduce the measured adhesion force at the interface. Similar findings have been described in the literature (Wang et al., 2014b, Mirshahidi, 2021).

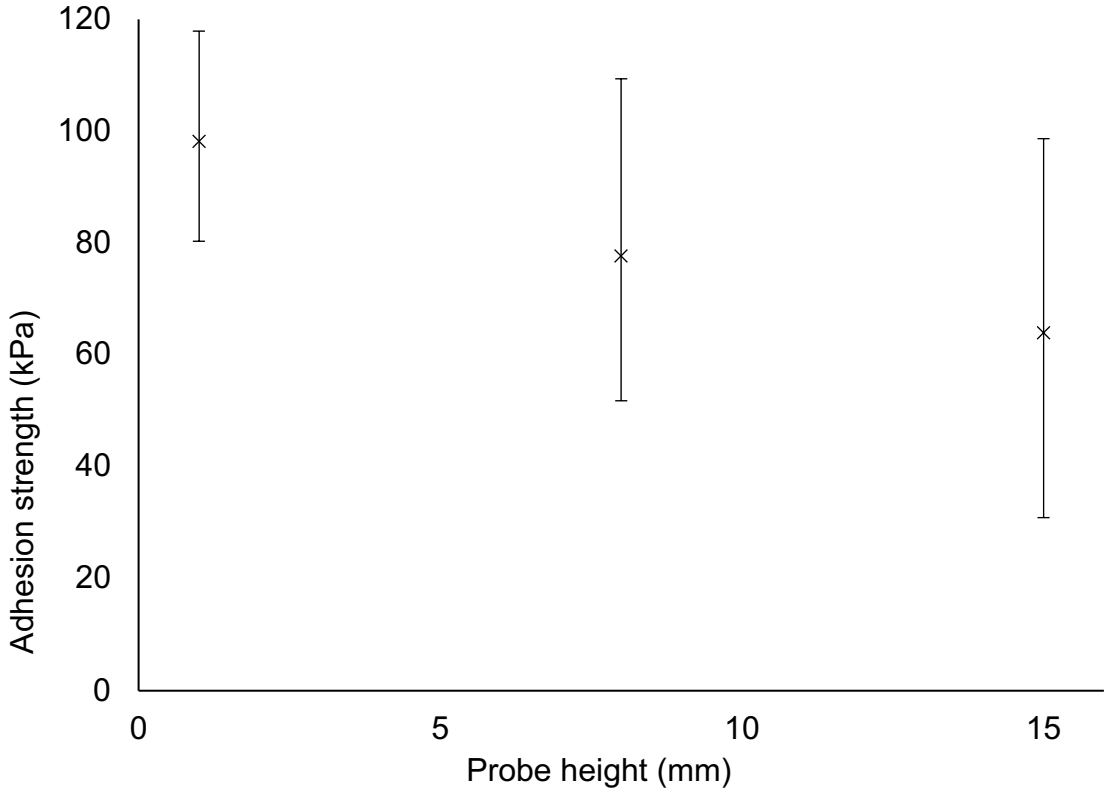

Figure 5.11 – Results from pilot tests on impact of probe height, showing a decline in adhesion strength with increasing probe height. Tests were performed on two 50% LMWSO specimens.

To best reflect the real shear adhesion force (probe height = 0 mm), the lowest probe height was selected for final testing. This is the generally adopted practice in other studies as well (Golovin et al., 2016, Ibáñez-Ibáñez et al., 2021a, Cui and Pakkanen, 2020).

5.3. Experimental results

For each coating type, two specimens were fabricated and used. Therefore, unless otherwise specified, all results presented below are an average of the values for both specimens.

5.3.1. Exemplar force-displacement curves

The ForceBoard™ generated force-time curves which were used to identify the peak detachment force. These were converted into force-displacement curves using:

$$displacement = speed\ x\ time \tag{5.2}$$

Equation (5.1) was then used to calculate the ice adhesion strength. Exemplar force-displacement curves for a specimen of PDMS 80°C and a specimen of 50% LMWSO are provided in Figure 5.12. For each specimen typical traces of representative behaviour and median force were selected (test 51 in both cases).

The two specimens show similar behaviour: upon probe contact the force rises sharply to reach the peak and then quickly falls back down as a crack forms and propagates, the fracture surfaces separate, and the ice detaches. There is slight curvature at the peak. The peak detachment force is 6 times smaller for the 50% LMWSO specimen (1.19 N) than the PDMS 80°C specimen (7.17 N). Upon detachment the force does not immediately return to 0 N, but instead oscillates slightly as the ice slides along the coating surface. The amplitude of the oscillation during sliding is slightly higher in the 50% LMWSO, with a peak of 0.50 N, versus the PDMS 80°C, which has a peak of 0.22 N. However, this friction behaviour is not of particular relevance in this study. The force eventually falls to 0 N once the ice has fallen off the specimen, at approximately 15 mm displacement.

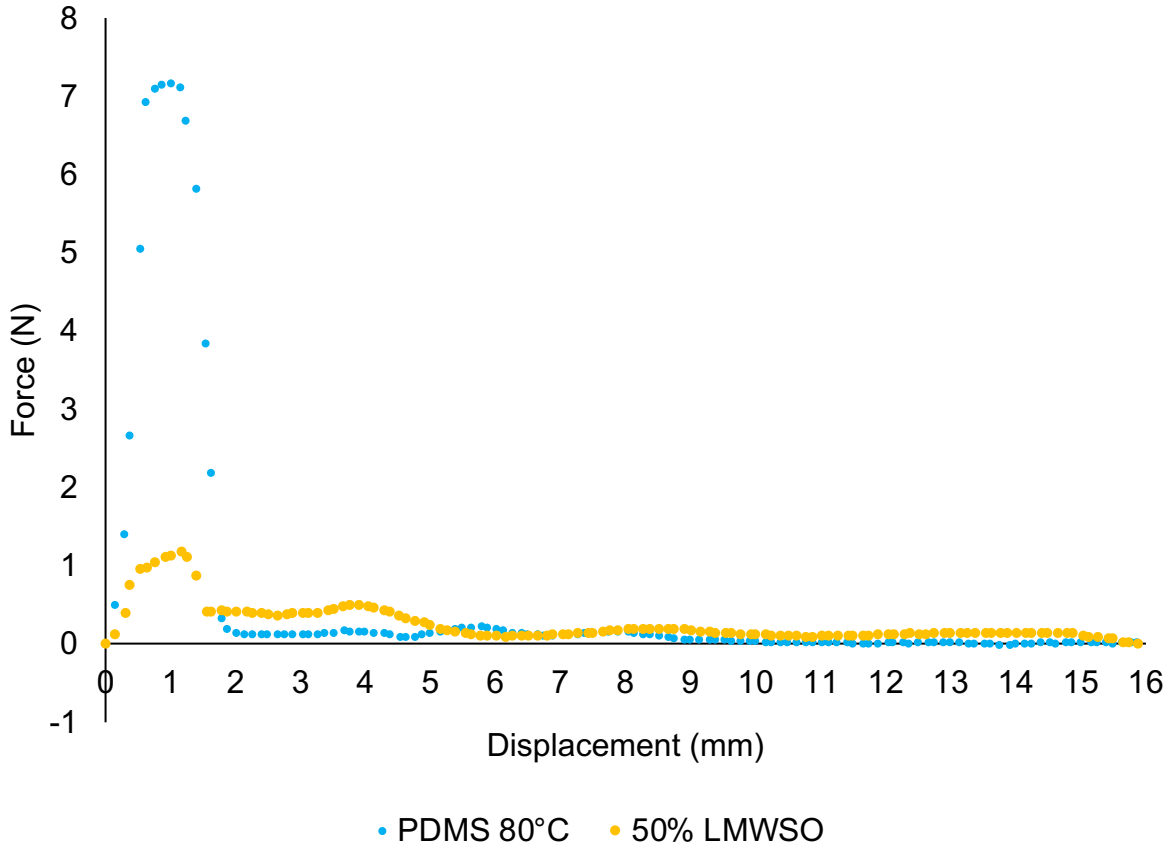

Figure 5.12 – Exemplar force-displacement curves for a PDMS 80°C specimen and a 50% LMWSO specimen.

Inspection of the initial 2 mm of displacement in Figure 5.13 shows the behaviour during detachment more clearly. The peak force data points are highlighted in red. The peak forces occurred at probe displacement of 1.01 mm and 1.16 mm for the PDMS 80°C specimen and 50% LMWSO specimen respectively. The de-icing process can be split into three stages: 1) probe contact, 2) peak force) and 3) detachment. These are demonstrated on the curves in Figure 5.13 and photos of the stages are presented in Figure 5.14.

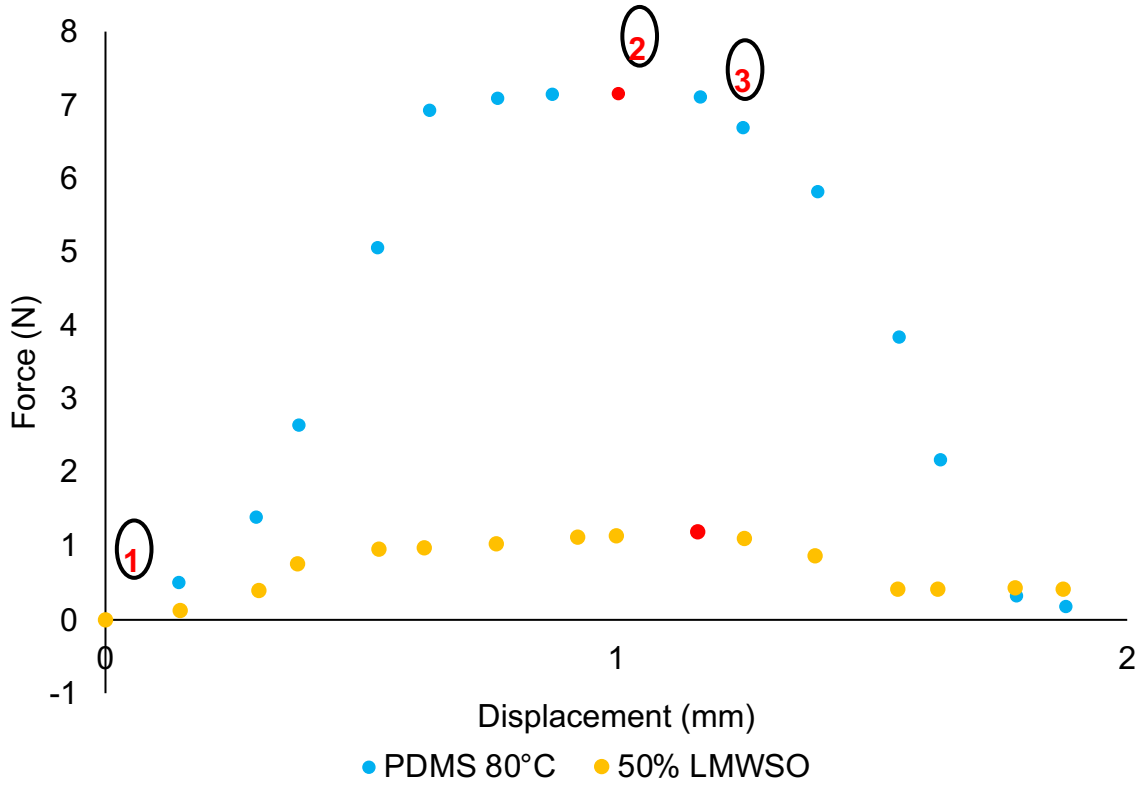

Figure 5.13 – Initial 2 mm of displacement of exemplar force-displacement curves. Data presented for a PDMS 80°C specimen and a 50% LMWSO specimen (both test no. 51). Peak measurements depicted in red. Numbers indicate the stages of 1) probe contact, 2) peak force and 3) detachment. Photos of these stages are presented in Figure 5.14

The 50% LMWSO specimen underwent greater elastic deformation prior to detachment than the PDMS 80°C specimen, despite the lesser force. In this, we can observe the lower modulus of the 50% LMWSO coating, as measured in Chapter 4.

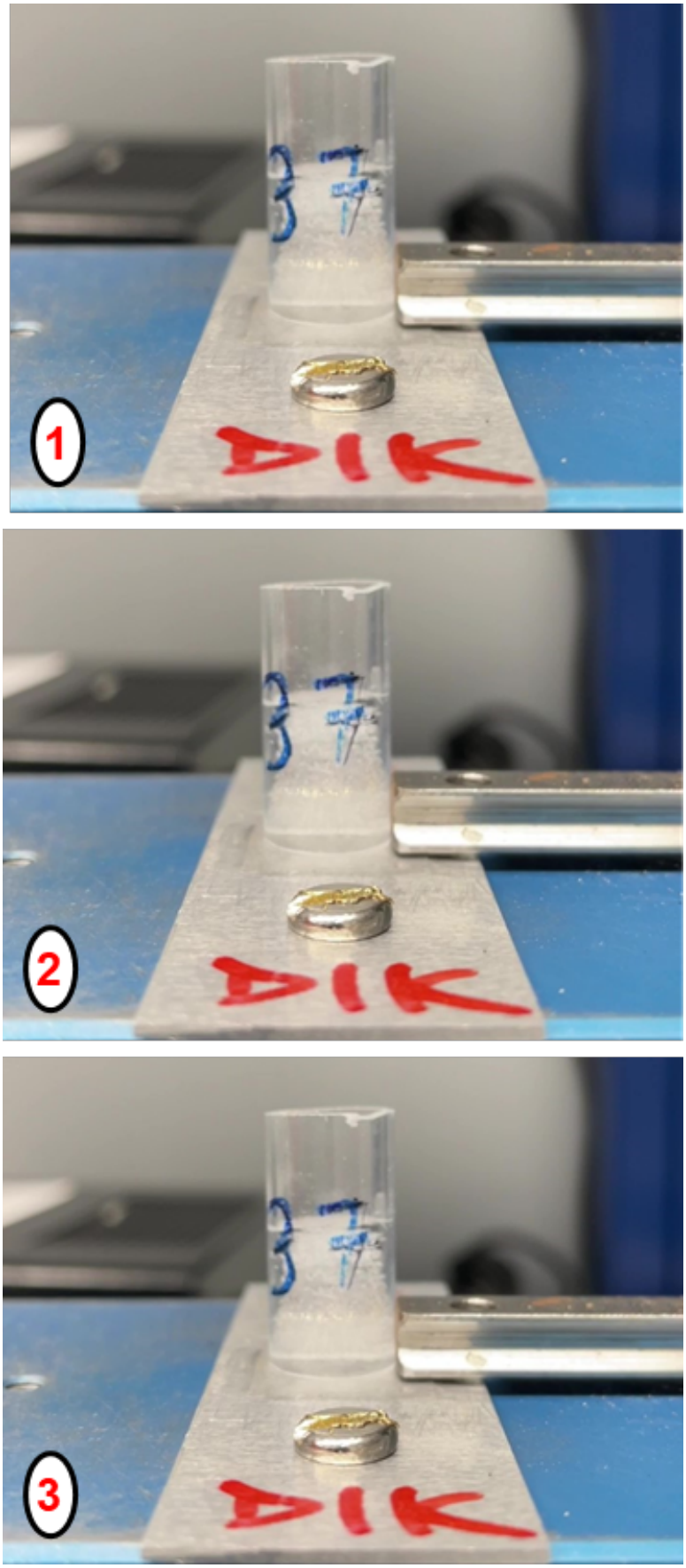

Figure 5.14 – Photos of an ice cylinder during the de-icing process, as shown in Figure 7. The stages are 1) probe contact 2) peak force and 3) detachment. All stages occur in less than 500 ms.

It is possible to see the separation of the interface in the comparison between stages 2) and 3). This is presented in Figure 5.15 for better clarity. The images show that, upon detachment, the front of the interface appears darker than before, as there is now a crack of air between the interfaces, changing the refraction of light.

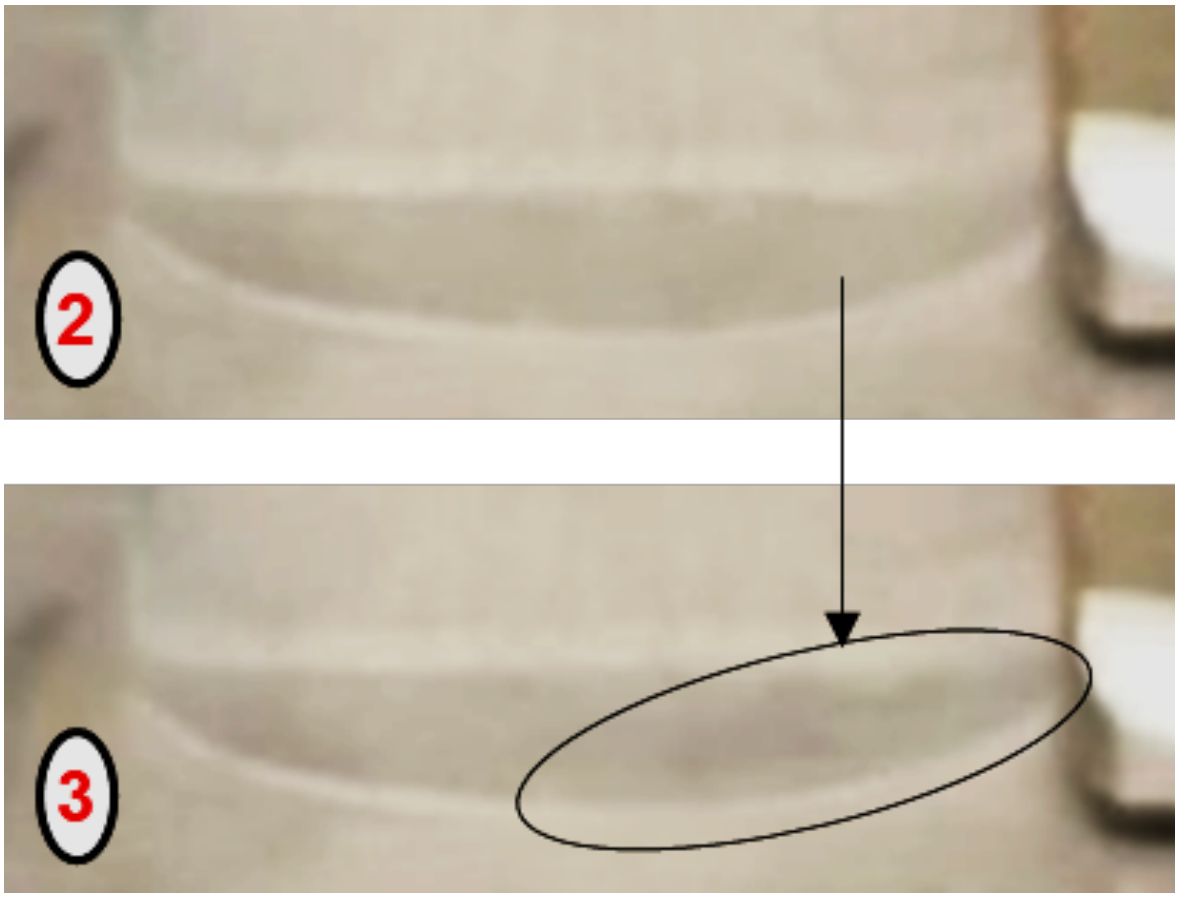

Figure 5.15 – Photos of the ice-coating interface at stage 2) peak force and stage 3) detachment. As the surfaces separate, the front of the interface becomes darker, as there is now a crack of air between the ice and the coating.

In all tests, the specimens showed exclusively adhesive fracture. In adhesive fracture the interface separates cleanly and surfaces are completely intact. No ice is left on the coating surface after detachment, or vice versa. Images of the undamaged fracture surfaces are provided in Figure 5.16.

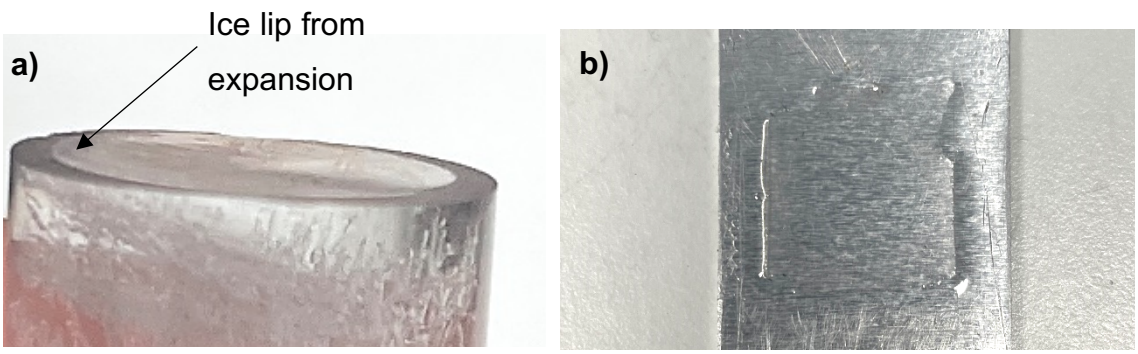

Figure 5.16 – Clean fracture surfaces showing adhesive failure with no damage to either the a) ice or b) coating. A lip is visible on the left side of the ice surface because of the expansion during freezing which lifts the mould off the coating and exposes the bottom of the ice cylinder.

5.3.2. Ice adhesion strength over 100 de-icing cycles

Figure 5.17 shows the results of all 100 adhesion tests for each coating specimen. Most of the measurements are below 200 kPa for the entire testing period, except for a handful of tests which appear at 650 kPa. As indicated on the graph, these high outlier tests are actually greater than 650 kPa, as the ice could not be detached by the testing equipment. The relevance of these high outlier tests is explored further in Section 5.3.4. To allow for equal analysis of the coatings, additional testing was carried out to replace these tests. Using replacement tests, the average ice adhesion of the two specimens for each coating across the testing period is presented in Figure 5.18.

Assessing the average values, adhesion strengths of the oil-infused coatings were approximately 5 times smaller than the non-infused coatings. The oil-infused coatings ≈ 20 kPa (the lower limit for icephobicity) and non-oil infused coatings ≈ 100 kPa (the higher limit for icephobicity). This holds true for the duration of the repeat testing presented in Figure 5.18. The NuSil R-2180 coatings showed a slight improvement on the PDMS coatings – 73.2 kPa vs 99.3 kPa (80°C) and 86.0 kPa (100°C) – when taking the average of all tests. The 50% LMWSO performed best over the testing regimen, averaging 16.5 kPa. The data for the oil-infused coatings is presented separately in Figure 5.19 for clarity.

The addition of silicone oil reduces the ice adhesion strength significantly. Furthermore, the greater the percentage of oil that was in the coating, the lower the

ice adhesion. The addition of low molecular weight silicone oil reduced the adhesion more than high molecular weight silicone oil.

Excluding the high outlier tests, the coatings demonstrated lower ice adhesion than bare metals over the testing regimen. The ice adhesion strengths of the oil-infused coatings were approximately 5 times smaller than the non-infused coatings. The 50% LMWSO coating even maintained ice adhesion strength of less than 20 kPa in 79% of the tests and averaged under 20 kPa in the final 10 tests. Applying these coatings would reduce the energy required for de-icing on bare metals.

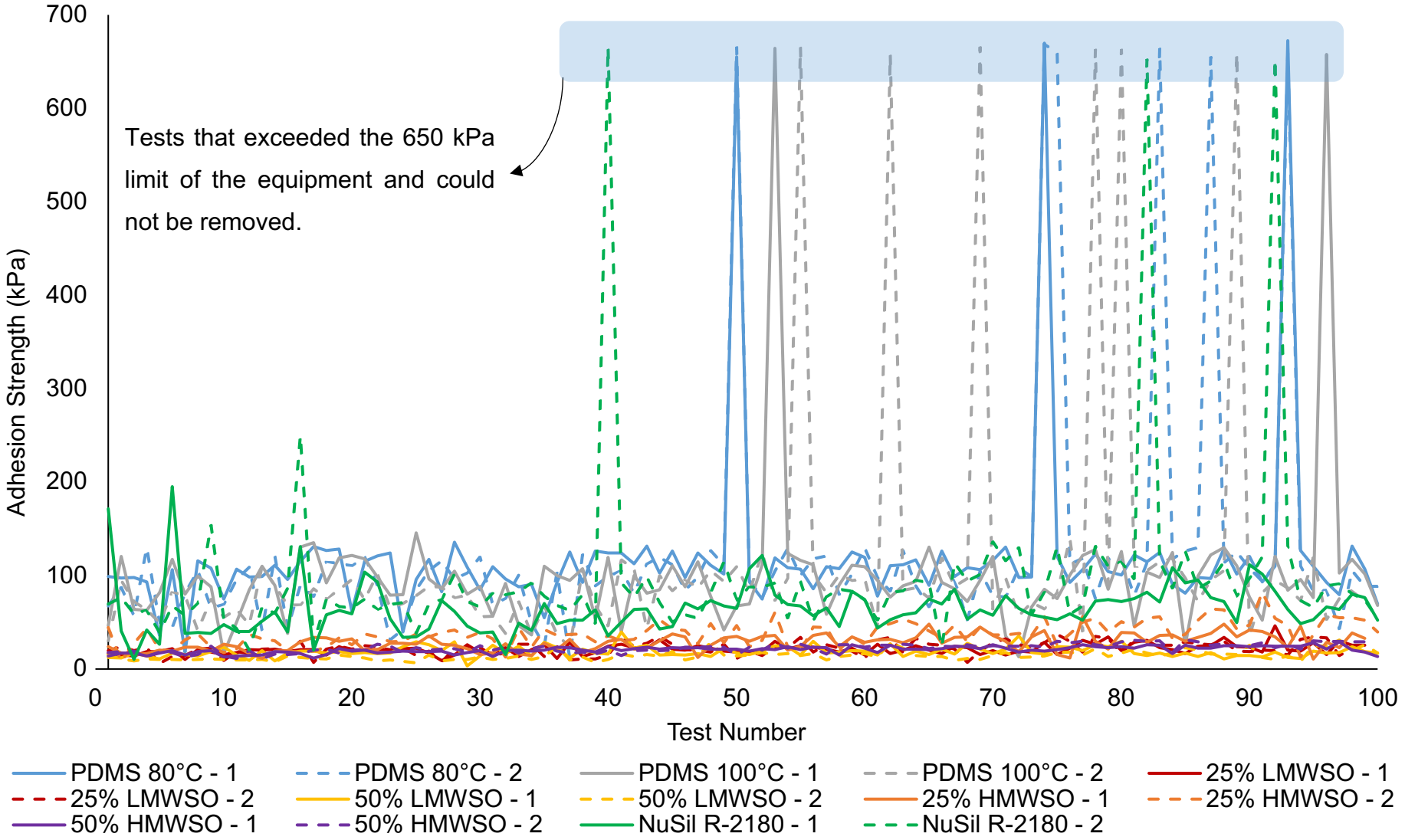

Figure 5.17 – Ice adhesion strengths for each specimen over the testing regimen of 100 repeat de-icing cycles. High outliers, in which the force required for detachment exceeded the load limits of the equipment (650 kPa), are highlighted at the top of the figure.

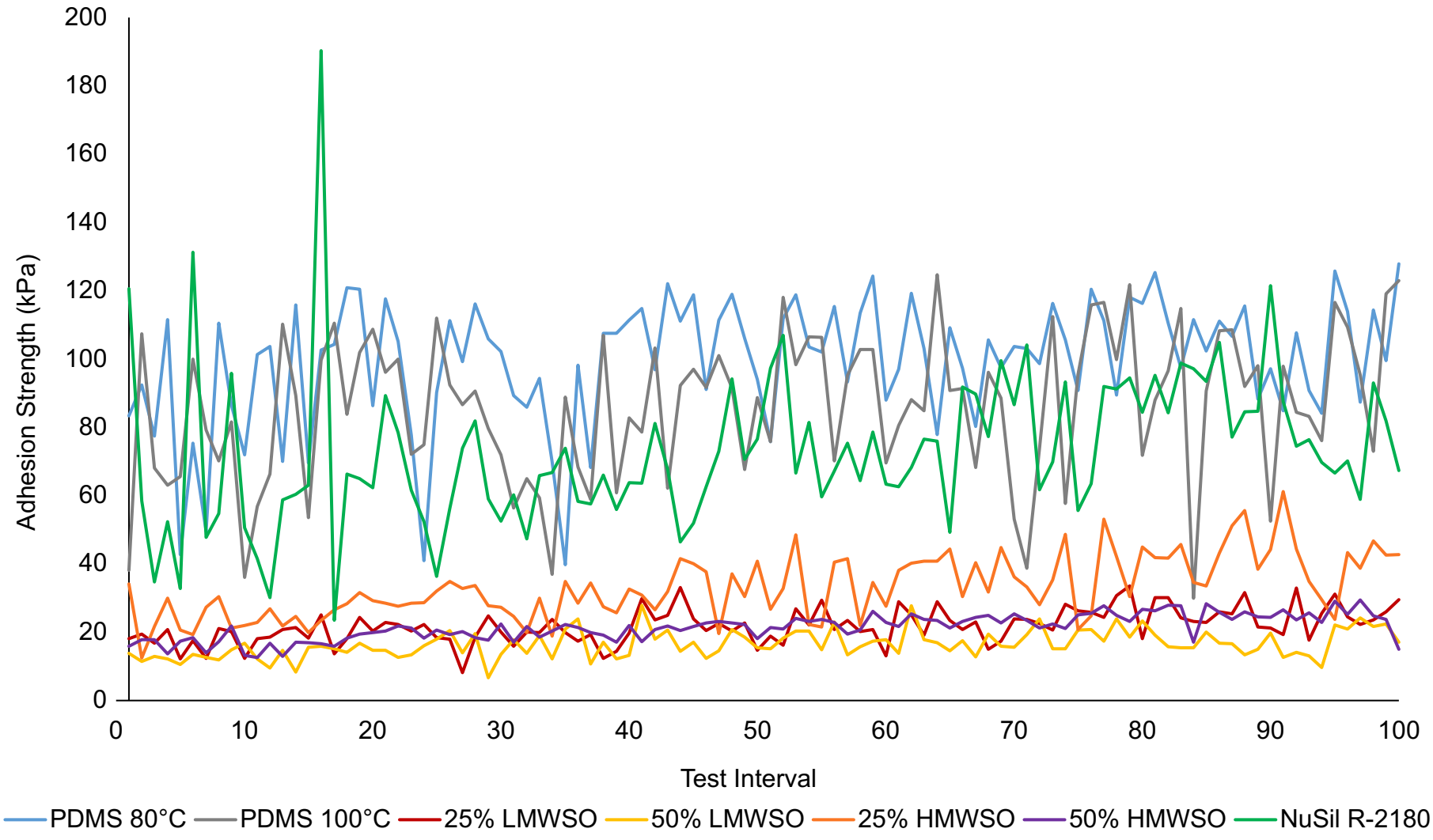

Figure 5.18 – Ice adhesion strength of the different coatings over 100 repeat tests, carried out over approximately 9 months. The data is the average value of two specimens for each coating. High outlier data has been replaced by additional tests.

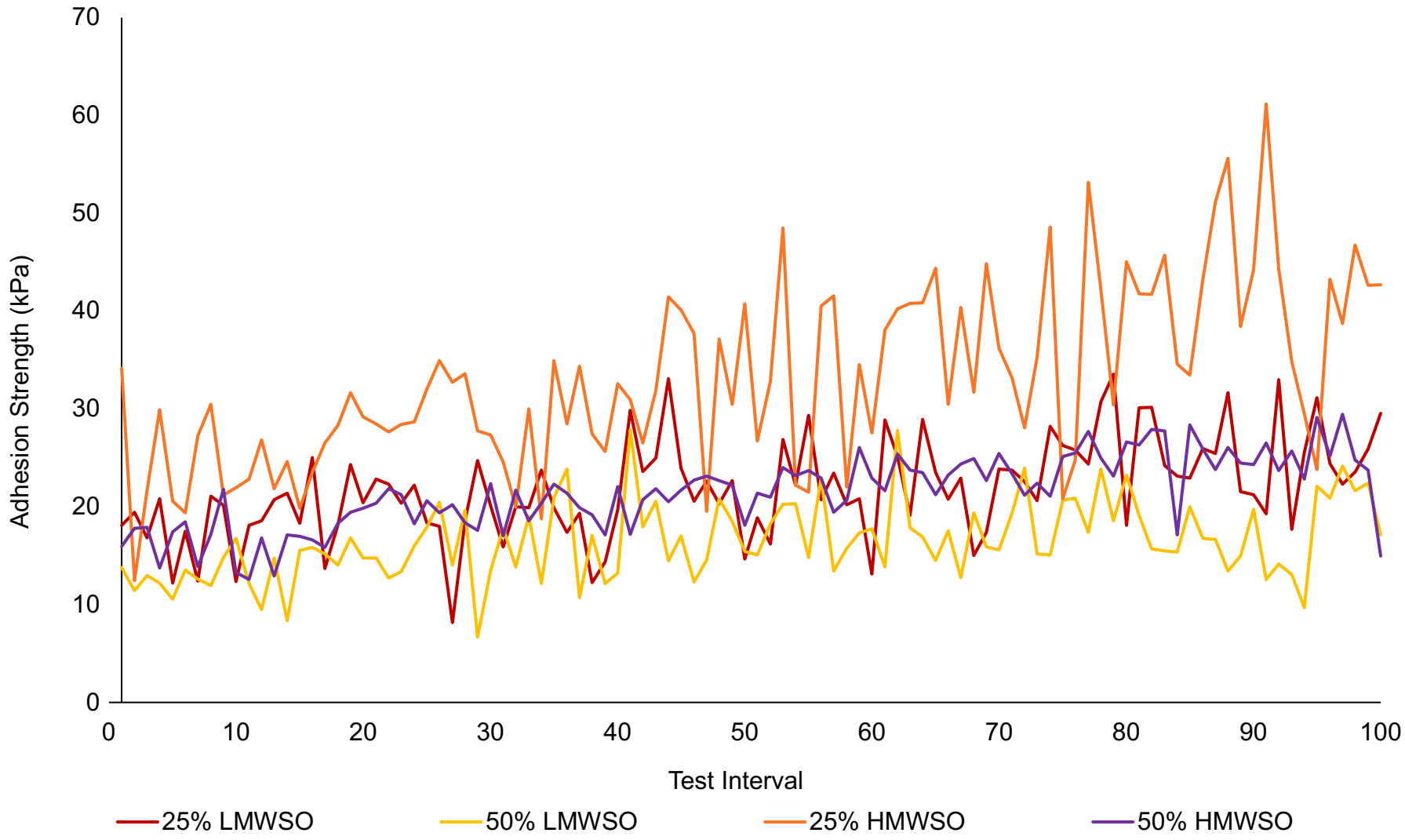

Figure 5.19 – Ice adhesion strength of the oil-infused coatings only over 100 repeat tests. The data is the average value of two specimens for each coating.

5.3.3. 10-test average ice adhesion strength

Testing broadly showed an increase in ice adhesion strength for all the coatings over the 100 tests. Assessing the average in the final 10 tests in Figure 5.20, the worst performing coating was the PDMS 100°C with 103.6 kPa, and the best coating was the 50% LMWSO with 17.8 kPa. There was a minimum 10% increase in average adhesion strength from start to end (Figure 5.21). NuSil R-2180 had the lowest increase of 10% and 25% HMWSO had the greatest increase of 71%. These results exclude the high outlier data points.

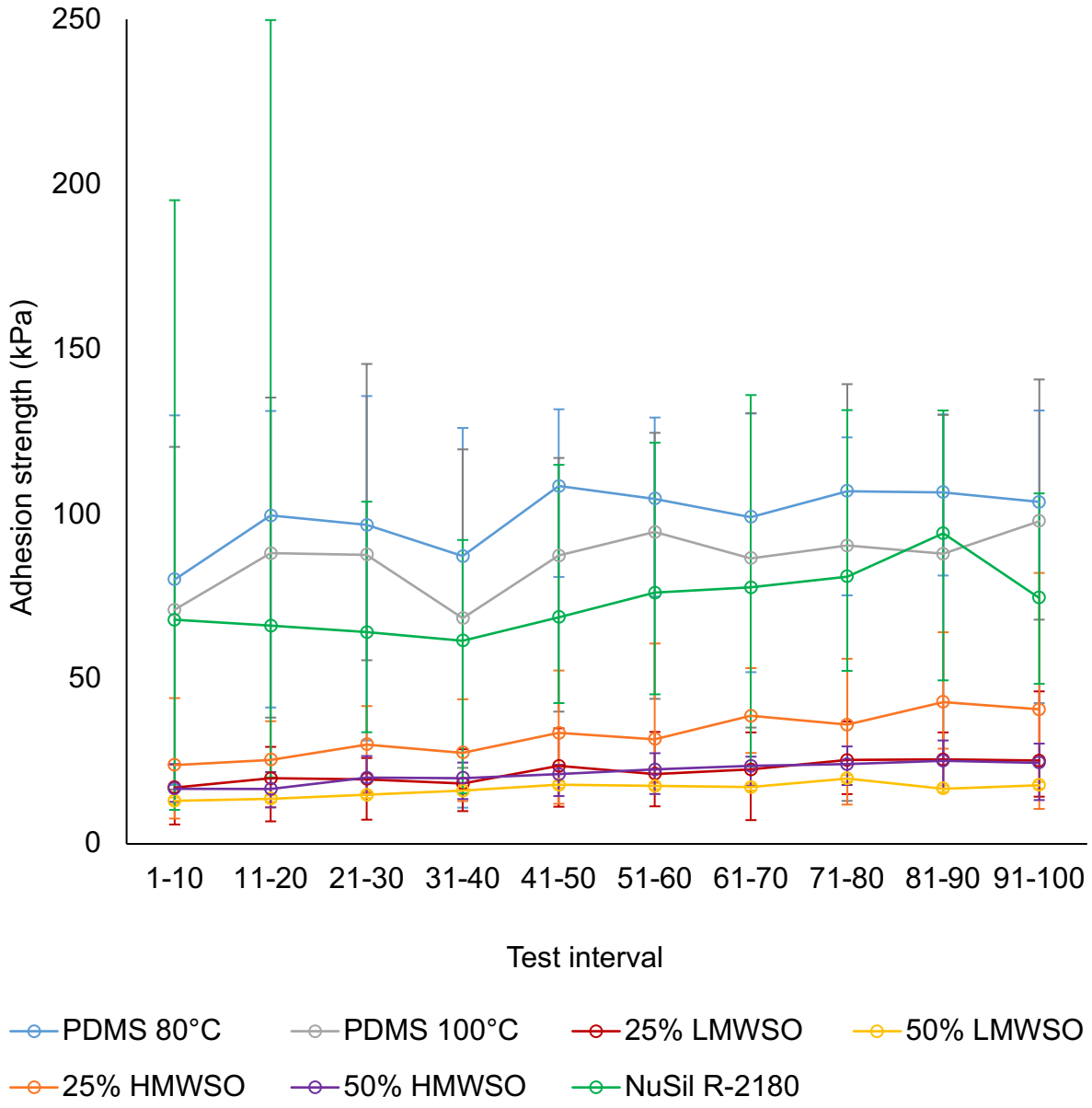

Figure 5.20 – 10-test average of ice adhesion strength for each coating, with range bars.

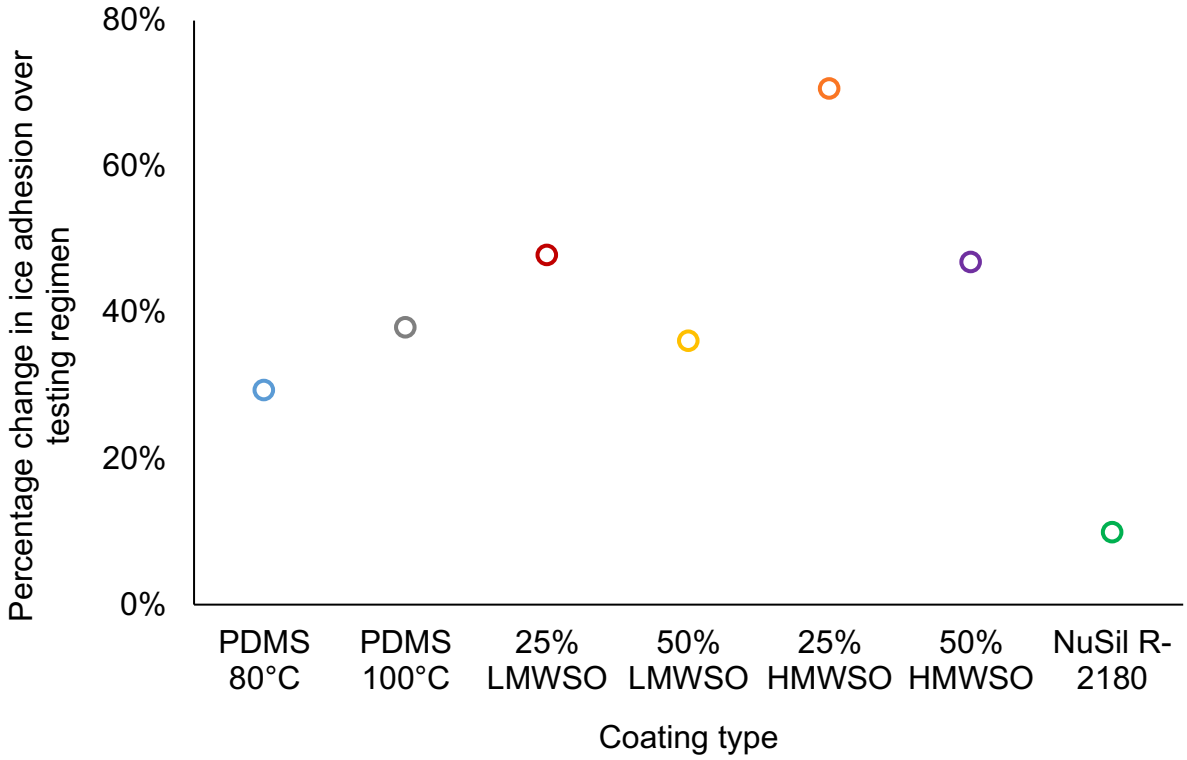

Figure 5.21 – Percentage change in the 10-test rolling average of ice adhesion strength between the first and last 10 tests for each coating.

These results suggest that the wear on the surfaces generated by the 100 de-icing cycles is insufficient to cause large, disadvantageous, increases in the ice adhesion strength. Much of the concern with application of elastomer coatings has been predicated on the assumption that they will degrade quickly. However, that is not the observation made here. The coatings maintained low ice adhesion throughout the testing, allaying concerns of poor durability limiting their usefulness.

In a plot of initial ice adhesion strength (average over first 10 tests) against the percentage increase (Figure 5.22) there is a slight negative correlation. This is expected, based on the observation that the oil-infused coatings, which have lower ice adhesion strengths, are weaker and more susceptible to wear. The initial ice adhesion strength can therefore be used as an approximate prediction of how a coating will change with repeated de-icing. However, this should not be viewed in isolation. Despite their greater percentage increase, the oil-infused coatings maintained lower ice adhesion than the non-oil infused coatings over the entire testing regimen. Suitability to anti-icing applications should take into account both percentage increase and the absolute value of the ice adhesion.

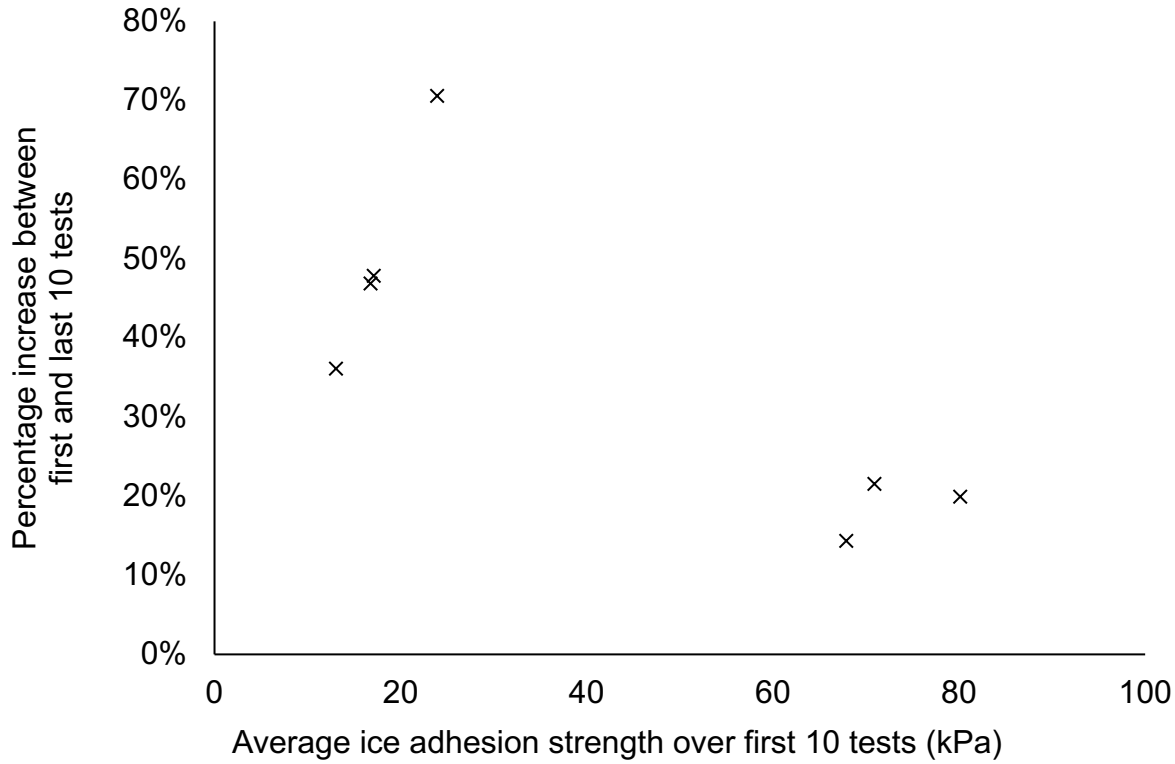

Figure 5.22 – Relationship between the initial ice adhesion and the percentage increase over the testing regimen, showing a slight negative correlation.

5.3.4. High-outlier data

One of the most interesting observations of the ice adhesion testing was that some of the tests exceeded the 50 N load limit of the equipment (corresponding to 650 kPa) and the ice could not be removed. These tests are highlighted at the top of Figure 5.17. Measurements with a strain gauge indicate the adhesion in these cases was greater than 1000 kPa. These high outlier tests occurred for all but one of the non-oil infused specimens and did not occur in any of the oil-infused specimens. The frequency of high outlier tests increased with repeat testing, as presented in Figure 5.23. The first occurrence was at test 40, but the rate rose to 7% for the non-infused coatings over tests 70-100. This trend suggests that performance is likely to continue worsening with further de-icing cycles.

The non-oil infused coatings cannot be classified as icephobic at these instances, as they exceeded the defined maximum ice adhesion strength of 100 kPa. This behaviour is not a singular outlier, but a tendency that increases over time. This is also not a gradual degradation, but a very sudden loss of anti-icing performance. Importantly,

this reduces the usability of these coatings in real applications, as any benefit they provide could be lost with repeated de-icing.

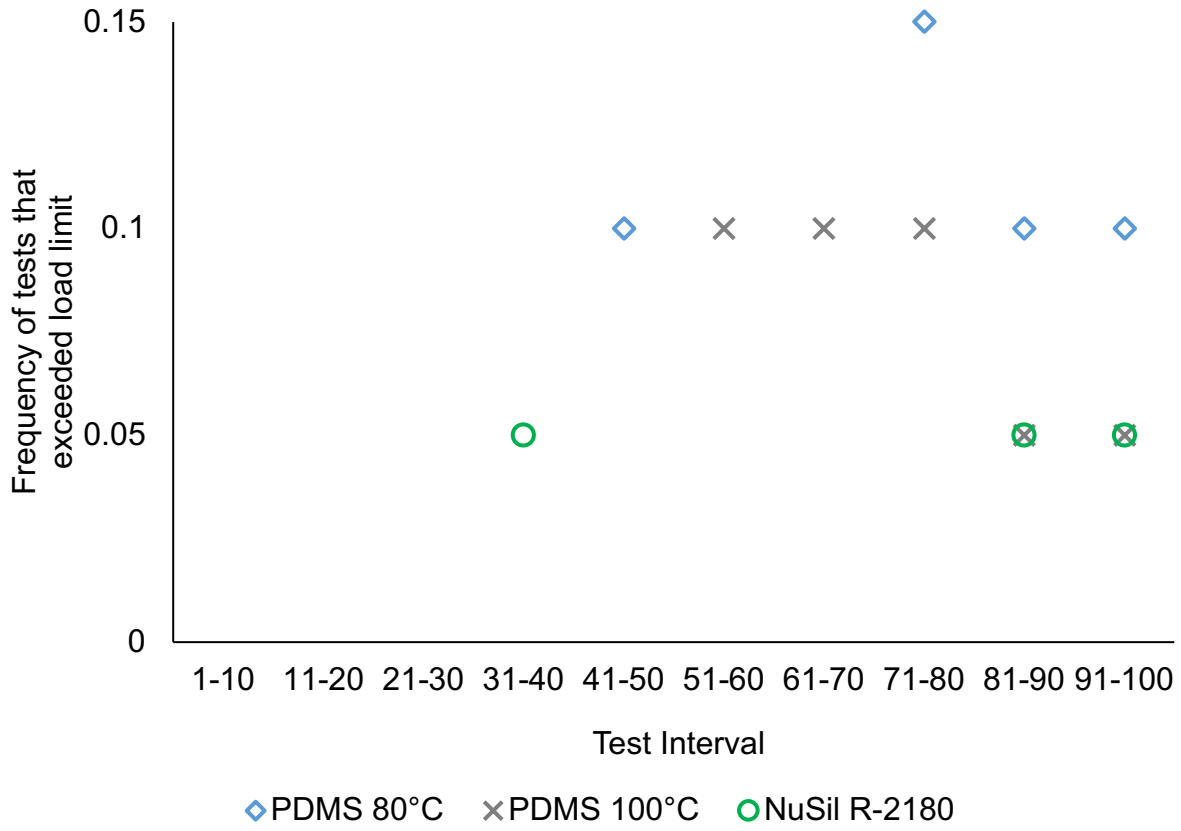

Figure 5.23 – Rate of high outlier tests in non-oil infused coatings. Outliers did not occur in oil-infused coatings. (20 tests per test interval.)

The drastic increase in ice adhesion strength may indicate that the ice detachment mechanism is different in these tests, as it seems somewhat independent of the surface wear, which was shown to be minimal in Chapter 4.

Broadly, the higher the average adhesion strength (when excluding outliers), the more frequent the outlier behaviour occurs. The oil-infused coatings also degraded, but it was gradual and never exceeded the load limits of the equipment. These findings suggest that the oil-infused coatings are a better choice for anti-icing applications than the non-oil infused coatings, which can lose their icephobicity.

5.4. Comparison with other studies

5.4.1. Adhesion strength

The data presented in this work was compared to the findings of other studies (Golovin et al., 2016, Wang et al., 2018a, Beemer et al., 2016, Ibáñez-Ibáñez et al., 2021a,

Susoff et al., 2013, Cui and Pakkanen, 2020, Meuler et al., 2010, Zhu et al., 2013). This comparison is presented in Figure 5.24. There is good agreement with literature values in most cases, with a few observations of note. However, inconsistencies between test methods mean that direct comparison between studies is often inappropriate. Therefore, the comparison presented here should be used more as an indication of relative performance, rather than commentary on fundamental differences.

To provide context for the comparisons made below, Table 5.1 presents selected experimental details from the respective studies. These include test geometry, coating type and curing schedule, testing temperature, strain rate, water purity, freezing time and thickness of the coating. However, there are many more factors that are not included here, for brevity. They include: the dimensions of the ice, contact height of probe in push test, the freezing method, the ice geometry, the number of tests performed, etc. The impact of these factors varies, and some are explored more in the literature (Work and Lian, 2018, Wang et al., 2018a, Wang et al., 2014a). It should be noted that the different loading geometries across test types leads to different adhesion strengths on the same surfaces, even when other factors are kept constant (Work and Lian, 2018, Ibáñez-Ibáñez et al., 2021a, Kasaai and Farzaneh, 2004, Maghsoudi et al., 2021, Rønneberg et al., 2019c, Ibáñez-Ibáñez et al., 2022). Adding to the uncertainty is the issue of missing experimental details. Studies rarely report the same factors, which leads to gaps in the relevant experimental details, as seen in Table 5.1. In future, fuller reporting of the experimental details would improve understanding across the field and allow for better comparison between studies.

Due to the specificity of the coating formulations, it is often not possible to find data for the exact formulation. In these cases, coatings with similar, but not identical, formulations are used. For details on formulation and curing schedule differences, see Table 5.1. The curing schedule used for fabrication of the NuSil R-2180 specimens is often not reported in studies, so it is assumed the manufacturer's recommended curing schedule was used (see Chapter 3). No values for 50% HMWSO coatings were found for comparison. This work presents the first investigation into this coating formulation.

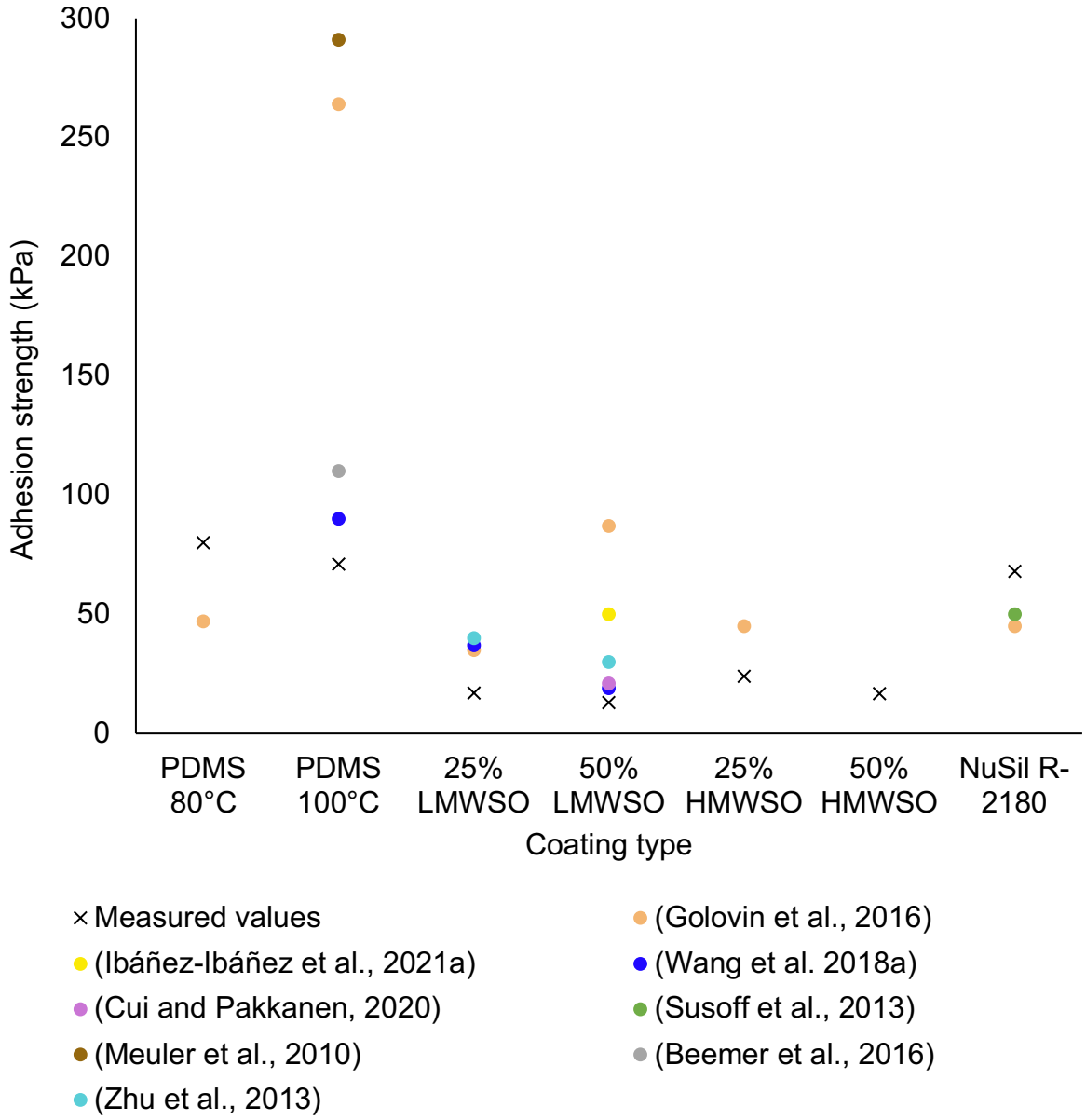

Figure 5.24 – A comparison of values measured in this work and the findings of other studies shows mostly good agreement, despite differences in methodology. Selected experimental details of the studies considered are provided in Table 5.1.

The data in this study shows good agreement with most literature values. There is a slight trend in the data in this work being lower than the literature values in most cases, excluding the NuSil R-1280 and PDMS 80°C. The oil-infused coatings show generally better agreement than the non-oil infused coatings and some values for the PDMS 100°C are more than 2 times greater than the data in this study. This is likely due to several differences in the experimental methodology.

In the case of Meuler et al. (2010), this may be explained by the difference in coating thickness. The coating thickness in their study is 0.1% of the thickness used here. Broadly, thickness has been shown to be negatively correlated with ice adhesion strength (Wang et al., 2014a, Beemer et al., 2016). This would increase the measured ice adhesion, and may be the cause of the difference in the values reported by Meuler et al. (2010) and the data collected here. The effect of thickness on ice adhesion will be discussed further in Section 5.4.2 and Section 5.5.1.2

In the case of the data point for PDMS 100°C reported by Golovin et al. (2016), they have not reported the thickness of the coatings used, so it is possible this is also the source of difference in the values. However, their results for the other surfaces are largely similar to the values in the work, so it is unlikely the difference is solely due to coating thickness. In discussion of their results, they suggest that a different detachment mechanism occurs in the PDMS 100°C coatings versus the other coatings. They believe that the PDMS 100°C surfaces experience interfacial cavitation, but the other surfaces exhibit interfacial slippage. This could explain the differences they observe but is not a distinction that can be made in the findings of this study. However, this difference in mechanism may be the source of the high outlier data noted in this work (as discussed in Section 5.3.4).

5.4.2. Coating thickness

For better understanding of the influence of coating thickness on the adhesion, a graph of the studies that reported coating thickness is provided in Figure 5.25. Where a range of thicknesses was reported in a study, the median value was plotted here. For the adhesion values plotted from this work, the average of the first 10 tests was used.

The results show that the there is a very weak negative correlation between adhesion strength and coating thickness for the studies examined here. Based on studies in the literature a negative correlation was to be expected (Wang et al., 2014a, Beemer et al., 2016). However, the weak trend seen here suggests that other properties of the coatings or test methods have a stronger impact on the adhesion than coating thickness. For the coatings within this work, the influence of selected parameters is discussed in Section 5.5.

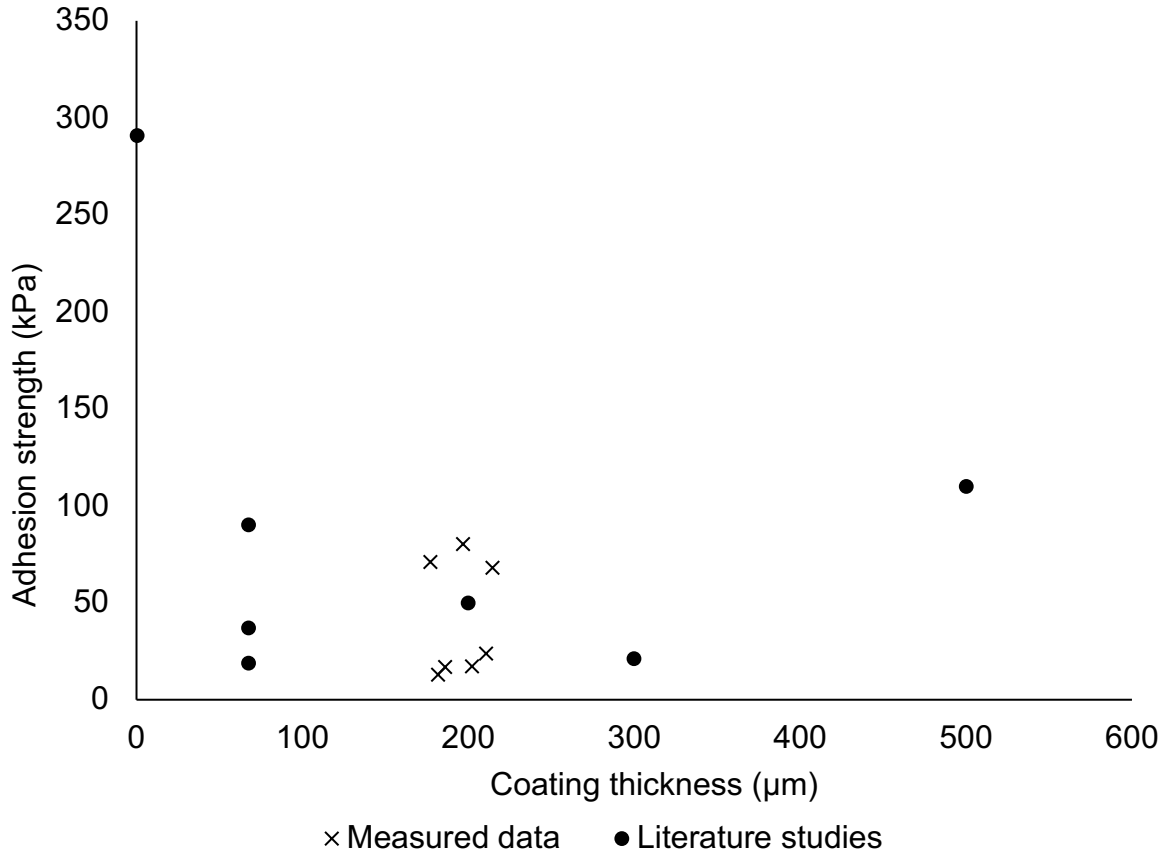

Figure 5.25 - Influence of coating thickness on adhesion strength in literature studies and data from this work. There is a very weak negative correlation.

5.4.3. Strain rate

The strain rates used in the literature selected are mostly lower than the strain rate used here, approximately 1000 times lower at the most extreme. The effect on ice adhesion strength of varying strain rate was investigated in Section 5.2.4.1 and showed a negative correlation. However, this was not in agreement with the findings from other studies, which found slight positive or no correlation.

A plot of the adhesion values and strain rates reported in the literature and this work, is provided in Figure 5.26. Where a range of strain rates was reported in a study, the median value was plotted here. For the adhesion values plotted from this work, the average of the first 10 tests was used.

The results show a slight negative correlation, which would agree with the findings from the pilot studies in Section 5.2.4.1. However, it is a very weak correlation and the data is largely similar, despite the great differences in strain rate. As with coating

thickness, this indicates that the strain rate must be a less significant contributor to the measured ice adhesion strength than other factors.

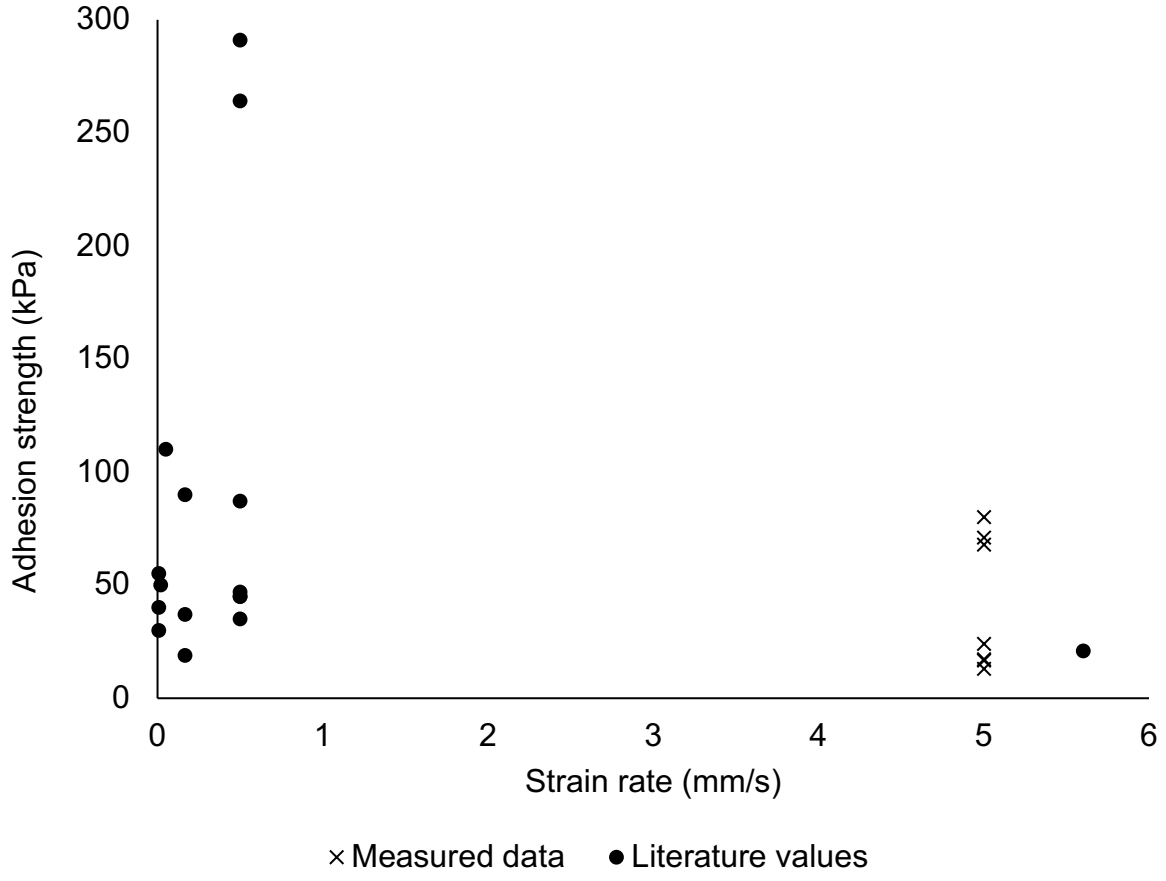

Figure 5.26 – Influence of strain rate on adhesion strength in literature studies and data from this work. There is a very weak negative correlation.

Table 5.1 - Experimental details of selected literature studies

Test Geometry	Coating Formula	Curing Schedule (°C/Hours)	Test Temp. (°C)	Strain Rate (mm/s)	Water Type	Freezing Time (hours)	Coating Thickness (μm)	Ref.
Push	PDMS	150/24	-10	0.5	Deionised	Overnight (10-15)	*Not stated*	(Golovin et al., 2016)
	PDMS	80/2						
	25% LMWSO							
	50% LMWSO							
	25% HMWSO							
	NuSil R-2180							
Push	20% HMWSO	70/24	-20	*Not stated*	Not stated	1	200	(Beemer et al., 2016)
Push	PDMS	25/48 + 100/1	-10	0.167	Milli-Q	1.5	58-77	(Ibáñez-Ibáñez et al., 2021a)
	20% LMWSO							
	50% LMWSO							

Push	60% LMWSO	80/overnight	-10	5.6	Tap	3	300	(Cui and Pakkanen, 2020)
Zero-degree cone	NuSil R-2180	*Not stated*	-14	0.0167	Deionised	Overnight	*Not stated*	(Susoff et al., 2013)
Push	PDMS	60/2	-10	0.5	Deionised	Overnight	0.2-0.3	(Meuler et al., 2010)
Push	PDMS	60/48 + 100/72	-10	0.05	Distilled	2-3	500	a
Zero-degree cone	29% LMWSO	*Not stated*	-10	0.008	*Not stated*	24	*Not stated*	(Zhu et al., 2013)

5.5. Application of adhesion models

The phenomena governing ice adhesion are complex. Many mechanisms for ice adhesion and detachment have been proposed, alongside mathematical models that aim to describe those mechanisms. Applying the models to experimental data will help reveal which models most accurately describe the real systems. Analysis of the constituent terms of the models can also help reveal which terms exert the most influence over the adhesion strength. A combination of these two analyses will lead to better predictions of the ice adhesion of a given coating and better coating design.

Two commonly proposed models are examined in this section. The models are discussed in greater detail in Chapter 2, but they are briefly described here, and a graphical representation of both behaviours is presented in Figure 5.27.

i. **Interfacial cavitation:**

When torque on the ice causes it to tilt, the front edge of the coating is put into tension and released when the adhesive forces are overcome. A crack is formed and then a wave of trapped air cavities propagates along the interface, detaching the ice from the surface (Kendall, 1971, Ghatak et al., 2005, Chaudhury and Kim, 2007, Beemer et al., 2016).

ii. Interfacial slippage:

When torque on the ice causes it to tilt and a crack to form, the elastomer chains adhered to the ice at the surface detach and flow along the crack that is forming at the interface. The viscous dissipation of the forces reduces the stress required for separation. Detachment becomes similar to the de-wetting process of a liquid (Ghatak et al., 2000, Vorvolakos and Chaudhury, 2003, Newby et al., 1995, Golovin et al., 2016, Zhang Newby and Chaudhury, 1997, Zhang Newby and Chaudhury, 1998, Hénot et al., 2018, Migler et al., 1993, Migler et al., 1994, Chernyak and Leonov, 1986).

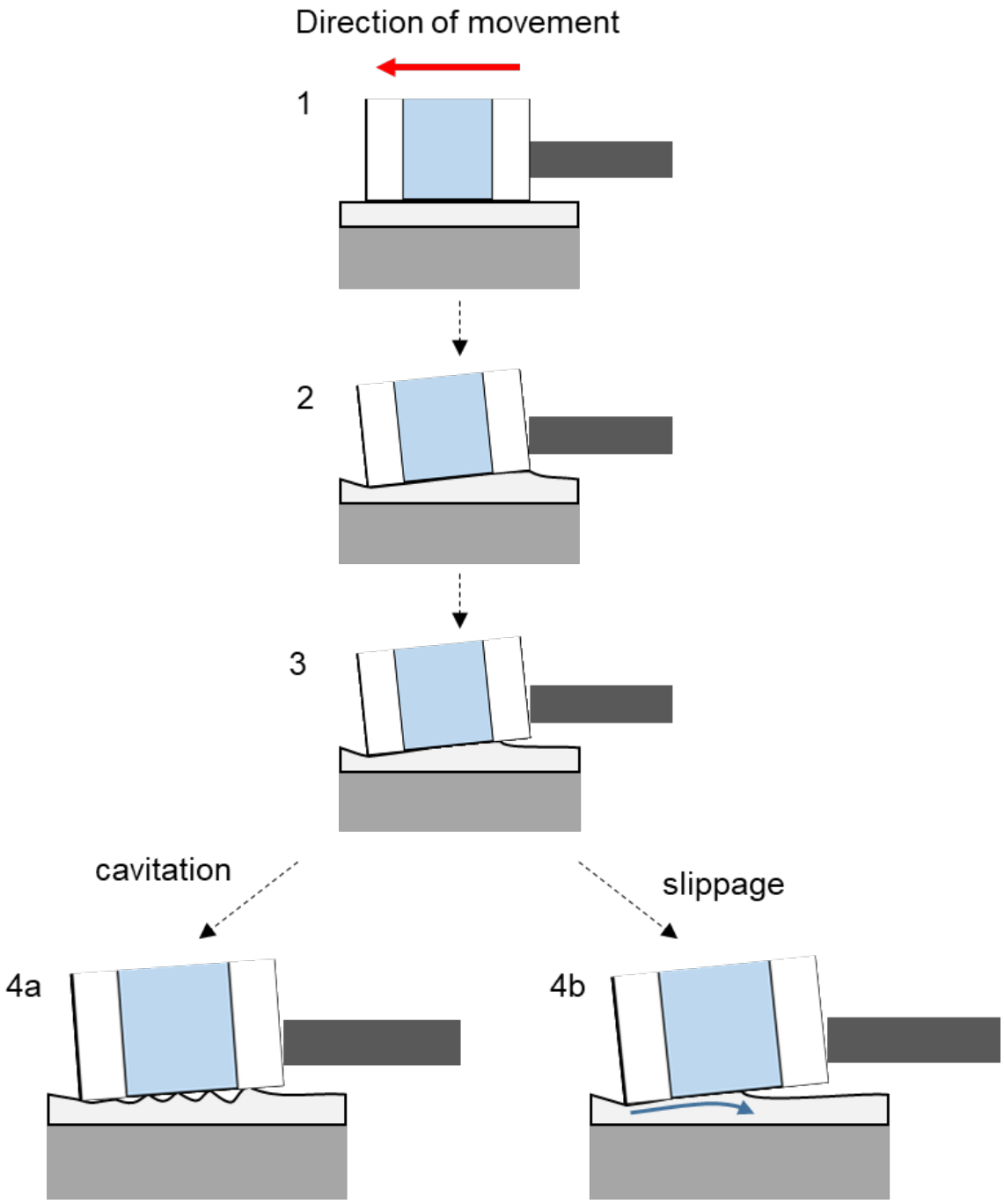

Figure 5.27 – Visualisation of interfacial cavitation and interfacial slippage. The initial stages are the same: 1) probe contact occurs; 2) torque on the ice cylinder causes it to tilt and peel off, with the front of the coating interface under tension and the back under compression; and 3) the adhesion between the coating and the ice is overcome at the front of the interface and a crack forms. In 4a) cavitation occurs – the collapse of the coating when the crack forms generates a wave across the coating surface, which separates the ice from the coating. In 4b) slippage occurs – stress in the coating generates shear flow of the polymer chains along the surface. Not to scale.

5.5.1. Interfacial cavitation between a rigid solid and an elastic substrate

The relationship proposed for the removal of a rigid solid from an elastic substrate under shear is given by (Chaudhury and Kim, 2007) Equation (2.5), reproduced here:

$$\sigma_A \propto \sqrt{\frac{W_A G}{l}} \tag{2.5}$$

This was combined with the Young-Dupré equation – Equation (2.2) – and the expression for shear modulus – Equation (2.7) – to determine the predicted ice adhesion strength. For calculation purposes the surface tension at 20°C was used to remain consistent with the temperature at which the contact angle was measured. A value of 0.07275 N/m was used (Vargaftik et al., 1983). The validity of applying the Young-Dupré equation is debated, but is used here, as is done in the literature (Meuler et al., 2010, Dotan et al., 2009, Andersson et al., 1994, He et al., 2017a).

Values for Poisson's ratio for PDMS are normally quoted from 0.48-0.5 (Dogru et al., 2018, Müller et al., 2019, Pritchard et al., 2013, Du et al., 2010, Johnston et al., 2014). For the purposes of this study, a Poisson's ratio of 0.5 was used.

5.5.1.1. Suitability of model and data

Examination of the relationship described by Equation (2.5) in Figure 5.28 shows a good linear fit. Fixing the intercept at (0,0) gives a correlation coefficient of 0.70. An initial assessment indicates a good possibility of interfacial cavitation. However, this will be compared to the fit when assuming interfacial slippage for better analysis.

It should be noted that the factors used in Equations (2.5-2.7) are not independent of the measurement conditions. Shear modulus is dependent on temperature, strain rate, and specimen thickness; as is Poisson's ratio, though the variation is fractional. As already stated, γ is temperature dependent, and θ is temperature and time-dependent. The fit of the model may be improved by more rigorous determination of these variables, at the correct temperature, strain rate, thickness etc. Shear modulus, for example, was measured at ambient temperature (20°C), but would be lower at the adhesion test temperature of -10°C.

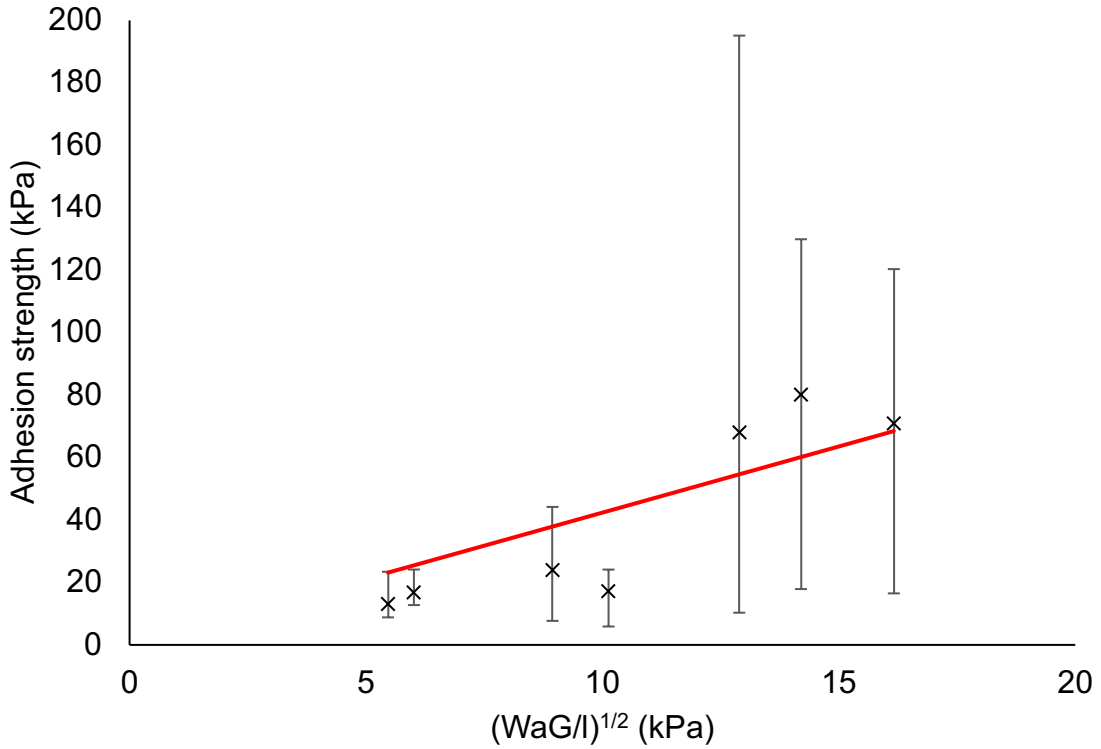

Figure 5.28 – Dependence of ice adhesion on work of adhesion, shear modulus and coating thickness, as proposed in Equation (2.5). A linear fit provides a weak correlation coefficient of 0.70. The proportionality constant derived from a linear fit is 4.16.

5.5.1.2. Influence of constituent terms

Further assessment of the variables of W_A, G and l in Figure 5.29 demonstrates the contribution of each to the ice adhesion behaviour. For $l^{-1/2}$ and $W_A^{1/2}$, it is observed there is negligible correlation between either of these terms and ice adhesion strength. In contrast, ice adhesion and $G^{1/2}$ also have a correlation coefficient of 0.70. Of the properties considered here, the ice adhesion strength of the coatings is most influenced by shear modulus. This makes sense when considering the degree of variability in shear modulus compared to thickness or work of adhesion. The largest value for shear modulus is nearly 10 times greater than the smallest, while the variation in thickness and work of adhesion is fractional.

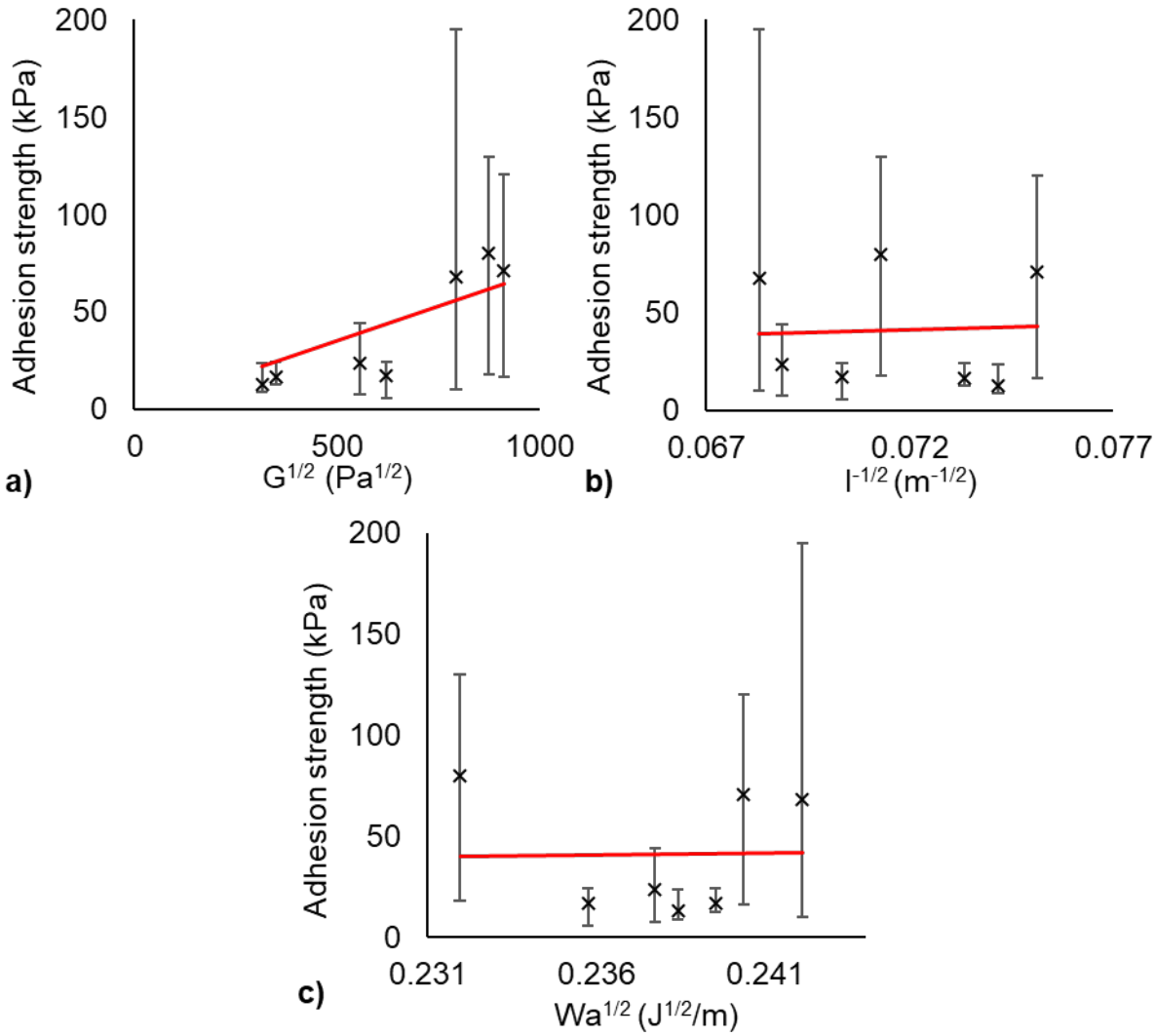

Figure 5.29 – Evaluation of relationship between ice adhesion and factors from the interfacial cavitation model a) shear modulus, b) coating thickness and c) work of adhesion. The relationship between ice adhesion strength and shear modulus is clearly the strongest; there is negligible correlation between ice adhesion and coating thickness or work of adhesion for these coatings.

It should also be noted that the practicality of altering either thickness or work of adhesion is limited. The work of adhesion, as a function of contact angle, is dependent on the chemical attraction between water and the coating. Extensive changes to chemistry of the coatings will also affect physical properties, like the shear modulus, as well as the processability, cost and environmental impact. Making minor adjustments, like changing the polymer chain length as in this work, has limited impact on the work of adhesion (Beemer et al., 2016).

The ability to affect the ice adhesion strength by controlling the thickness of the coating is limited by the range of thickness for which the relationship holds true. It has been shown that there is a critical thickness, above which the ice adhesion is independent

of the coating thickness. Literature suggests this is in the order of 0.5 – 2 mm (Wang et al., 2014a, Kim et al., 2007a) and therefore the lowest ice adhesion strengths achievable for a given coating are around this thickness. However, increasing coating thickness will also increase the weight of a system. The benefits in reducing ice adhesion strength must be balanced against the added weight, which is of great importance in some systems. Contact angle is one of the properties most commonly measured in the literature when attempting to predict ice adhesion. This assumes that work of adhesion is strongly linked to the ice adhesion strength and uses the Young-Dupré Equation (2.2) as rationale for measuring contact angle. As already shown, $W_A^{1/2}$ does not show strong correlation with the ice adhesion strength.

Additional analysis has been performed in the literature showing moderate correlation between ice adhesion strength and W_A directly. Meuler et al. presented a correlation coefficient of 0.8 for ice adhesion and (1 + $cos\theta$) (2010). They examined coatings with a much greater variation in chemistry and contact angle than those here, but which encompassed the values of (1 + $cos\theta$) measured in this study. Performing the same analysis in Figure 5.30 shows no correlation for these coatings.

Figure 5.30 also presents plots of ice adhesion versus θ and $cos\theta$, to determine if there was correlation between any of these variables. The results show no strong correlation in any of these plots. It can be concluded that static contact angle measurements are not a useful indicator for ice adhesion among PDMS based elastomers. It should be noted that other studies have found better correlation between ice adhesion and dynamic water contact angles ($cos\theta_{receding}$, $cos\theta_{advancing}$, *contact angle hysteresis*). However, within this there is still a lack of agreement on which parameter best reflects the ice adhesion strength.

It can be concluded that for these coatings, the dependence on shear modulus is the most significant. Based on the cavitation model, ice adhesion strength can be best predicted via the shear modulus, specifically the square root of the shear modulus.

From a physical perspective of the findings: the lower the shear modulus of the coating, the bigger the mismatch between the ice's modulus and the coating's modulus. This leads to larger strains in the coating when force is applied at the interface, which cannot be matched by the ice. Therefore, cavitation and separation will occur at lower forces.

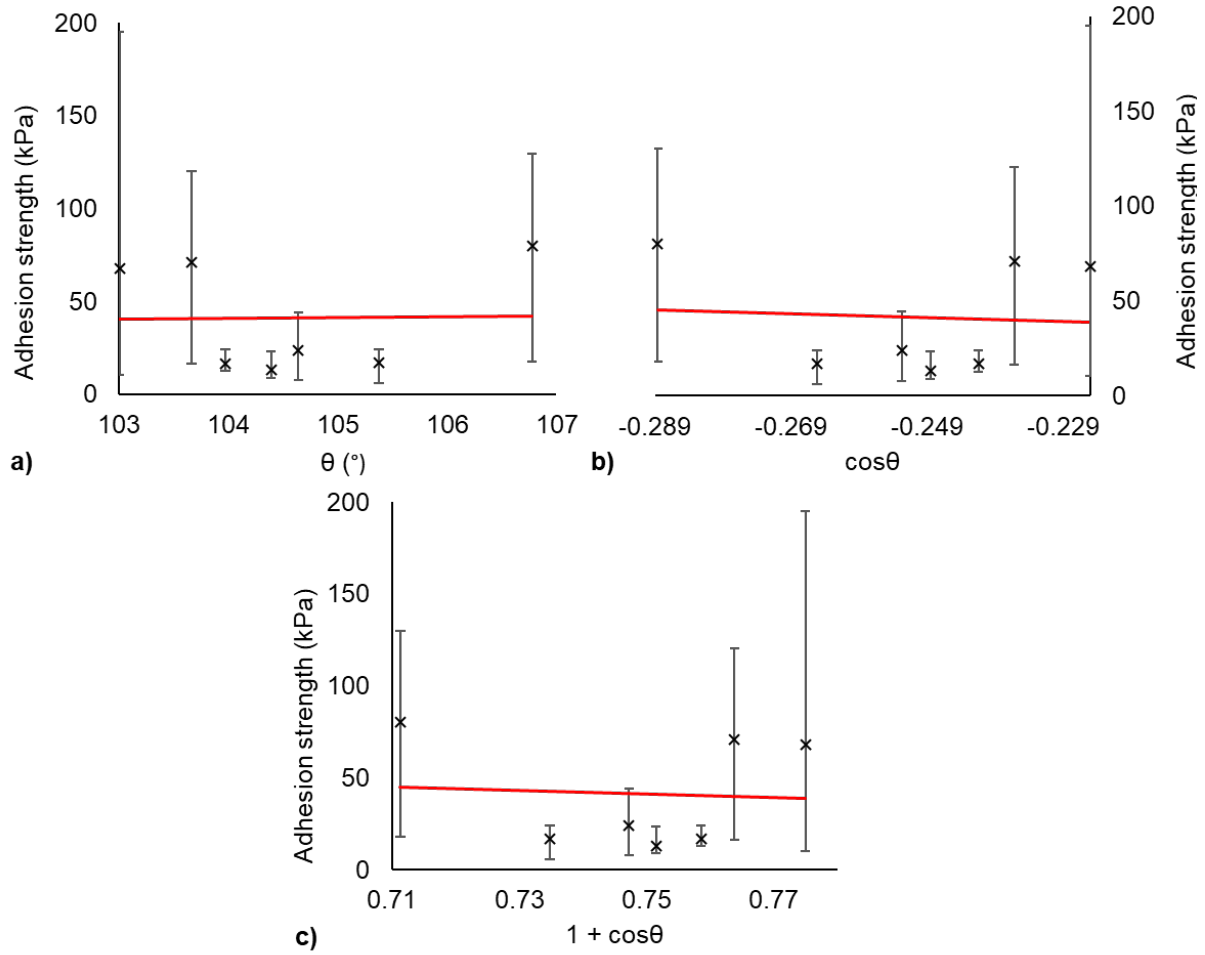

Figure 5.30 – The relationship between ice adhesion and contact angle. Three possible dependences are shown: a) θ, b) cosθ and c) 1 + cosθ. The results show no strong correlation between ice adhesion strength and any of the terms.

5.5.2. Interfacial slippage at an adhesive elastomer interface

The use of an interfacial slippage model to describe the ice adhesion behaviour of elastomer coatings is touched on briefly here. The physical basis for the model and development are described in more detail in Chapter 2. In addition, Chapter 8 examines the possible existence of interfacial slip at the ice-coating boundary more comprehensively. This section provides an initial comparison in the suitability of this model versus the cavitation model through analysis of the fit against shear modulus.

Ice adhesion when interfacial slip occurs was previously described in Chapter 2 via Equation (2.8) and is reproduced here (Golovin et al., 2016, Vorvolakos and Chaudhury, 2003):

$$\sigma_A = \frac{G f_a a}{kT} \tag{2.8}$$

5.5.2.1. Dependence on shear modulus, G

The model states that ice adhesion is directly proportional to shear modulus. Figure 5.31 presents a plot of σ_A versus G and shows an improved correlation coefficient of 0.88. This is a better correlation than that observed with the interfacial cavitation model, which suggests that interfacial slippage might be occurring during ice detachment.

As stated previously, G is temperature and strain rate dependent, and a better fit may be achieved by more rigorous characterisation of G.

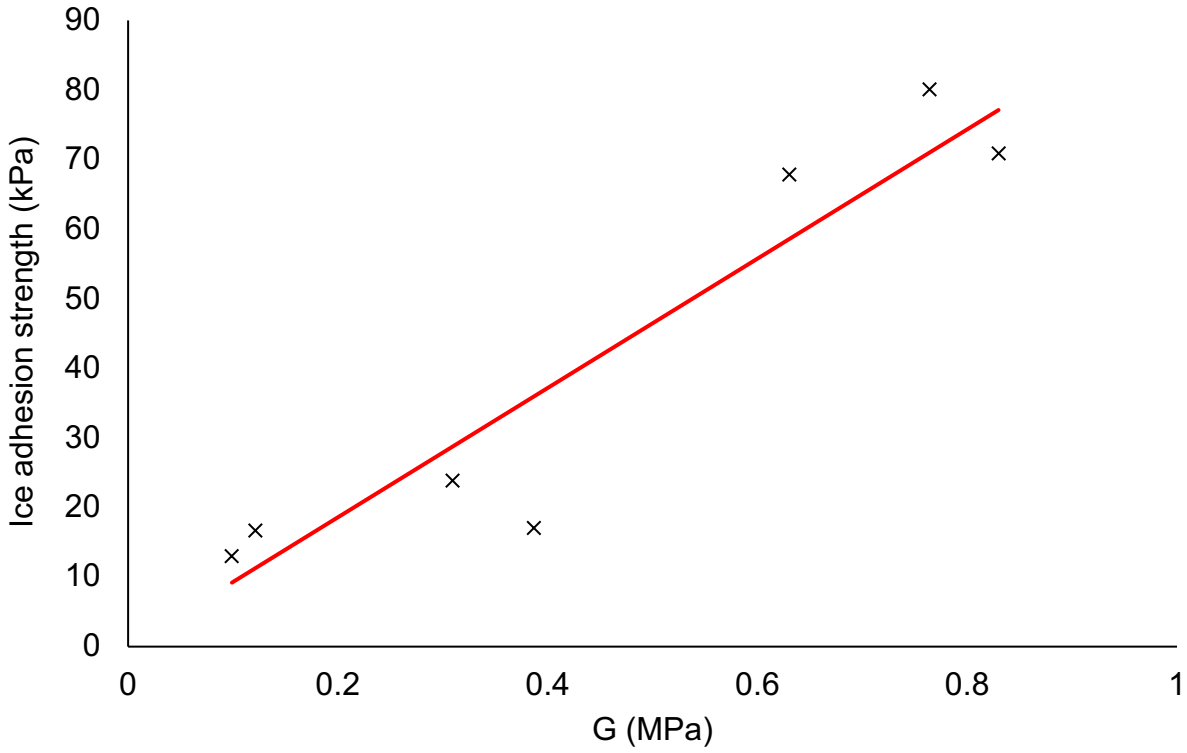

Figure 5.31 – Direct dependence of ice adhesion on the shear modulus.

Whether interfacial slippage is occurring in these systems remains unconfirmed and is investigated further in Chapter 8. Golovin et al. (2016), and Regulagadda et al. (2022), have suggested that interfacial slippage is accompanied by characteristic force/stress curves, presented in Figure 5.32, that were not observed here.

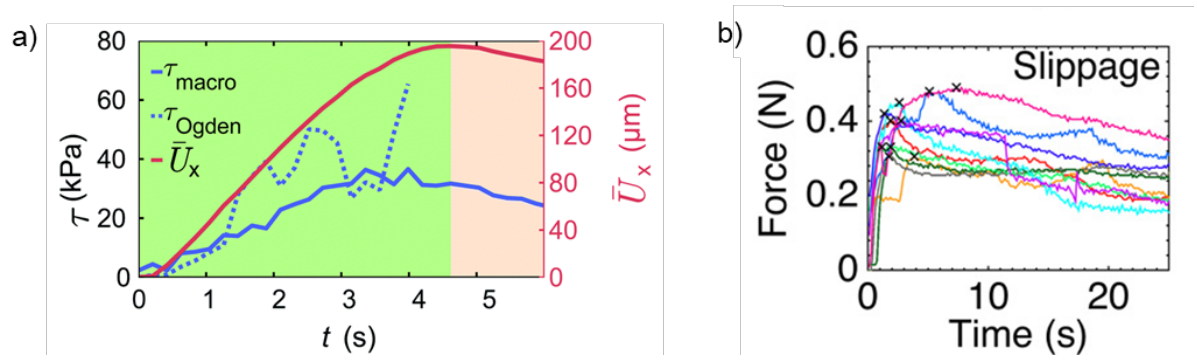

Figure 5.32 – Characteristic interfacial slippage curves. For both a) stress-time curves (solid blue line) (Regulagadda et al., 2022) and b) force-time curves (Golovin et al., 2016), interfacial slippage cases show a slow decay of the stress/force after the peak. The force-displacement curves in this work show a quick drop off in force after the peak (Figure 5.13). It should be noted the probe speed in both studies was lower than in this work at a) 0.1 mm/s and b) 0.5 mm/s respectively.

The influence of the addition of oil on the physical mechanisms of the system will be explored and discussed further in Chapter 8. Nevertheless, it can be concluded that the ice adhesion for these coatings is better correlated to G than $G^{1/2}$. In future elastomer coating design, measurement of shear modulus is the best predictor of ice adhesion strength.

5.6. Conclusion

Using a push test method at –10°C, 100 repeat ice adhesion tests were performed on coating specimens over 9 months. Despite greater degradation over time, the oil-infused coatings exhibited consistently lower ice adhesion strengths than the non-oil infused coatings and are an excellent choice for some anti-icing applications. In most tests they were less than 50% of the non-oil infused coatings. The 50% LMWSO specimens performed the best of all the coatings, with average adhesion strength of 16.5 kPa over all 100 tests, and 17.8 kPa over the final 10 tests. In contrast, the worst coating was the PDMS 80°C, with 99.3 kPa over all 100 and 103.6 kPa in the final 10. Application of the oil-infused coatings would reduce de-icing requirements and lessen the energy, time and resources spent on removing surface ice from, for example, bare metals. They would also reduce damage caused by accumulation and detachment of heavy ice loads. Wear-based degradation was shown not to be a concern over the testing period, as the coatings maintained low ice adhesion.

The non-oil infused coatings, though sometimes an improvement on bare metal surfaces, exhibited high outlier tests. These tests exceeded the limits of the apparatus (>650 kPa) and the ice could not be removed. Measurements indicated ice adhesion

in these instances was greater than 1000 kPa, which presents a marked and sudden increase in ice adhesion, sufficient to make the surfaces not icephobic. This remarkable behaviour casts doubt on the long-term viability of these coatings as anti-icing surfaces, as this was not a singular instance but increased in frequency as testing progressed. Over time, the benefit they provide by reducing the ice adhesion may be lost. The coatings could even be detrimental due to the weight they add to a system. This reinforces the argument that the oil-infused coatings are a better solution for anti-icing purposes.

There was good agreement when comparing between the data in this work and ice adhesion values from other studies, particularly for the oil-infused coatings. This is despite even large differences in test methods and properties that contribute to ice adhesion strength, for example, strain rate and coating thickness – as shown in pilot testing here. The implication is that other properties of the system and coatings exert greater influence over the measured ice adhesion. This was examined by the application of two ice adhesion models.

The physical mechanisms of the system were analysed using two different ice adhesion models: interfacial cavitation and other interfacial slippage. Assessing the fit of the models against the data, and the relative influence of the constituent parameters, will aid understanding of the controlling mechanisms of ice adhesion and inform future coating design. The analysis showed that the adhesion strength is much more strongly influenced by shear modulus, G, than coating thickness, work of adhesion or static water contact angle. Shear modulus is the best property for predicting ice adhesion of elastomers in the design of future coatings. Additionally, the adhesion strength showed stronger correlation with G than $G^{1/2}$, suggesting the interfacial slippage model better describes the detachment of ice from the elastomer surfaces. The possible occurrence of interfacial slippage at the interface is examined in Chapter 8.

6. Freezing Delay

Summary

By measuring the time for a water droplet to completely freeze, freezing delay is determined for each of the coatings and aluminium. The average of 10 measurements on each surface shows that coatings have a minimum improvement in freezing delay of 51 s (59%) pre-adhesion testing and 17 s (20%) post-adhesion testing (both NuSil R-2180) compared to aluminium with 87 s. There is a slight decrease in freezing delay post-adhesion testing. The best coating pre-adhesion was 25% LMWSO with a total freezing delay of 295 s (240% increase). The best coating post-adhesion was 50% HMWSO with total freezing delay of 193 s (122% increase). Coated surfaces also show more frequent indefinite nucleation delay than aluminium. No obvious trends are present between the oil-infused and non-oil infused coatings.

The results broadly agree with those of other studies, though scatter in the data reflects the stochasticity of the governing nucleation processes. Semi-quantitative analysis using classical nucleation theory supports the conclusion that the coatings all provide better freezing delay than aluminium, with little difference between the coatings. The differences that do exist in the coatings likely arise from undefinable surface factors and the probabilistic nature of nucleation, rather than measurable properties of the coatings.

6.1. Introduction

The second icephobicity metric, freezing delay, has been less widely studied than ice adhesion strength. Reasons for this may include: the belief that smooth surfaces have negligible impact on nucleation delay, the stochastic behaviour of nucleation, and the difficulty with replicating real-life icing processes. Most research that does exist is carried out on textured surfaces, in the belief that textured surfaces can better manipulate the nucleation ability of ice, and thus prevent ice formation (Yue et al., 2019, Yue et al., 2018, Tourkine et al., 2009, Oberli et al., 2014, Zhang et al., 2018, Hao et al., 2014, Guo et al., 2021, Mohammadian et al., 2020, Montes Ruiz-Cabello et al., 2021, Heydari et al., 2013).

Prevention of ice formation is an important method for achieving the overall aim of reducing ice accumulation. If ice cannot form on a surface, it cannot accumulate. Ice formation from warm liquid water can be simplified into three stages: cooling, nucleation and growth. For the purposes of this work, the following system is assumed: heterogeneous nucleation, from warm water (above 0°C), where the heat transfer mechanism is predominantly conductive. The system is expressed visually in Figure 6.1.

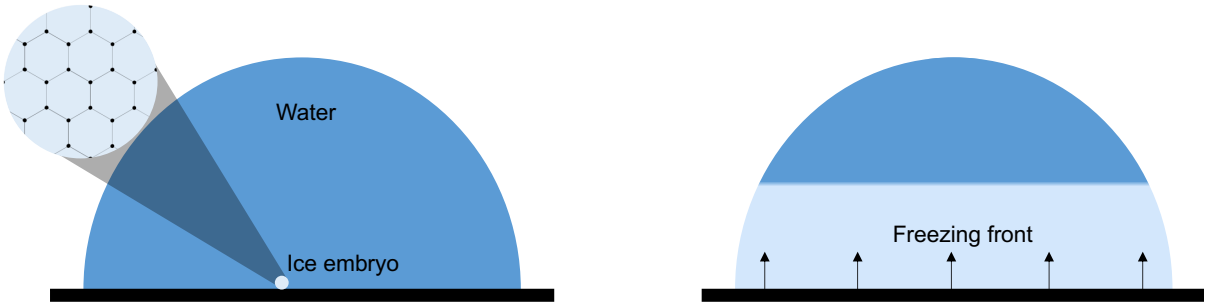

Figure 6.1 – Ice formation process. Ice embryo of critical size is formed, then growth occurs, and the freezing front rises up the droplet.

As the temperature of the water falls to 0°C, the water molecules change arrangement to the solid ice arrangement. This starts in small parts, called ice embryos, and once a critical size has been reached an ice nucleus is formed. It is energetically favourable for the nucleus to expand. As the nucleus expands more of the water solidifies into ice; this is the growth process. When heterogeneous nucleation occurs at the water-substrate interface, the freezing front (the water-ice interface) grows upwards until all of the water has solidified.

Both nucleation and growth are necessary for ice formation on a surface. Inhibiting either process will reduce the formation and accumulation of ice. Less energy is then required for ice removal. The two processes are governed by different phenomena. Nucleation is dependent on the thermodynamics of the phase change from liquid to solid, and the growth is determined by the heat transfer properties of the system (Irajizad et al., 2019b). The methods for characterising the inhibition of ice formation are therefore complicated.

Similarly to the research on ice adhesion, there is no standardised test method for measuring inhibition of ice formation. Studies can be split into two categories which describe the primary measurement objective: time-based or temperature-based. In both methods, a droplet is placed on the surface and allowed to freeze. A temperature-based test will reduce the temperature of the water at a fixed rate and measure the temperature at which nucleation occurs. A time-based approach fixes the temperature at one value, and then measures the time for nucleation or complete freezing to occur.

This study uses a time-based approach The freezing delay is measured for each of the coatings, as well as the aluminium substrate as a reference surface. A graphical representation of the definition used in this study for freezing delay, $t_{freezing}$, is presented in Figure 6.2.

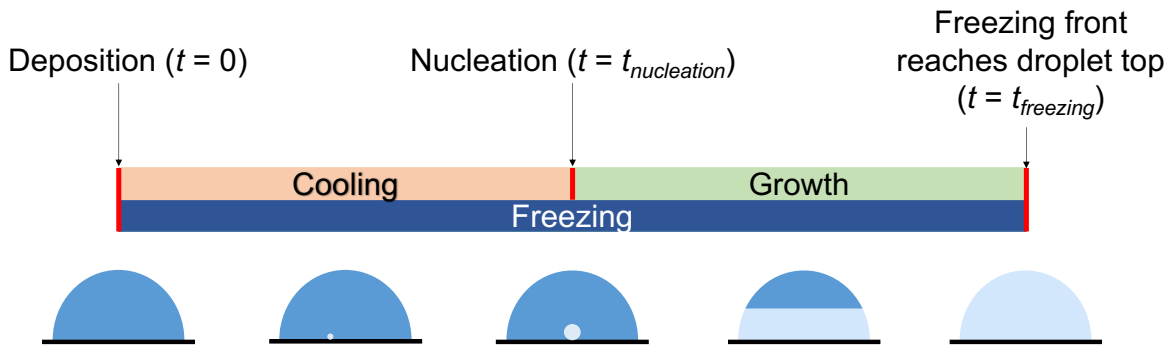

Figure 6.2 – The freezing delay, $t_{freezing}$, is made up of cooling, nucleation and growth of ice in a water droplet once it has been deposited on a surface.

The data was analysed, and the freezing delay was determined for each coating. Testing was carried out prior to and after the adhesion testing regimen, to determine the effect that surface wear and ageing have on performance. The results are compared to literature values and numerical calculations.

6.2. Experimental method

6.2.1. Development of method

Due to the lack of a standardised test method, the method used in this study underwent testing and development before finalisation. Some very preliminary testing was carried out using a Peltier stage and a temperature-based approach. However, determination of the temperature lag between the surface of the Peltier stage and the surface of the coating proved prohibitively difficult. Issues with the local humidity inside the stage also meant visualisation of the droplet was inconsistent. For this reason, it was decided to change to a time-based approach.

The primary benefit of the time-based approach was that it could be carried out inside the cold laboratory, alongside the ice adhesion testing. This meant the surfaces could be left to reach thermal equilibrium with the surroundings prior to testing. The humidity of the cold laboratory was also fairly constant, and because testing was carried out in the open air rather than a constrained space, differences in local humidity around the droplet did not present any visualisation issues.

6.2.1.1. Initial testing methodology

Within the time-based approach, there are further factors which must be considered. These include droplet volume, starting water temperature, surface and air temperature, humidity and choice of finish point. As the nucleation testing was performed alongside the ice adhesion testing, both tests were carried out at the same temperature (−10°C ± 1°C) for ease of operation. As detailed in Chapter 5, the cold laboratory is made up of a series of rooms which are maintained at −10°C by supply of chilled air. The humidity is dictated by the air supply and was 80% ± 10%. Pilot testing was carried out on PDMS 80°C specimens and aluminium substrates.

The droplets were deposited via 1 ml syringe. The droplet volume chosen was the smallest volume able to be dispensed by the syringe, as dictated by the surface tension of the water and the syringe tip diameter. The droplet volume was 0.05 ml and deionised water was used to limit interference of foreign particles on nucleation.

It was decided that the starting water temperature would be varied and the effect of this measured, to be fixed in the final procedure. The ambient temperature outside of the cold laboratory was approximately 15°C at the time of testing. The water

temperatures used as the starting temperatures were: ambient, 15.0°C, 10.0°C, 5.0°C, 1.0°C, 0.1°C.

The finish point was decided to be the point at which the growth phase was complete and the freezing front had reached the top of the droplet. Pilot testing was carried out by visual observation of the specimens in real-time, with freezing time measured by stopwatch.

The procedure was as follows:

i. Test surfaces were left in the cold laboratory for 1 day to ensure thermal equilibrium with the environment.
ii. A beaker of deionised water was brought into the cold room and a thermocouple inserted to measure the water temperature.
iii. Either a droplet was immediately placed onto the surface (ambient starting temperature), or the water was allowed to cool to the designated starting temperature.
iv. A 0.05 ml droplet was placed on the surface and left to freeze. The time from deposition to the completion of the growth phase was monitored visually and measured by stopwatch.
v. The droplets were observed continuously for the first four minutes of testing. If the droplet had not nucleated in that time, the specimens were checked every minute. If the droplets had not nucleated after 30 minutes, the test was terminated.

6.2.1.2. Initial testing results and observations

The results from the initial testing are presented in Figure 6.3. The most significant observation in Figure 6.3 is the occurrence of incomplete tests, defined as those which did not nucleate within 30 minutes of deposition. The droplets in these incomplete tests have supercooled and reached thermal equilibrium with the surroundings (−10°C), without nucleation.

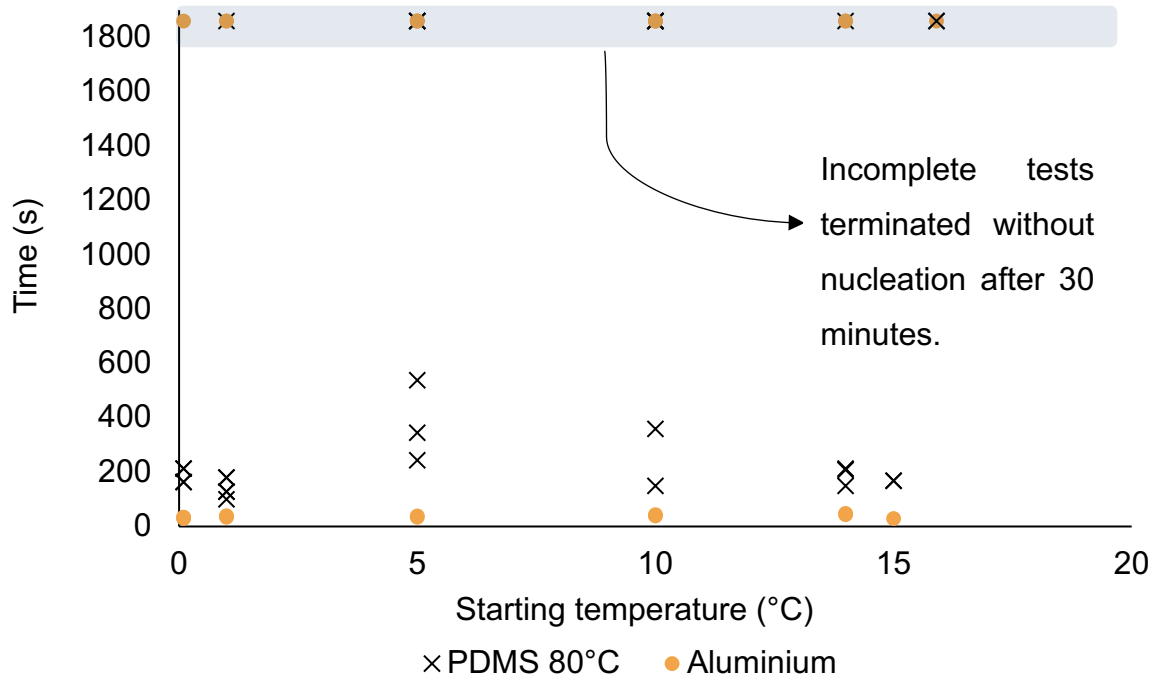

Figure 6.3 – Results of initial freezing delay tests with various water starting temperatures on PDMS 80°C and aluminium specimens. Incomplete tests, in which nucleation did not occur within 30 minutes, are highlighted at the top of the figure. Freezing time was measured from droplet deposition to completion of growth phase.

The complete series of tests are presented separately in Figure 6.4. The results show little correlation between the starting temperature of the water and the freezing time. A possible reason for this is that the droplets are sufficiently small that they cool to 0°C quickly enough to be nearly independent of starting temperature. The remaining time for nucleation and complete freezing would have thus been dependent on the surface characteristics, which are largely unchanged between tests (small amounts of dust may be introduced to the system). The implication of these results is that, within the examined range, the starting temperature is independent of the freezing time and is of practical concern only. For this reason, a starting temperature of 8°C was chosen. This is always below the ambient temperature in the external lab across the year, but reduces the time required for the beaker of deionised water to cool once in the cold laboratory.

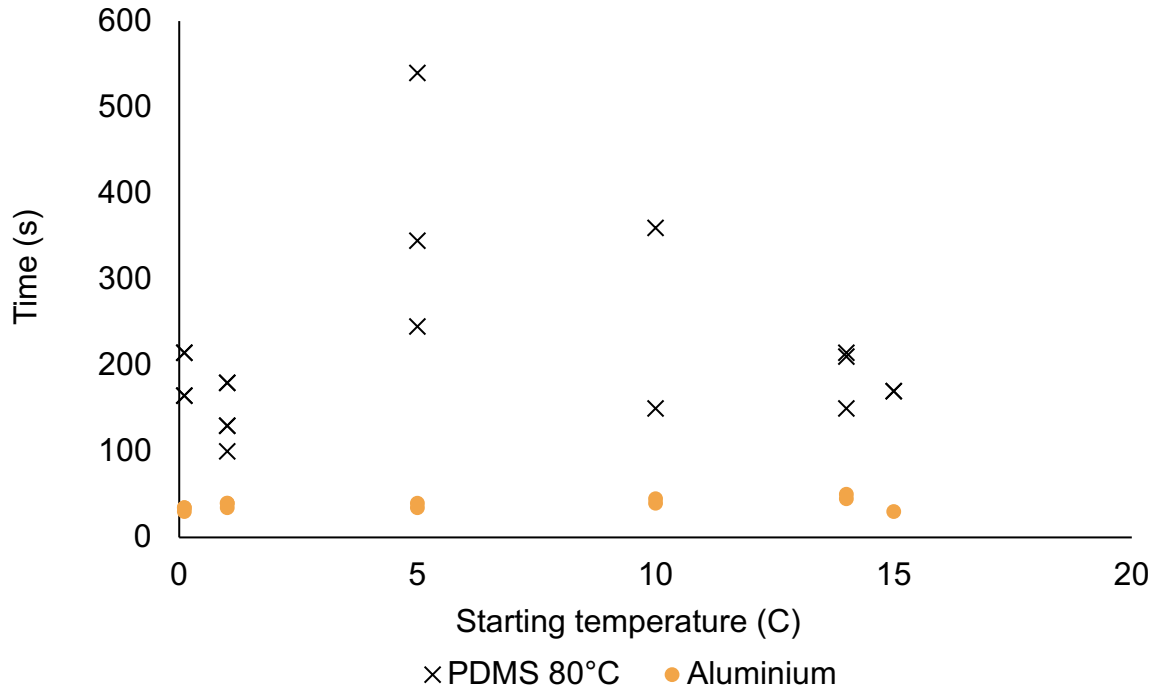

Figure 6.4 – Results of initial testing for freezing delay, showing only the complete tests.

Of the complete tests, the initial results show the aluminium substrate has shorter freezing times than the PDMS 80°C specimen. Incomplete tests were common in both PDMS 80°C and aluminium specimens.

As well as the freezing time measurements, the initial testing generated some qualitative observations of interest. Firstly, when nucleation occurred, it was often accompanied by formation of a condensation halo around the edge of the droplet. An example of this is visible in Figure 6.5. Condensation halos were noticeably larger on the PDMS 80°C specimen than the aluminium substrate: annulus thickness is approximately 2 x larger in the PDMS than the aluminium. The evaporation rate on both surfaces is also very different. Within 30 s, the halo had evaporated off of the aluminium surface, whereas this can take several minutes on the PDMS surface. Notably, the slower evaporation rate on the PDMS allowed the condensation to freeze in some tests. It is possible this could lead to concerns of frost bridging, in which freezing of condensation between water droplets accelerates the nucleation of other droplets.

The ice droplet shape was the same on both surfaces: a smooth droplet topped by a peak. The droplet base was slightly wider on the aluminium due to its higher surface energy. There is a difference in the opacity of the frozen droplets. On the aluminium

substrate the droplets were almost completely opaque, while the droplets on the PDMS were much clearer. This is likely a result of different growth rates in the droplets from their different heat transfer properties. The aluminium droplets are likely to freeze faster, trapping more dissolved oxygen and causing greater internal stresses as the ice solidifies and expands, than the PDMS.

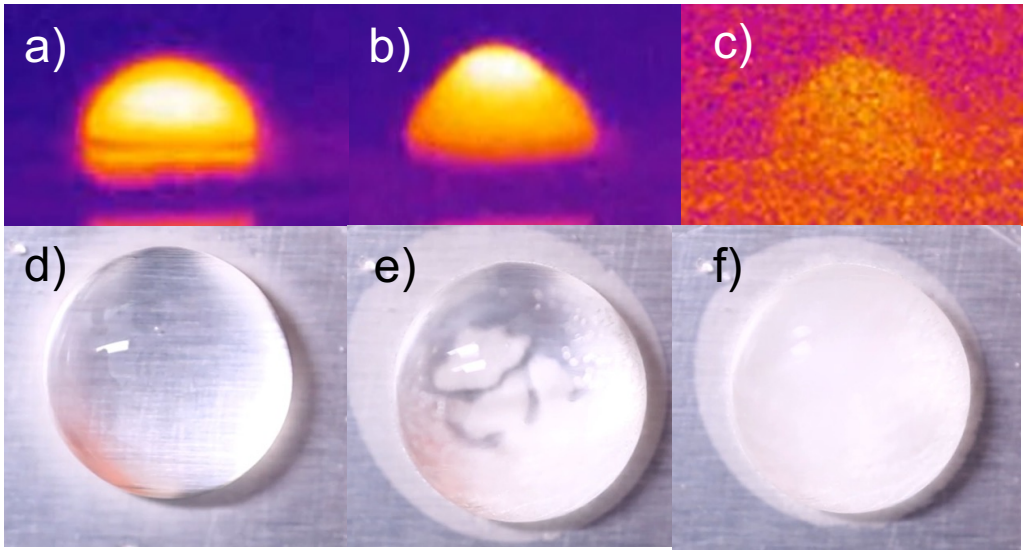

Figure 6.5 – Infrared and camera images of a droplet freezing on a PDMS surface. Images a), b) and c) show infrared images of the droplet at 0 s, 189 s and 248 s, respectively. The temperature of the droplet at 0 s is 8°C. Temperature of the droplet at 108 s is within 1°C of the lab temperature (–10°C). Images d), e) and f) show DSLR images of the droplet at 0 s, 189 s and 248 s, respectively. Condensation is visible around the edge of the droplet, but it has not frozen.

6.2.2. Final test set up and apparatus

For the finalised test procedure, a FLIR A655sc infrared camera was used in conjunction with a Canon 6D DSLR to gather video footage to observe visual and thermal changes in the water droplets during the nucleation and freezing process. The test set-up is shown in Figure 6.6.

6.2.2.1. Coating dimensions and preparation

The specimens used in the freezing and nucleation testing were the same as those used in the ice adhesion testing. To summarise: coating surface area measured approximately 20 mm x 20 mm, with thicknesses of 200 µm ± 11%, as measured by profilometer (Mitutoyo SJ-410). The elastomers were prepared as described in Chapter 3. The specimens were cast on aluminium substrates, in square silicone moulds. For each coating type, two specimens were made and tested.

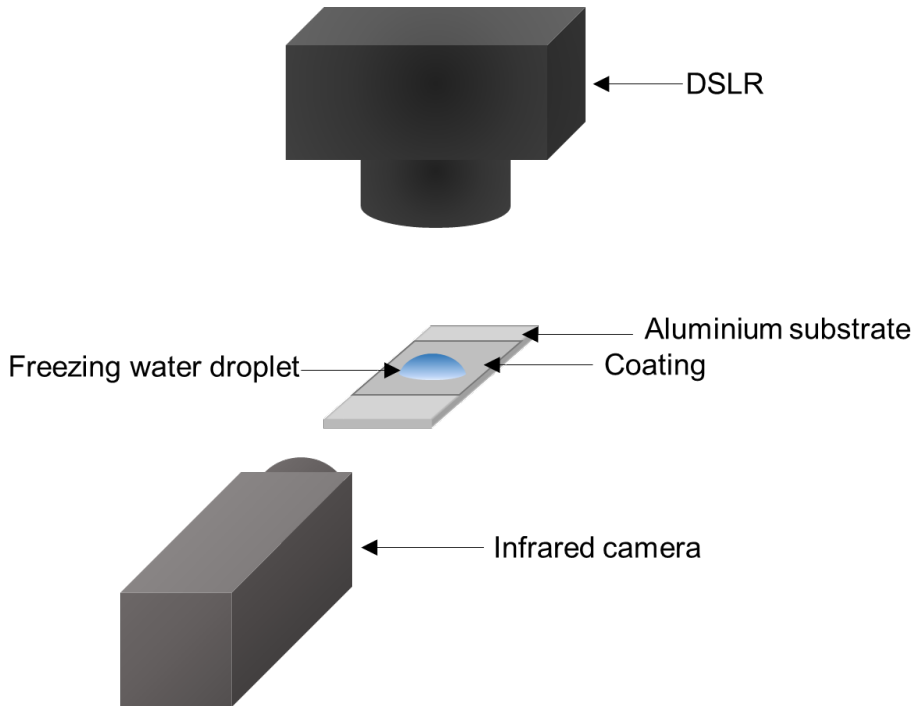

Figure 6.6 – Schematic showing the freezing delay test set up.

For the aluminium reference specimens, uncoated aluminium (alloy 5521) substrates were used as received, but cleaned with isopropanol and deionised water prior to use.

6.2.2.1.1. Test conditions and procedure

Freezing delay testing was carried out in the cold room (–10°C, 80% RH). The testing procedure is described here, and was repeated 5 times for each specimen (10 tests per surface type):

i. Test surfaces were left in the cold laboratory for 1 day to ensure thermal equilibrium with the environment.
ii. A beaker of deionised water was brought into the cold room and a thermocouple inserted to measure the water temperature.
iii. The water was cooled to 8°C before dispensing.
iv. A 0.05 ml droplet was placed on the surface and left to freeze. Videos of the deposition and entire freezing process were captured using the DSLR and infrared camera. The test endpoint was the completion of the growth process, when the freezing front had reached the top of the droplet.
v. If nucleation had not occurred within 7 minutes the test was terminated. (Observations from infrared imaging identified that within 7 minutes the droplets

had reached thermal equilibrium at –10°C. The droplet was deemed to have supercooled and supressed nucleation indefinitely.)

After the tests were complete, the DSLR and infrared videos were processed to measure the time between the droplet being placed on the coating surface and the end of the growth phase. This was determined to be the point at which the freezing front within the droplet had reached the top of the droplet. The appearance of these visual indications is demonstrated in Figure 6.5. Testing was carried out on specimens before and after adhesion testing to see the effect that wear from de-icing cycles and long-term exposure to the cold room environment had on freezing time.

6.3. Results

6.3.1. Freezing delay

All the coatings exhibited improved freezing delay when compared to bare aluminium, showing a minimum of a 52 s increase (60%) pre-adhesion and a 24 s increase (27%) post-adhesion testing (both NuSil R-2180), as presented in Figure 6.7. The improved freezing delay time is likely due to i) fewer nucleation sites on the smoother elastomer coatings when compared to the aluminium surface and ii) the lower thermal conductivity of the elastomers. This would delay nucleation, and slow the growth progression via the reduction in heat transfer rate from the droplet (Irajizad et al., 2019b).

The NuSil R-2180 showed less improvement compared to the PDMS based coatings. The oil did not have a significant effect on the freezing delay compared to the plain PDMS coatings. The coatings, except for the 50% HMWSO, had decreased freezing delay after the adhesion testing. This is possibly due to an increase in nucleation sites from wear damage or dust accumulation. All coatings maintained better freezing delay compared to aluminium, even after the adhesion testing.

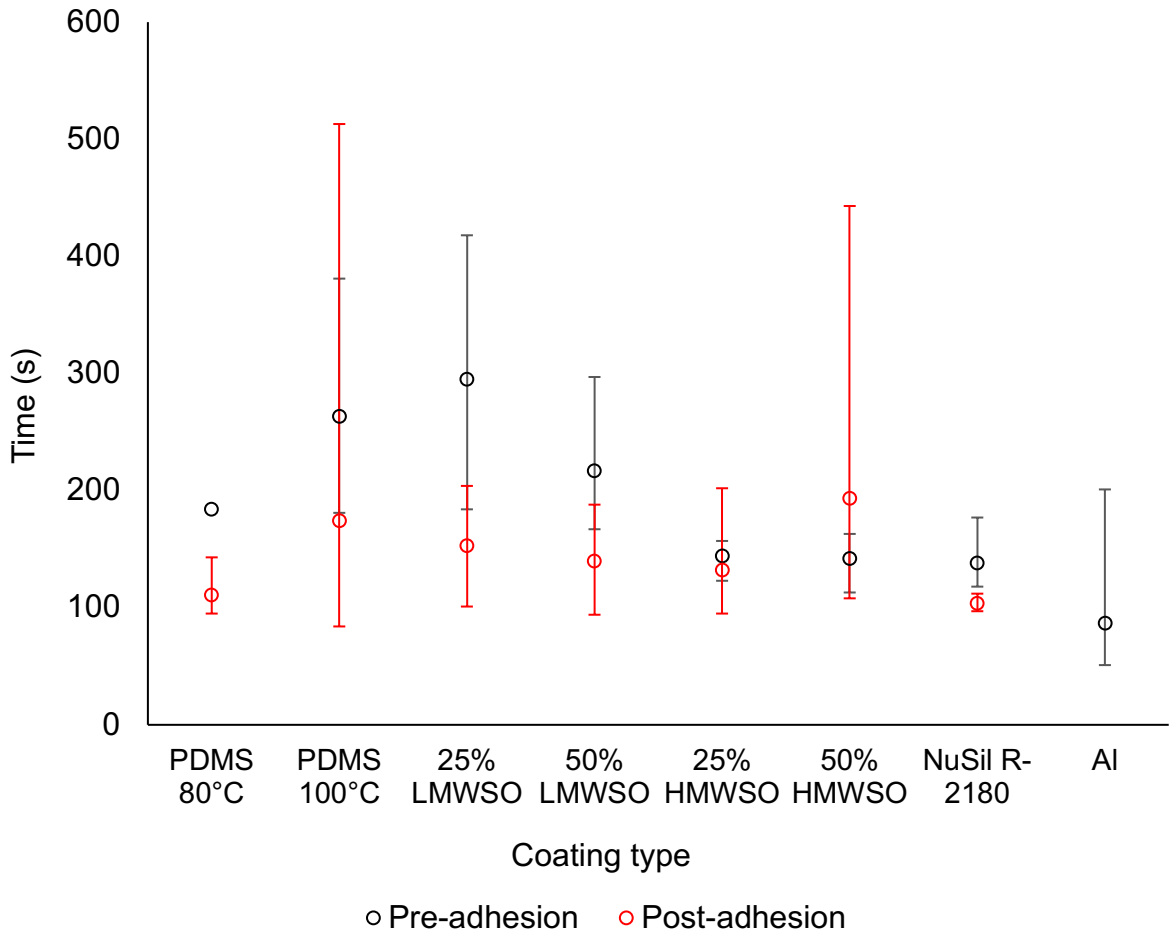

Figure 6.7 – Average freezing delay of distilled water droplets on the different surfaces, with range bars. Measured from start of contact until freezing front reaches top of droplet. PDMS 80°C only nucleated once in the 10 pre-adhesion tests.

6.3.2. Indefinite nucleation delay

An additional finding from these tests was the frequency with which nucleation was delayed indefinitely on the coatings. This is defined here as being beyond the time taken for thermal equilibrium of the droplets. Supercooling of the droplets below 0°C was anticipated and has been demonstrated as a method of improving overall freezing delay, largely via engineered surface textures. However, due to the lack of designed surface texture and relative smoothness of these coatings, this was not expected to be a common observation in these experiments. Yet the data presented in Figure 6.8 shows significant supercooling and indefinite nucleation delay was observed on all the coatings. The PDMS 80°C had an exceptional indefinite nucleation delay rate of 90% pre-adhesion testing. All the coatings had more frequent indefinite nucleation delay than aluminium pre-adhesion testing.

Examination of the frequency of indefinite nucleation delay in Figure 6.8 does show a difference between 100% PDMS coatings and the oil-infused coatings. When comparing pre- and post-adhesion testing data, the frequency of indefinite nucleation delay fell to 20% for both pure PDMS coatings, while the oil-infused coatings, except the 25% HMWSO, maintained or increased in frequency.

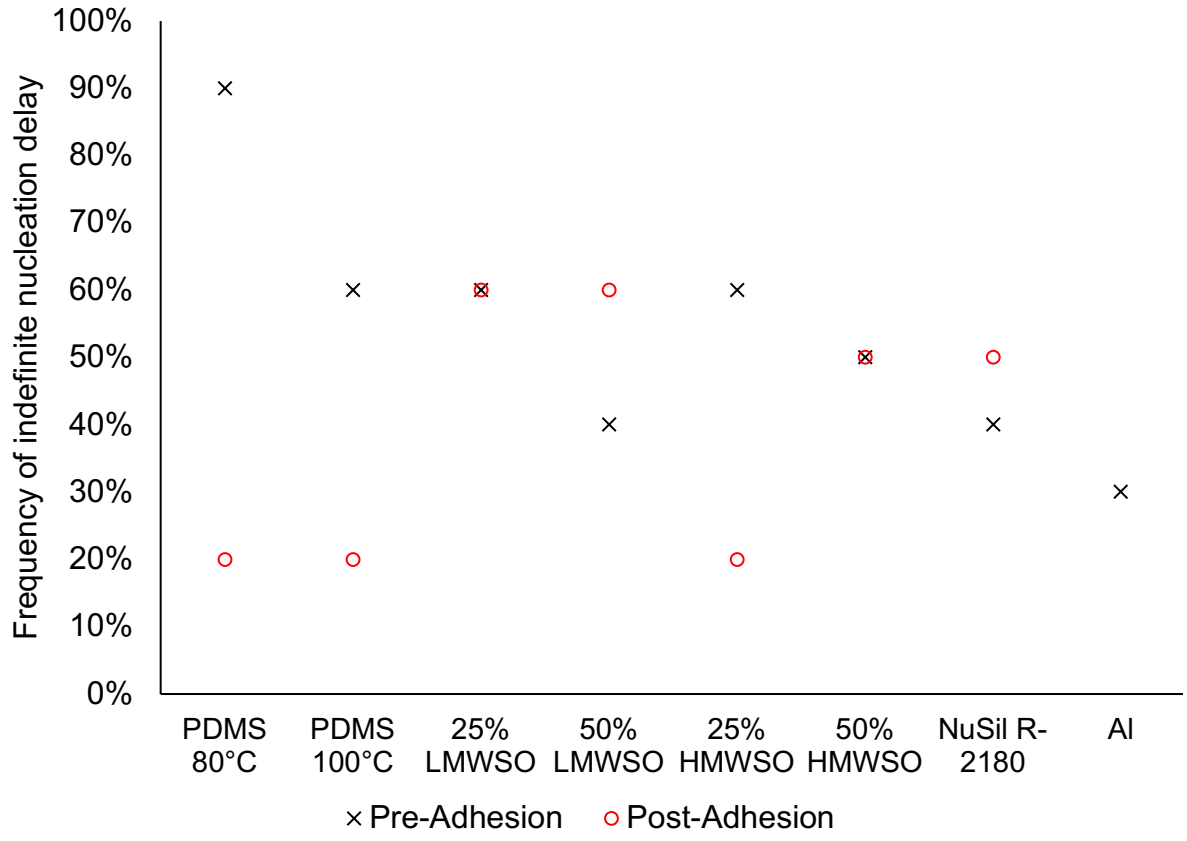

Figure 6.8 – Frequency of indefinite nucleation delay on the different surfaces, before and after adhesion testing regimen.

6.4. Comparison with other studies

In a comparison between the data from this work and values collected from other studies, there is large scatter in the reported freezing delay times for the surfaces. Graphical representation of the comparison is presented in Figure 6.9. No exact replica of the test methodology used in this work was available in literature. The studies that are used for comparison are similar, but with some differences in the experimental details. A selection of the most relevant experimental details of the studies is provided in Table 6.1. These include the initial and final temperature of the droplets, the type and volume of water used, the thickness of the coating and the atmosphere in which the test was performed. These will all affect the time for freezing delay. As with the ice

adhesion comparison, the studies presented for comparison here do not all report the same experimental details, so some information is missing from Table 6.1. This is, again, an argument for agreement or standardisation of the experimental details that are reported.

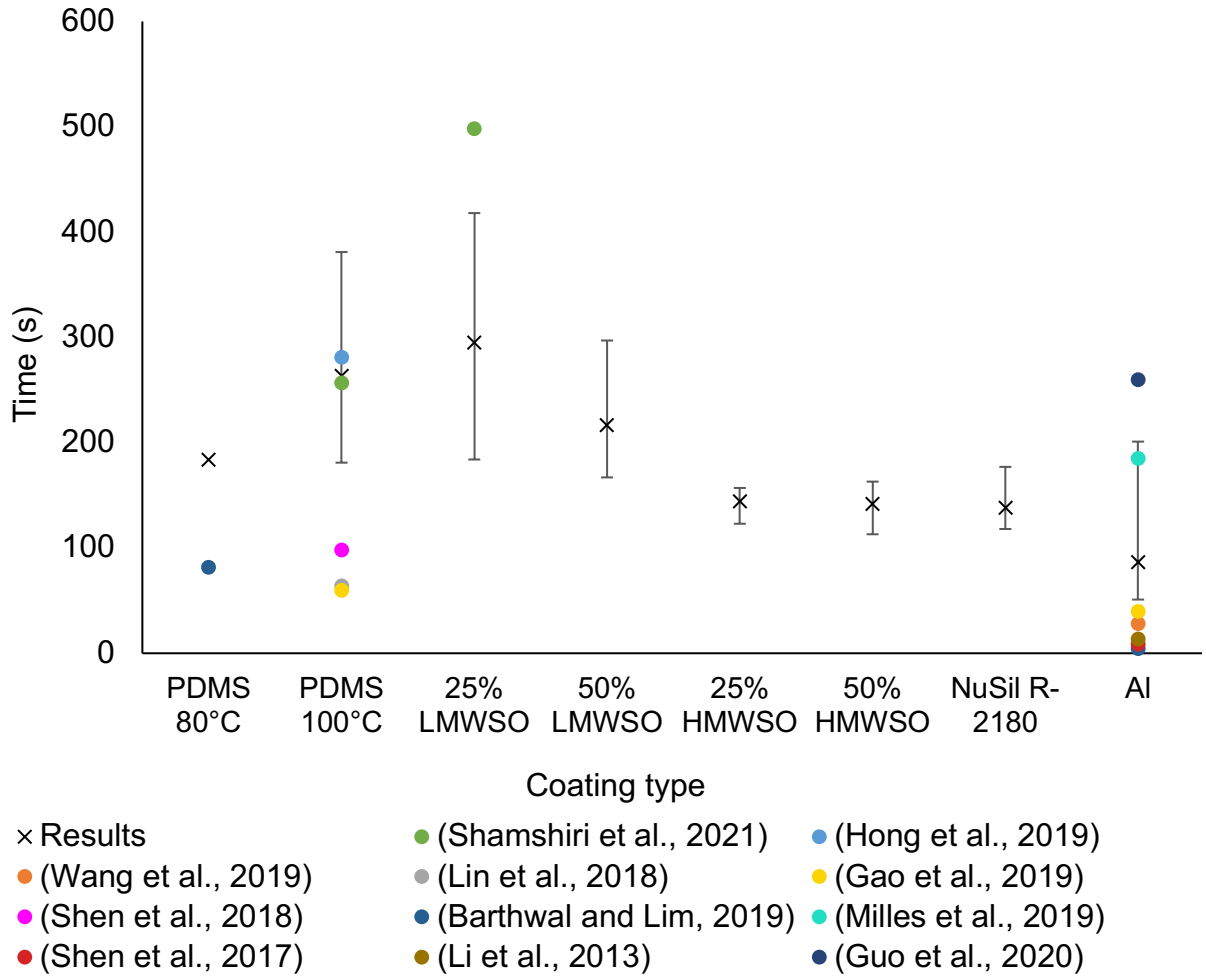

Figure 6.9 – Comparison of data collected in this work to values from other studies. The pre-adhesion data is used.

Estimating the finish point is also a source of error. The studies used the same definition of endpoint, but most use visual clues to determine this. The inherent ambiguity of this method, combined with human error, creates uncertainty in the results.

The evaluation of freezing delay is complicated by the randomness of nucleation. This inherently makes comparison difficult when working with small data sets. As mentioned, 10 tests were performed for each coating type in this work. Other studies use different numbers of tests, including some instances of fewer tests, or do not report how many tests were performed for each data point.

As the literature studies discussed here all carried out testing on pristine specimens, the pre-adhesion results were used for comparison. No data was found for the oil-infused coatings, except for the 25% LMWSO coating. However, the structure of the PDMS used in that study is different, and the coating was comprised of only 20% LMWSO. The data is still used for comparison purposes here. This work presents the first significant examination of the freezing delay on oil-infused elastomer coatings.

The broad trend observed is that the values from this work are slightly higher than those of other studies. This can be seen in the PDMS 80°C, PDMS 100°C and aluminium coatings. The most likely reason for this is that the volume of the water droplets used in most of the studies is ≤10 µL, which is a third of the volume of the droplets used here. The lower mass will lead to faster heat loss during cooling and growth. There are a few instances where the literature values fall within the range bars of the results of this study, in the PDMS 100°C and aluminium. Despite the discrepancies in experimental methodologies, there is some agreement between the results from this work and the literature. There are only two cases, in the 25% LMWSO and aluminium surfaces, where the literature values exceed the upper limit of the range bars from this work.

Of particular interest is the comparison to Gao et al. (2019), which presents data for a pure PDMS and an oil-infused coating. Their results strongly indicate that there is an improvement in the freezing delay time upon the addition of oil. This disagrees with the results of this work, which only shows a small increase upon the addition of 25% LMWSO, and a decrease when adding 50% LMWSO. Differences in experimental details such as droplet temperatures, droplet volume and coatings thickness may contribute to the disparity between their work and the results here. However, the freezing delay time reported for the PDMS 100°C is very close to the results of this study, so it is unlikely to be the primary cause. In their study, the disparity was attributed to differences in roughness and hydrophobicity. Their pure PDMS specimen had R_q = 0.5 nm and water contact angle of 106.1°, versus R_q = 0.4 nm and 105.9° for the oil-infused coating. However, these differences are less than what was measured here, casting doubt on that assertion. They do claim a large error in their measurement of ± 138 s, which would bring the oil-infused coating within the range of values recorded here. It is more likely that the disparity is caused by stochasticity in the data.

Table 6.1 – Abridged details of literature studies

Surface type	Freezing time (s)	Initial temp. (°C)	Final temp. (°C)	Water type	Water volume (µL)	Coating thickness (µm)	Atmosphere	Ref.
(Branched and vinyl-terminated) PDMS	257		-15	Deionised	5	40-45	N_2	(Gao et al., 2019)
(Branched and vinyl PDMS) 20% LMWSO	498							
PDMS	281.2		-20	Deionised	5	20	Low humidity	(Shamshiri et al., 2021)
Al	28		-15		40	-	70% humidity	(Hong et al., 2019)
PDMS	64	Room temp (>20)	-20	Deionised	7	300	15% humidity	(Wang et al., 2019)
PDMS	60	23	-5	Deionised	10	5-20	22% humidity	(Lin et al., 2018)
Al	40					-		
PDMS	98	20	-15	Deionised	6	200	50% humidity	(Guo et al., 2020)
Al	4.8		-15	Deionised	4	-	<5% humidity	(Shen et al., 2018)
PDMS	81.9							

Al	185	Room temp	-10			-	45% humidity	(Barthwal and Lim, 2019)
Al	8.7		-20	Deionised	8	-		(Milles et al., 2019)
Al	13.5		-10		4	-	65% humidity	(Shen et al., 2017)
Al	260	21	-10	Tap	8	-	60% humidity	(Li et al., 2013)

6.5. Semi-quantitative numerical analysis

As discussed above, nucleation is an inherently random behaviour, often best described via statistical models rather than purely physical, fundamental expressions. It is difficult to precisely calculate expected freezing delay times without accurate knowledge of micro- and nano-scale properties of the system. To provide some explanation for the results presented in this chapter, a semi-quantitative analysis is provided here.

The freezing process has been split into the following two stages, which will be assessed separately:

1) Nucleation
2) Ice growth

6.5.1. Nucleation

As discussed in Chapter 2, the heterogeneous nucleation rate, *J*, on a surface for a given temperature is (Fletcher, 1958) described by Equation (2.9) and reproduced here.:

$$J(T) = K \exp\left(-\frac{\Delta G^*}{kT}\right) \tag{2.9}$$

In general, the pre-exponential kinetic constant is poorly defined, and is eclipsed by the exponential term (Irajizad et al., 2019b).

Using Equations (2.9)-(2.18) we can determine approximate values for the predicted nucleation rates on the coatings.

However, the value of *R* is inherently difficult to quantify, so a broader view of the behaviour of *f(m,x)* is used. Plots of *f(x)*, given the contact angles of the surfaces and values of *x* between 0.01 and 1000, are presented in Figure 6.10. For both concave and convex plots, the icephobic coatings have very similar responses to changes in *x*. On aluminium surfaces *f(x)* will be lower than on the coated surfaces. The graphs show that in both concave and convex cases, *f(x)* remains virtually constant when $x > 2$, and for convex nucleation sites, *f(x)* approaches 1 for all surfaces when $x < 0.2$. This latter case corresponds to homogeneous nucleation, (*f(x)* = 1 when $x = 0$), with no nucleating surfaces. At –10°C, r_c is in the order of 1 nm, (calculated to be 3 nm via molecular dynamics simulations (Pereyra et al., 2011)). From this we can observe that for convex

nucleation sites, *f(x)* is only dependent on *x* when *R* is approximately 0.2-10 nm. For concave nucleation sites there is logarithmic behaviour below *x* = 2, with *f(x)* approaching 0 at *x* = 0 (equivalent to nucleation immediately at 0°C, without supercooling). For convex surfaces, all values of *f(x)* for the surfaces of interest lay between 1 and 0.4 at the extreme. For concave surfaces, though *f(x)* falls quickly when *x* < 2, the values of *f(x)* for all surfaces are in the same order of magnitude for a given value of *x*. These findings agree with similar studies (Irajizad et al., 2019b, Conrad et al., 2005, Wan et al., 2021).

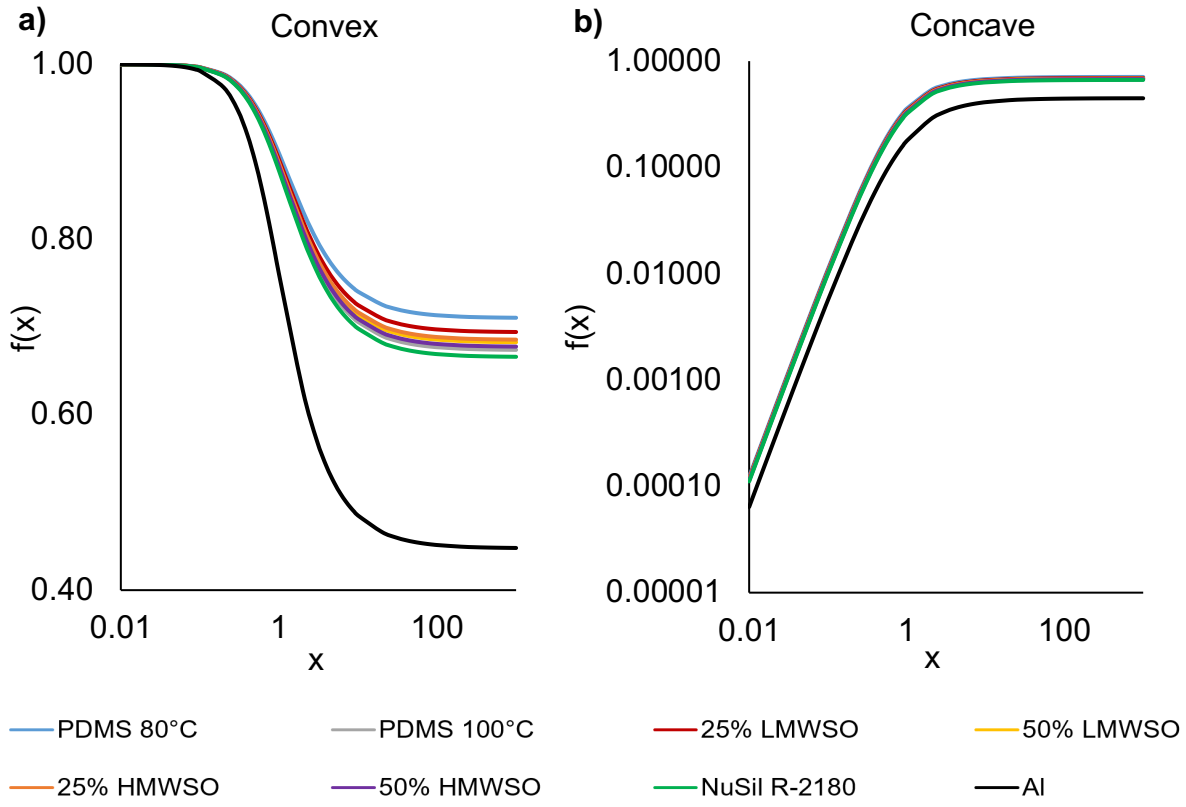

Figure 6.10 – Behaviour of surface factor f(x) for given surface contact angles. Panel a) shows convex nucleating surfaces and panel b) shows concave nucleating surfaces.

Both *K* and *x* are undefinable values in this experimental work. Selecting a value of *x* = 1 and assuming *K* as a constant, determination of *J*(263K) via Equation (2.9) gives the results presented in Figure 6.11.

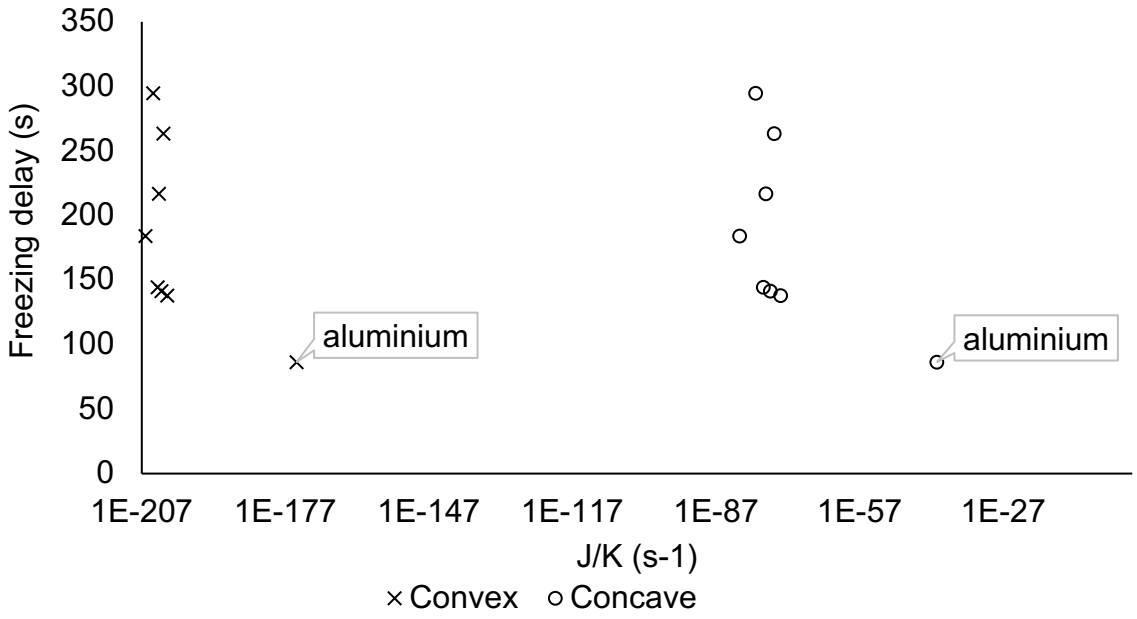

Figure 6.11 – Plot of nucleation rate versus freezing delay of surfaces, for x = 1 on both concave and convex nucleation sites.

The results show no strong correlation between the freezing delay and the nucleation rate for the coated surfaces. As expected, the aluminium has a faster predicted nucleation rate, which suggests that for large differences in θ there is a link between surface chemistry and nucleation rate. But across the chemically similar coated surfaces there is negligible difference in the predicted nucleation rate. Any differences in freezing delay must be controlled by other factors.

The differences in freezing delay that do exist across the coated surfaces are admittedly very small. The probabilistic behaviour of nucleation could be one source of these differences, as might the micro- and nano-scale terms which could not be defined in this system: K and R.

An additional consideration is the time required for the droplet to supercool and for growth to happen. The next section will calculate the time for ice growth on each of the surfaces.

6.5.2. Ice growth

As discussed in Chapter 2, Ice growth time, t_{growth}, can be determined via Equation (2.19) (Irajizad et al., 2019b):

$$t_{growth} = \frac{\rho_I H}{\Delta T} l \left(\frac{2d_0 - d}{2k_I} + \frac{d_s}{k_s} \right) \quad (2.19)$$

This assumes conductive heat transfer greatly exceeds convective heat transfer, which is a fair assumption in this case as there was little airflow over the droplet. Convection-dominant heat transfer would also likely form a shell of ice that grew inwards, rather than an interface that grew from the bottom up, as was observed visually. Equation (2.19) assumes quasi-steady state heat transfer based on fast thermal diffusion through the ice compared to the time scale for growth (Irajizad et al., 2019b).

Data used for this calculation is provided in Table 6.2 below, with references given where applicable. The results of the analysis are presented in Figure 6.12.

Table 6.2 – Material properties for ice growth

Property	Value	Ref.
l_0	0.002 m	
k_l	2.32 W/mK	(Petrenko and Whitworth, 1999)
ΔT	10 K	
ρ_l	918 kg/m^3	(Bader, 1964)
H	334,000 J/kg	(Legates, 2005)

The results in Figure 6.12 show similar time scales across the projected growth time and the measured freezing delay times. There is little difference in projected ice growth times for the different coating surfaces, and a drop in time for the aluminium. The freezing delays of the coating surfaces show greater variance than the projected growth time. However, freezing delay also includes the cooling and nucleation time, so small differences in each step may add together and account for the greater variance in freezing delay.

Additionally, the freezing delay should be longer than the growth time. The nucleation itself occurs in fractions of a second, but the cooling is in the order of minutes. So the freezing delay time should be greater than the projected growth time, which is only the

case for three of the coatings. Possible reasons for this are inaccurate determination of the thermal conductivities, or over-simplification in the assumptions made.

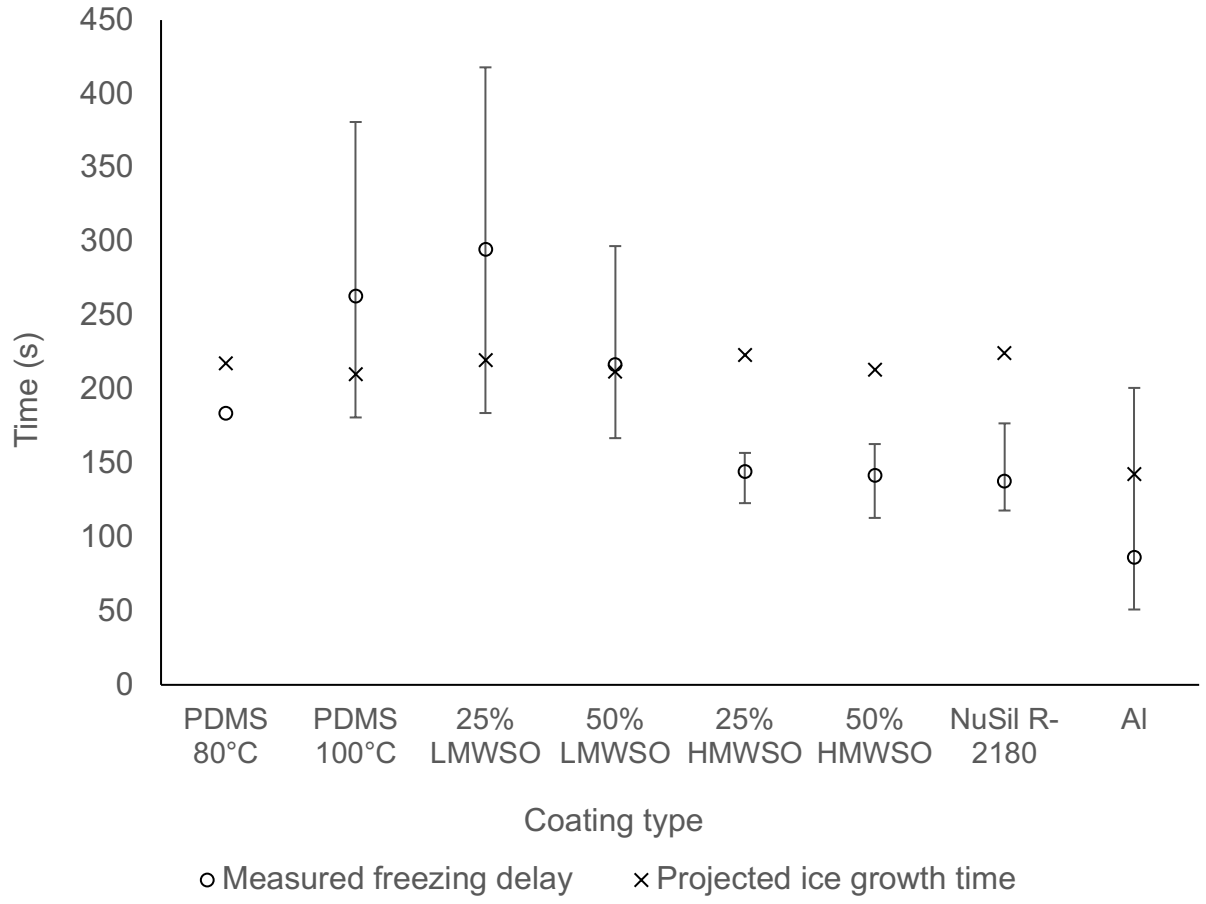

Figure 6.12 – Projected growth times and pre-adhesion freezing delay times for the surfaces.

The primary finding from these results is that the small differences observed in the freezing delay between the coated surfaces cannot solely be attributed to differences in predicted growth time. The results do predict an increase in growth time in the coated surfaces compared to the aluminium, which likely contributes to the difference in better freezing delay in the coated surfaces.

6.6. Commentary on application to real icing scenarios

There is much discussion about the suitability of freezing delay tests like this in reflecting real icing scenarios. The simplifications of the methodology used here are listed below:

- Neglect of icing via frost formation from atmospheric water vapour
- Use of distilled water
- Low velocity droplet impact

- Use of warm (not supercooled) water

The practicalities of simulating real environmental icing conditions are very complex. Some studies attempt improvements using small and large-scale wind tunnels. This can allow for higher velocity droplet impact and supercooled water. In some cases, careful attenuation of air humidity can mimic natural frosting processes.

While it is true that the methodology used here is a simplification of real icing environments, the data is still useful in the broader context of a comparison between un-coated (aluminium) and coated surfaces. We can see that the improvement in the heat transfer characteristics of the system should provide an improvement in the freezing delay of the system. Though this improvement may be lessened with alteration of the test conditions to be more realistic, the trends are likely to remain true from a fundamental perspective.

Though there has been work on replicating environmental icing conditions, there is enormous variability in the precise conditions of different scenarios. The icing processes that occur during aerospace flight differ greatly from frost formation on a car window or sea-ice on marine infrastructure. Even within a specific scenario, the geographic location and daily weather conditions can impact the particulars of the ice formation. It can be argued that measuring the freezing delay in this ‘perfect/unreal’ situation is equally as important as replicating a given icing scenario. This allows us to generate replicable and comparable results across research groups and provides a first screening of the resistance to ice formation of a surface. Subsequent testing in a wind tunnel, for example, would then provide additional information on specific surfaces for high level comparison and modelling.

6.7. Conclusion

There was not a significant difference in the freezing delay of the different coating types. However, all coatings showed better freezing delay than aluminium. There was a minimum improvement in freezing delay of 51 s (59%) pre-adhesion testing and 17 s (20%) post adhesion testing (both NuSil R-2180) compared to aluminium with 87 s. The best coating pre-adhesion was 25% LMWSO with a total freezing delay of 295 s (240% increase). The best coating post-adhesion was 50% HMWSO with total freezing delay of 193 s (122% increase). After adhesion testing, freezing delay

generally fell across the coating types. Indefinite nucleation delay was more frequent on all of the coatings compared to aluminium, pre-adhesion.

All the coatings studied here would be an improvement on aluminium in reducing ice formation. The coatings reduce the requirement for active de-icing as they can better delay nucleation and increase the freezing delay time. This would decrease the costs, materials and labour associated with de-icing. The addition of oil has little effect on this ability. The coatings will wear over time, particularly the less durable oil-infused coatings. This will lead to a loss in performance. However, even with wear, their freezing delay remains better than aluminium. The application of these coatings remains beneficial despite performance loss from wear susceptibility.

The findings are generally in agreement with those from other studies. There is some scatter, which is likely due to a combination of variation in experimental parameters, as well as the naturally random processes that govern ice nucleation. A semi-quantitative comparison of the findings against analytical expressions for nucleation rates and growth times confirmed that the very small differences in chemistry of the coatings were insufficient to cause the variation observed in the coatings' freezing delay. Instead, the variation is likely a result of undefined micro- and nano-scale terms, as well as system stochasticity. On the other hand, the differences across very chemically different surfaces (bare aluminium versus coated) were captured in the experimental and numerical analysis.

7. Effect of Deliberate Damage

Summary

The effect of deliberate damage on icephobicity is investigated to examine the belief that elastomers are too soft to sustain good icephobicity over time. Specimens are fabricated and cut with a scalpel or abraded with grit paper. Surface characterisation shows morphological changes in the coatings from damage and de-icing on the surfaces, as well as changes in wetting. A newly developed cryo-FIB/SEM method shows a mixture of Wenzel and Cassie-Baxter wetting at the ice-coating (abraded) interface, depending on the angle of the opening. There is mixed evidence for the penetration of ice into the scalpel cut.

Ultimately, moderate abrasive damage to the surfaces does not overwhelmingly worsen the ice adhesion strength or average freezing delay but will increase the nucleation rate of ice on a surface. Some damage can actually lower the ice adhesion strength, possibly due to Cassie-Baxter wetting. However, severe damage to the surface, such as large gouges or cuts, can accelerate deterioration and lead to loss of icephobicity, particularly on the softest (50% HMWSO) coating. Recoating is an effective method of returning even severely damaged surfaces to their initial icephobicity, in essence repairing them. Elastomers remain a promising anti-icing solution.

7.1. Introduction

One of the most common concerns about elastomer coatings for anti-icing use is their durability. The elastomers used in this study, and particularly the oil-infused elastomers, are soft and weak, leading to poor damage-resistance. It has been suggested that damage, from de-icing wear or external impacts, may diminish icephobicity and make elastomer coatings no longer effective anti-icing solutions (Zhuo et al., 2019, Kreder et al., 2016).

The results in Chapter 5 indicate damage from the de-icing cycles was minimal and the ice adhesion did not increase drastically, which agrees with other reports (Beemer et al., 2016, Irajizad et al., 2019a). Nor was there a large difference in the freezing delay as a result of the de-icing cycles. From this, the de-icing process was shown to be minimally damaging to the coatings, and not significantly detrimental to the icephobicity. There were some high outlier data in the ice adhesion results of the non-oil infused coatings, which saw instances of severe increases in ice adhesion strength as testing progressed. However, when combined with the surface characterisation, it was determined this was not a solely morphologically dependent occurrence.

There is some evidence in the literature that significant surface damage does increase the ice adhesion strength of the coatings (Golovin et al., 2016, Ibáñez-Ibáñez et al., 2022). To investigate this possibility, the icephobicity of specimens with deliberate damage was investigated. Similar work has been carried out in other studies, with an emphasis on the impact on ice adhesion strength and neglecting freezing delay. Though there are multiple methods of imparting damage on a surface, the most common method in the literature is abrasion. In this study two methods are used: abrasion with grit paper, and cutting with a scalpel. The effect of administering a more defined type of damage (scalpel cut) has not been investigated previously and allows for more easily measurable morphological changes. This may provide a clearer image of the effect of damage.

After damaging the surfaces and performing characterisation and icephobicity tests, the specimens were recoated by spray coating. This was to determine whether any performance degradation caused by damage to the surface could be recovered by repairing the coating. If the coatings are repairable, it could mitigate the issue of their perceived poor durability. Additionally, a method for imaging the ice-coating interface

was developed with the use of cryo-FIB/SEM, in the aim of assessing the interfacial contact.

A diagrammatic timeline showing the testing stages is provided in Figure 7.1.

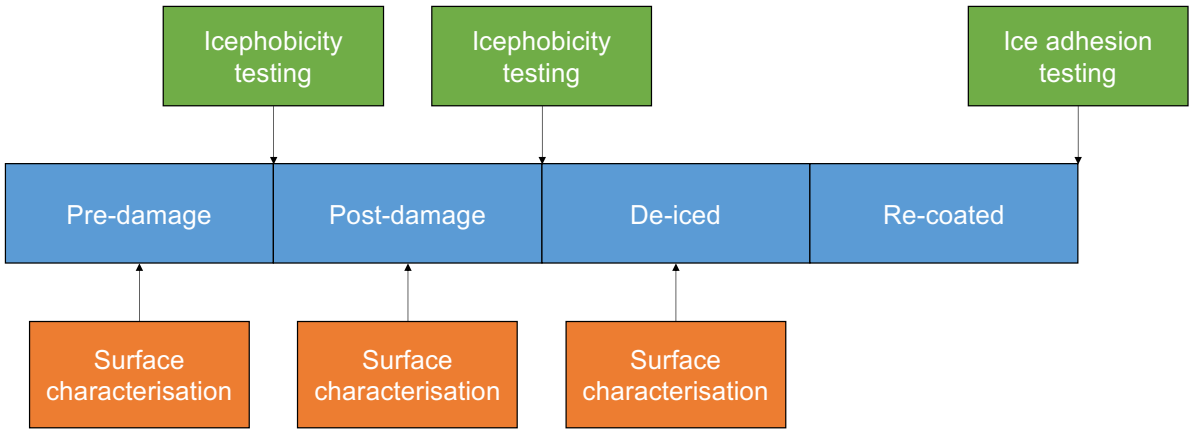

Figure 7.1 – Timeline of testing. Specimen conditions are in blue; occurrences of icephobicity testing and surface characterisation are denoted in green and orange, respectively.

7.2. Experimental method

7.2.1. Specimen preparation

The specimens used for damage testing were fabricated by the same methods as the undamaged icephobicity specimens. Aluminium substrates were prepared with coatings measuring 20 mm x 20 mm and thickness of 200 μm ± 11%. The elastomers were prepared as described in Chapter 3. Four specimens of each coating type were prepared. Two of the specimens were cut with a scalpel along the length of the specimen, and two of the specimens were manually abraded with 400-grit paper. Images of example specimens are provided in Figure 7.2.

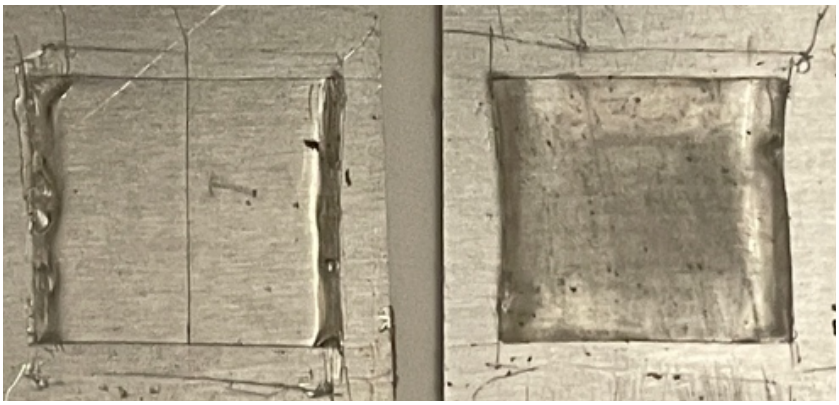

Figure 7.2 – Damaged icephobicity specimens, showing a specimen cut with a scalpel, lengthwise, on the left and a specimen abraded with grit paper on the right.

7.2.2. Surface characterisation

The damaged specimens were characterised using the same methods as the original undamaged specimens, measuring contact angle, thickness and roughness. Images were collected via optical microscopy, room temperature SEM and cryo-FIB/SEM of the damaged surfaces and ice-coating interface. Details of the characterisation methods are provided briefly below but are described in greater detail in Chapter 4. Characterisations were performed on the surfaces pre-damage, post-damage and after the second set of de-icing tests (de-iced).

7.2.2.1. Thickness

A Mitutoyo SJ-410 stylus profilometer was used to measure the thickness. Five evenly-spaced profile traces were performed along the length of each specimen, starting and ending on the aluminium substrate. The average thickness was determined from the 10 traces across the two specimens for each damage type.

7.2.2.2. Contact angle

Static water contact angles were measured by placing a 0.05 ml droplet of deionised water on the surface. A picture of the droplet was taken with a Canon 6D DSLR. Three droplets were placed, one at a time, on a specimen and a picture was taken of each droplet. Photos were taken of both specimens of each damage and coating type. These six photos were then analysed using the software ImageJ to calculate the average contact angle.

7.2.2.3. Roughness

The roughness was also measured using the Mitutoyo SJ-410 stylus profilometer. 10 evenly spaced traces were performed on each specimen, 5 along the length and 5

along the width. Arithmetic average roughness, R_a, was calculated by the profilometer. The roughness of a specimen type was the average of 20 traces. The accuracy of stylus profilometry for measuring roughness of soft coatings is discussed in Chapter 4 but has been shown to be able to detect moderate-to-severe surface damage.

7.2.2.4. Optical microscopy and room temperature SEM

Room temperature SEM and optical microscopy were used for visualising the surfaces. A Zeiss Axioscope 2 was used for optical microscopy. A Hitachi TM4000 plus was used for SEM imaging. Secondary electron imaging was carried out using a 5 kV accelerating voltage under a moderate vacuum, which allowed the surfaces to be imaged without sputter coating.

Due to the presence of oil on the surface, the 25% HMWSO and 50% HMWSO coatings were not imaged using the SEM, so as not to be disrupted by the vacuum.

7.2.2.5. Cryo-FIB/SEM

Cryo-FIB/SEM imaging was used to image the ice-coating interface. The significance of damage creating asperities on the coatings is that droplets on the surface can either be in Cassie-Baxter or Wenzel wetting states, as described in Chapter 2. There has previously been no direct evidence for either case. Performing cryo-FIB/SEM allows for direct observation. The method developed for imaging the interface is described here.

Steel SEM stubs with diameter 10 mm and thickness 8 mm were coated with PDMS 80°C, using the procedure described in Chapter 3. Two specimens were made of each damage type. Photographs of the specimens are presented in Figure 7.3.

Figure 7.3 – Cryo-FIB/SEM specimens. All specimens are PDMS 80°C. Specimens 1 and 3 are cut with a scalpel, and specimen 4 was abraded. Specimens 3 and 4 have been platinum coated and imaged.

Small droplets of deionised water were deposited on the surface of the specimens with a syringe. The droplets were left to freeze in the cold laboratory for 1 hour at −10°C. Details of the cold laboratory environment can be found in Chapter 5. The specimens were placed in a stub holder which was transferred to a Taylor Wharton CX100 cryo-storage vessel for transport to the cryo-FIB/SEM facility. Initial freezing was carried out at −10°C to ensure the ice phase and morphology were consistent with the icephobicity testing, and not formed by fast freezing in liquid nitrogen.

A Zeiss Crossbeam 550 was used for imaging. Once removed from the cryo-storage vessel, the specimens were mounted into a shuttle while under a liquid nitrogen reservoir. The shuttle and specimen were plunged into nitrogen slush and then into the antechamber of the cryo-FIB/SEM chamber. The specimen was put under vacuum and sputter coated with platinum before being transferred into the SEM chamber.

Images of the droplet on the surface were collected before the specimens were coated with a second layer of platinum using a gas injection system. This second layer was approximately 1 μm thick and was applied to prevent the surface from charging and deflecting the ion beam during FIB milling. Sections of the droplet-coating interface were then exposed by milling. The FIB was comprised of gallium ions, with a voltage of 30 kV and a current of 15 nA. This is similar to other research that has imaged ice interfaces (Rykaczewski et al., 2012, Rykaczewski et al., 2013). 30 successive slices of 1 μm thickness were milled and imaged, to view any changes along the interface.

Both secondary electrons and back-scattered electrons were used to image the interface, and the scanning beam had a voltage of 1.2 kV and a current of 100 pA.

7.2.3. Ice adhesion

The ice adhesion test method is explained in full in Chapter 5. It is described briefly here.

Testing was performed in a cold laboratory environment at −10°C, with a relative humidity of 80%. A push test method was used in which acrylic cylindrical moulds with 10 mm internal diameter, wall thickness of 1 mm and height of 25 mm were placed on coated aluminium substrates. The moulds were filled with 1 ml of deionised water, which was left to freeze in situ overnight. The following day the specimens were bolted to a ForceBoard™. A probe arm moving at a constant speed of 5 mm/s toward the mould, parallel to the coating surface, detached the ice cylinders. In the case of the

scalpel cut specimens, the specimens were oriented, so the cut was perpendicular to the direction of probe movement. Force-displacement curves were generated and the peak force converted to adhesion strength, σ_A, via the equation:

$$\sigma_A = \frac{peak\ detachment\ force\ (N)}{interfacial\ contact\ area\ (m^2)} \tag{5.1}$$

7.2.4. Freezing delay

The freezing delay test method is explained in full in Chapter 5. It is described briefly here.

A 0.05 ml droplet of deionised water at 8°C was placed on the specimen surface and left to freeze in the cold laboratory at −10°C. Videos of the process were recorded using a Canon 6D DSLR, and the time between deposition and droplet freezing was measured. For the scalpel cut specimens the droplet was placed on top of the cut.

7.3. Results

7.3.1. Surface characterisation

7.3.1.1. Thickness

The thicknesses of the specimens in Figure 7.4 were 200 µm ± 25%. This is in keeping with the original icephobicity test specimens. The data presented in Figure 7.4 is the average across the four specimens for each coating – two of each damage type. There is more scatter in the thickness of the oil-infused coatings, and particularly the HMWSO coatings. This is a result of the reduction in viscosity of the pre-polymer mixture by the addition of oil, which lead to leaking from the moulds during curing. In the case of the HMWSO specimens there is also some excess oil that is not trapped in the polymer network as it cures. Some of this is present as surface oil, but some drains away after removal from the mould. The non-oil infused coatings, which have much higher viscosity and no free oil, have very small variance in the specimen thicknesses.

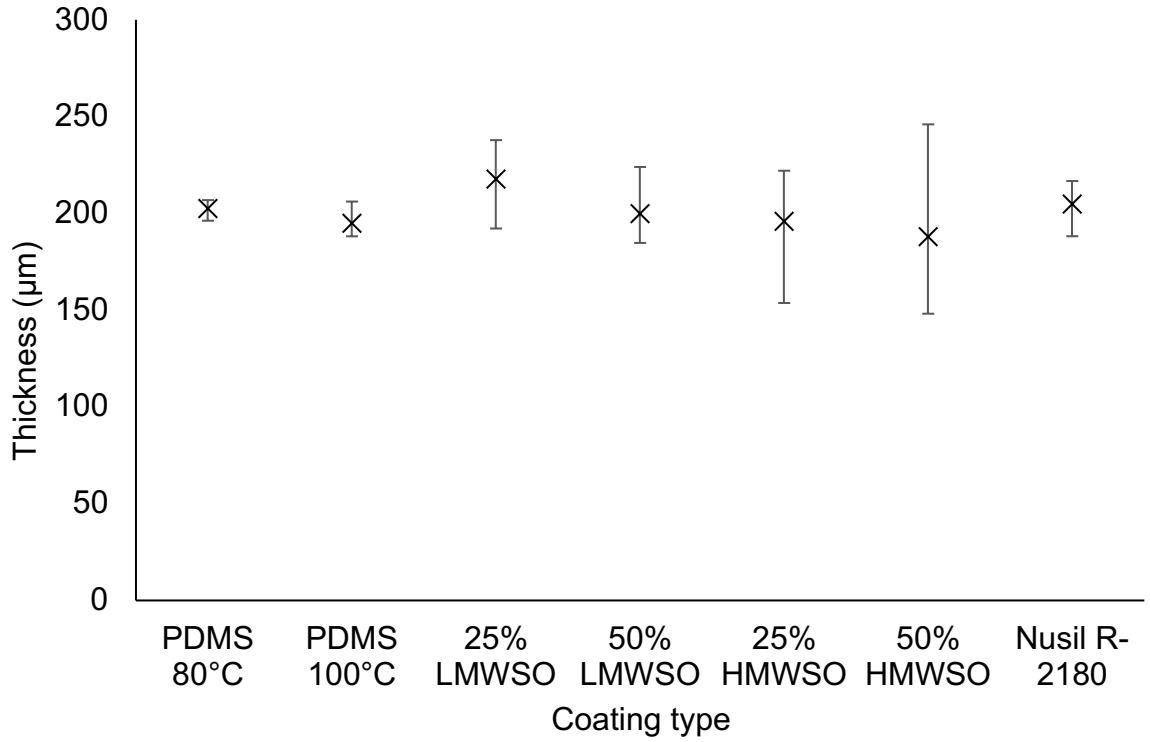

Figure 7.4 – Thickness of the coatings. Measurements were performed on the specimens before damage was applied. Averages of the four specimens of each coating type are presented, with range bars.

7.3.1.2. Contact angle

The static water contact angles for the damaged coatings are presented in Figure 7.5. All the specimens at the initial, pre-damage condition, have similar contact angles, ranging from 100-107°. There is little difference or trend between the coating types. These results mirror the findings in Chapter 4, which is expected as the surfaces should be nearly identical.

However, the specimen behaviour diverges significantly post-damage. There is a notable increase in the post-damage contact angles of the abraded coatings. The specimens now range from 106-117°. These results imply that the damaged surfaces are able to generate Cassie-Baxter wetting. In the de-iced state, there is then further increase in the contact angle to 109-130°, which suggests that as the surfaces get rougher the contact angle will increase. There are no distinct trends across the coating types, but the non-oil infused coatings had slightly higher contact angles than the oil-infused coatings. Example images of the contact angles on a 25% LMWSO abraded specimen at each condition are presented in Figure 7.6.

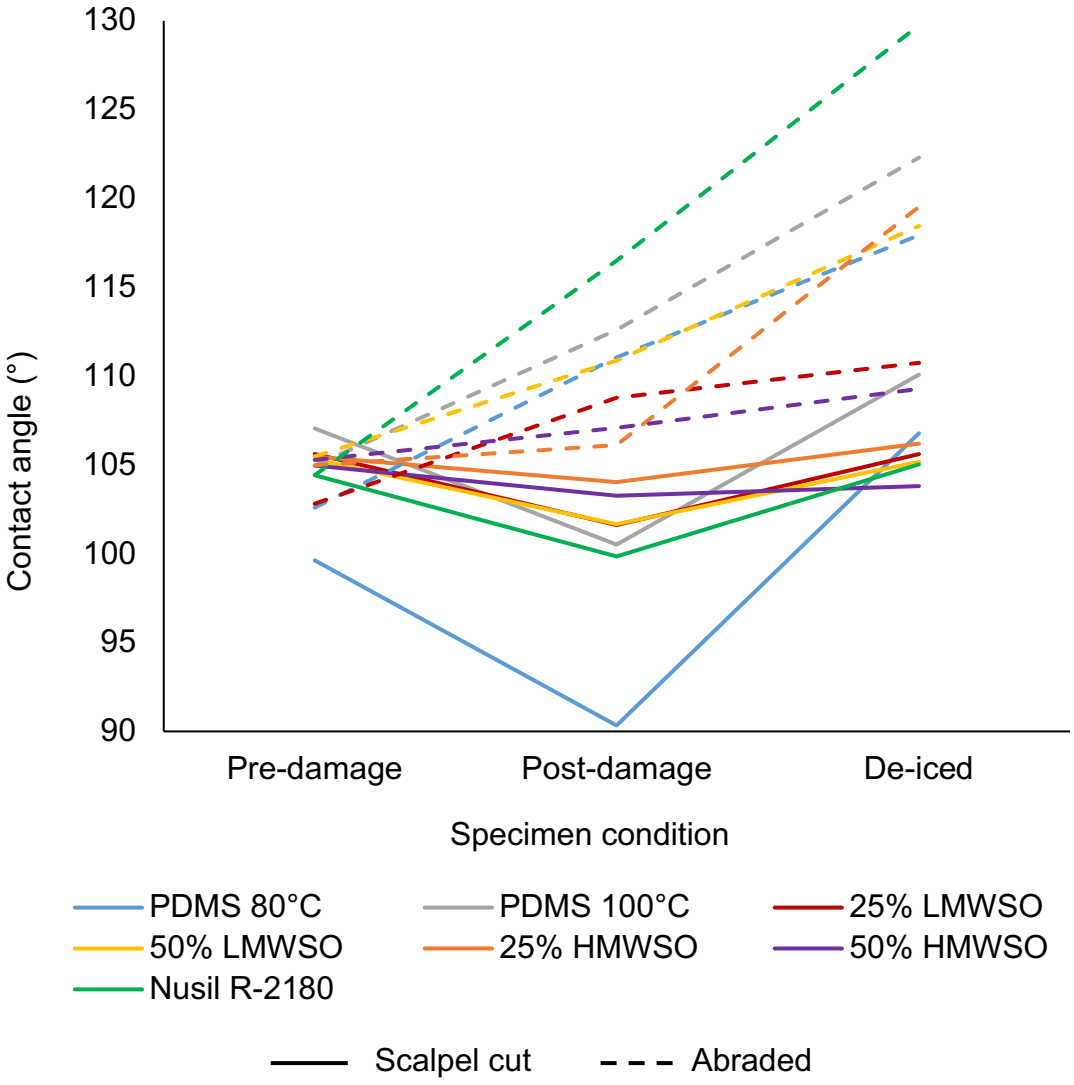

Figure 7.5 – Contact angles of the specimens at three conditions: pre-damage, post-damage and de-iced. Values are an average of the two specimens for each coating/damage type.

The scalpel cut specimens showed very different behaviour to the abraded specimens. All the scalpel cut specimens showed a decrease in contact angle post-damage to 93-104°. This reduction is most notable in the PDMS 80°C specimen, for which images of contact angles at all three conditions are presented in Figure 7.7. It is possible that the decrease in contact angle is a result of contact line pinning where the droplet edge crosses the scalpel cut line, or capillary forces causing the water to penetrate the cut.

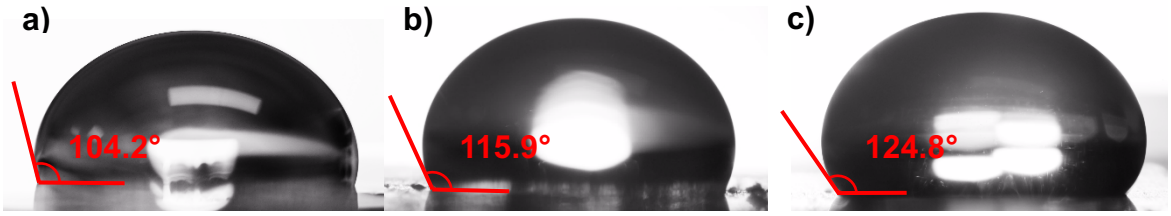

Figure 7.6 – Photos of water droplets on a 25% LMWSO abraded specimen a) pre-damage, b) post-damage and c) de-iced. Contact angles as measured using ImageJ are denoted on each image. There is a distinct increase in the contact angle post-damage and then again after de-icing.

After the icephobicity tests the contact angles largely increase again, returning to values similar to the pre-damage condition at 104-110°. This may be a result of the scalpel line widening during the de-icing cycles, which is discussed in Section 7.3.1.4

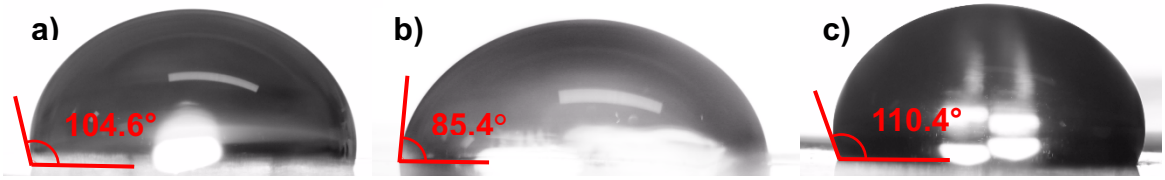

Figure 7.7 – Photos of water droplets on a PDMS 80°C scalpel cut specimen a) pre-damage, b) post-damage and c) after de-icing. Contact angles as measured using ImageJ are denoted on each image. There is a distinct decrease in the contact angle post-damage, followed by an increase again after de-icing.

7.3.1.3. Roughness

As discussed in Chapter 4, stylus profilometry is not suitable for high accuracy roughness measurements, due to the softness of the coatings and the presence of surface oil on the HMWSO specimens. However, it was able to detect large changes in surface roughness in Chapter 4 and has been used in other studies for micron-scale measurements (Gevaux et al., 2018, Lucas et al., 2008, Dahlberg et al., 2018, Trantidou et al., 2017). The results of roughness measurements on the damaged specimens show the profilometer was able to detect the changes in the surface morphology caused by the damage. The R_a values for the coatings are presented in Figure 7.8.

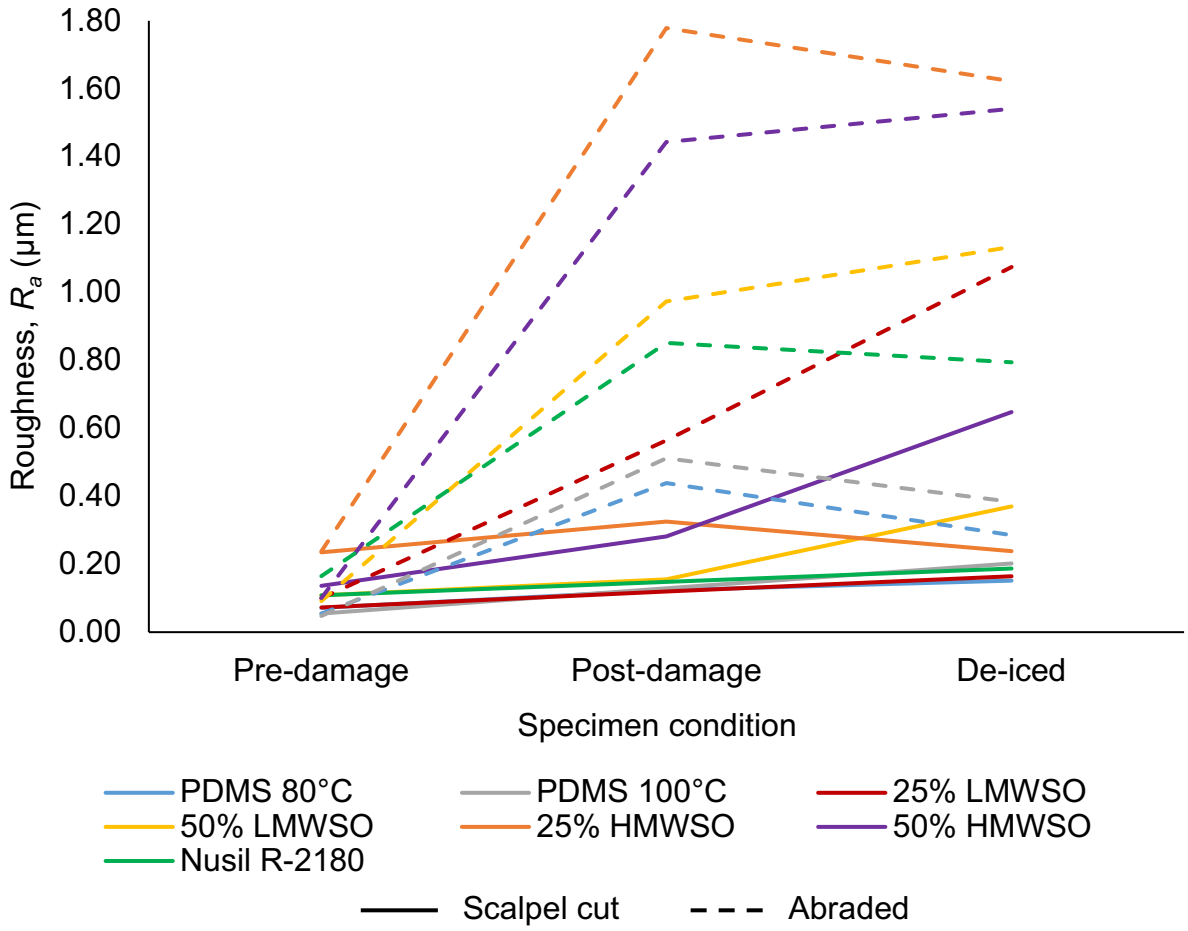

Figure 7.8 – Average roughness (R_a), measured on the specimens at three conditions: pre-damage, post-damage and de-iced. Values are an average of the two specimens for each coating/damage type.

The abraded specimens show marked increase in measured roughness post-damage. The findings generally reflect the softness – the softer, oil-infused coatings show greater increase in measured roughness than the non-oil infused coatings. This is to be expected, as the softer coatings are less damage resistant. There is not a significant trend after the de-icing. Some of the coatings increase and some decrease. Most of the changes are small, so it is unlikely the profilometer is able to accurately resolve these differences. De-icing can cause cohesive damage in the coatings, as demonstrated in the SEM images in Chapter 4, which showed gouging and abrasive wear damage. However, it is difficult to know whether any cohesive damage on an already abraded surface would minimise or exacerbate asperities. This will be examined further in Section 7.3.1.4. Traces of selected specimens at each measurement condition are presented in Figure 7.9.

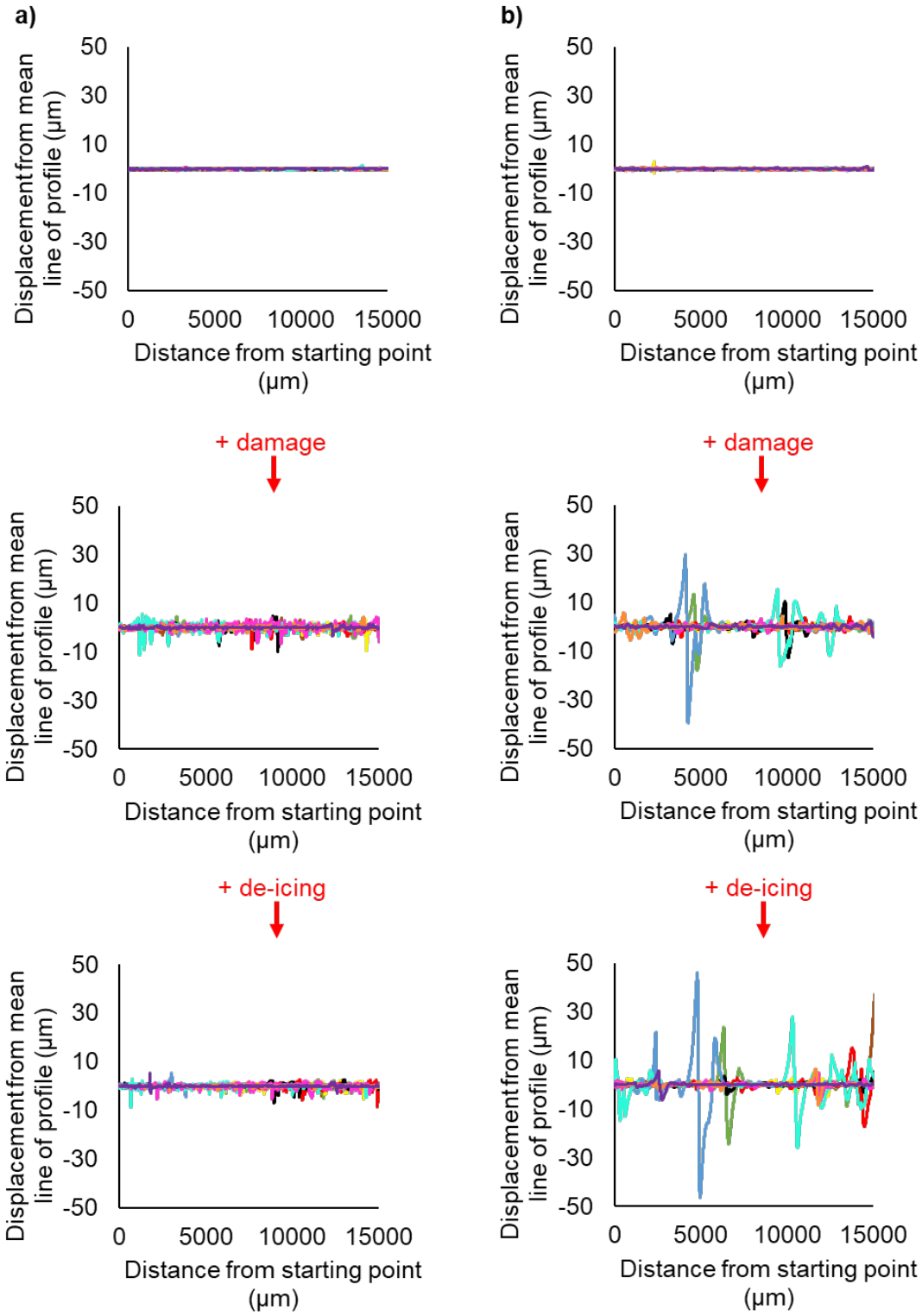

Figure 7.9 – Traces of selected abraded specimens: a) PDMS 80°C and b) 50% LMWSO, at the three measurement states (pre-damage, post-damage and de-iced). The measured roughness increases greatly in both specimens post-damage, though notable more in the softer 50% LMWSO. After de-icing, the PDMS 80°C specimen shows a very small decrease, while the 50% LMWSO increases further. Each plot has 5 lengthwise and 5 width-wise traces.

The increase in measured roughness of the scalpel cut specimens post-damage is considerably less than the abraded specimens as the surface are largely still smooth, with only one deep trench in them. The profilometer is able to detect the trench, and traces to this effect are presented in Figure 7.10. The increase is similar across all the specimens.

After de-icing, most of the specimens see further increase, though the 25% LMWSO specimen decreases. The two softest specimens, the 50% LMWSO and 50% HMWSI specimens, see the greatest increase after de-icing. The increase in roughness is expected as de-icing likely damages the cut, causing the trench to widen, as in Section 7.3.1.4. It should be noted that, as the scalpel cut runs lengthwise along the specimen, it is primarily detected in the width-wise traces.

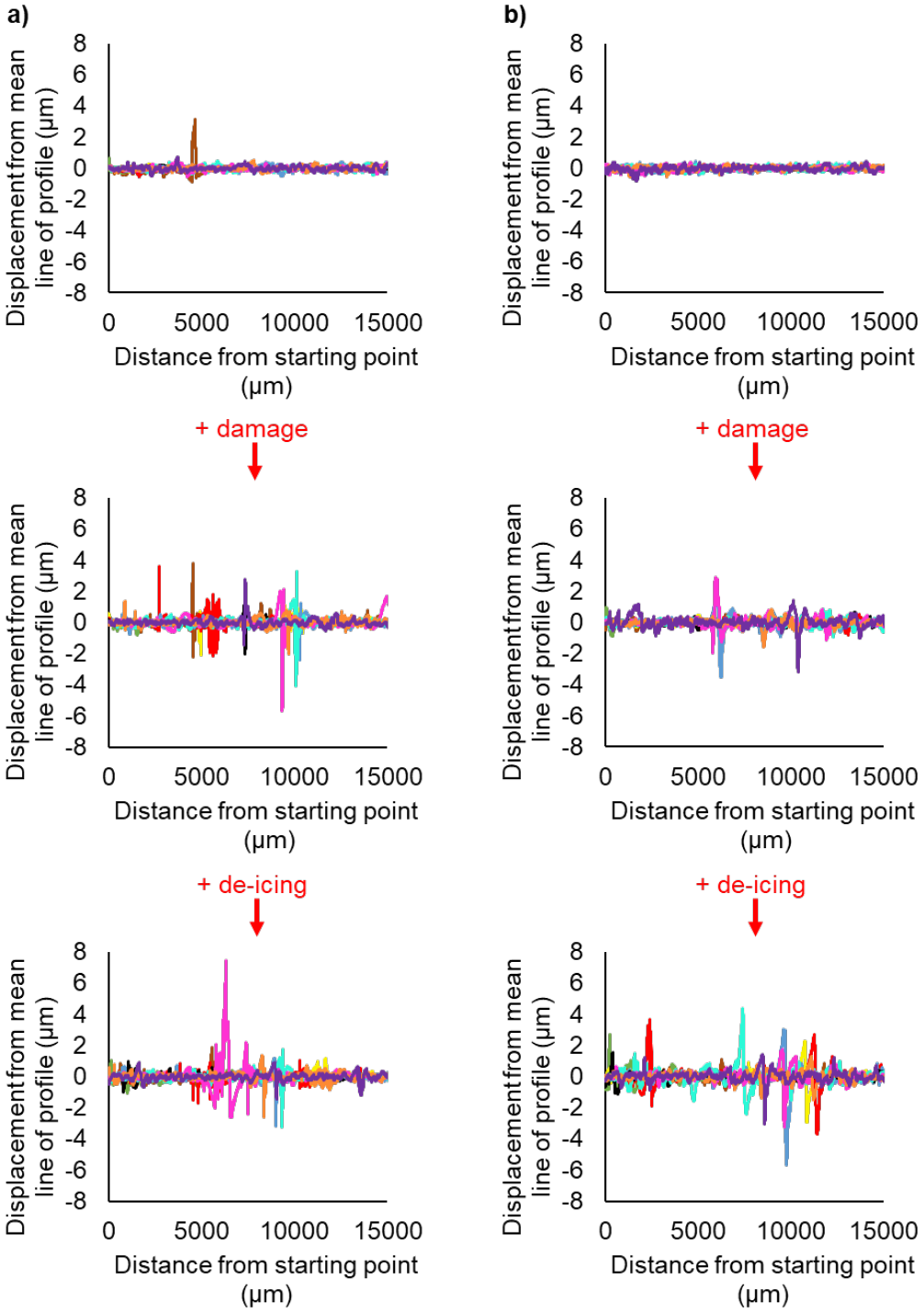

Figure 7.10 – Traces of selected scalpel cut specimens: a) PDMS 80°C and b) 50% LMWSO, at the three measurement states (pre-damage, post-damage and post de-icing). The difference in the y-axis scale from Figure 7.9 should be noted: the degree of damage is considerably less in the scalpel cut specimens. Both specimens show an increase in measured roughness post-damage, with the primary difference being the presence of a few large peaks, which are the trace of the cut. After de-icing, the measured roughness of both specimens sees a small increase. Each plot has 5 lengthwise and 5 width-wise traces.

7.3.1.4. Optical microscopy and room temperature SEM

Optical microscopy and SEM were used to image the surfaces. Images of the specimens pre-damage show similar results to the undamaged specimens in Chapter 4, pre-adhesion. Dust and fibres are the only surface features of note.

Inspection of the surfaces post-damage and after de-icing reveals whether surfaces that are already significantly damaged experience further wear and deterioration at a faster rate. With the abraded specimens this is largely a qualitative assessment of the surface, but for the scalpel cut surfaces it is possible to measure the width of the scalpel cut at the post-damage and de-iced conditions to see if de-icing has caused the gap to widen.

7.3.1.4.1. Scalpel cut specimens

Selected images showing representative findings on the scalpel cut specimens are presented in Figure 7.11, Figure 7.12, and Figure 7.13. Figure 7.11 shows the SEM images of the PDMS 80°C, PDMS 100°C, 25% LMWSO, 50% LMWSO and NuSil R-2180 specimens. Optical microscopy images of the HMWSO specimens are shown in Figure 7.12, with additional images of surface damage from the de-icing on the HMWSO specimens in Figure 7.13.

The SEM imaging in Figure 7.11 shows the scalpel cuts noticeably increase in width after de-icing. There is also clear damage to the specimens, at the edges of the cuts. The damage is similar to that seen in Chapter 4. Crack networks formed in the more brittle (non-oil infused) coatings of PDMS 100°C and NuSil R-2180, in panels (b2) and (e2) respectively. There is a crack in the 25% LMWSO specimen – panel (c2) – but the material is less brittle and the crack has not formed a network, even with one edge pulled out-of-plane. There is minor cohesive damage (from material being removed) in the PDMS 80°C specimen and major cohesive damage on the 50% LMWSO specimen, panels (a2) and (d2) respectively, where pieces of the coating have been ripped out. There is also debris in the cuts in panels (a2) and (e2), though the scale of it suggests it is more likely from the initial scalpel cut than the de-icing. The damage is primarily concentrated on the left edge of the cuts, as this is the rear edge which faced towards the probe, opposite to the direction of detachment.

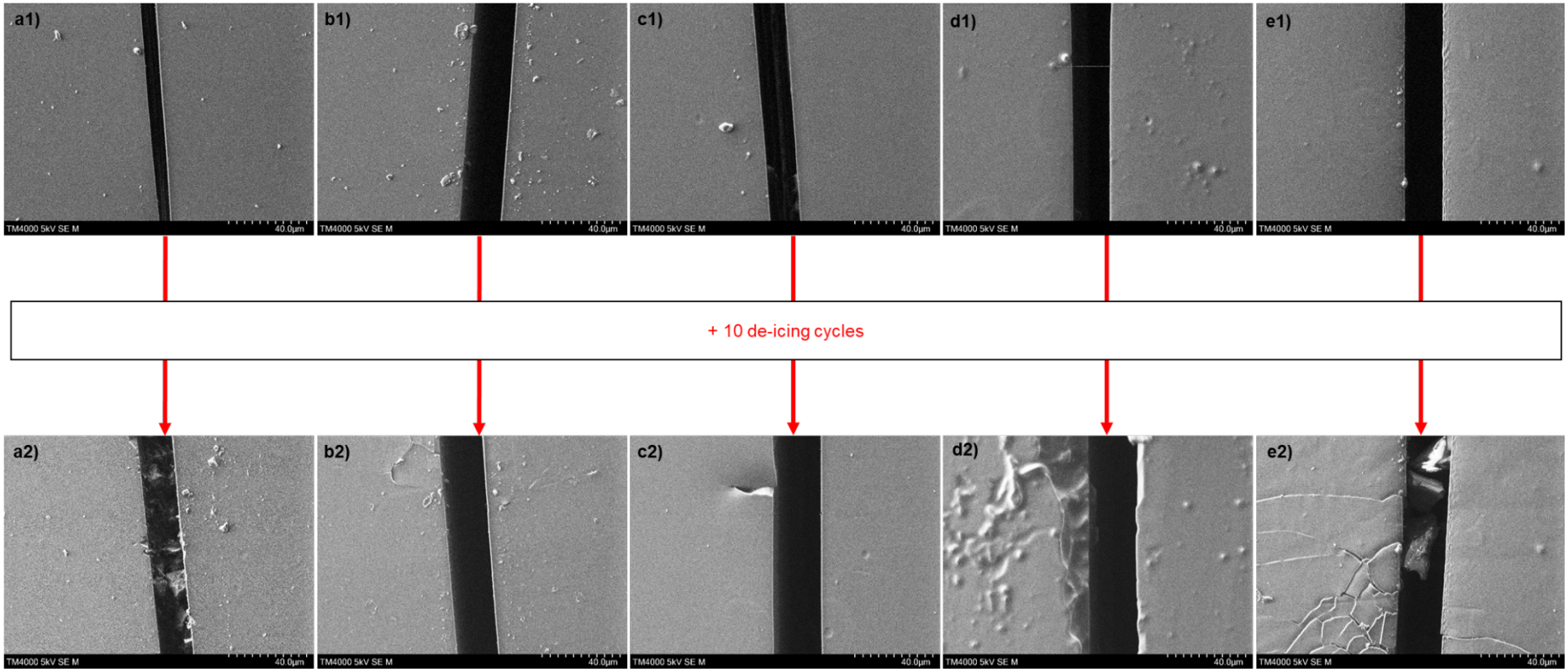

Figure 7.11 – SEM images of scalpel cut specimens a) PDMS 80°C, b) PDMS 100°C, c) 25% LMWSO, d) 50% LMWSO and e) NuSil R-2180, post-damage (1) and after de-icing (2). After de-icing the scalpel cuts are wider on most of the specimens and there is damage at the edges. Damage is greater on the left side, which is the rear edge, facing toward the detaching probe. There is debris in the cuts in panels (a2) and (e2).

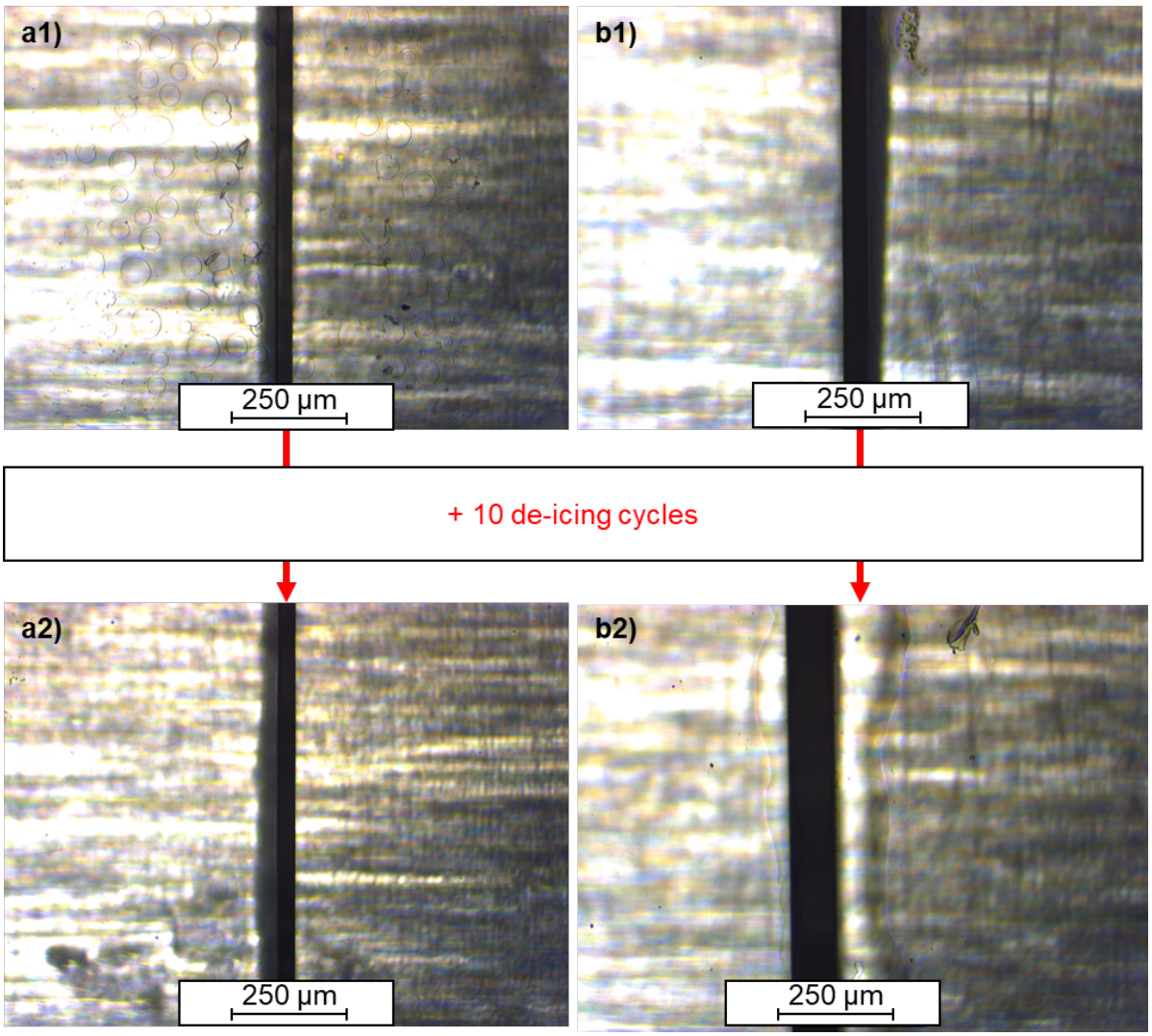

Figure 7.12 – Optical microscopy images of scalpel cut specimens a) 25% HMWSO, b) 50% HMWSO: post-damage (1) and after de-icing (2). After de-icing the scalpel cuts are wider on both specimens.

The images in Figure 7.12 similarly show an increase in the width of the scalpel cuts after de-icing the HMWSO specimens. Damage of the scale seen on the SEM imaging was not visible, but this may have been due to light-scattering and shadows in the images obscuring this detail. However, large scale damage did occur on the 50% HMWSO specimen as a result of the de-icing, and examples of this are presented in Figure 7.13. Large chunks of the coating were ripped off during detachment of the ice. This was mostly along the scalpel cut, and at the rear edge or bisecting the cut. Some of these areas were very large, in the order of millimetres, revealing patches of aluminium below. Therefore, the 50% HMWSO specimen is highly susceptible to further damage once large damage has occurred and may quickly lose icephobicity or be removed entirely.

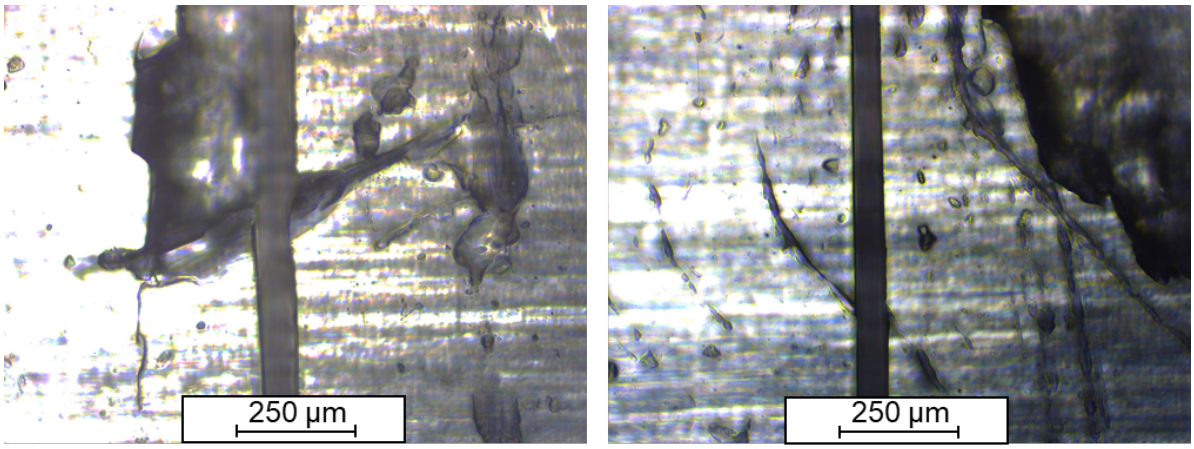

Figure 7.13 – Damage from de-icing specimens of a) 25% HMWSO, b) 50% HMWSO. Large chunks were ripped from the coating. This mostly originated at the scalpel cut and tears in the coating often bisected the cut.

The width of the scalpel cut was measured post-damage and after de-icing, and the results are presented in Figure 7.14. The specimens saw an increase in their width from the de-icing, excluding the PDMS 100°C, which saw no change. Most of the specimens widened by similar magnitudes, about 5-10 µm. The 25% and 50% HMWSO specimens measured the widest cuts both post-damage and after de-icing with the 50% HMWSO widening the most, by 50 µm. This is likely a combination of being weakest, so more easily deformed, and less precision in the measurement of the optical microscopy images than the SEM images. As stated before, the optical microscopy images are affected by light-scattering and shadows obscuring the fine details.

The PDMS 100°C specimen was the only specimen to see no change. The width measured 22 µm both post-damage and after de-icing. Upon inspection of the SEM images, it can be seen that the scalpel cut is at a slight angle into the coating. This will have increased the measured width but may also have reduced the damage experienced by the specimen during ice detachment as the rear edge is obtuse.

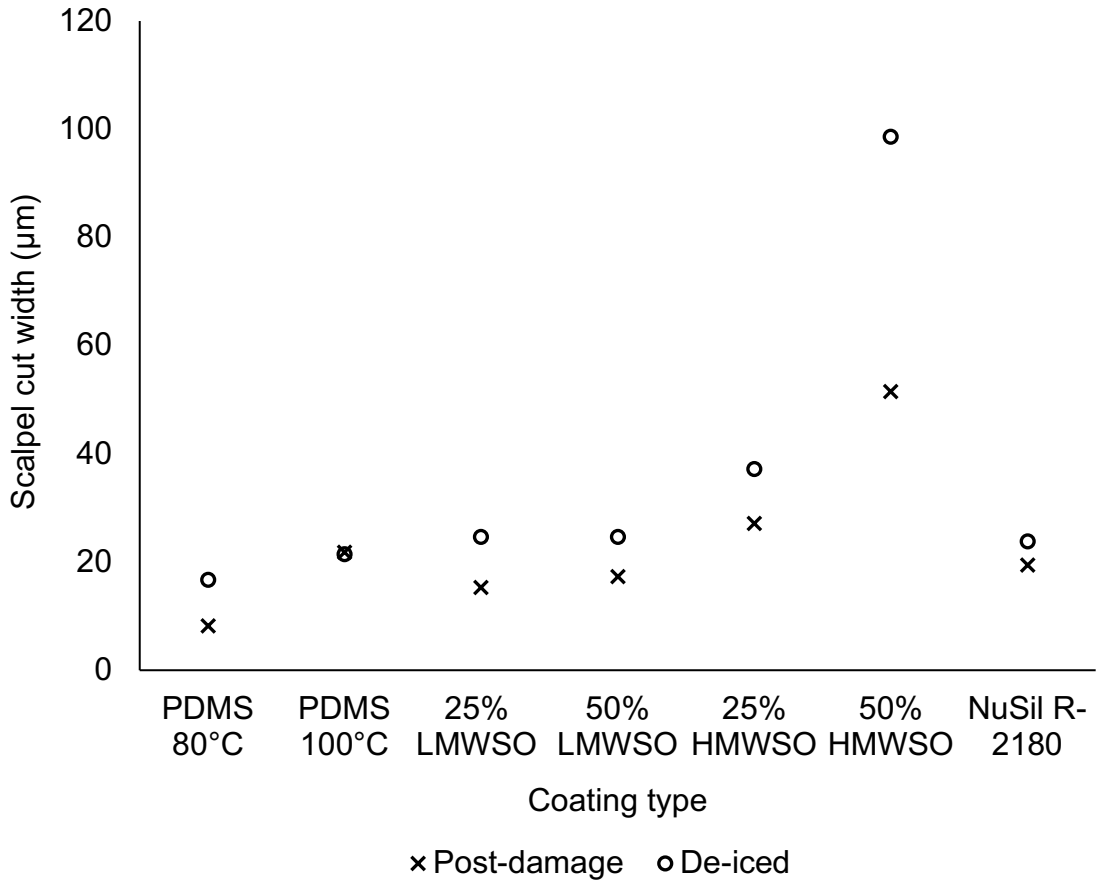

Figure 7.14 – Width of scalpel cuts post-damage and after de-icing for each coating type. The specimens see an increase in the width from de-icing, excluding the PDMS 100°C, which did not change.

7.3.1.4.2. Abraded specimens

Selected images showing representative findings on the abraded specimens are presented in Figure 7.15 and Figure 7.16. Figure 7.15 shows the SEM images of the PDMS 80°C, PDMS 100°C, 25% LMWSO, 50% LMWSO and NuSil R-2180 specimens. Optical microscopy images of the HMWSO specimens are shown in Figure 7.16.

The SEM imaging shows only minimal differences between the specimens post-damage and after de-icing. While efforts were made to image the same area in both instances for better comparison, this proved difficult at higher magnifications. A yellow circle on panels (c1) and (c2) have been added to identify shared features for direct comparison.

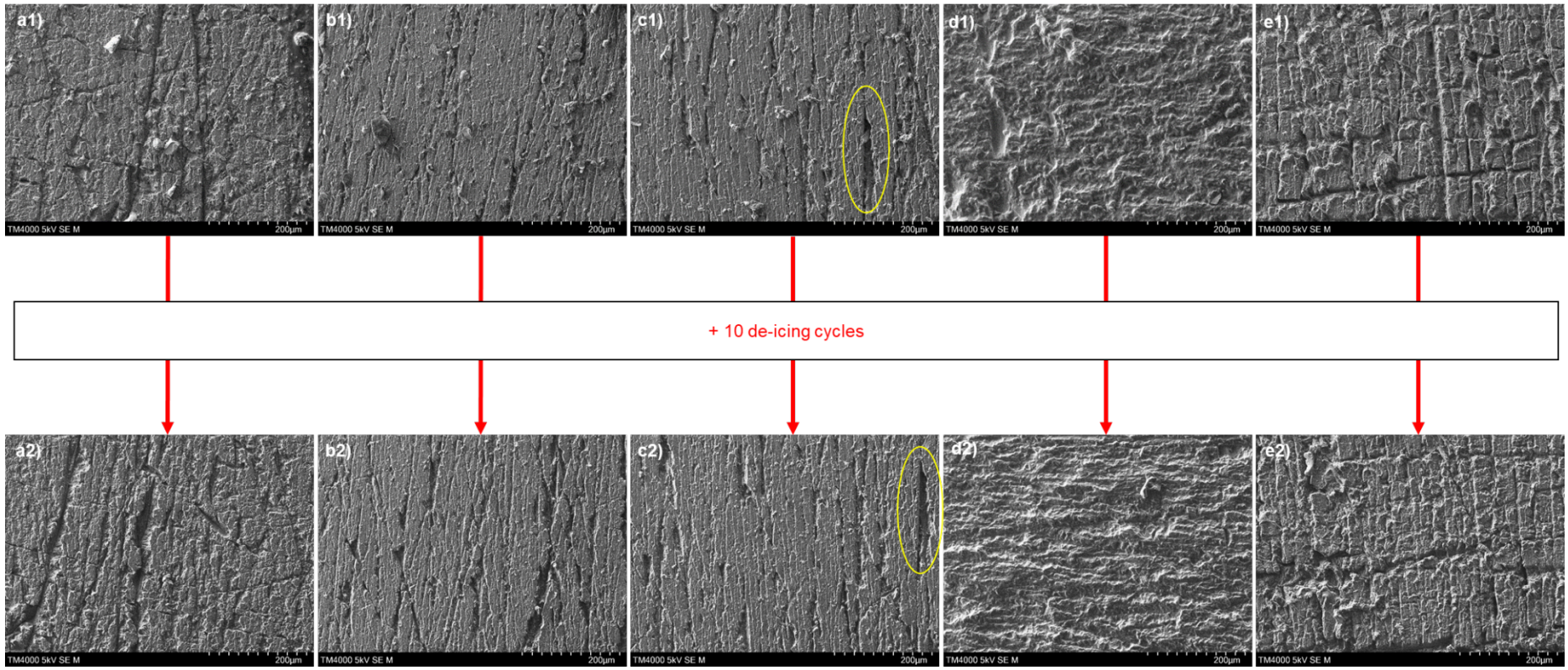

Figure 7.15 – SEM images of abraded specimens a) PDMS 80°C, b) PDMS 100°C, c) 25% LMWSO, d) 50% LMWSO and e) NuSil R-2180: post-damage (1) and after de-icing (2). There is little difference between the specimens post-damage and after de-icing. In most cases the only notable effect is the removal of pieces of debris. The yellow circles on panels (c21) and (c2) indicate the position of a common feature, for direct comparison between specimen conditions.

The only clear difference is the absence of larger pieces of coating debris on the de-iced surfaces. The adhesion and detachment of ice on the specimen surfaces removed the debris. There is no significant increase in the finer roughness of the specimens. There were a handful of instances in which larger gouges made by the grit paper (approximately > 50 μm) were widened, but this was not widespread.

There is a notable difference in the appearance of the 50% LMWSO specimen compared to the other specimens, both post-damage and after de-icing, panels (c1) and (c2) respectively. While the exterior of the other specimens is mostly intact, the top layer of the 50% LMWSO has been completely abraded away. Even accounting for variance from manual abrading, the difference is stark. This is likely a consequence of the coating being significantly softer and weaker than the other specimens, as discussed in Chapter 3.

The optical microscopy images of the HMWSO specimens in Figure 7.16 show similar findings. There is little evidence for the change of finer surface detail, but larger gouges generally increased in size. As with the scalpel cut specimens, there were instances of large-scale damage on the surface of the 50% HMWSO specimen, as a result of its weaker physical properties. A gouge, circled in yellow in panels (b1) and (b2), experienced significant further damage and widening after the de-icing.

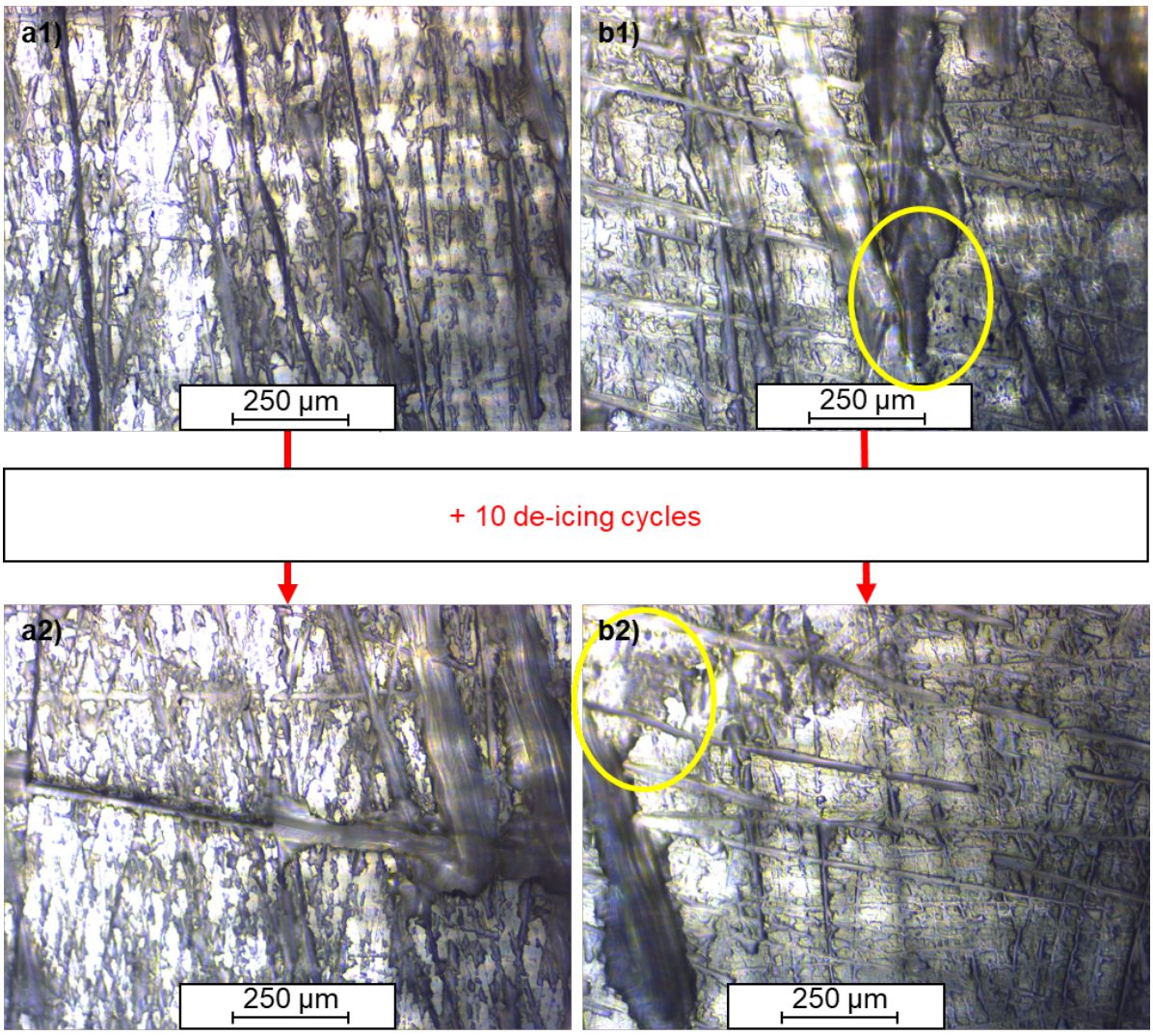

Figure 7.16 – Optical microscopy images of abraded specimens a) 25% HMWSO, b) 50% HMWSO: post-damage (1) and after de-icing (2). There was generally an increase in the size of larger damage features, but no clear change in the finer features. The 50% HMWSO shows evidence for the widening of a gouge – highlighted with yellow circles in the panels (b1) and (b2).

7.3.1.5. Cryo-FIB/SEM

The primary objective of cryo-FIB/SEM was to image the ice-coating interface and observe the contact between the ice and the damaged surface. This may identify wetting states and contact area effects, which can influence the ice adhesion strength and freezing delay.

7.3.1.5.1. Scalpel cut specimens

Images of the exterior and interface of the ice and scalpel cut specimen are presented in Figure 7.17 and Figure 7.18. The exterior image in panel (a) of Figure 7.17 locates the area where the subsequent cross-sections were milled. It also shows the presence of cracks in the droplet. The cryogenic temperature of the chamber means both the

ice and coating will be more brittle than at the temperature used for icephobicity testing (−10°C). The coatings will be well below their glass transition temperature (approximately −120°C (Luo and Mather, 2009, Brounstein et al., 2021, Olima, 2017, Wang et al., 2014a, Lahiff et al., 2006)). The probability of cracking is therefore greater, but the location of the cracks at the edge of the cut suggests the edges act as crack initiators. Panel (b) shows the final mill that was made. In further support of the crack initiating ability of the cut, we can see that the crack identified in panel (a) continues to follow the cut edge along its length. There is another small crack at the opposite edge in Figure 7.18 (depth = 0 μm). Crack initiation has been proposed as a method for lowering ice adhesion strength in other studies (He et al., 2017b, He et al., 2020b), and may contribute to the icephobicity results of the scalpel cut specimens in this work.

Figure 7.18 shows three cross-sections of the interface at 0, 15 and 30 μm depth, measuring from the first cross-section. The total depth of the final cross-section is approximately 50 μm from the exterior of the droplet. In these images, and panel (b) in Figure 7.17, the ice does not seem to penetrate the scalpel cut, but sits above it. However, when comparing the three depths, the ice lowers towards the cut with increasing depth from the exterior.

The hydrophobicity of the coatings suggests it is possible the droplets would resist wetting the coating and penetrating the cut. However, if the trend of the ice lowering towards the cut progresses further inwards, then it is possible the ice does penetrate the cut in the middle of the droplet, but not at the edge. If this is the case, possible explanations include greater hydrostatic pressure overcoming the resistance to wetting in the middle of the droplet, or sublimation at the edges removing ice that had penetrated the cut.

In support of the idea that the ice penetrates the cut deeper into the droplet, visual inspection of the ice surfaces after de-icing tests showed small ridges were present where the ice had sat on top of the scalpel cut. This was primarily noticeable in the later ice adhesion test, when the scalpel cut was wider. It is therefore likely there is a critical width which the ice will penetrate the cut, either by hydrostatic pressure overcoming the surface tension, or expansion of the ice during freezing.

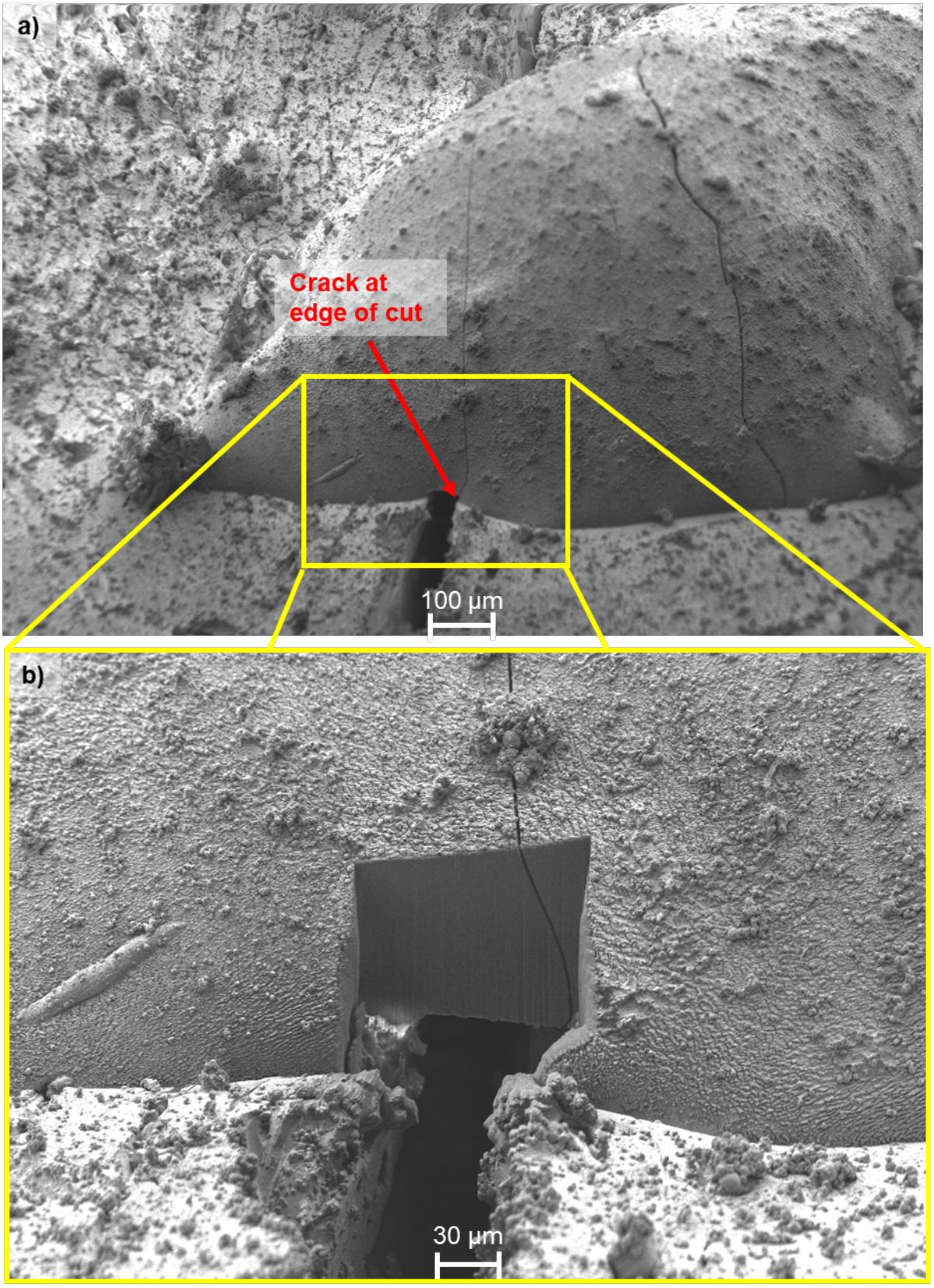

Figure 7.17 – Cryo-FIB/SEM images of a) the exterior and b) final cross-section of the ice-coating interface along a scalpel cut. The cross-section was exposed by FIB milling. A crack in the ice appears to have initiated at the edge of the cut. The ice does not penetrate the cut at this depth from the exterior.

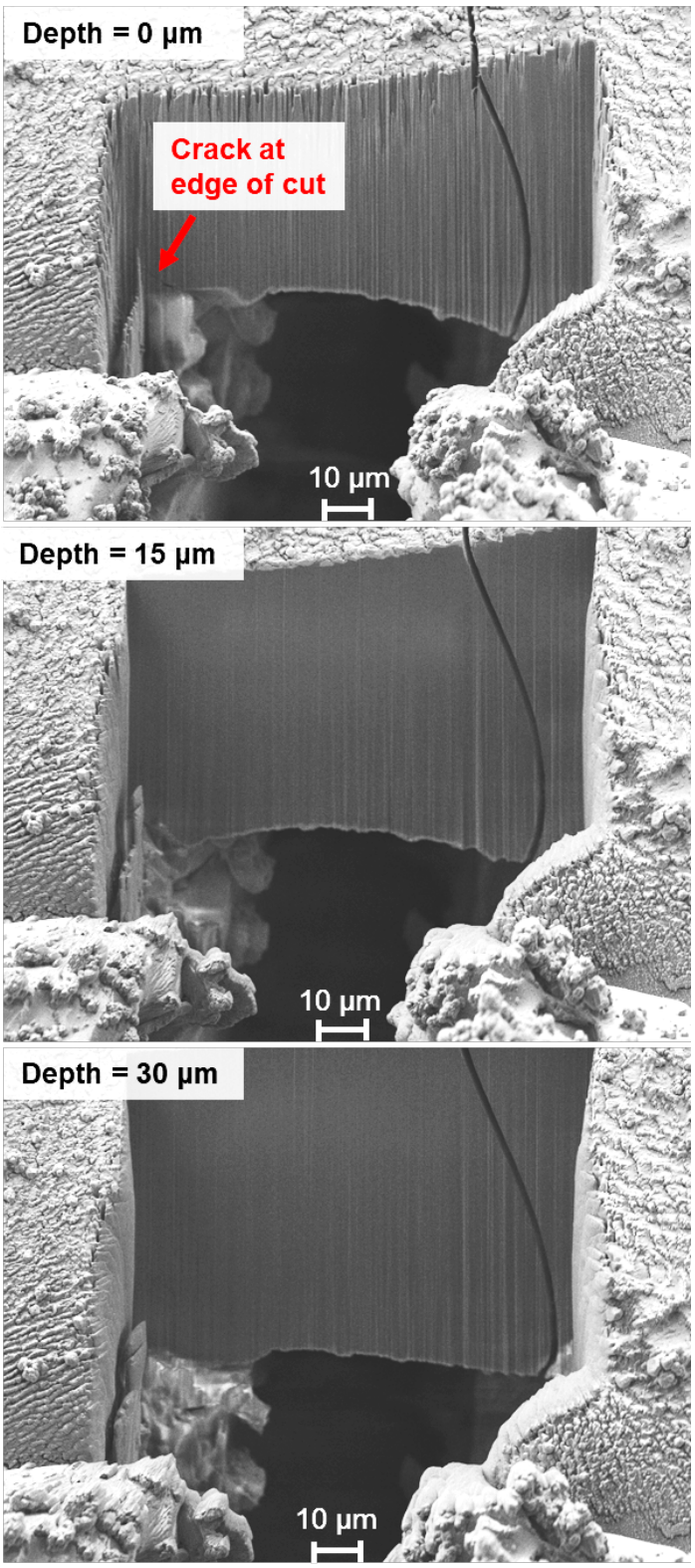

Figure 7.18 – Successive cross-sections of the ice-coating interface milled by a FIB. Images are at depths of 0, 15 and 30 µm from the first cross-section. The total depth of the final mill is approximately 50 µm from the exterior. The ice does not seem to penetrate the scalpel cut but does lower towards the cut as the depth increases.

7.3.1.5.2. Abraded specimens

Images of the exterior and interface of the ice and abraded specimen are presented in Figure 7.19 and Figure 7.20, respectively. The image in panel (a) of Figure 7.19 locates the area where the subsequent cross-sections were imaged, while panel (b) shows the location of the initial FIB mill. From the exterior view, the ice clearly penetrates the small gouges in the coating.

In Figure 7.20, there are three cross-sections of the interface at 0, 17 and 30 μm depth, measuring from the first cross-section. The total depth of the final cross-section is approximately 40 μm from the exterior of the droplet. There are two primary gouges visible in these images. From the exterior views in Figure 7.19 the ice penetrates both. However, the cross-sections show that a few microns into the droplet, the ice does not penetrate the gouge on the right side, but sits above it. At the depths of 17 μm and 30 μm there is also penetration of the coating into ice. These results show a combination of Cassie-Baxter and Wenzel wetting states.

Visual clues suggest the explanation for these mixed regimes is that the angle of the opening of the gouge determines the penetration. If the angle is > 90° the ice will not penetrate but instead sit on top, and penetration will occur if the angle is < 90°, as a result of water's surface tension and the coating's hydrophobicity. This behaviour is exploited in the design of superhydrophobic surfaces and SLIPS, in which re-entrant and double re-entrant geometries pin water droplets and prevent penetration (Liu and Kim, 2014). These images therefore provide direct evidence that abraded PDMS surfaces can show both Wenzel and Cassie-Baxter wetting.

When considering this information with the scalpel cut findings, the penetrated gouges are much narrower and shallower than the cut in Figure 7.18, so it is unlikely its width is the sole reason for the ice not penetrating. If the ice indeed does not penetrate the cut along the entire length of the droplet, then it is likely a combination of contact angle and width.

Like with superhydrophobic surfaces and SLIPS, preventing penetration through the entry angles is limited by the ability of the droplet's surface tension to resist external forces. However, these results show Cassie-Baxter wetting can arise from surface damage, without being superseded by ice expansion into the geometry.

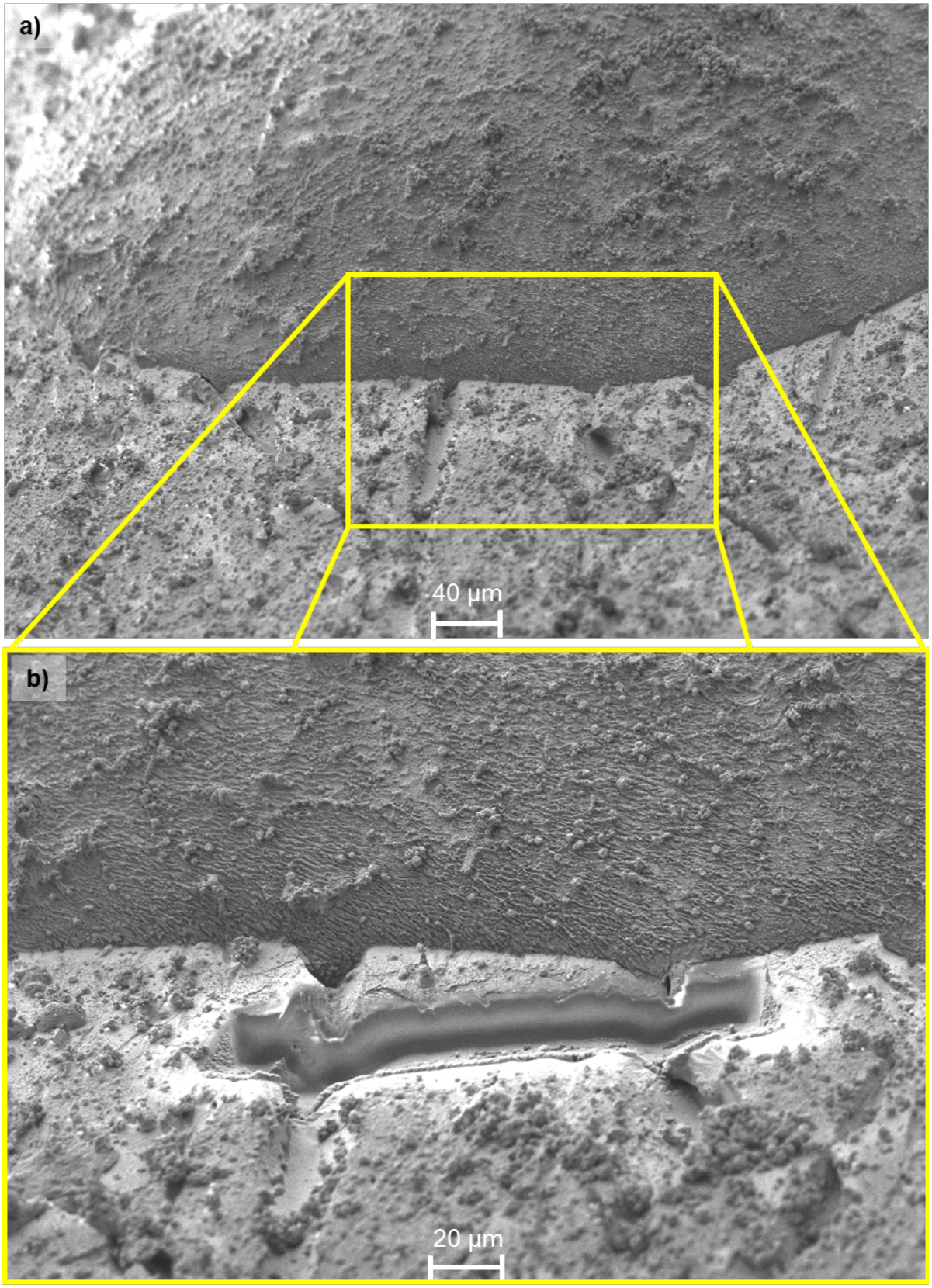

Figure 7.19 – Cryo-FIB/SEM images of a) the exterior of a droplet and b) a milled slice, on an abraded specimen. Small gouges are visible in the coating, into which the ice penetrates.

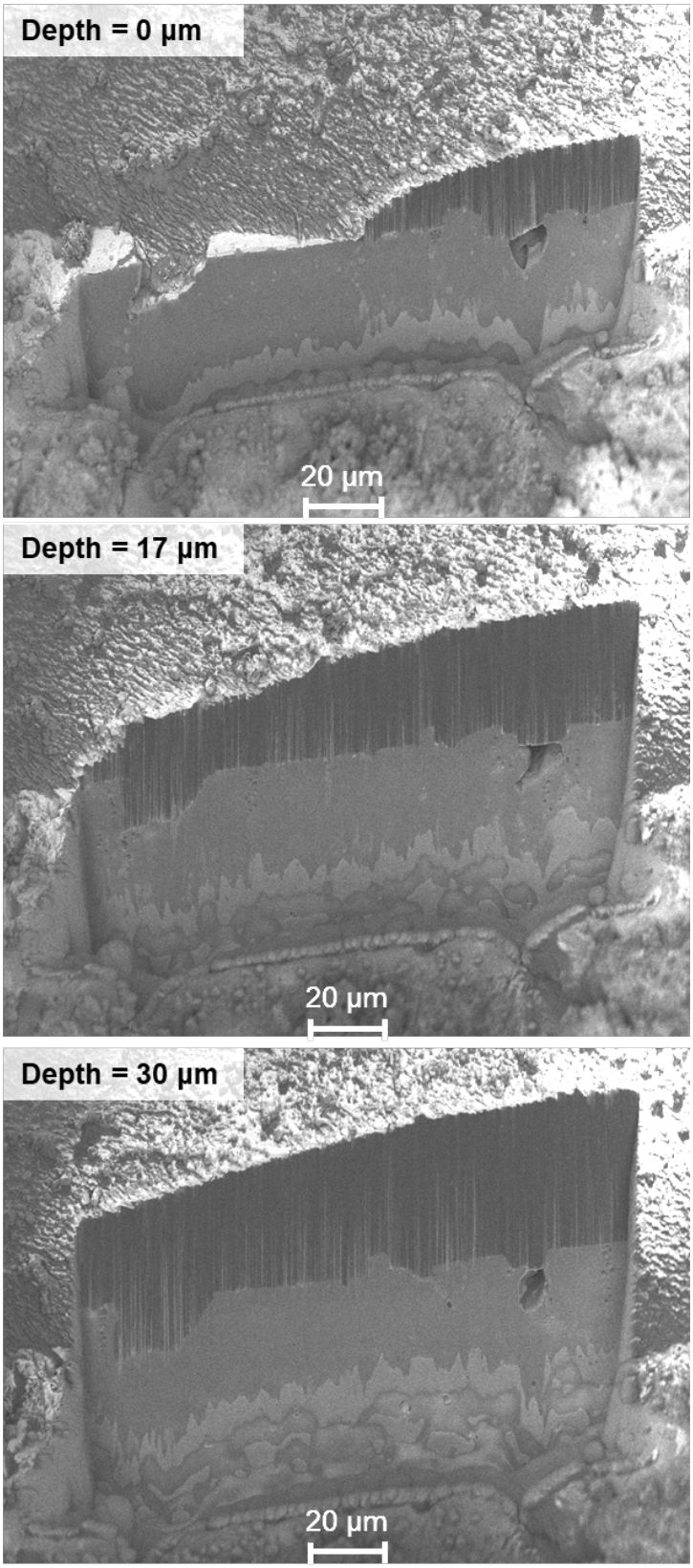

Figure 7.20 – Successive cross-sections of the ice-coating interface milled by FIB. Images are at depths of 0, 17 and 30 µm from the first cross-section. The total depth of the final mill is approximately 40 µm from the exterior. There is interpenetration of the ice and coating. The ice does not penetrate the gouge on the right side.

7.3.2. Ice adhesion

The ice adhesion results are presented in Figure 7.21. For the scalpel cut specimens, all the coatings experienced a small increase in ice adhesion post-damage. When taking the average value across the pre- and post-damage condition, the softer, oil-infused coatings showed greater increase in adhesion strength at a 29-44% increase, compared to an increase of 14-31% for the non-oil infused coatings, as presented in Figure 7.22. As the de-icing cycles progress post-damage, ice adhesion also increases. When comparing these results to those in Chapter 5, there are similar percentage increases in ice adhesion over 100 de-icing cycles on the undamaged specimens as 10 de-icing cycles on the scalpel cut specimens. The presence of the scalpel cuts accelerates the deterioration in ice adhesion strength.

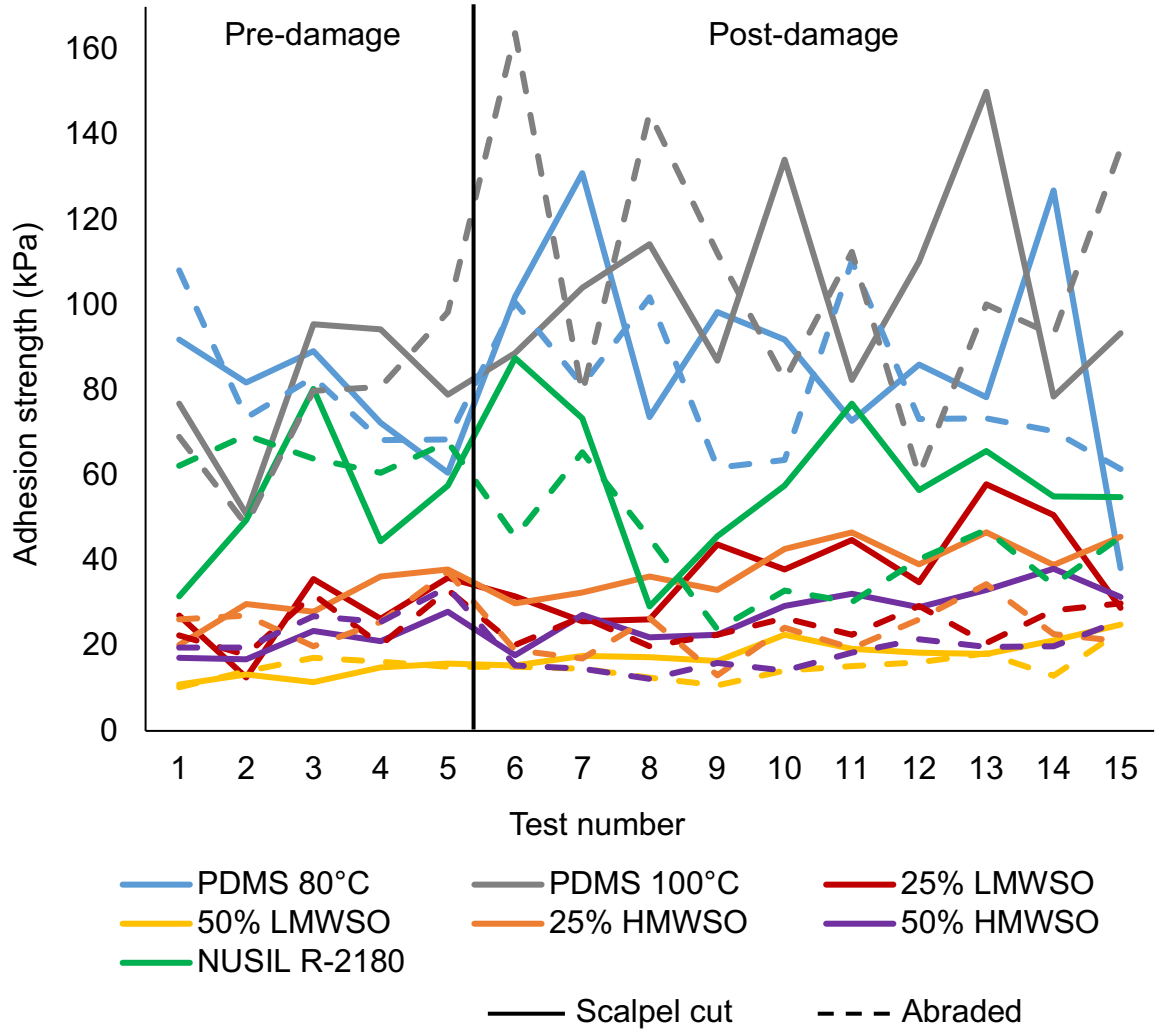

Figure 7.21 – Ice adhesion strength of coatings pre- and post-damage for scalpel cut and abraded specimens. Values are an average of the two specimens. Tests 1-5 were performed on the specimens pre-damage, and test 6-15 were performed post-damage.

The advanced deterioration likely stems from the damage to the edges of the scalpel cut from de-icing which widen the cut and increase the penetration of ice. Despite the findings of the cryo-FIB/SEM imaging in Section 7.3.1.5, it is possible the interfaces are insufficiently brittle at the test temperatures for crack initiation to significantly lower the ice adhesion strength.

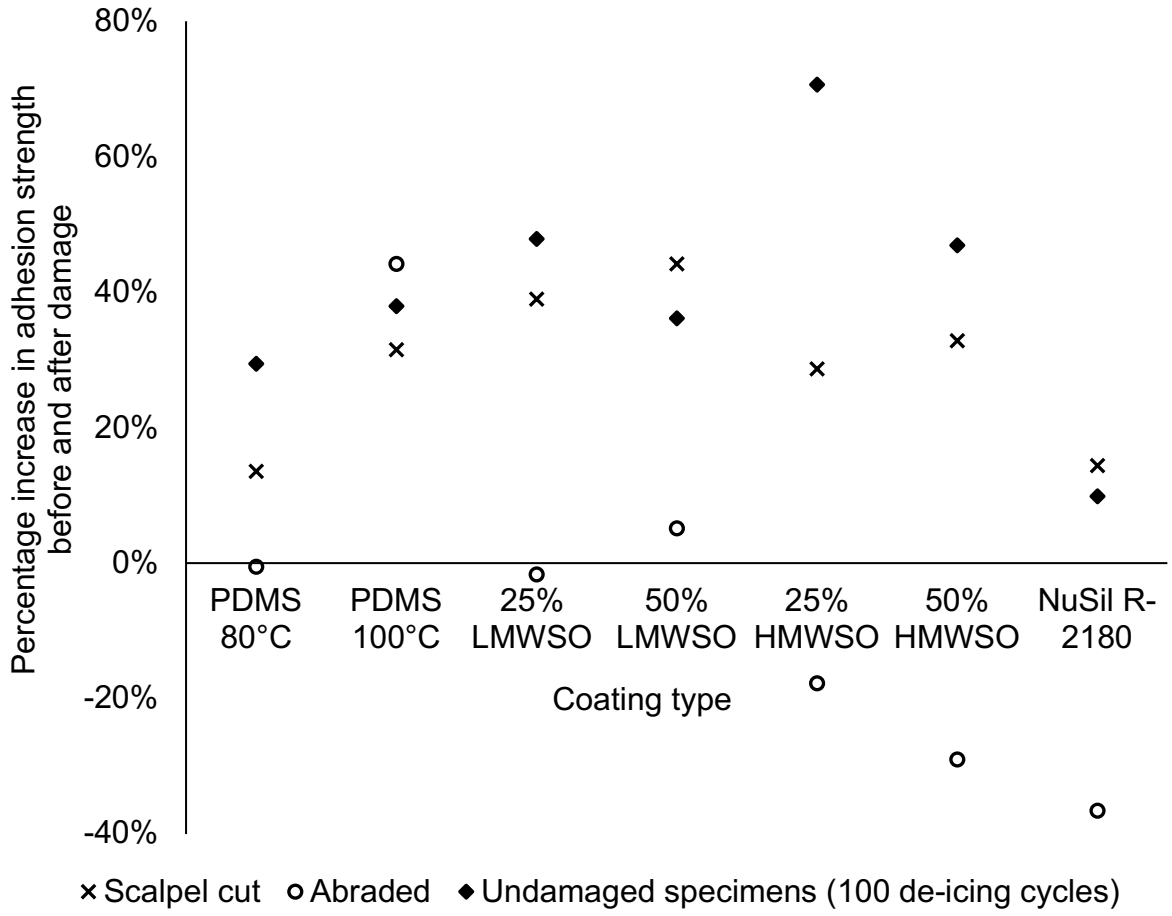

Figure 7.22 – Percentage increase in adhesion strength of the coatings between pre- and post-damage conditions of scalpel cut and abraded specimens. This is presented alongside the data for the undamaged specimens from Chapter 5, which were subjected to 100 de-icing cycles.

The results for the abraded specimens show disparate responses to the damage. Three of the specimens, the PDMS 80°C, 25% LMWSO and 50% LMWSO, saw little change, while the PDMS 100°C increased at a similar rate as the scalpel cut and undamaged specimens. The 25% HWMSO, 50% HWMSO and NuSil R-2180 specimens actually saw a decrease in the ice adhesion strength post-damage. There is little clear trend between the types of surfaces and their response to damage.

The diverse results may be a consequence of the mixed wetting regimes that can occur on the specimens, leading to different interfacial contact. Inspection of the images in Figure 7.15 and Figure 7.16 does not provide much indication of the precise morphology of the damage on each specimen, and therefore whether certain surfaces are likely to generate more of one wetting regime. This is a possible area of future research.

It should be noted that none of the specimens exceeded the equipment load limit. These results support the argument that the instances of tests exceeding the 650 kPa limit in Chapter 5 are not solely a result of morphological changes from surface damage.

7.3.3. Freezing delay

The results of the freezing delay tests are presented in Figure 7.23. As with the undamaged specimens in Chapter 6, there are only small differences between the freezing delay of the different surfaces, pre- or post-damage. The type of damage does not have a strong influence on the freezing delay either. The NuSil R-2180 has a slightly lower freezing delay, as in Chapter 6, likely due to small differences in thermal conductivity and surface chemistry compared to the purely PDMS based coatings. However, the average for all the coatings is generally in the range of 100-250 s across all specimen conditions and damage types, and there is significant overlap of the range bars.

The frequency of indefinite nucleation delay on the specimens, in Figure 7.24, did show a stark difference between the pre-damage and post-damage conditions, despite similar results across the coating types. The specimens are all able to delay nucleation indefinitely in around 30-90% of tests pre-damage, and all saw a drop-off to ≤ 40% post-damage. There is also a difference between the damage types. The abraded specimens lost nearly all ability to delay nucleation indefinitely, with only the 50% LMWSO maintaining any occurrences. A few of the scalpel cut specimens (PDMS 80°C, 25% LMWSO, 50% LMWSO and NuSil R-2180) had some instances of indefinite nucleation delay, but at frequencies of 10-40%, notably down on their pre-damage frequencies.

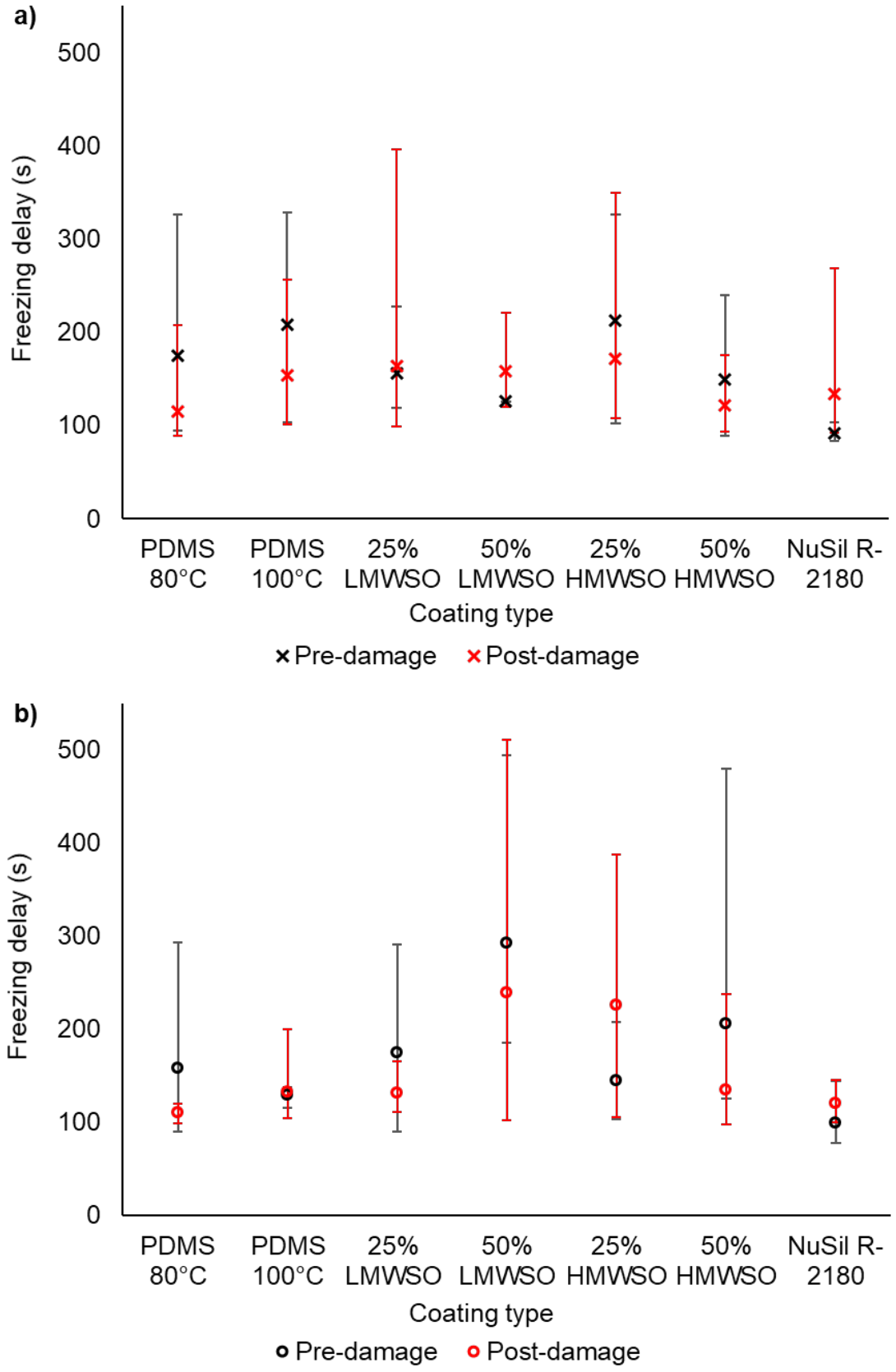

Figure 7.23 – Graphs of the freezing delay for the a) scalpel cut specimens and b) abraded specimens pre-damage and post-damage, with range bars. There is no clear trend between the coatings, or when comparing across specimen condition or damage type.

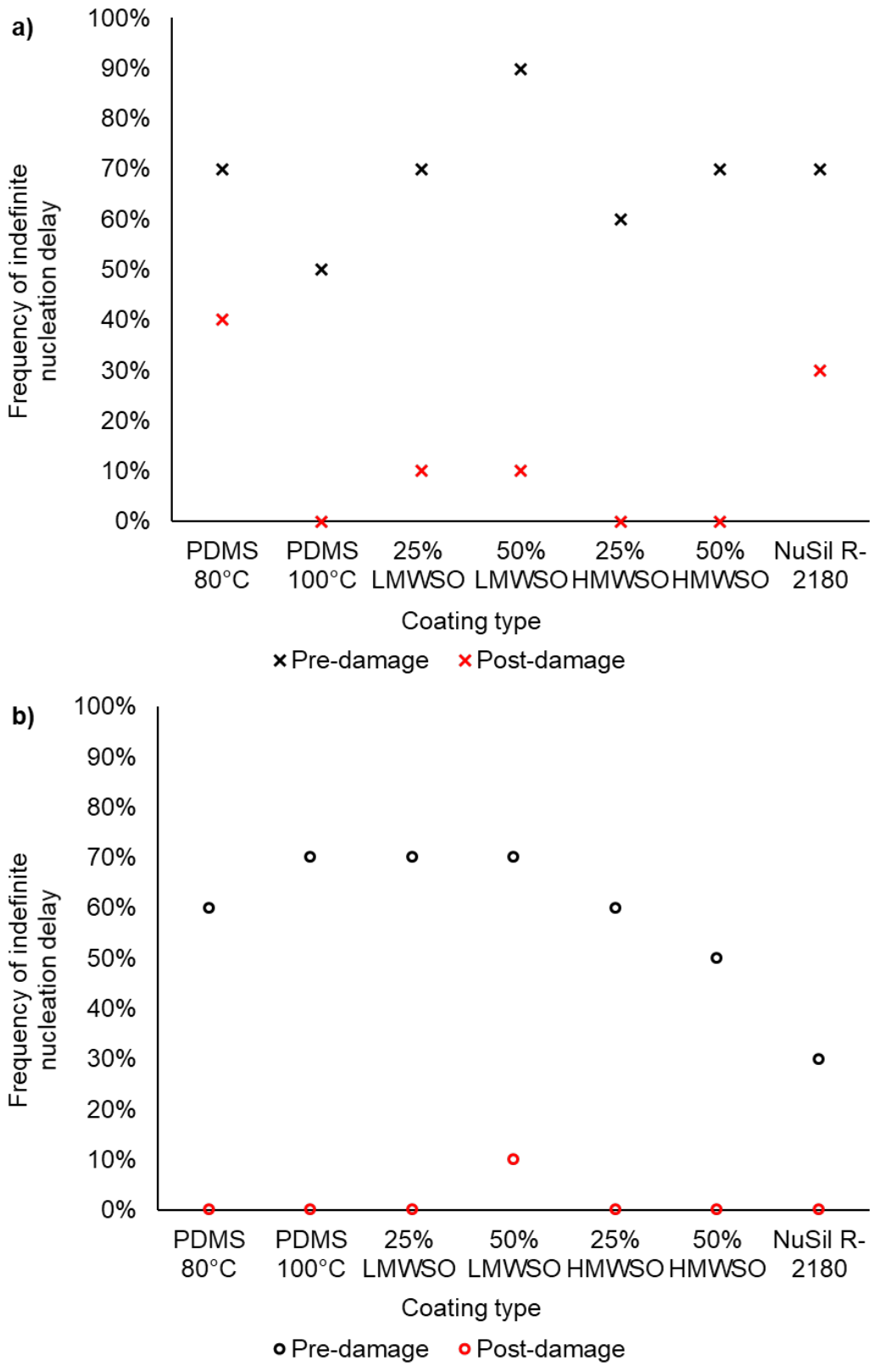

Figure 7.24 – Graphs of the frequency of indefinite nucleation delay for a) the scalpel cut specimens and b) the abraded specimens pre-damage and post-damage. There is a clear decrease in the specimens' ability to supress nucleation once damage has occurred, across both damage types. This degradation is greater in the abraded specimens.

These results can be explained by the increase in available nucleation sites on the surfaces as a result of the damage. The edge of the scalpel cut and the asperities on the abraded surfaces increase the likelihood of nucleation. The higher frequency of indefinite nucleation delay on the scalpel cut specimens post-damage compared to the abraded specimens can be attributed to the percentage of the contact area that remained undamaged, which was greater on the scalpel cut specimens. The scalpel cut specimens will therefore have fewer viable nucleation sites than the abraded specimens.

The 50% LMWSO specimen arguably had the best performance, with the highest average freezing delay on the abraded specimens both pre-damage and post-damage and maintaining instances of indefinite nucleation delay in both damage types. However, these differences are likely statistically insignificant and insufficient as the sole argument for use of the 50% LWMSO over other coatings.

7.4. Surface repair

7.4.1. Repair method

To investigate the ability of the surfaces to be repaired, the damaged coatings were recoated. Spray coating was deemed to be the most appropriate choice, as it is easy to apply in situ, on surfaces during their service. To ensure good coverage of the surface damage, a new coating of approximately 100 μm was sprayed on top of the damaged specimens.

The spray coating was applied via airbrush. The preparation of the elastomers is described in Chapter 3. The viscosity of the pre-polymer mixtures had to be reduced so that it could be sprayed. The diluent was hexane, which has good miscibility with the pre-polymers, and is miscible with the xylene carrier of the NuSil R-2180. The ratio of hexane to pre-polymer mixture used was 4:1. Due to its high volatility, most of the hexane evaporated during the spraying. The coatings were then left for 30 minutes, to allow any bubbles to dissipate and any remaining hexane to evaporate. The coatings were then cured using the method detailed in Chapter 3.

Respraying the NuSil R-2180 coatings was unsuccessful. Due to the high percentage of xylene in the pre-polymer mixture (> 80%), a large volume of the mixture had to be sprayed, and the solvents did not evaporate completely during deposition. Instead, the

solvents caused delamination of the original coating. Therefore, the NuSil R-2180 damaged specimens could not be easily repaired by spray coating and further tested.

7.4.2. Ice adhesion results

The effect of re-coating on the specimens' ice adhesion strengths is shown in Figure 7.25. For additional clarity, the percentage change in adhesion strengths is given in Figure 7.26.

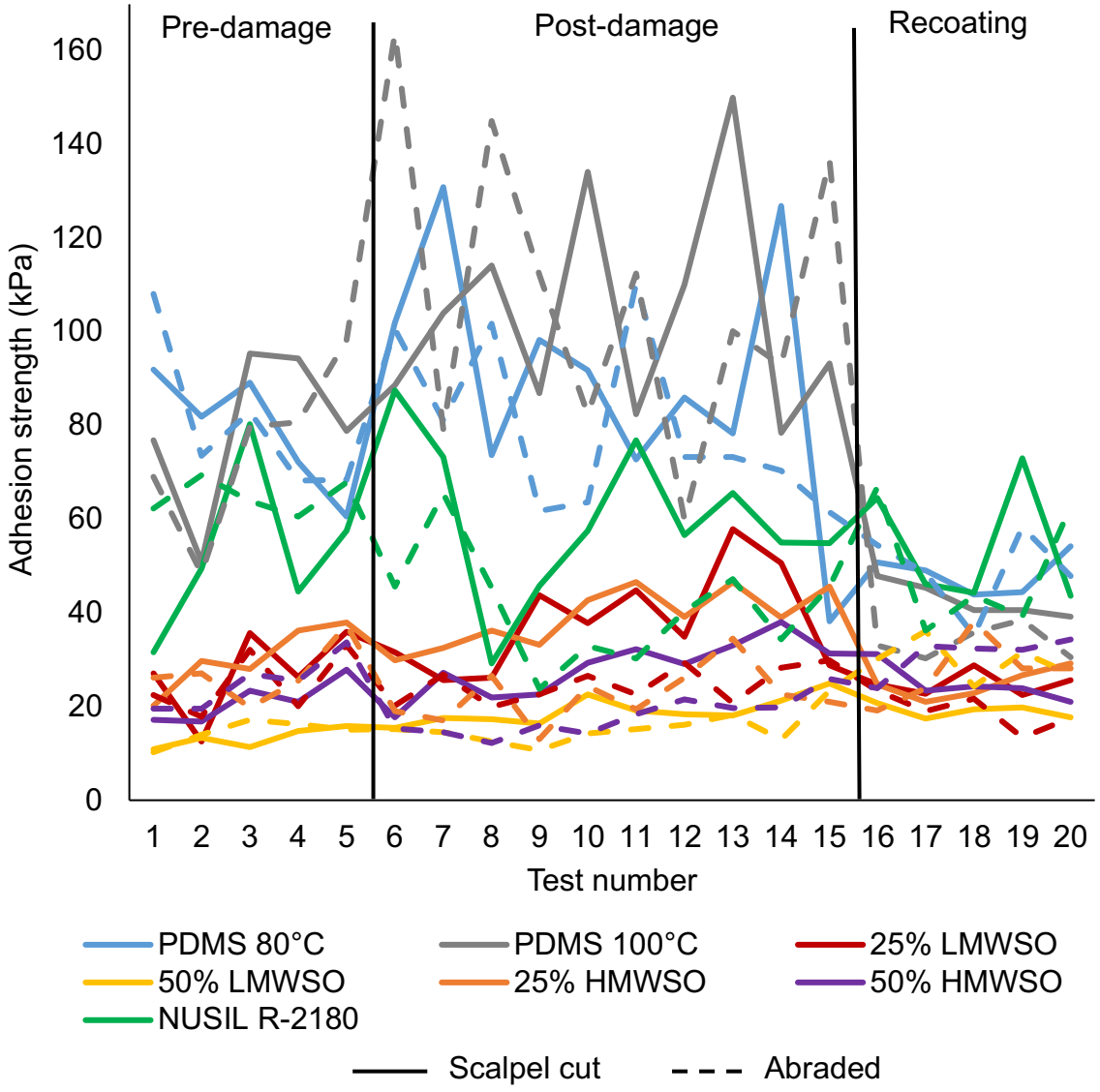

Figure 7.25 – Ice adhesion strength of coatings pre-damage, post-damage and after recoating for scalpel cut and abraded specimens. Values are an average of the two specimens. Tests 1-5 were performed on the specimens pre-damage, test 6-15 were performed on the specimens post-damage, and tests 16-20 were performed after recoating.

There is a clear reduction in the adhesion strength of many of the specimens. The scalpel cut specimens all see a reduction, though this is only 1% in the 50% LMWSO specimen. The respraying successfully filled in the scalpel cut and reversed the effect of the damage.

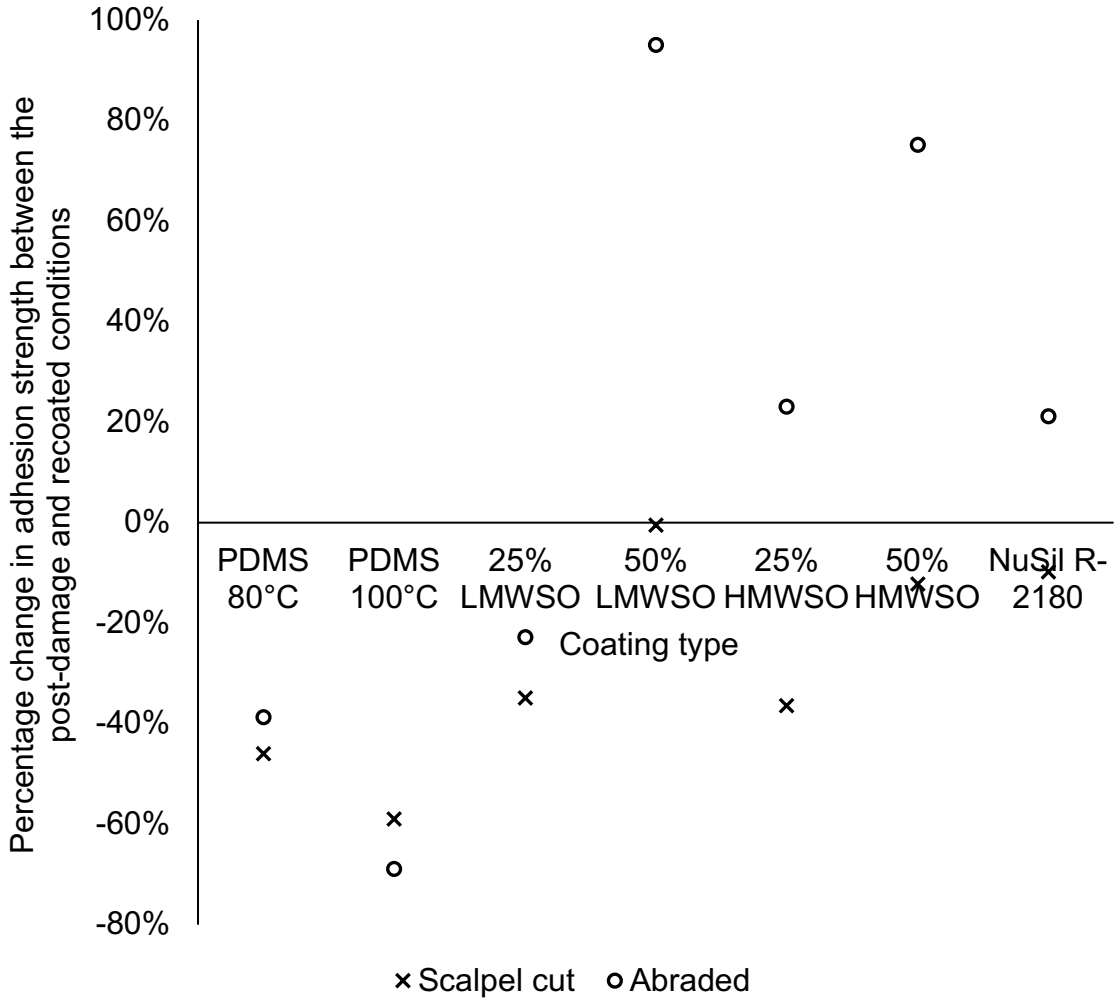

Figure 7.26 – Percentage change in the ice adhesion strength of the coatings between the post-damage condition and the recoated condition.

The abraded specimens, like in the post-damage results, saw mixed responses. In the case of the PDMS 100°C, which had increased after the abrasion, recoating saw it decrease. Similarly, the specimens that had seen a decrease in adhesion (25% HWMSO, 50% HWMSO and NuSil R-2180) increased after recoating. In this way, recoating reversed the effect that abrading the surfaces had on the ice adhesion strength of these specimens.

The PDMS 80°C and 25% LMWSO, which had seen little change in the adhesion strength as a result of the damage, both saw a decrease in the adhesion strength upon recoating. This is likely a result of the increased thickness of the coating, corresponding to a lower ice adhesion strength – a phenomenon which is discussed in Chapter 5.

The 50% LMWSO was an outlier, in that it experienced little change in ice adhesion strength after the abrasion, but then a large increase after recoating. The reason for this is unclear, but the absolute value of the adhesion strength remains at low 30 kPa, and the coating is still a viable anti-icing solution. Additionally, if there were damage-caused deterioration of the coating, it is likely recoating would return it to near the original adhesion strength, as with the other specimens.

7.5. Conclusion

Coating specimens were damaged by cutting with a scalpel or abrading with grit-paper, to generate severe damage. Contact angle and roughness measurements, and SEM, optical microscopy and cryo-FIB/SEM imaging, were performed alongside icephobicity tests.

All the specimens had similar contact angles of 100-107° pre-damage. The abraded coatings increased to 106-117° post-damage and then to 109-130° after de-icing, suggesting the occurrence of Cassie-Baxter wetting. The non-oil infused coatings had slightly higher contact angles than the oil-infused coatings. The scalpel cut specimens showed a decrease post-damage to 93-104°, possibly because of contact line pinning at the scalpel cut, or capillary forces causing penetration. After de-icing, the angles were similar to the pre-damage condition 104-110°, maybe due to widening of the scalpel cut during de-icing.

Stylus profilometry detected changes in the surface morphology from the damage. The abraded specimens greatly increased in measured roughness post-damage. The findings generally reflected the softness; the less damage-resistant, oil-infused coatings increased more than the non-oil infused coatings. The changes after de-icing were small and unlikely to be accurately resolved. The scalpel cuts were detected and caused a small increase in measured roughness across most of the specimens post-damage, and after de-icing as the scalpel cut widened. The softest specimens, the 50% LMWSO and 50% HMWSO, saw the greatest increase.

Optical microscopy and SEM imaging showed increases in scalpel cut width after de-icing and damage at the cut edges, such as crack formation and cohesive fracture. The 50% HMWSO specimen had large-scale cohesive damage from de-icing along the cut, making it highly susceptible to further damage and loss of icephobicity. Most of the specimens' cuts widened by 5-10 μm after de-icing. This excluded the 50% HMWSO specimen which widened by 50 μm, likely as a result of being more easily deformed, and less precision when measuring the optical microscopy images. The only clear difference in the abraded specimens was the absence of larger pieces of debris, removed by the de-icing cycles. There is no significant increase in the finer roughness of the specimens, but large gouges in the surface were enlarged by de-icing.

The ice-coating interfaces were imaged with a new cryo-FIB/SEM method. The ice did not penetrate the scalpel cut but lowered towards it with increasing depth from the exterior. Ice penetration was visually observed on an ice surface after de-icing, so it is likely the ice penetrates the cut, at least in the middle. It is possible the greater hydrostatic pressure overcomes the wetting resistance, or there was sublimation at the droplet edge. Imaging also showed crack initiation at the cut edges. The images of the abraded specimen showed both Wenzel wetting and Cassie-Baxter wetting. It is believed the regime is determined by the angle of the opening, with the critical angle = 90°. This behaviour is leveraged in the design of superhydrophobic surfaces and SLIPS. These images provide direct evidence that ice droplets can show mixed Wenzel and Cassie-Baxter wetting of abraded PDMS surfaces.

Ice adhesion testing showed mixed results depending on the damage type. The scalpel cut specimens increased post-damage, by 29-44% for the oil-infused coatings and 14-31% for the non-oil infused, similar to the results over 100 de-icing cycles on the undamaged specimens. The advanced deterioration likely stems from damage to the scalpel cut from de-icing, which widens the cut and increases ice penetration. The abraded specimens showed mixed responses, which may be a consequence of mixed wetting regimes.

There is little difference between the freezing delay of the different surfaces or the damage types, pre- or post-damage. The average for all the coatings is generally in the range of 100-250 s. The frequency of indefinite nucleation delay showed a clear

difference between the pre-damage and post-damage conditions. The specimens were all able to delay nucleation indefinitely in around 50-70% of tests, pre-damage, but worsened post-damage. The abraded specimens lost nearly all ability to delay nucleation indefinitely, while the scalpel cut specimens fell to 10-40%. This is explained by the increase in nucleation sites on the surfaces because of the damage.

The damaged coatings were recoated by spraying a 100 μm layer to fill in the damage. The scalpel cut specimens saw a reduction in ice adhesion strength. The recoating reversed the effect of abrading the surfaces on the ice adhesion strength. The specimens that had been minimally affected by the abrasion generally saw a decrease in ice adhesion strength after recoating, likely a result of the increased thickness. Recoating effectively returns the specimens to their original adhesion strength.

The effect of surface damage is shown to be insufficient to preclude the use of soft elastomer coatings as anti-icing solutions. Only the most severe damage causes significant degradation in the icephobicity of the coatings. Damage can sometimes even lower ice adhesion strength, possibly because of Cassie-Baxter wetting. Furthermore, deterioration can be reversed by recoating the surface.

8. Interfacial Slippage

Summary

A new method for investigating evidence of interfacial slippage is developed. A modified microtribometer, mounted underneath an optical microscope, performs a push test on an ice droplet frozen on a coated polyethylene terephthalate glycol (PETG) substrate. Fluorescent microparticles are fully embedded in the surface of the coating. The microparticle depth ranges from 8-35 μm. Using fluorescent light filters, the microparticles at the interface are imaged during the push test to observe their movement.

The microparticles display large global elastic deformation at contact, followed by oscillation and gradual relaxation during ice sliding. However, no oscillation is observed prior to sliding, nor is there partial relaxation at the onset of sliding, and no visually observable local displacement at any time. Upon removal of stress, full relaxation with permanent global displacement is observed. The only coatings with significant permanent displacement are the PDMS 80°C, 25% LMWSO 50% LMWSO and 25% HMWSO. The 50% LMWSO had the highest permanent displacement at 13 μm. Despite this, the findings do not conclusively demonstrate interfacial slippage on the coatings.

Suggestions for future work are given, focusing on improvements to the experimental method and better understanding of the requirements and parameters of interfacial slippage.

8.1. Introduction

Interfacial slippage is the ability of a surface at an interface to flow under shear stress. In the results from Chapter 5, the fit of the ice adhesion data to *G,* as described by Equation (2.8), suggested interfacial slippage might be occurring at the ice-elastomer interface. However, the shape of the stress-strain curves did not indicate this and further investigation was deemed necessary, ideally by direct observation of interfacial slippage in the elastomer coating.

$$\sigma_A = \frac{G f_a a}{kT} \tag{2.8}$$

(σ_A is the adhesion strength, G is the shear modulus, f_a is the force needed to detach a single chain of segmental length a, k is the Boltzmann constant, and T is temperature.)

The idea that interfacial slippage is the governing ice detachment mechanism, and the source of the exceptionally low ice adhesion of oil-infused elastomers, has been proposed throughout the literature. It has been primarily attributed to the work of Golovin et al. (2016, 2017), though other studies have claimed its presence (Ibáñez-Ibáñez et al., 2021a, Sivakumar et al., 2019, Gao et al., 2019, Shen et al., 2018). Golovin et al. used indirect observations as evidence for interfacial slippage (2016). This included: the shape of the force-displacement curve; the direct correlation of the ice adhesion strength to shear modulus, G, and the crosslink-density of the elastomer, ρ^{CL}; and independence of the ice adhesion strength on oil viscosity and abrasion. The correlation with G and the independence of ice adhesion on oil viscosity and abrasion were also observed in this work.

The application of interfacial slippage mechanisms by Golovin et al. is primarily rooted in the theoretical and experimental work by Zhang Newby, Chaudhury and others (Newby et al., 1995, Zhang Newby and Chaudhury, 1997, Vorvolakos and Chaudhury, 1999, Ghatak et al., 2005). One of the works most relevant to this study is their visualisation of interfacial slippage with the use of fluorescent microparticles to observe polymer flow under shear stresses (Zhang Newby and Chaudhury, 1997). The work examined an adhesive tape stuck to a PDMS surface with a layer of microparticles at the interface. As the tape was peeled from the substrate, the particle movement was imaged and showed lateral flow towards and away from the

propagating crack, which Zhang Newby and Chaudhury asserted was evidence of interfacial slippage. The particles were partially embedded in the tape adhesive and were sitting on top of a previously cured PDMS surface, but particles embedded deeper in the adhesive showed plug flow behaviour up to a depth of 40 μm. (Plug flow is defined here as having a constant velocity profile through the depth of the fluid). Their experiments have often been used as an analogue for ice-elastomer interfaces, but the validity of applying the findings of adhesives-PDMS interfaces to elastomer-ice surfaces is debatable: Ghatak et al. (2000) performed numerical analysis of slippage in elastomers and determined only partial slippage was achieved.

So far, only one study has attempted to visualise interfacial slippage at the ice-elastomer interface (Regulagadda et al., 2022). The study used a similar principle as Zhang Newby and Chaudhury (1997) but placed quantum dots at the interface. Push tests, like those in Chapter 5, were performed on the ice-coating specimens and tracking the quantum dots showed permanent global and local displacement of the dots during de-icing, indicating flow of the dots.

However, the validity of these results is called into question due to the uniqueness of ice surfaces, which have a constant liquid-like layer at the surface, and readily generate a lubricating liquid layer upon sliding (Parkanyi, 2016). There is the risk that, by not embedding the particles in the surface, the flow observed during shear could be flow of the liquid layer, not the polymer chains. To address this, a method has been developed here which uses accessible equipment and techniques to visualise fully embedded microparticle movement under shear at the ice-elastomer interface.

8.2. Development of experimental method

To briefly describe the intended experimental technique: fluorescent microparticles are embedded in the surface of the elastomer coatings. Ice is frozen on the surface, above the microparticles, and a push test is performed on the specimen. During detachment, fluorescent light is shone on the microparticles, which are viewed by optical microscope. The movement of the microparticles is video recorded and tracked to observe the movement and possible flow of the polymer.

This experimental method required significant development. The details of this process are described in the following sections.

8.2.1. Testing equipment

A requirement of the test set up was the ability to image the ice-coating interface during detachment. To observe the movement of embedded fluorescent microparticles, equipment was designed which would perform a push test similar to that in Chapter 5, while providing a clear view of the interface. This can either be achieved by imaging the interface through the substrate and coating, or through the ice.

It was decided to visualise the interface through the coating and substrate. The main advantage of this is that viewing the interface is not complicated by the transparency of the ice. Images of the push test set up in Chapter 5 show that the ice in the cylindrical mould is not completely transparent because it is occluded by trapped air bubbles, which make it appear white. As the coating is transparent, and provided the selected substrate is transparent, this is not an issue when looking at the interface through the coating and substrate.

Using the work by Parkanyi (2016) as inspiration alongside Zhang Newby and Chaudhury's work (1997), an existing Deben microtribometer, which is similar to a microtensile stage but with one fixed grip and one moving grip, was modified. A simplified diagram showing the set-up is provided in Figure 8.1, alongside photographs in Figure 8.2 and Figure 8.3. The microtribometer is mounted below an optical microscope (Leica DM2700H) with fluorescent light filters. The microtribometer used was the same as that in Parkanyi's work (2016). Technical drawings of the modified components are provided in Appendix 1.

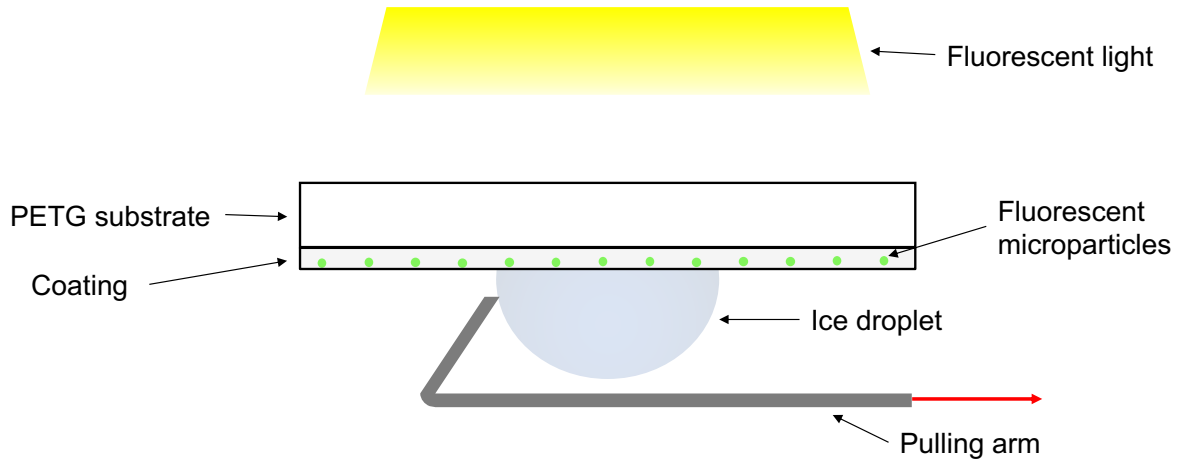

Figure 8.1 - Diagram of the interfacial slippage experimental set up. Not to scale

As the stage operated in tension, an arm was designed which ‘pulled’ the specimen rather than pushing it. The ‘pulling’ arm is angled towards the droplet, with a sharp corner contacting the droplet. This would provide more consistent tests than a flat edge, which, depending on the precise shape of the droplet, could have greater variation in the contact geometry.

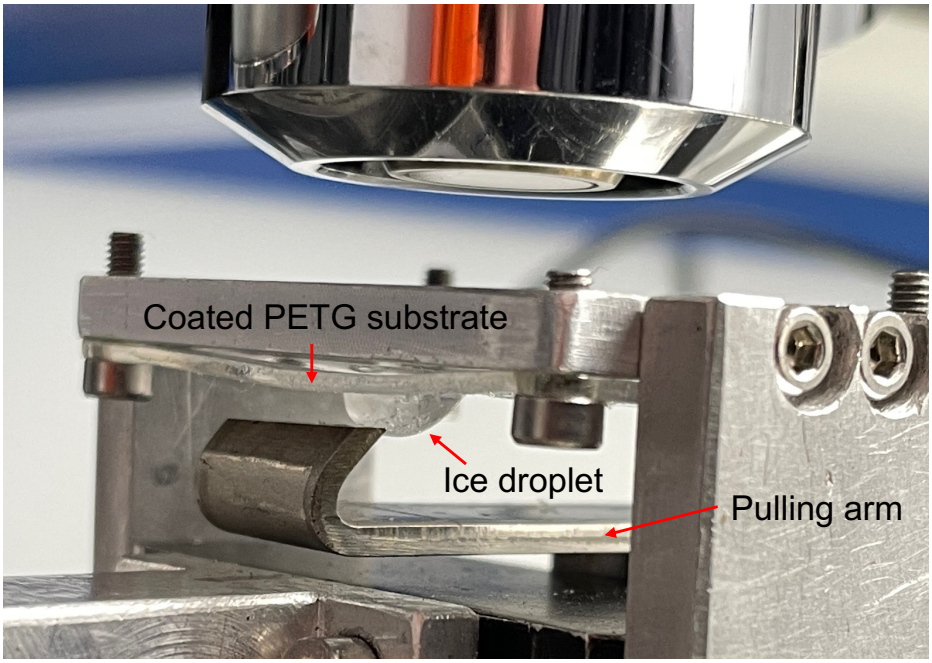

Figure 8.2 – Close-up view of the specimen with ice droplet and the pulling arm mounted underneath the microscope.

To allow for visualisation, a transparent substrate had to be used instead of the aluminium slides. Polyethylene terephthalate glycol (PETG) slides were used as they are transparent and tougher than acrylic or glass, which was beneficial in manufacturing the slides.

8.2.2. Coating fabrication and particle embedding

As discussed in Section 8.1, an issue when working with ice interfaces is the presence of a liquid layer at the surface. If the microparticles are not embedded in the surface, observed movement could be because of sliding along the surface during de-icing, rather than polymer flow. Embedding the particles in the surface of the coating ensures that any movement observed must be in the coating itself.

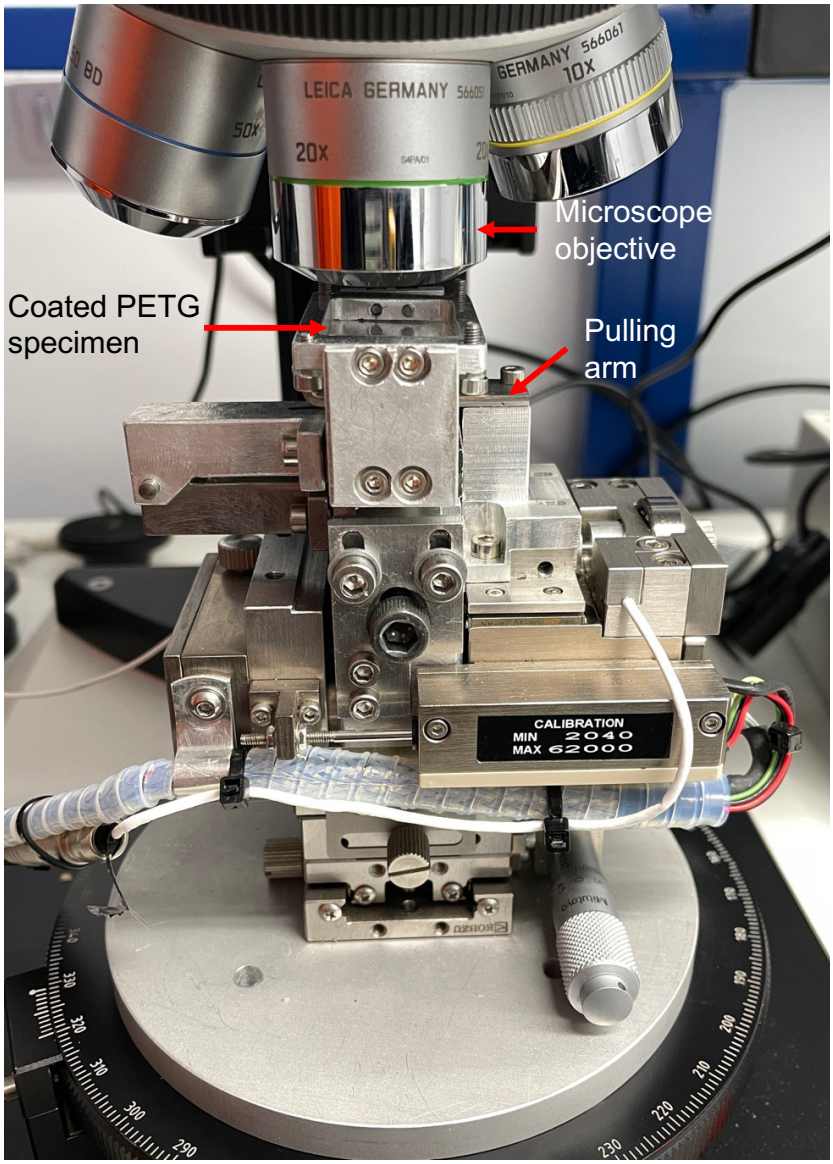

Figure 8.3 – Microtribometer stage mounted underneath an optical microscope. The specimen, pulling arm and microscope are highlighted.

The particles used in this work were polystyrene microspheres internally dyed with green, fluorescent dye and with a nominal diameter of 1 μm. They were supplied dispersed in aqueous suspension at a concentration of 1% (10 mg/ml). The microparticles are hydrophilic, which poses an issue when considering how to transfer them to the hydrophobic elastomer coatings. Zhang Newby and Chaudhury (1997) deposited droplets of the suspension onto a glass slide and allowed the water to evaporate, before using adhesive tape to pick up the particles. In their study, the adhesive tape was one of the surfaces under consideration, so the microparticles did not need to be subsequently removed from the tape.

Using this as inspiration, a similar method was devised. The coatings were initially prepared as described in Chapter 3, on the PETG substrates. After 25% of the curing time, the specimens were removed from the oven and some of the diluted suspension was deposited in the mould on top of the pre-polymer mixture. The specimens then finished heat curing, during which time the water evaporated, and the particles were dispersed on the coating surface. It was hoped that, by doing this during the curing process, the coatings might still be slightly liquid when the water evaporated and the microparticles would be partially embedded in the surface as it solidified. In their work, Regulagadda et al. (2022) employed a similar strategy in which they printed quantum dots on the surfaces pre-curing. Trials in which the suspension was placed on the coating before any curing resulted in the suspension being trapped in bubbles of the coating, preventing evaporation of the water. This was a result of the suspension being denser than the pre-polymer liquid. Initial partial curing was required to prevent this.

There was some concern that, because of the hydrophilicity of the microparticles and the hydrophobicity of the coating, even dispersion of the microparticles across the surface would not be possible. As evaporation proceeds the water layer turns into a droplet and retracts towards the middle of the surface. It was suspected that contact line pinning of the microparticles at the droplet edge could cause them to aggregate in the middle (Yu et al., 2017). However, this did not prove to be an issue, as is demonstrated in Figure 8.4.

Because of the concentration at which the microparticles were supplied, the aqueous suspension had to be diluted before deposition onto the surface. Without dilution the concentration would have been too high to image individual particles. Calculations based on the desired surface area concentration of the microparticles (approximately 1 particle per 25 μm^2) and the minimum volume of water required to wet the coating surface (2 ml) gave a dilution factor of 2000. This was achieved by dilution with deionised water.

Examination of the partially embedded microparticles with optical microscopy showed that very lightly brushing the surface with a swab de-bonded the particles. Micrographs of the surface before and after swabbing, in Figure 8.4, show that some of the particles remain in position, but many others have shifted.

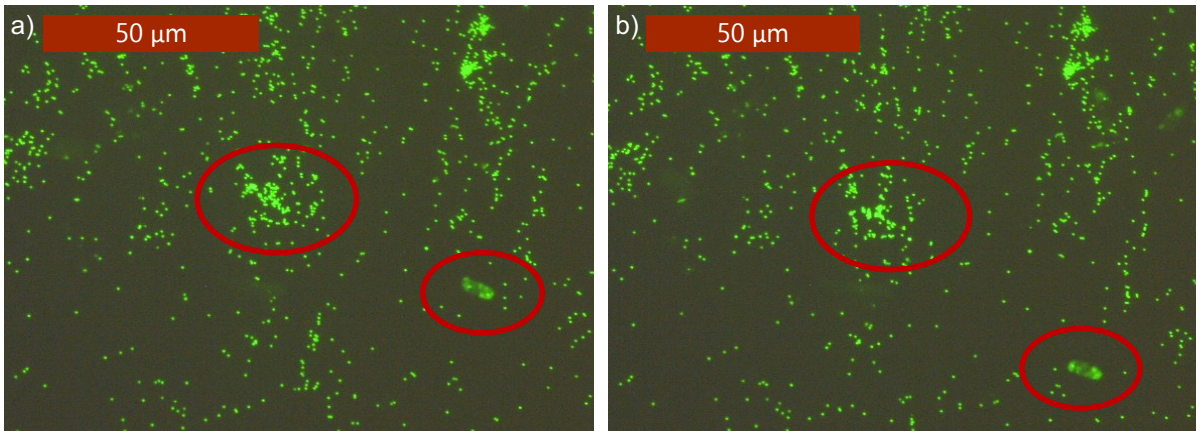

Figure 8.4 – Micrographs of fluorescent microparticles partially embedded in an elastomer coating a) before swabbing and b) after swabbing. The circled areas show groups of particles for comparison – the particles have clearly shifted from their original position. The particles are randomly spread across the surface, and do not show evidence of aggregation from contact line pinning.

To prevent this from interfering with the results, it was decided that fully embedding the particles was required. This was achieved by covering the partially embedded particles in an additional coating layer. After the water had completely evaporated and the standard curing time had finished, the specimens were spray coated with a thin layer of the coating. Zhang Newby and Chaudhury (1997) observed plug flow to 40 µm depth during interfacial slippage in an adhesive, but to minimise issues of any flow gradients through the depth of the coating while ensuring complete embedding, the covering layer was designed to be ≤ 10 µm thick. A diagram to show the embedding process is provided in Figure 8.5.

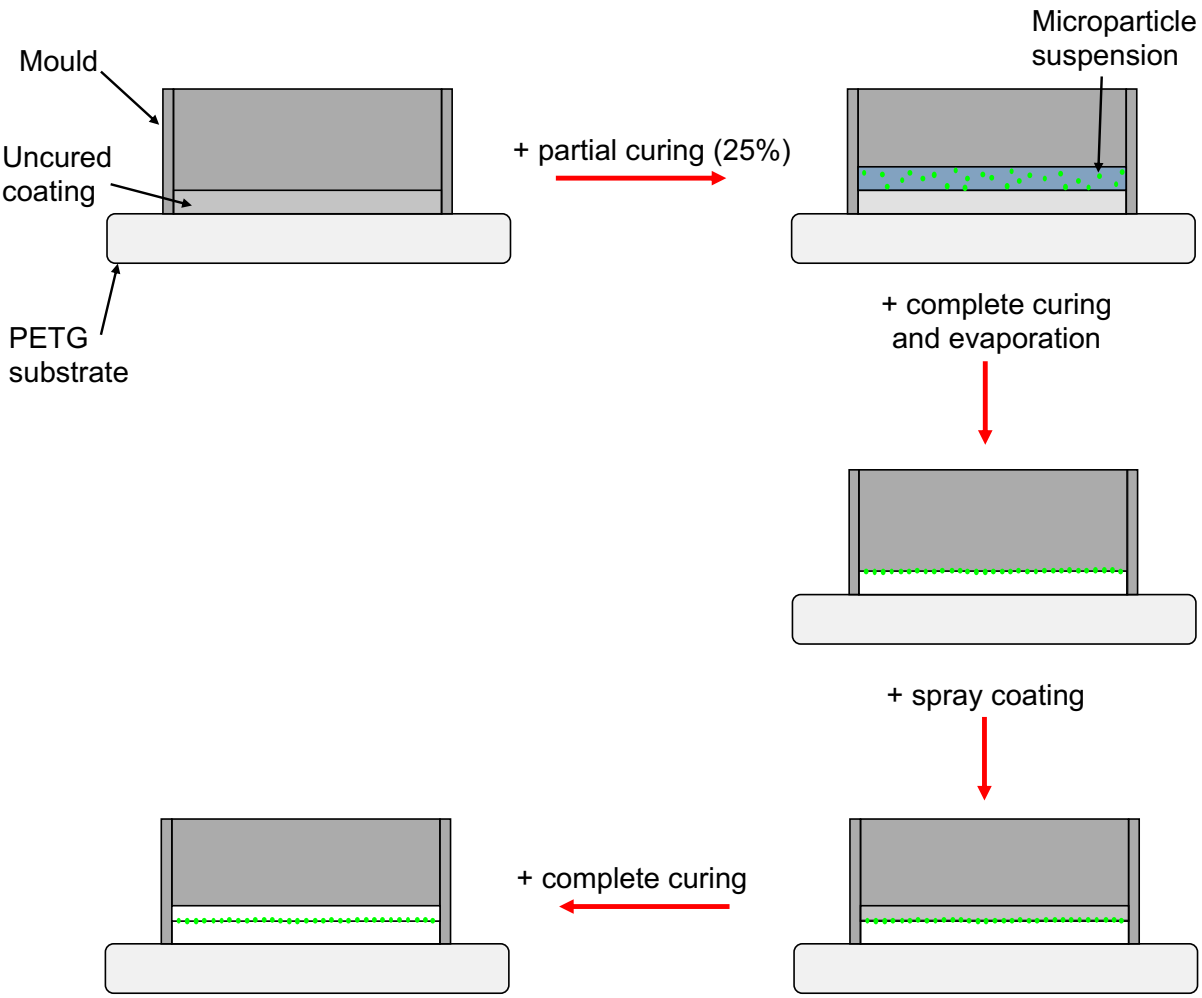

Figure 8.5 – Schematic of the microparticle embedding method. The coatings are initially prepared as standard, then removed from the oven after 25% of the curing time and the microparticle suspension deposited on top. The specimens are returned to the oven to complete curing. The cured specimens are spray coated to cover the partially embedded particles. After curing completely again the particles are fully embedded. Not to scale.

As with spray coating to repair the damaged coatings, described in Chapter 7, the coatings were diluted with hexane by a factor of 4 to reduce their viscosity enough to be sprayable. As was the case in Chapter 7, spray coating of the NuSil R-2180 was unsuccessful due to the high proportion of xylene, which caused delamination of the already cured coating. After spray coating the specimens were cured again using the standard method. This additional curing was unlikely to change the properties of the bottom layer, as the curing kinetics and physical properties plateau once the coatings are fully cured (Johnston et al., 2014). There will be an interface between the two layers, but losses across the interface were shown to not significantly affect the icephobicity of the coatings in Chapter 7. This method is similar to the technique used

by Zhang Newby and Chaudhury (1997), who placed particles at the interface of two layers of tape adhesive to simulate the 'bulk'. The results showed flow was still observed during detachment of the combined layers from the PDMS surface, suggesting minimal loss across the layer interface.

8.2.3. Particle depth measurement

Using the microscope, a simple method was used to measure the embedded depth of the particles. A feeler gauge measuring 40 µm thick was taped to an aluminium slide and mounted underneath the microscope. The upper surface of the gauge was brought into focus. A mark was made on the handwheel controlling the height of the microscope stage and a photograph taken of the handwheel. The microscope stage was then lowered to bring the aluminium slide into focus, at which point a second photo was taken of the handwheel. The two photos were overlaid and the angle through which the handwheel had been turned was calculated. The relationship between the handwheel angle change and the change of the stage height is given by Equation (8.1):

$$\text{Change in stage height} = \text{handwheel angle change x } 1.14\ \mu\text{m}/^\circ \qquad (8.1)$$

The overlaid photos of the marked handwheel are provided in Figure 8.6 , with the measured angle annotated on the image.

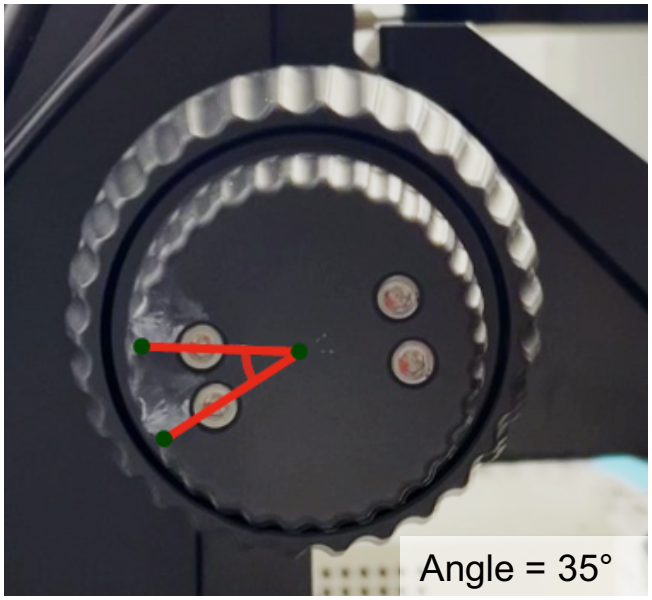

Figure 8.6 – Overlaid photos showing the angle through which the handwheel was turned to focus on the surface of the feeler gauge and surface of the slide – corresponding to a distance of 40 µm.

For corroboration, this method was used to measure the thickness of a feeler gauge of 100 μm. The measured thickness was 110 μm, an error of 10%.

This method was then applied to the embedded particles. The surface of the coating was marked and brought into focus and then the stage was shifted to focus on the microparticles. A photograph of the handwheel was taken at both heights and the depth calculated from angle of the handwheel turn and Equation (8.1).

8.2.4. Test method

Push tests were performed by the modified Deben microtribometer. They were similar to the push tests performed in Chapter 5 to measure ice adhesion, with one notable change. Where the probe speed range on the ForceBoard™ was 5-15 mm/s, the speed range of the microtribometer was 5-30 mm/min. The slowest probe speed was selected (5 mm/min) as it should allow for clearer viewing of the particle movement. This is also most similar to the speed at which Regulagadda et al. (Regulagadda et al., 2022) consistently observed interfacial slippage.

The test method is outlined here:

i. The coated substrates were placed right-side up and a droplet of 0.1 ml of deionised water was deposited on the surface by syringe.
ii. The droplet was left to freeze on the surface for 1 hour before the specimen was mounted upside-down on the microtribometer.
iii. The microtribometer and specimen were placed underneath the microscope and the microscope feed was recorded.
iv. The microparticles were brought into focus, with fluorescent light filters in place.
v. The test was started and the moving jaw opened, bringing the pulling arm into contact with the ice droplet, detaching and sliding the droplet along the surface.
vi. Once the test was complete, if the microparticles had shifted out of focus, the microscope was refocused.

The videos were processed and the movement of the particles during the test was noted. The initial and final positions of the microparticles were compared visually for changes. If there was movement, the displacement of 5 particles was measured, and the average taken. To ensure that the changes in position were in the coating and not in the stage or fixtures, a mark was placed on the uncoated side of the PETG substrate, and the position of the specimen was noted before and after the test. The

displacement of the specimen was subtracted from the particle movement, to get the true distance displacement by the particles. This was combined with qualitative observations of the movement during the test, which were compared to the observations of Zhang Newby and Chaudhury (1997) and Regulagadda et al. (2022).

8.3. Results

8.3.1. Particle depths

The particle depth measurements are presented in Figure 8.7 and show some specimens with particles embedded deeper than intended. The 25% HMWSO and 50% HMWSO specimens had particles embedded around 10 μm deep, which was within the desired range. However, the PDMS 80°C, PDMS 100°C, 25% LMWSO and 50% LMWSO were all deeper than 10 μm. This is likely due to imprecision in the spray coating technique.

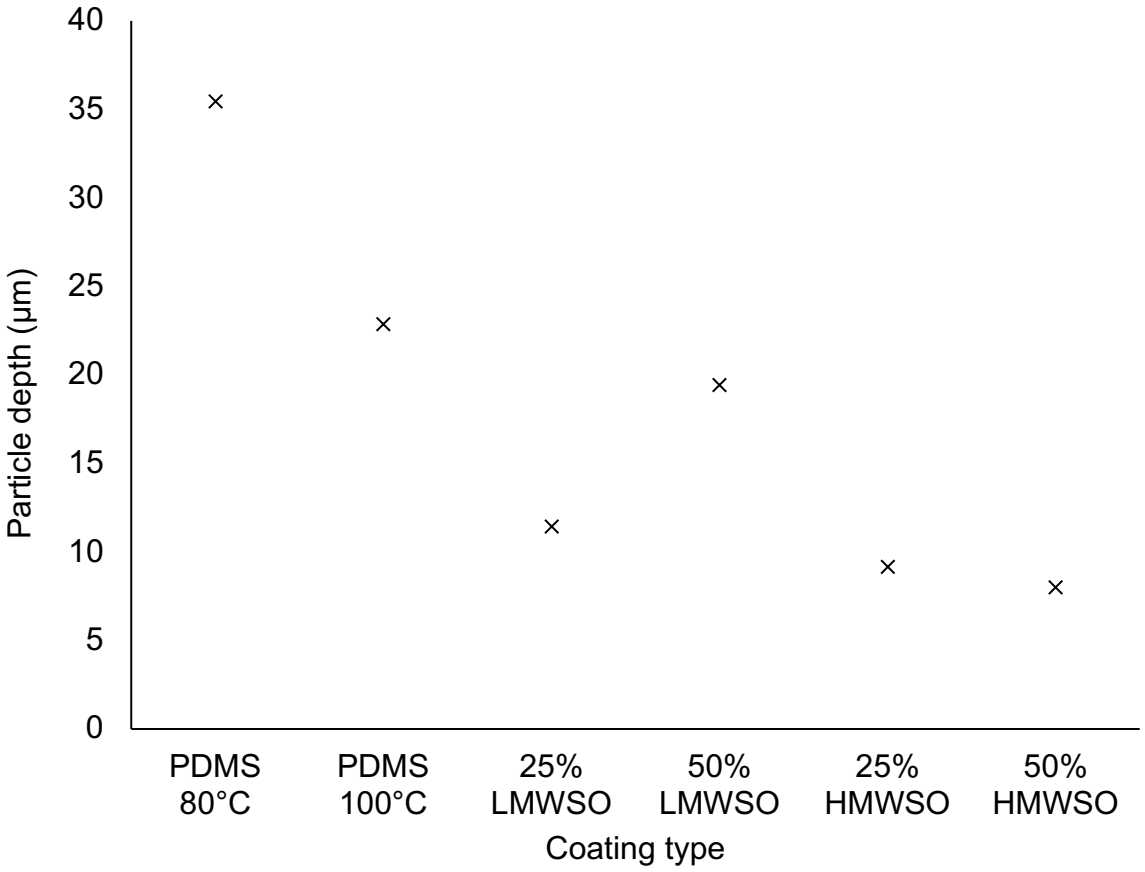

Figure 8.7 – Measured particle depth of each coating specimen calculated using the change in handwheel angle and Equation 8.1. The measurement error is approximately 10%.

It is possible that the depth of the particles plays a role in any observed movement. Though Zhang Newby and Chaudhury (1997) observed plug flow in interfacial slippage of adhesive tapes, the potential flow profile in these coatings has not been characterised, and velocity may decrease with increasing depth from the surface. This will be discussed in Section 8.4.

8.3.2. Ice sliding

During the microtribometer de-icing tests, upon contact by the pulling arm, the ice droplet slid across the surface and then remained adhered when the shear force was removed. This was different to the ice adhesion tests on the ForceBoard™ in Chapter 5, in which the ice was immediately detached from the coating completely, falling off. Both cases are described in Figure 8.8. The primary difference between the mechanical test methods was the strain rate, which was 60 times faster in the ForceBoard tests.

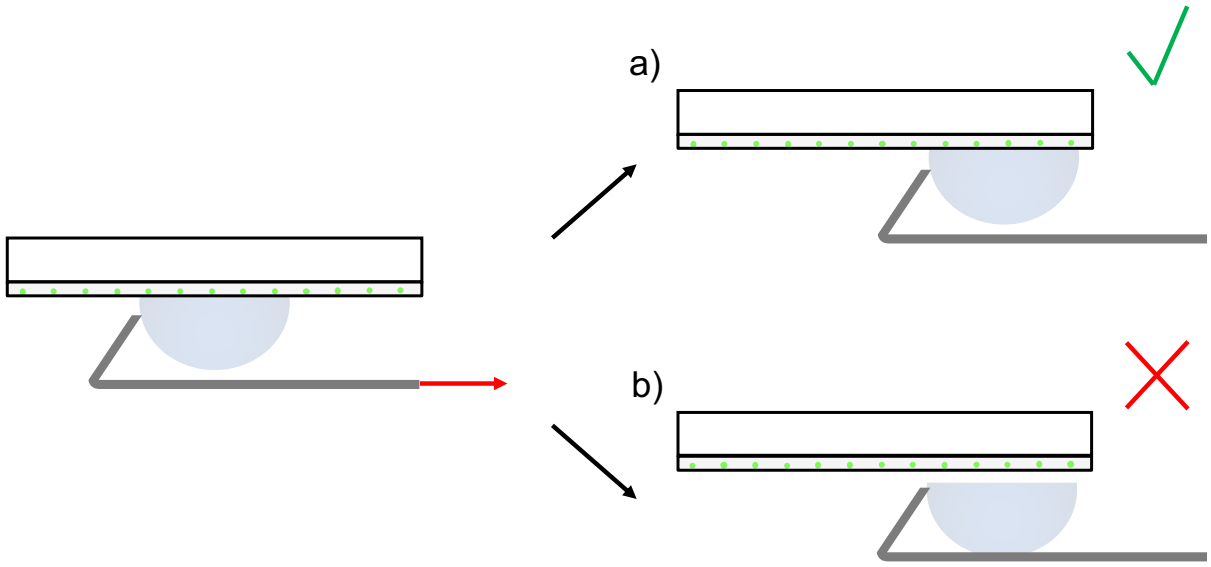

Figure 8.8 – Diagram showing movement of the ice droplet upon contact by the pulling arm. The ice droplets displayed a) sliding along the surface while remaining adhered, and not b) complete detachment from the coating surface.

In Chapter 5, the complete detachment of the ice, plus the shape of the force-displacement curves in Figure 5.12 indicated cavitation rather than slippage.

It is likely the tests here, in which sliding occurred, would exhibit force-displacement curves similar to those observed by Golovin et al. (2016) and Regulagadda et al. (2022). In their tests the response showed a peak force upon contact, followed by a gradual decay as the ice slid along the surface. However, this sliding could be a result

of melt water formation by frictional heating of the ice, rather than slippage in the coating. These results do support the claim (Regulagadda et al., 2022) that the detachment behaviour is strain rate dependent, but are not proof of interfacial slippage.

8.3.3. Particle movement

The results of the microparticle tracking are quantitative (the permanent particle displacement that was measured) and qualitative (the direction and patterns of movement), both of which will be discussed in this section. First though, is a summary of the observations made by Zhang Newby and Chaudhury (1997) and Regulagadda et al. (2022), by which they characterised interfacial slippage. The findings of this study will subsequently be compared to those observations.

8.3.3.1. Qualitative assessment

Zhang Newby and Chaudhury (1997) visualised microparticles embedded in adhesive tape stuck to PDMS. As the tape was peeled from the PDMS a crack propagated at the interface. The particle under observation exhibited lateral movement towards and away from the propagating crack tip. This oscillation was attributed to hydrodynamic flow in the adhesive induced by Poisson contraction.

Regulagadda et al. (2022) printed light emitting quantum dots on the coatings pre-curing. The quantum dots perform the same function as the fluorescent microparticles in this study, in providing trackable reference points for observing flow. Ice was frozen on top of the coatings and then detached, while recording the quantum dot movement. The dots showed initial global displacement from elastic deformation, followed by partial relaxation attributed to the onset of slippage. The ice then slid across the coating, accompanied by oscillation of the dots. After the ice was removed there was full relaxation of the dots, with a slight permanent offset. There was local displacement of the quantum dots throughout the de-icing process.

The behaviour observed in this study has some similarities to that observed by Regulagadda et al. The particles underwent large global displacement (> 50 μm) from elastic deformation of the coating upon initial contact of the pulling arm. There was no instantaneous partial relaxation at the detachment/onset of sliding but, there was gradual relaxation during sliding. As with Regulagadda et al., there was oscillation during sliding, and full relaxation when the shear force was removed. Small permanent

offsets were also observed, which are measured in the following section. However, no local displacement was visually observable throughout the test.

A difference between the work by Regulagadda et al. (2022) and this study was the practice of fully embedding the particles. In the study by Regulagadda et al, it is not clear whether the dots were embedded in the coating, either partially or fully. Schematics suggest they sit on top of the surface, precisely at the interface. This could lead to uncertainty in their findings because of possible mixed contributions to the quantum dot movement by polymer flow, flow of liquid water at the interface and removal of the dots. Efforts to disentangle these contributions would improve the confidence of the findings.

The similarity in behaviour of their quantum dots and the fully embedded microparticles in this study suggest much of the movement can be attributed to the elastomer itself. However, it is possible that differences such as the local particle displacements are caused by either melt water flow or particle debonding. In Figure 8.4, local particle displacement was observed on the coatings of this study, when lightly brushing the surface with a swab. This de-bonded the partially embedded particles and led to local displacement. A similar effect could be the source of the local quantum dot movement in the findings of Regulagadda et al.

In comparison to the observations of Zhang Newby and Chaudhury (1995), no oscillation of the particles was observed prior to sliding.

8.3.3.2. Quantitative assessment

The results of push tests are presented in Figure 8.9. Using the interfacial slippage visualisation technique, the permanent global displacement of the coatings measured from 0-13 μm. The 50% LMWSO specimen, which had the lowest ice adhesion strength during icephobicity testing and the lowest elastic and shear moduli, also had the highest displacement of all the specimens, double that of the other coatings. It should be noted that the permanent global displacements are of a similar order to permanent offsets recorded by Regulagadda et al., excluding the PDMS 100°C and 50% HMWSO. There is no clear trend across the coating types: both oil-infused and non-oil infused coatings show high and low particle displacement.

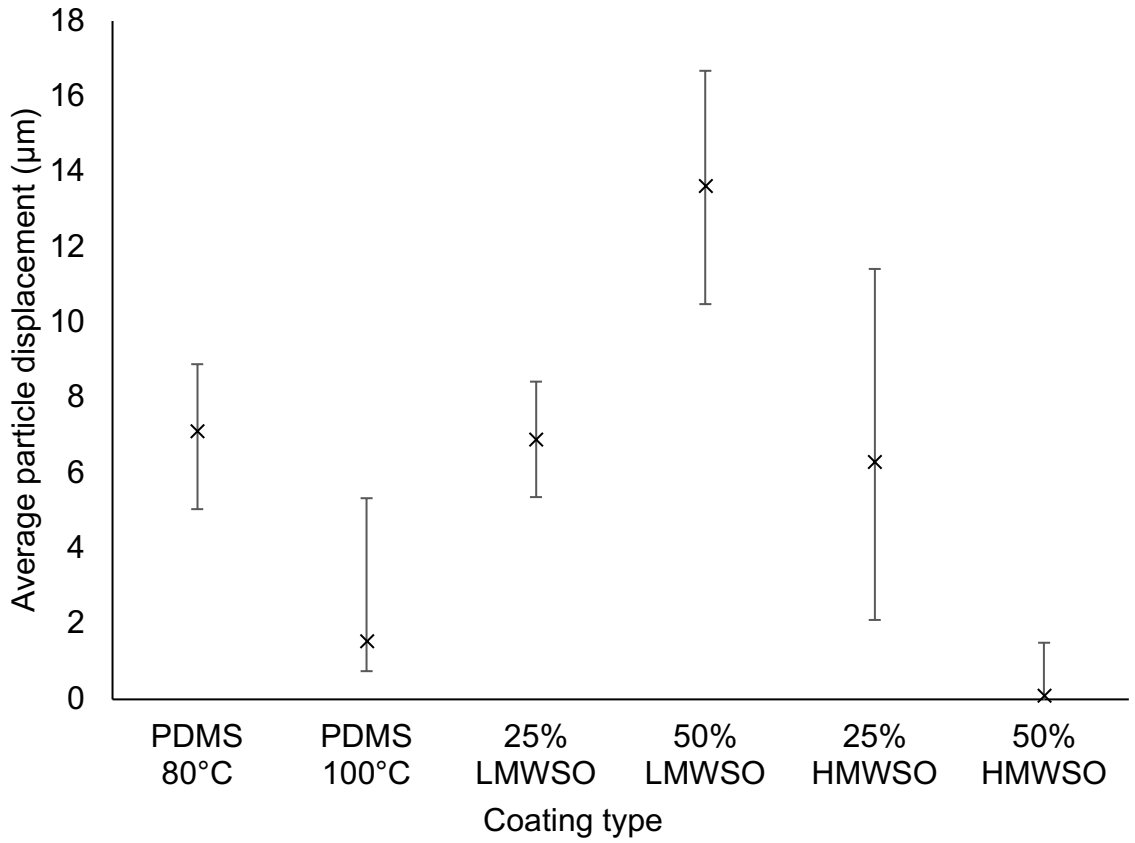

Figure 8.9 – Average permanent particle displacement for each coating type, with range bars.

Visual inspection of the displacement of the 25% HMWSO specimen and its embedded particles in Figure 8.10 shows negligible local displacement between the particles. Features have been highlighted for comparison between the initial and final positions. The particle displacement is very uniform and in the direction of the push test. This was found across all the specimens, including the 50% LMWSO specimen. No local displacement was observed during the test.

Figure 8.10 shows the movement of the entire specimen, due to slack in the fixtures of the microtribometer. As described in Section 8.2.4, the displacement of the specimen was subtracted from the displacement of the particles to determine their true displacement. The order of magnitude of the specimen displacement was approximately 50 times greater than the displacement of the particles.

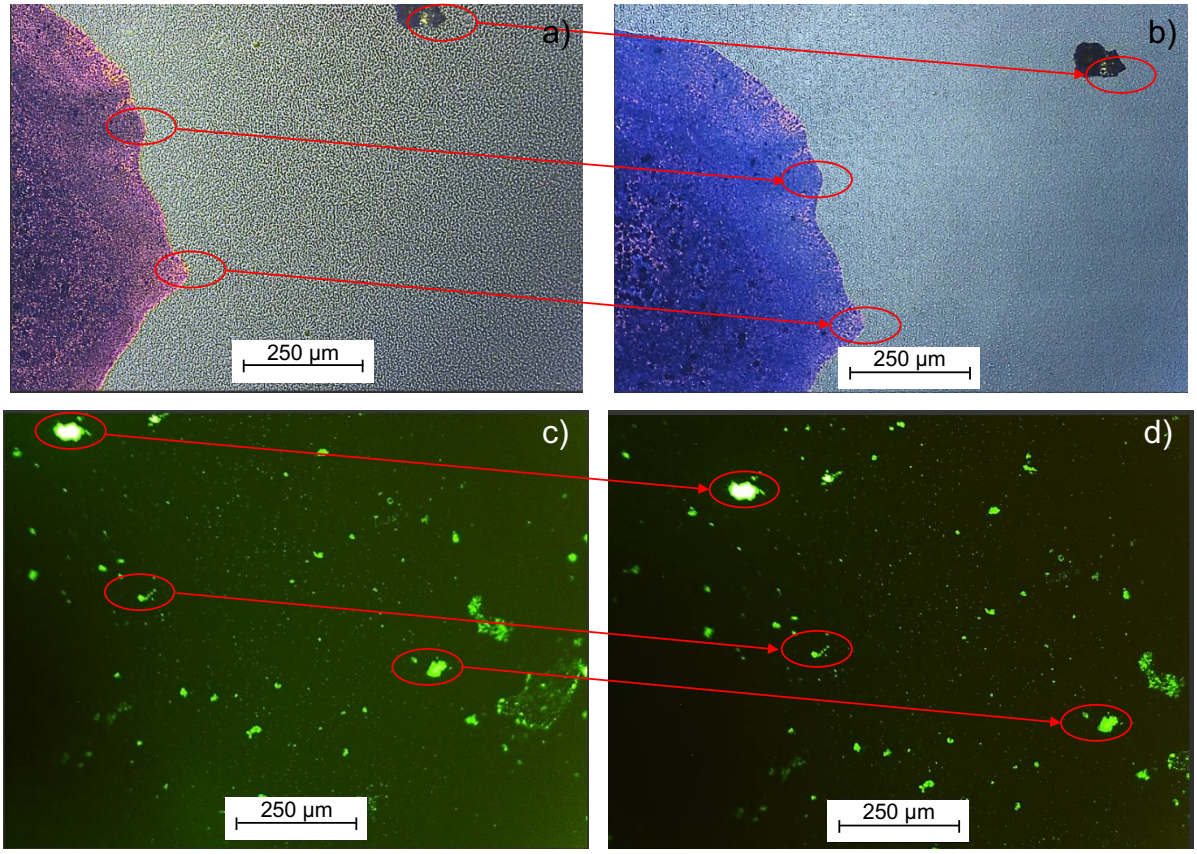

Figure 8.10 – Micrographs showing the a) initial specimen position, b) final specimen position, c) initial particle positions and d) final particle positions in the 25% HMWSO specimen. Common features across the initial and final positions are circled, with arrows showing the change in position after the test

Despite being unable to visually observe local particle movement, the range bars in Figure 8.9 show variation in the five displacement measurements taken for each specimen. This may indicate some small local movement indistinguishable by eye. However, the measurements were performed manually, and the error in the measurements is around ± 2 µm. This means the results for the PDMS 80°C, 25% LMWSO and 50% HMWSO specimens do not conclusively show either local or global permanent displacement.

8.3.4. Interpretation of results

Ultimately the findings are inconclusive. Uncertainty in the manual measurements means only the PDMS 100%, 50% LMWSO and the 25% HMWSO specimens showed significant permanent global displacement. At no point was there visually identifiable local displacement on any of the specimens, which would be indicative of flow.

Differences between the particle movement observed here and by Zhang Newby and Chaudry. (1997) and Regulagadda et al. (2022) lend further doubt.

The 50% LMWSO coating had the lowest elastic modulus, lowest ice adhesion strength and greatest particle displacement. These observations suggest that the 50% LMWSO coating has the greatest mobility, which would make it the most likely to demonstrate interfacial slippage. However, similar results would be expected in the other oil-infused coatings, especially the 50% HMWSO coating which has very similar physical properties and icephobicity to the 50% LMWSO.

Though the interfacial slippage results are inconclusive, these findings do support the broader observation that the 50% LWMSO coating would be the best choice for anti-icing solutions,.

It should also be noted that the ice adhesion strength results in Chapter 5 contribute to the uncertainty in the findings. The results found a good correlation with *G,* which would suggest interfacial slippage, but the shape of the curves suggested cavitation.

Questions remain as to whether interfacial slippage truly is present at ice-elastomer interfaces. These will be discussed in the following section.

8.4. Further considerations and future work

The results in this chapter did not provide clear observation of interfacial slippage during de-icing of elastomer coatings. It may be that interfacial slippage did occur but was not clearly observed due to the experimental methodology employed. Alternatively, the experimental parameters could be outside the values in which interfacial slippage can occur. This could be improved via better understanding and definition of the principles of interfacial slippage.

This section will address both possibilities.

8.4.1. Improving experimental methodology

The absence of clear observation of interfacial slippage may be a result of the experimental method, rather than the absence of interfacial slippage itself. There were some assumptions made during the design which may have affected the ability to observe interfacial slippage. Improvements to the experimental method are detailed here.

8.4.1.1. Particle depth

Firstly, the depth of the microparticles in the coating. The intended particle depth was ≤ 10 µm, to hopefully account for a possible flow gradient within the coating. The closer

the particles to the surface, the better chance they would demonstrate flow at the surface. However, only half of the specimens were in this range, the other three were up to 3 times deeper. It is possible that, if there were a flow gradient in the coating, the velocity at the examined particle depth was negligible. To investigate this possibility, further studies at consistent, shallower particle depths would be advised, aiming to get the particles as close to the surface as possible while remaining embedded.

8.4.1.2. Embedding technique

A further consideration in the particle embedding is the presence of two coating layers, with the particles at the interface. An assumption was made in the experimental design that the presence of an interface would not significantly affect the possible particle flow. However, it is possible the small shear forces during de-icing experience losses when being transmitted across the interface. This could lead to an imbalance in the shear strains in the layers which prevents the particles from flowing. For example, if the top layer is flowing but the bottom layer is not, the particles may be restricted from flowing because they are partially embedded in the bottom layer.

This design arose as a solution to embedding the particles in the coating from an aqueous suspension. An ideal solution to this would be to develop hydrophobic microparticles dispersed in a non-polar solvent, which could be added directly into the prepolymer mixture without the need to be removed from aqueous suspension first. This would also improve the slight issue of particle aggregation that occurred. Though the particles were dispersed across the entire coating, they tended to clump together, which made the distribution uneven.

Alternatively, only embedding the particles in the top layer, rather than top and bottom, could improve any issue of strain mismatch across the layers preventing particle movement. This could be attempted by depositing the aqueous solution on the bottom layer after it has already cured, evaporating the water and then spray coating, so the particles are only embedded in the top layer.

8.4.1.3. Particle tracking

The measurement of particle displacement could also be improved. Rather than manual measurements, tracking the particles during de-icing through a system like direct image correlation, particle velocimetry or specialised image post-processing could provide more accurate and comprehensive displacement measurements. Using

faster frame rates and equipment less sensitive to out of plane movement would also improve particle tracking ability.

8.4.2. Improving understanding of interfacial slippage

8.4.2.1. Phenomenological definition of interfacial slippage

As stated in the introduction, interfacial slippage is the ability of a surface at an interface to flow under shear stress – essentially having non-zero slip at a boundary. Beyond this definition, the precise implications and requirements of interfacial slippage are unclear in much of its discussion.

For example, there is debate as to whether interfacial slippage can be even considered a detachment mechanism, as it has been associated with sliding along a surface (Regulagadda et al., 2022) instead of complete separation. Complete detachment only occurs if the ice reaches the limits of the surface; if the shear force is removed before the edge of the surface, the ice will remain attached. In interfacial cavitation, detachment is instant and not recovered. The force required for interfacial slippage is therefore different than for interfacial cavitation. This is reflected in the strain rate dependence of sliding observed by Regulagadda (2022). It is possible that at high strain rates, interfacial cavitation occurs and the peak force is greater than at low strain rates, at which slippage occurs. A thorough study of the phenomenological differences of these mechanisms on real surface de-icing has not been undertaken.

8.4.2.2. Dedicated ice-elastomer parametric studies

The field would also be improved by better understanding of the limiting parameters for interfacial slippage, specifically with respect to ice-elastomer interfaces. Much of the existing evidence for interfacial slippage at polymer interfaces has been carried out on interfaces of adhesives (Newby et al., 1995, Zhang Newby and Chaudhury, 1997) or polymer melts (Hénot et al., 2018, Migler et al., 1993). The validity of applying observations of interfacial slippage in those materials to the ice-elastomer interface is debatable, as it assumes the systems are analogous. They may have interfaces with materials of very disparate elasticity, but the physical properties of the components are different. The adhesives and polymer melts are much more fluid than the cross-linked elastomer surfaces examined here, so are more likely able to display interfacial slippage.

To this end, the molecular mobility required for interfacial slippage in an elastomer should be investigated. Though flowability may seem a binary consideration – either a material can flow or it cannot – it is likely there is a minimum mobility for interfacial slippage. This threshold has been insufficiently examined, particularly in oil-infused coatings, which have both free and cross-linked chains as conflicting contributions to mobility. The oil-infusion will reduce the cross-link density, but the impact of this on viscoelasticity and chain mobility should be more rigorously assessed.

In their studies on ice-elastomer systems, Golovin et al. identified a maximum cross-link density of 7,000 mol/m^3, beyond which the addition of oil did not improve mobility enough to allow for interfacial slippage (2016). However, they used indirect evidence, such as the shape of the force-displacement curve, to identify this transition point. A thorough investigation of this, employing direct observation methods, would add confidence to these findings. This may be complemented by further characterisation of the viscoelastic properties of the coatings, such as the loss and storage moduli of the elastomers at sub-zero temperatures.

Another important parameter is the range of strain rates at which interfacial slippage can occur for a given system. This is likely dependent on the mobility of the polymer chains in question and should be studied either analytically or experimentally for any ice-elastomer interfaces under investigation.

8.4.2.3. Flow profiles

Better characterisation of flow profiles during interfacial slippage in confined films would be beneficial. Though plug flow may be an adequate assumption in some cases, a more accurate flow profile should be determined throughout the complete depth of the film. Due to the strong adhesion of the bottom surface of the film to the substrate, it follows there must be no slippage at that interface and therefore a flow gradient must arise at some point. The flow profile would likely also be dependent on the thickness of the film, which leads to questions about a critical or optimal film thickness for interfacial slippage in a given system.

These questions remain unanswered. Further definition would give greater confidence in experimental findings about interfacial slippage in ice-elastomer interfaces.

8.5. Conclusion

A new method for investigating the presence of interfacial slippage at the ice-elastomer interface was developed, inspired by the work of Zhang Newby and Chaudhury (Newby et al., 1995) and Parkanyi (Parkanyi, 2016). A microtribometer was modified to perform a push test on an ice droplet that had been frozen in-situ on coated PETG slides. The microtribometer was mounted underneath an optical microscope fitted with fluorescent light filters.

Fluorescent microparticles were embedded by deposition of the aqueous suspension onto a partially cured coating. After curing and evaporation was complete, the particles were spray coating then fully cured again. Partially embedding the microparticles, without spray coating, proved unsuccessful in trapping the microparticles; they were removed from the coating under negligible shear force.

The particle depths measured between 8-35 μm ± 10%, 4 out of 6 of which were deeper than the desired depth of ≤ 10 μm. Observation of the microparticle movement during the push test showed similarities and differences to the observations of Regulagadda et al. (2022) and Zhang Newby and Chaudhury (1997). The particles underwent large global elastic deformation at contact, followed by gradual relaxation and oscillation during ice sliding. Upon removal of stress, full relaxation with permanent global displacement were observed. In most of the coatings this permanent displacement was small, < 2 μm. The only coatings with significant permanent displacement were the PDMS 80°C, 25% LMWSO, 50% LMWSO and 25% HMWSO specimens, in which the average permanent particle displacement exceeded the error in the measurements.

However, no particle oscillation prior to detachment was observed, nor was there visually identifiable local particle displacement, to indicate flow. Therefore, interfacial slippage was not clearly observed.

The results do support the broader recommendation from earlier chapters that the 50% LMWSO would be the best anti-icing coating, as it had the greatest permanent, global particle displacement. The results also agree with the findings of Regulagadda et al. (2022) that droplet sliding is strain rate dependent.

Suggestions for future work include refining the particle embedding technique to improve the likelihood of observing interfacial slippage; improving the particle tracking method; and further investigation into defining the bounds of interfacial slippage, particularly on ice-elastomer interfaces.

9. Conclusions

9.1. Conclusions

This study provided a comprehensive experimental study into the effect of oil-infusion on elastomer icephobicity – measuring both ice adhesion strength and freezing delay – and developed new techniques to visualise the ice-elastomer detachment mechanisms and interfacial contact of ice on damaged coatings.

The seven coatings investigated were: two PDMS coatings (cured at 80°C for two hours, and 100°C for 45 minutes respectively); four silicone-oil/PDMS coatings (two molecular weights of oil, at two concentrations – 25% and 50%, cured at 80°C for two hours); and a commercial coating (NuSil R-2180).

Ice adhesion was measured via 100 repeated push tests of ice cylinders on coating specimens using a ForceBoard™ operating at 5 mm/s and a contact height of < 1 mm. De-icing tests were performed over nine months. Freezing delay was measured via the time taken for a 0.05 ml droplet of deionised water to freeze on the coating. The endpoint was denoted by visual observation of the freezing front progression. All icephobicity testing was performed at −10°C in a cold laboratory environment with a relative humidity of 80%.

To complement the icephobicity testing, the following properties of the coating specimens were characterised: elastic modulus, contact angle, thickness, surface roughness and room temperature adhesion. Room temperature SEM and optical microscopy were utilised to image the surfaces. The influence of contributing factors was investigated by comparing changes in the icephobicity data to the findings of the additional characterisation.

As the coatings are very soft, additional durability testing was performed to determine their long-term usability. Cutting and abrasion damage was deliberately imposed on specimens while monitoring their surface characteristics and icephobicity. For the first time, cryo-FIB/SEM was used to visualise the interfacial contact between ice and damaged PDMS surfaces.

To investigate the governing ice detachment mechanisms, ice adhesion data was compared to models for interfacial cavitation and interfacial slippage. A new method was developed for visual observation of interfacial slippage. A push test was performed on ice droplets under fluorescent microscopy at 0.5 mm/min. The

movement of embedded fluorescent microparticles was tracked and analysed qualitatively and quantitatively.

From this experimental work the following conclusions were made:

i. **Oil-infusion lowers ice adhesion strength.** Adhesion strengths of the oil-infused coatings were consistently less than 50% of the non-oil infused coatings over the 100 de-icing tests. The non-oil infused coatings also had instances of high outlier tests, in which the ice adhesion strength was higher than the accepted definition of ‘icephobic’. This was not caused by morphological changes and occurred with increasing frequency, reducing the long-term viability of non-oil infused elastomers as anti-icing coatings.

ii. **Shear modulus has the greatest influence on the ice adhesion strength**. This is when compared against contact angle, coating thickness or work of adhesion. Fitting ice adhesion strength to models for interfacial cavitation and interfacial slippage showed a better correlation to slippage.

iii. **Oil-infusion does not affect freezing delay.** Freezing delay on bare aluminium was improved by an average of 84 s. There was little difference in the freezing delay times of the coatings, though the NuSil R-2180 had a slightly lower freezing delay time than the PDMS-based elastomers. De-icing caused a small decrease in the measured freezing delays. The frequency of indefinite nucleation delay was significant on the coatings before and after de-icing.

iv. **Only severe damage to the surfaces impairs the icephobicity**. De-icing does not cause significant damage to the specimens or changes in the ice adhesion strength. The oil-infused coatings are more susceptible to damage but retain good icephobicity unless large scale cohesive fracture occurs.

v. **Both Cassie-Baxter and Wenzel wetting states are present on abraded PDMS coatings.** Cryo-FIB/SEM imaging showed mixed conformation at the ice-PDMS interface, dependent on the geometry of the asperities and gouges. Scalpel-cut edges initiated crack growth in the ice. The ice did not penetrate the scalpel cut at the edges of the droplet, but may have done so in the middle of the droplet.

vi. **The coatings can be repaired by spray coating.** Excluding the NuSil R-2180, all the coatings can be easily resprayed. This reverses the effect of damage and returns the coatings to their original performance.

vii. **Visualisation of interfacial slippage was inconclusive.** Ice droplets slid along the coating at the slower detachment speed, suggesting strain rate dependence of detachment mechanisms. Microparticle tracking showed oscillation and gradual relaxation during sliding, but local displacement was not visually identifiable.

viii. **The best anti-icing coating in this study is 50% LMWSO.** It had the lowest ice adhesion strength and shear modulus of all the coatings, commensurate freezing delay, and greater damage resistance than the 50% HMWSO. It demonstrated the greatest fluorescent microparticle displacement and highest likelihood of promoting interfacial slippage.

ix. **Oil-infused elastomers are better anti-icing coatings than non-oil infused elastomers.** They would also be a significant improvement on bare metal surfaces. Their usage would reduce the energy, costs, labour, and hazards associated with ice-accumulation and de-icing.

9.2. Future work

Though the study addressed the initial objectives, additional questions were raised during testing.

i. The biggest unresolved question is the occurrence of interfacial slippage. Recommendations for future work include improvements to the experimental method, such as better embedding of the particles within the surface and better particle tracking methods, and clearer definitions of the parameters limiting interfacial slippage.

ii. An unexpected finding was the instances of high outlier tests in the ice adhesion of the non-oil infused coatings. This had not been observed in the literature previously. Visual examination of the surfaces showed morphological changes could not account for the drastic increase in adhesion. It is possible some other surface phenomenon is the cause. For example, the removal of free chains

from the elastomer during de-icing may cause temporary or local differences in the coating's properties and influence the detachment mechanism.

iii. The cryo-FIB/SEM imaging designed in this work could be extended to the other coatings, to see if there is a difference in the interfacial contact of the different coating types. Investigating whether the observations about re-entrant geometries hold true on the other coatings would improve understanding of the changes in interfacial contact caused by abrasive damage. Deeper cross-sections of the scalpel-cut interfaces would also provide more clarity on the ability of ice droplets to penetrate the scalpel cut.

iv. To improve the understanding of how these coatings perform in real icing scenarios, steps could be taken to simulate realistic icing processes. This could be achieved in a laboratory setting, or by field work in cold climates.

9.3. Developing coatings for real applications

The data produced in this work showed that the oil-infused coatings were better anti-icing coatings than non-oil infused coatings, having lower ice adhesion strengths and similar freezing delay times, and not significantly worsened by wear. Specifically, the 50% LMWSO coating showed most promise. However, these observations should primarily be used as an initial, broad assessment of the coating's icephobicity as the methods and test conditions used in this work do not accurately reflect real, environmental icing and de-icing conditions. To progress the 50% LMWSO coating (or any coating) from this exploratory stage to use in a real application, or to make finer comparisons between the coatings, further steps are needed:

i. Identification of the desired application, e.g., wind turbine blades, airplanes, power cables, road infrastructure, heat exchange surfaces, etc., and geographic location.

ii. Thorough assessment of the climatological conditions of the application, such as the temperature and humidity. This is a complex assessment, as it will vary throughout the year, the day, and by location. Application of the coating on the surfaces of transportation such as airplanes, ships, or cars must also consider the climate of each location travelled to. This will also include identifying the type of ice that may form on the surfaces, such as glaze or rime ice.

iii. The coating/s should be applied to the surface of choice, which should mimic the real surface composition and shape. The icephobicity should be tested in the real icing conditions, either in situ, or in a wind tunnel that is equipped with icing capabilities. Wind tunnel testing allows for faster and more versatile testing but may suffer slight climatic inaccuracies compared to in situ testing.

iv. As well as the icephobicity of the undamaged coating/s, testing should include durability assessments that replicate the real environment as closely as possible. This can include UV or chemical ageing to replicate sun exposure and chemical contact, as well as sandblasting or other methods to replicate surface wear. Icephobicity testing should also be performed on the damaged coatings to understand how it will change over time.

This detailed testing is expensive and time-consuming. It should be carried out after initial icephobicity testing (using methods such as those in this work) has been performed and coatings, such as the 50% LMWSO, have been identified as being of further interest for anti-icing applications.

References

ADAM, N. K. 1957. Use of the Term 'Young's Equation' for Contact Angles. *Nature,* 180**,** 809-810.

ALIZADEH, A., YAMADA, M., LI, R., SHANG, W., OTTA, S., ZHONG, S., GE, L., DHINOJWALA, A., CONWAY, K. R., BAHADUR, V., VINCIQUERRA, A. J., STEPHENS, B. & BLOHM, M. L. 2012. Dynamics of Ice Nucleation on Water Repellent Surfaces. *Langmuir,* 28**,** 3180-3186.

ANDERSSON, L.-O., GOLANDER, C.-G. & PERSSON, S. 1994. Ice adhesion to rubber materials. *Journal of Adhesion Science and Technology,* 8**,** 117-132.

ANDREWS, E. H., MAJID, H. A. & LOCKINGTON, N. A. 1984. Adhesion of ice to a flexible substrate. *Journal of Materials Science,* 19**,** 73-81.

ARIANPOUR, F., FARZANEH, M. & KULINICH, S. A. 2013. Hydrophobic and ice-retarding properties of doped silicone rubber coatings. *Applied Surface Science,* 265**,** 546-552.

BADER, H. 1964. Density of ice as a funciton of temperature and stress.

BARTHWAL, S., LEE, B. & LIM, S.-H. 2019. Fabrication of robust and durable slippery anti-icing coating on textured superhydrophobic aluminum surfaces with infused silicone oil. *Applied Surface Science,* 496**,** 143677.

BARTHWAL, S. & LIM, S.-H. 2019. Rapid fabrication of a dual-scale micro-nanostructured superhydrophobic aluminum surface with delayed condensation and ice formation properties. *Soft Matter,* 15**,** 7945-7955.

BEEMER, D. L., WANG, W. & KOTA, A. K. 2016. Durable gels with ultra-low adhesion to ice. *Journal of Materials Chemistry A,* 4**,** 18253-18258.

BI, Y., CAO, B. & LI, T. 2017. Enhanced heterogeneous ice nucleation by special surface geometry. *Nature Communications,* 8**,** 15372.

BIXLER, G. D. & BHUSHAN, B. 2013. Fluid drag reduction and efficient self-cleaning with rice leaf and butterfly wing bioinspired surfaces. *Nanoscale,* 5**,** 7685-7710.

BLESZYNSKI, M. & CLARK, E. 2021. Current Ice Adhesion Testing Methods and the Need for a Standard: A Concise Review. *Standards,* 1**,** 117-133.

BONN, D., EGGERS, J., INDEKEU, J., MEUNIER, J. & ROLLEY, E. 2009. Wetting and spreading. *Reviews of Modern Physics,* 81**,** 739-805.

References

BRASSARD, J.-D., LAFORTE, C., GUERIN, F. & BLACKBURN, C. 2018. Icephobicity: Definition and Measurement Regarding Atmospheric Icing. *In:* WOHL, C. J. & BERRY, D. H. (eds.) *Contamination Mitigating Polymeric Coatings for Extreme Environments.* Cham: Springer International Publishing.

BROCHARD, F. & DE GENNES, P. G. 1992. Shear-dependent slippage at a polymer/solid interface. *Langmuir,* 8**,** 3033-3037.

BROUNSTEIN, Z., ZHAO, J., GELLER, D., GUPTA, N. & LABOURIAU, A. 2021. Long-Term Thermal Aging of Modified Sylgard 184 Formulations. *Polymers,* 13**,** 3125.

CAI, L., WANG, R., HOU, P. & ZHANG, X. 2011. Study on restraining frost growth at initial stage by hydrophobic coating and hygroscopic coating. *Energy and Buildings,* 43**,** 1159-1163.

CAMPBELL, J. M., MELDRUM, F. C. & CHRISTENSON, H. K. 2017. Observing the formation of ice and organic crystals in active sites. *Proceedings of the National Academy of Sciences,* 114**,** 810-815.

CAO, P., CHEN, Z., CAO, H., CHEN, B. & ZHENG, Z. 2020. Anti-icing performance of hydrophobic material used for electromechanical drill applied in ice core drilling. *Journal of Glaciology,* 66**,** 618-626.

CAO, Y., TAN, W. & WU, Z. 2018. Aircraft icing: An ongoing threat to aviation safety. *Aerospace Science and Technology,* 75**,** 353-385.

CASSIE, A. B. D. & BAXTER, S. 1944. Wettability of porous surfaces. *Transactions of the Faraday Society,* 40**,** 546-551.

CHANG, S. E., MCDANIELS, T. L., MIKAWOZ, J. & PETERSON, K. 2007. Infrastructure failure interdependencies in extreme events: power outage consequences in the 1998 Ice Storm. *Natural Hazards,* 41**,** 337-358.

CHAUDHURY, M. K. & KIM, K. H. 2007. Shear-induced adhesive failure of a rigid slabin contact with a thin confined film. *The European Physical Journal E,* 23**,** 175-183.

CHEN, D., GELENTER, M. D., HONG, M., COHEN, R. E. & MCKINLEY, G. H. 2017. Icephobic Surfaces Induced by Interfacial Nonfrozen Water. *ACS Applied Materials & Interfaces,* 9**,** 4202-4214.

CHERNYAK, Y. B. & LEONOV, A. I. 1986. On the theory of the adhesive friction of elastomers. *Wear,* 108**,** 105-138.

CONRAD, P., EWING, G. E., KARLINSEY, R. L. & SADTCHENKO, V. 2005. Ice nucleation on BaF2(111). *The Journal of Chemical Physics,* 122**,** 064709.

COOPER, W. A., SAND, W. R., POLITOVICH, M. K. & VEAL, D. L. 1984. Effects of icing on performance of a research airplane. *Journal of Aircraft,* 21**,** 708-715.

CUI, W. & PAKKANEN, T. A. 2020. Fabrication of transparent icephobic surfaces with self-reparability: Effect of structuring and thickness of the lubricant-elastomer layer. *Applied Surface Science,* 504**,** 144061.

DAHLBERG, T., STANGNER, T., ZHANG, H., WIKLUND, K., LUNDBERG, P., EDMAN, L. & ANDERSSON, M. 2018. 3D printed water-soluble scaffolds for rapid production of PDMS micro-fluidic flow chambers. *Scientific Reports,* 8**,** 3372.

DOGRU, S., AKSOY, B., BAYRAKTAR, H. & ALACA, B. E. 2018. Poisson's ratio of PDMS thin films. *Polymer Testing,* 69**,** 375-384.

DOTAN, A., DODIUK, H., LAFORTE, C. & KENIG, S. 2009. The Relationship between Water Wetting and Ice Adhesion *Journal of Adhesion Science and Technology,* 23**,** 1907-1915.

DOU, R., CHEN, J., ZHANG, Y., WANG, X., CUI, D., SONG, Y., JIANG, L. & WANG, J. 2014. Anti-icing Coating with an Aqueous Lubricating Layer. *ACS Applied Materials & Interfaces,* 6**,** 6998-7003.

DU, P., LIN, I., LU, H. & ZHANG, X. 2010. Extension of the beam theory for polymer bio-transducers with low aspect ratios and viscoelastic characteristics. *Journal of Micromechanics and Microengineering,* 20**,** 95016-13.

EMELYANENKO, K. A., EMELYANENKO, A. M. & BOINOVICH, L. B. 2020. Water and Ice Adhesion to Solid Surfaces: Common and Specific, the Impact of Temperature and Surface Wettability. *Coatings,* 10**,** 648.

ENDRES, M., SOMMERWERK, H., MENDIG, C., SINAPIUS, M. & HORST, P. 2017. Experimental study of two electro-mechanical de-icing systems applied on a wing section tested in an icing wind tunnel. *CEAS Aeronautical Journal,* 8**,** 429-439.

ESKANDARI, A., LEOW, T. C., RAHMAN, M. B. A. & OSLAN, S. N. 2020. Antifreeze Proteins and Their Practical Utilization in Industry, Medicine, and Agriculture. *Biomolecules,* 10**,** 1649.

FARHADI, S., FARZANEH, M. & KULINICH, S. A. 2011. Anti-icing performance of superhydrophobic surfaces. *Applied Surface Science,* 257**,** 6264-6269.

FERRICK, M. G., MULHERIN, N. D., HAEHNEL, R. B., COUTERMARSH, B. A., DURELL, G. D., TANTILLO, T. J., ST CLAIR, T., WEISER, E., CANO, R. J. & SMITH, T. M. 2006. Double lap shear testing of coating modified ice adhesion to liquid oxygen feed line bracket, space shuttle external tank.

FLETCHER, N. H. 1958. Size Effect in Heterogeneous Nucleation. *The Journal of Chemical Physics,* 29**,** 572-576.

FORTIN, G. & PERRON, J. 2012. Ice Adhesion Models to Predict Shear Stress at Shedding. *Journal of Adhesion Science and Technology,* 26**,** 523-553.

GALLIANO, A., BISTAC, S. & SCHULTZ, J. 2003. Adhesion and friction of PDMS networks: molecular weight effects. *Journal of Colloid and Interface Science,* 265**,** 372-379.

GAO, S., LIU, B., PENG, J., ZHU, K., ZHAO, Y., LI, X. & YUAN, X. 2019. Icephobic Durability of Branched PDMS Slippage Coatings Co-Cross-Linked by Functionalized POSS. *ACS Applied Materials & Interfaces*.

GEVAUX, L., LEJARS, M., MARGAILLAN, A. & BRESSY, C. 2018. Water erodible coatings based on a hydrolyzable PDMS/polyester network. *Materials Today Communications,* 17**,** 517-526.

GHATAK, A., MAHADEVAN, L. & CHAUDHURY, M. K. 2005. Measuring the Work of Adhesion between a Soft Confined Film and a Flexible Plate. *Langmuir,* 21**,** 1277-1281.

GHATAK, A., VORVOLAKOS, K., SHE, H., MALOTKY, D. L. & CHAUDHURY, M. K. 2000. Interfacial Rate Processes in Adhesion and Friction. *The Journal of Physical Chemistry B,* 104**,** 4018-4030.

GOLOVIN, K., KOBAKU, S. P. R., LEE, D. H., DILORETO, E. T., MABRY, J. M. & TUTEJA, A. 2016. Designing durable icephobic surfaces. *Science Advances,* 2.

GOLOVIN, K. & TUTEJA, A. 2017. A predictive framework for the design and fabrication of icephobic polymers. *Science Advances,* 3.

GRIFFITH, M. & YAISH, M. W. F. 2004. Antifreeze proteins in overwintering plants: a tale of two activities. *Trends in Plant Science,* 9**,** 399-405.

GUERIN, F., LAFORTE, C., FARINAS, M.-I. & PERRON, J. 2016. Analytical model based on experimental data of centrifuge ice adhesion tests with different substrates. *Cold Regions Science and Technology,* 121**,** 93-99.

GUO, C., ZHANG, M. & HU, J. 2021. Icing delay of sessile water droplets on superhydrophobic titanium alloy surfaces. *Colloids and Surfaces A: Physicochemical and Engineering Aspects*, 126587.

GUO, H., LIU, M., XIE, C., ZHU, Y., SUI, X., WEN, C., LI, Q., ZHAO, W., YANG, J. & ZHANG, L. 2020. A sunlight-responsive and robust anti-icing/deicing coating based on the amphiphilic materials. *Chemical Engineering Journal,* 402, 126161.

HAEHNEL, R. & MULHERIN, N. J. I. I. S. W., SHEN, ROTTERDAM 1998. The bond strength of an ice–solid interface loaded in shear. 597-604.

HAKIMIAN, A., NAZIFI, S. & GHASEMI, H. 2020. Metrology of Ice Adhesion. *Ice Adhesion.*

HAO, Q., PANG, Y., ZHAO, Y., ZHANG, J., FENG, J. & YAO, S. 2014. Mechanism of Delayed Frost Growth on Superhydrophobic Surfaces with Jumping Condensates: More Than Interdrop Freezing. *Langmuir,* 30, 15416-15422.

HE, J., TIAN, H., YANG, K., JIE, J., CHEN, B., SHU, Z., BAO, J. & PU, M. 2022. Study on Lubrication-Photothermal Synergistic Deicing of CNT Coating on Wind Turbine Blades. *International Journal of Photoenergy,* 2022, 6094360.

HE, Z., LIU, K. & WANG, J. 2018a. Bioinspired Materials for Controlling Ice Nucleation, Growth, and Recrystallization. *Accounts of Chemical Research,* 51, 1082-1091.

HE, Z., VÅGENES, E. T., DELABAHAN, C., HE, J. & ZHANG, Z. 2017a. Room Temperature Characteristics of Polymer-Based Low Ice Adhesion Surfaces. *Scientific Reports,* 7, 42181.

HE, Z., WU, C., HUA, M., WU, S., WU, D., ZHU, X., WANG, J. & HE, X. 2020a. Bioinspired Multifunctional Anti-icing Hydrogel. *Matter,* 2, 723-734.

HE, Z., XIAO, S., GAO, H., HE, J. & ZHANG, Z. 2017b. Multiscale crack initiator promoted super-low ice adhesion surfaces. *Soft Matter,* 13, 6562-6568.

HE, Z., XIE, W. J., LIU, Z., LIU, G., WANG, Z., GAO, Y. Q. & WANG, J. 2016. Tuning ice nucleation with counterions on polyelectrolyte brush surfaces. 2.

HE, Z., ZHUO, Y., HE, J. & ZHANG, Z. 2018b. Design and preparation of sandwich-like polydimethylsiloxane (PDMS) sponges with super-low ice adhesion. *Soft Matter,* 14, 4846-4851.

HE, Z., ZHUO, Y., WANG, F., HE, J. & ZHANG, Z. 2020b. Design and preparation of icephobic PDMS-based coatings by introducing an aqueous lubricating layer

and macro-crack initiators at the ice-substrate interface. *Progress in Organic Coatings,* 147**,** 105737.

HEDEROS, M., KONRADSSON, P., BORGH, A. & LIEDBERG, B. 2005. Mimicking the Properties of Antifreeze Glycoproteins: Synthesis and Characterization of a Model System for Ice Nucleation and Antifreeze Studies. *The Journal of Physical Chemistry B,* 109**,** 15849-15859.

HEJAZI, V., SOBOLEV, K. & NOSONOVSKY, M. 2013. From superhydrophobicity to icephobicity: forces and interaction analysis. *Scientific Reports,* 3**,** 2194.

HEYDARI, G., THORMANN, E., JÄRN, M., TYRODE, E. & CLAESSON, P. M. 2013. Hydrophobic Surfaces: Topography Effects on Wetting by Supercooled Water and Freezing Delay. *The Journal of Physical Chemistry C,* 117**,** 21752-21762.

HOBBS, P. V. 1974. *Ice Physics,* UK, Oxford University Press.

HONG, S., WANG, R., HUANG, X. & LIU, H. 2019. Facile one-step fabrication of PHC/PDMS anti-icing coatings with mechanical properties and good durability. *Progress in Organic Coatings,* 135**,** 263-269.

HUOVINEN, E., TAKKUNEN, L., KORPELA, T., SUVANTO, M., PAKKANEN, T. T. & PAKKANEN, T. A. 2014. Mechanically Robust Superhydrophobic Polymer Surfaces Based on Protective Micropillars. *Langmuir,* 30**,** 1435-1443.

HÉNOT, M., DROCKENMULLER, É., LÉGER, L. & RESTAGNO, F. 2018. Friction of Polymers: from PDMS Melts to PDMS Elastomers. *ACS Macro Letters,* 7**,** 112-115.

IBÁÑEZ-IBÁÑEZ, P. F., JAVIER MONTES RUIZ-CABELLO, F., CABRERIZO-VÍLCHEZ, M. A. & RODRÍGUEZ-VALVERDE, M. A. 2021a. Ice adhesion of PDMS surfaces with balanced elastic and water-repellent properties. *Journal of Colloid and Interface Science*.

IBÁÑEZ-IBÁÑEZ, P. F., MONTES RUIZ-CABELLO, F. J., CABRERIZO-VÍLCHEZ, M. A. & RODRÍGUEZ-VALVERDE, M. A. 2021b. Contact line relaxation of sessile drops on PDMS surfaces: A methodological perspective. *Journal of Colloid and Interface Science,* 589**,** 166-172.

IBÁÑEZ-IBÁÑEZ, P. F., MONTES RUIZ-CABELLO, F. J., CABRERIZO-VÍLCHEZ, M. A. & RODRÍGUEZ-VALVERDE, M. A. 2022. Mechanical Durability of Low Ice Adhesion Polydimethylsiloxane Surfaces. *ACS Omega,* 7**,** 20741-20749.

IRAJIZAD, P., AL-BAYATI, A., ESLAMI, B., SHAFQUAT, T., NAZARI, M., JAFARI, P., KASHYAP, V., MASOUDI, A., ARAYA, D. & GHASEMI, H. 2019a. Stress-Localized Durable Icephobic Surfaces. *Materials Horizons*.

IRAJIZAD, P., NAZIFI, S. & GHASEMI, H. 2019b. Icephobic surfaces: Definition and figures of merit. *Advances in Colloid and Interface Science,* 269**,** 203-218.

JAFARI, R., MOMEN, G., FARZANEH, M. J. J. O. C. T. & RESEARCH 2016. Durability enhancement of icephobic fluoropolymer film. 13**,** 405-412.

JAMIL, M. I., ALI, A., HAQ, F., ZHANG, Q., ZHAN, X. & CHEN, F. 2018. Icephobic Strategies and Materials with Superwettability: Design Principles and Mechanism. *Langmuir,* 34**,** 15425-15444.

JAMIL, M. I., WANG, Q., ALI, A., HUSSAIN, M., AZIZ, T., ZHAN, X. & ZHANG, Q. 2021. Slippery Photothermal Trap for Outstanding Deicing Surfaces. *Journal of Bionic Engineering,* 18**,** 548-558.

JAMIL, M. I., ZHAN, X., CHEN, F., CHENG, D. & ZHANG, Q. 2019. Durable and Scalable Candle Soot Icephobic Coating with Nucleation and Fracture Mechanism. *ACS Applied Materials & Interfaces,* 11**,** 31532-31542.

JANJUA, Z. A., TURNBULL, B., CHOY, K.-L., PANDIS, C., LIU, J., HOU, X. & CHOI, K.-S. 2017. Performance and durability tests of smart icephobic coatings to reduce ice adhesion. *Applied Surface Science,* 407**,** 555-564.

JIANG, G., CHEN, L., ZHANG, S. & HUANG, H. 2018. Superhydrophobic SiC/CNTs Coatings with Photothermal Deicing and Passive Anti-Icing Properties. *ACS Applied Materials & Interfaces,* 10**,** 36505-36511.

JIN, Z., ZHANG, H. & YANG, Z. 2017. Experimental investigation of the impact and freezing processes of a water droplet on an ice surface. *International Journal of Heat and Mass Transfer,* 109**,** 716-724.

JOHNSTON, I. D., MCCLUSKEY, D. K., TAN, C. K. L. & TRACEY, M. C. 2014. Mechanical characterization of bulk Sylgard 184 for microfluidics and microengineering. *Journal of Micromechanics and Microengineering,* 24**,** 035017.

JUNG, K. H. 2019. Fundamental Studies on Cassie equation and Cassie-Baxter to Wenzel transition.

JUNG, S., DORRESTIJN, M., RAPS, D., DAS, A., MEGARIDIS, C. M. & POULIKAKOS, D. 2011. Are Superhydrophobic Surfaces Best for Icephobicity? *Langmuir,* 27**,** 3059-3066.

KASAAI, M. R. & FARZANEH, M. 2004. A Critical Review of Evaluation Methods of Ice Adhesion Strength on the Surface of Materials. 919-926.

KENDALL, K. 1971. The adhesion and surface energy of elastic solids. *Journal of Physics D: Applied Physics,* 4**,** 1186.

KIM, J., CHISHOLM, B. J. & BAHR, J. 2007a. Adhesion study of silicone coatings: the interaction of thickness, modulus and shear rate on adhesion force *Biofouling,* 23**,** 113-120.

KIM, J., CHISHOLM, B. J. & BAHR, J. 2007b. Adhesion study of silicone coatings: the interaction of thickness, modulus and shear rate on adhesion force. *Biofouling,* 23**,** 113-120.

KIM, P., WONG, T.-S., ALVARENGA, J., KREDER, M. J., ADORNO-MARTINEZ, W. E. & AIZENBERG, J. 2012. Liquid-Infused Nanostructured Surfaces with Extreme Anti-Ice and Anti-Frost Performance. *ACS Nano,* 6**,** 6569-6577.

KIM, Q., KO, J.-H., KIM, S. & JHE, W. 2020. GCIceNet: a graph convolutional network for accurate classification of water phases. *Physical Chemistry Chemical Physics,* 22**,** 26340-26350.

KOCH, K., BHUSHAN, B., JUNG, Y. C. & BARTHLOTT, W. 2009. Fabrication of artificial Lotus leaves and significance of hierarchical structure for superhydrophobicity and low adhesion. *Soft Matter,* 5**,** 1386-1393.

KREDER, M. J., ALVARENGA, J., KIM, P. & AIZENBERG, J. 2016. Design of anti-icing surfaces: smooth, textured or slippery? *Nature Reviews Materials,* 1**,** 15003.

KULINICH, S. A., FARHADI, S., NOSE, K. & DU, X. W. 2011. Superhydrophobic Surfaces: Are They Really Ice-Repellent? *Langmuir,* 27**,** 25-29.

LAFORTE, C. & BEISSWENGER, A. Icephobic material centrifuge adhesion test. Proceedings of the 11th International Workshop on Atmospheric Icing of Structures, IWAIS, Montreal, QC, Canada, 2005. 12-16.

LAFORTE, C., BLACKBURN, C. & PERRON, J. 2015. A Review of Icephobic Coating Performances over the Last Decade. SAE International.

LAHIFF, E., LEAHY, R., COLEMAN, J. N. & BLAU, W. J. 2006. Physical properties of novel free-standing polymer–nanotube thin films. *Carbon,* 44**,** 1525-1529.

LAROCHE, A., GRASSO, M. J., DOLATABADI, A. & BONACCURSO, E. 2020. Tensile and Shear Test Methods for Quantifying the Ice Adhesion Strength to a Surface. *Ice Adhesion.*

LEGATES, D. R. 2005. Latent Heat. *In:* OLIVER, J. E. (ed.) *Encyclopedia of World Climatology.* Dordrecht: Springer Netherlands.

LI, C., TAO, R., LUO, S., GAO, X., ZHANG, K. & LI, Z. 2018. Enhancing and Impeding Heterogeneous Ice Nucleation through Nanogrooves. *The Journal of Physical Chemistry C,* 122**,** 25992-25998.

LI, S., HOU, Y., KAPPL, M., STEFFEN, W., LIU, J. & BUTT, H.-J. 2022. Vapor Lubrication for Reducing Water and Ice Adhesion on Poly(dimethylsiloxane) Brushes. *Advanced Materials,* 34**,** 2203242.

LI, W., ZHANG, X., YANG, J. & MIAO, F. 2013. In situ growth of superhydrophobic and icephobic films with micro/nanoscale hierarchical structures on the aluminum substrate. *Journal of Colloid and Interface Science,* 410**,** 165-171.

LIN, G., ZHANG, Q., DIKIN, D. A. & YIN, J. 2018. Constrained droplet base in condensed water on carbon nanoparticle coating for delayed freezing. *Extreme Mechanics Letters,* 24**,** 38-46.

LIU, K., WANG, C., MA, J., SHI, G., YAO, X., FANG, H., SONG, Y. & WANG, J. 2016. Janus effect of antifreeze proteins on ice nucleation. *Proceedings of the National Academy of Sciences,* 113**,** 14739-14744.

LIU, M., SUN, J., SUN, Y., BOCK, C. & CHEN, Q. 2009. Thickness-dependent mechanical properties of polydimethylsiloxane membranes. *Journal of Micromechanics and Microengineering,* 19**,** 035028.

LIU, T. L. & KIM, C.-J. C. 2014. Turning a surface superrepellent even to completely wetting liquids. *Science,* 346**,** 1096-1100.

LIU, Y. & LI, G. 2012. A new method for producing “Lotus Effect” on a biomimetic shark skin. *Journal of Colloid & Interface Science,* 388**,** 235-242.

LIU, Y., WU, Y., LIU, Y., XU, R., LIU, S. & ZHOU, F. 2020. Robust Photothermal Coating Strategy for Efficient Ice Removal. *ACS Applied Materials & Interfaces,* 12**,** 46981-46990.

LIU, Z., GOU, Y., WANG, J. & CHENG, S. 2008. Frost formation on a super-hydrophobic surface under natural convection conditions. *International Journal of Heat and Mass Transfer,* 51**,** 5975-5982.

LO, C.-W., SAHOO, V. & LU, M.-C. 2017. Control of Ice Formation. *ACS Nano,* 11**,** 2665-2674.

LOBBAN, C., FINNEY, J. L. & KUHS, W. F. 1998. The structure of a new phase of ice. *Nature,* 391**,** 268-270.

LUCAS, N., DEMMING, S., JORDAN, A., SICHLER, P. & BÜTTGENBACH, S. 2008. An improved method for double-sided moulding of PDMS. *Journal of Micromechanics and Microengineering,* 18**,** 075037.

LUO, X. & MATHER, P. T. 2009. Preparation and Characterization of Shape Memory Elastomeric Composites. *Macromolecules,* 42**,** 7251-7253.

MACKLIN, W. C. 1962. The density and structure of ice formed by accretion. *Quarterly Journal of the Royal Meteorological Society,* 88**,** 30-50.

MAGHSOUDI, K., VAZIRINASAB, E., MOMEN, G. & JAFARI, R. 2021. Icephobicity and durability assessment of superhydrophobic surfaces: The role of surface roughness and the ice adhesion measurement technique. *Journal of Materials Processing Technology,* 288**,** 116883.

MAITRA, T., JUNG, S., GIGER, M. E., KANDRICAL, V., RUESCH, T. & POULIKAKOS, D. 2015. Superhydrophobicity vs. Ice Adhesion: The Quandary of Robust Icephobic Surface Design. *Advanced Materials Interfaces,* 2**,** 1500330.

MAKKONEN, L. 2012. Ice Adhesion —Theory, Measurements and Countermeasures. *Journal of Adhesion Science and Technology,* 26**,** 413-445.

MEMON, H., DE FOCATIIS, D. S. A., CHOI, K.-S. & HOU, X. 2021. Durability enhancement of low ice adhesion polymeric coatings. *Progress in Organic Coatings,* 151**,** 106033.

MEMON, H., LIU, J., DE FOCATIIS, D. S. A., CHOI, K.-S. & HOU, X. 2020. Intrinsic dependence of ice adhesion strength on surface roughness. *Surface and Coatings Technology,* 385**,** 125382.

MEULER, A. J., SMITH, J. D., VARANASI, K. K., MABRY, J. M., MCKINLEY, G. H. & COHEN, R. E. 2010. Relationships between Water Wettability and Ice Adhesion. *ACS Applied Materials & Interfaces,* 2**,** 3100-3110.

MIGLER, K. B., HERVET, H. & LEGER, L. 1993. Slip transition of a polymer melt under shear stress. *Physical Review Letters,* 70**,** 287-290.

MIGLER, K. B., MASSEY, G., HERVET, I. & LEGER, L. 1994. The slip transition at the polymer-solid interface. *Journal of Physics: Condensed Matter,* 6**,** A301.

MILLES, S., SOLDERA, M., VOISIAT, B. & LASAGNI, A. F. 2019. Fabrication of superhydrophobic and ice-repellent surfaces on pure aluminium using single and multiscaled periodic textures. *Scientific Reports,* 9**,** 13944.

MIRSHAHIDI, K. 2021. *Exploring the tensile ice adhesion strength of surfaces using a newly designed and verified measurement apparatus.* University of British Columbia.

MISHCHENKO, L., HATTON, B., BAHADUR, V., TAYLOR, J. A., KRUPENKIN, T. & AIZENBERG, J. 2010. Design of Ice-free Nanostructured Surfaces Based on Repulsion of Impacting Water Droplets. *ACS Nano,* 4**,** 7699-7707.

MOHAMMADIAN, B., ANNAVARAPU, R. K., RAIYAN, A., NEMANI, S. K., KIM, S., WANG, M. & SOJOUDI, H. 2020. Delayed Frost Growth on Nanoporous Microstructured Surfaces Utilizing Jumping and Sweeping Condensates. *Langmuir,* 36**,** 6635-6650.

MONTES RUIZ-CABELLO, F. J., BERMÚDEZ-ROMERO, S., IBÁÑEZ-IBÁÑEZ, P. F., CABRERIZO-VÍLCHEZ, M. A. & RODRÍGUEZ-VALVERDE, M. A. 2021. Freezing delay of sessile drops: Probing the impact of contact angle, surface roughness and thermal conductivity. *Applied Surface Science,* 537**,** 147964.

MULHERIN, N., HAEHNEL, R. & JONES, J. Toward developing a standard shear test from ice adhesion. Proceedings, 8th International Workshop on Atmospheric Icing Structures, 1998.

MURAKAMI, D., JINNAI, H. & TAKAHARA, A. 2014. Wetting Transition from the Cassie–Baxter State to the Wenzel State on Textured Polymer Surfaces. *Langmuir,* 30**,** 2061-2067.

MÜLLER, A., WAPLER, M. C. & WALLRABE, U. 2019. A quick and accurate method to determine the Poisson's ratio and the coefficient of thermal expansion of PDMS. *Soft Matter,* 15**,** 779-784.

NEWBY, B.-M. Z., CHAUDHURY, M. K. & BROWN, H. R. 1995. Macroscopic Evidence of the Effect of Interfacial Slippage on Adhesion. 269**,** 1407-1409.

NOSONOVSKY, M. & HEJAZI, V. 2012. Why Superhydrophobic Surfaces Are Not Always Icephobic. *ACS Nano,* 6**,** 8488-8491.

OBERLI, L., CARUSO, D., HALL, C., FABRETTO, M., MURPHY, P. J. & EVANS, D. 2014. Condensation and freezing of droplets on superhydrophobic surfaces. *Advances in Colloid and Interface Science,* 210**,** 47-57.

OLIMA, M. 2017. Mechanical Characterization of Polydimethylsiloxane.

ORTIZ-ACOSTA, D. 2012. Sylgard® Cure Inhibition Characterization. United States.

PARKANYI, T. 2016. *Rubber friction on ice: investigation of frictional heating and melt water film thickness.* University of Edinburgh.

PEREYRA, R. G., SZLEIFER, I. & CARIGNANO, M. A. 2011. Temperature dependence of ice critical nucleus size. *The Journal of Chemical Physics,* 135**,** 034508.

PETRENKO, V. & WHITWORTH, R. 1999. Thermal properties of ice. Physics of ice. Oxford University Press, Oxford.

POOTS, G. & MAKKONEN, L. 2000. Models for the growth of rime, glaze, icicles and wet snow on structures. *Philosophical Transactions of the Royal Society of London. Series A: Mathematical, Physical and Engineering Sciences,* 358**,** 2913-2939.

PRITCHARD, R. H., LAVA, P., DEBRUYNE, D. & TERENTJEV, E. M. 2013. Precise determination of the Poisson ratio in soft materials with 2D digital image correlation. *Soft Matter,* 9**,** 6037-6045.

QIAN, C., LI, Q. & CHEN, X. 2020. Droplet Impact on the Cold Elastic Superhydrophobic Membrane with Low Ice Adhesion. *Coatings,* 10**,** 964.

RAMAKRISHNA, D. M. & VIRARAGHAVAN, T. 2005. Environmental Impact of Chemical Deicers – A Review. *Water, Air, and Soil Pollution,* 166**,** 49-63.

REGULAGADDA, K., GERBER, J., SCHUTZIUS, T. M. & POULIKAKOS, D. 2022. Microscale investigation on interfacial slippage and detachment of ice from soft materials. *Materials Horizons,* 9**,** 1222-1231.

RICHARD, D., CLANET, C. & QUÉRÉ, D. 2002. Contact time of a bouncing drop. *Nature,* 417**,** 811.

RYKACZEWSKI, K., ANAND, S., SUBRAMANYAM, S. B. & VARANASI, K. K. 2013. Mechanism of Frost Formation on Lubricant-Impregnated Surfaces. *Langmuir,* 29**,** 5230-5238.

RYKACZEWSKI, K., LANDIN, T., WALKER, M. L., SCOTT, J. H. J. & VARANASI, K. K. 2012. Direct Imaging of Complex Nano- to Microscale Interfaces Involving Solid, Liquid, and Gas Phases. *ACS Nano,* 6**,** 9326-9334.

RØNNEBERG, S., HE, J. & ZHANG, Z. 2019a. The need for standards in low ice adhesion surface research: a critical review. *Journal of Adhesion Science and Technology***,** 1-29.

RØNNEBERG, S., LAFORTE, C., VOLAT, C., HE, J. & ZHANG, Z. 2019b. The effect of ice type on ice adhesion. *AIP Advances,* 9**,** 055304.

RØNNEBERG, S., ZHUO, Y., LAFORTE, C., HE, J. & ZHANG, Z. 2019c. Interlaboratory Study of Ice Adhesion Using Different Techniques. *Coatings,* 9**,** 678.

SALEEMA, N., FARZANEH, M., PAYNTER, R. W. & SARKAR, D. K. 2011a. Prevention of Ice Accretion on Aluminum Surfaces by Enhancing Their Hydrophobic Properties AU -. *Journal of Adhesion Science and Technology,* 25**,** 27-40.

SALEEMA, N., SARKAR, D. K., GALLANT, D., PAYNTER, R. W. & CHEN, X. G. 2011b. Chemical Nature of Superhydrophobic Aluminum Alloy Surfaces Produced via a One-Step Process Using Fluoroalkyl-Silane in a Base Medium. *ACS Applied Materials & Interfaces,* 3**,** 4775-4781.

SAMEL, B., GRISS, P. & STEMME, G. 2007. A Thermally Responsive PDMS Composite and Its Microfluidic Applications. *Journal of Microelectromechanical Systems,* 16**,** 50-57.

SANTIAGO-ALVARADO, A., CRUZ-FELIX, A., ITURBIDE, F. & LICONA-MORÁN, B. 2014. Physical-chemical properties of PDMS samples used in tunable lenses. *International Journal of Engineering Science and Innovative Technology,* 3**,** 563-571.

SHAMSHIRI, M., JAFARI, R. & MOMEN, G. 2021. Icephobic properties of aqueous self-lubricating coatings containing PEG-PDMS copolymers. *Progress in Organic Coatings,* 161**,** 106466.

SHEN, Y., WANG, G., TAO, J., ZHU, C., LIU, S., JIN, M., XIE, Y. & CHEN, Z. 2017. Anti-Icing Performance of Superhydrophobic Texture Surfaces Depending on Reference Environments. *Advanced Materials Interfaces,* 4**,** 1700836.

SHEN, Y., WU, X., TAO, J., ZHU, C., LAI, Y. & CHEN, Z. 2019. Icephobic materials: Fundamentals, performance evaluation, and applications. *Progress in Materials Science,* 103**,** 509-557.

SHEN, Y., WU, Y., TAO, J., ZHU, C., CHEN, H., WU, Z. & XIE, Y. 2018. Spraying Fabrication of Durable and Transparent Coatings for Anti-Icing Application: Dynamic Water Repellency, Icing Delay, and Ice Adhesion. *ACS Applied Materials & Interfaces*.

SIVAKUMAR, G., JACKSON, J., CEYLAN, H. & SUNDARARAJAN, S. 2019. Effect of plasticizer on the wear behavior and ice adhesion of elastomeric coatings. *Wear,* 426-427**,** 212-218.

SIVAS, S. L., RIEGLER, B., THOMAIER, R. & HOOVER, K. 2007. A silicone-based ice-phobic coating for aircraft. *NuSil Technology LLC, 37th ISTC*.

SKOUVAKLIS, G. 2010. *Rubber Friction on Ice and Snow Surfaces*, University of Edinburgh.

SUBRAMANYAM, S. B., RYKACZEWSKI, K. & VARANASI, K. K. 2013. Ice Adhesion on Lubricant-Impregnated Textured Surfaces. *Langmuir,* 29**,** 13414-13418.

SUSOFF, M., SIEGMANN, K., PFAFFENROTH, C. & HIRAYAMA, M. 2013. Evaluation of icephobic coatings—Screening of different coatings and influence of roughness. *Applied Surface Science,* 282**,** 870-879.

TETTEH, E. Y., JEONG, M. W. & LOTH, E. Ice Shear Adhesion Test Methods Review and New In Situ Test Method. *AIAA Scitech 2021 Forum.*

TOURKINE, P., LE MERRER, M. & QUÉRÉ, D. 2009. Delayed Freezing on Water Repellent Materials. *Langmuir,* 25**,** 7214-7216.

TRANTIDOU, T., ELANI, Y., PARSONS, E. & CES, O. 2017. Hydrophilic surface modification of PDMS for droplet microfluidics using a simple, quick, and robust method via PVA deposition. *Microsystems & Nanoengineering,* 3**,** 16091.

URATA, C., DUNDERDALE, G. J., ENGLAND, M. W. & HOZUMI, A. 2015. Self-lubricating organogels (SLUGs) with exceptional syneresis-induced anti-sticking properties against viscous emulsions and ices. *Journal of Materials Chemistry A,* 3**,** 12626-12630.

URATA, C., NAGASHIMA, H., HATTON, B. D. & HOZUMI, A. 2021. Transparent Organogel Films Showing Extremely Efficient and Durable Anti-Icing Performance. *ACS Applied Materials & Interfaces,* 13**,** 28925-28937.

VARGAFTIK, N. B., VOLKOV, B. N. & VOLJAK, L. D. 1983. International Tables of the Surface Tension of Water. *Journal of Physical and Chemical Reference Data,* 12**,** 817-820.

VOETS, I. K. 2017. From ice-binding proteins to bio-inspired antifreeze materials. *Soft Matter,* 13**,** 4808-4823.

VORVOLAKOS, K. & CHAUDHURY, M. K. 1999. The Role of Interfacial Slippage in Adhesive Release. *Microstructure and Microtribology of Polymer Surfaces.* American Chemical Society.

VORVOLAKOS, K. & CHAUDHURY, M. K. 2003. The Effects of Molecular Weight and Temperature on the Kinetic Friction of Silicone Rubbers. *Langmuir,* 19**,** 6778-6787.

WAN, X., LIU, E. & QIU, E. 2021. Study on ice nucleation temperature and water freezing in saline soils. *Permafrost and Periglacial Processes,* 32**,** 119-138.

WANG, C., FULLER, T., ZHANG, W. & WYNNE, K. J. 2014a. Thickness Dependence of Ice Removal Stress for a Polydimethylsiloxane Nanocomposite: Sylgard 184. *Langmuir,* 30**,** 12819-12826.

WANG, C., GUPTA, M. C., YEONG, Y. H. & WYNNE, K. J. 2018a. Factors affecting the adhesion of ice to polymer substrates. *Journal of Applied Polymer Science,* 135**,** 45734.

WANG, C., ZHANG, W., SIVA, A., TIEA, D. & WYNNE, K. J. 2014b. Laboratory Test for Ice Adhesion Strength Using Commercial Instrumentation. *Langmuir,* 30**,** 540-547.

WANG, D., BA, D., HAO, Z., LI, Y., SUN, F., LIU, K., DU, G. & MEI, Q. 2018b. A novel approach for PDMS thin films production towards application as substrate for flexible biosensors. *Materials Letters,* 221**,** 228-231.

WANG, F., SUN, Y., LIANG, W., HE, H., YANG, B. & BONSU, A. O. 2021. The three-line synergistic icephobicity of conductive CNTs/PDMS nanocomposite with bio-inspired hierarchical surface. *Surfaces and Interfaces,* 26**,** 101424.

WANG, F., TAY, T. E., SUN, Y., LIANG, W. & YANG, B. 2019. Low-voltage and -surface energy SWCNT/poly(dimethylsiloxane) (PDMS) nanocomposite film: Surface wettability for passive anti-icing and surface-skin heating for active deicing. *Composites Science and Technology,* 184**,** 107872.

WANG, Y., YAO, X., WU, S., LI, Q., LV, J., WANG, J. & JIANG, L. 2017. Bioinspired Solid Organogel Materials with a Regenerable Sacrificial Alkane Surface Layer. 29**,** 1700865.

WEI, C., JIN, B., ZHANG, Q., ZHAN, X. & CHEN, F. 2018. Anti-icing performance of super-wetting surfaces from icing-resistance to ice-phobic aspects: Robust hydrophobic or slippery surfaces. *Journal of Alloys and Compounds,* 765**,** 721-730.

WENZEL, R. N. 1936. RESISTANCE OF SOLID SURFACES TO WETTING BY WATER. *Industrial & Engineering Chemistry,* 28**,** 988-994.

WOLL, T. R. 2018. *Ice Adhesion Analysis of Severely Aged PDMS Rubbers.* 10841332 M.S., University of Denver.

WONG, T.-S., KANG, S. H., TANG, S. K. Y., SMYTHE, E. J., HATTON, B. D., GRINTHAL, A. & AIZENBERG, J. 2011. Bioinspired self-repairing slippery surfaces with pressure-stable omniphobicity. *Nature,* 477**,** 443.

WORK, A. & LIAN, Y. 2018. A critical review of the measurement of ice adhesion to solid substrates. *Progress in Aerospace Sciences,* 98**,** 1-26.

WORK, A. H., GYEKENYESI, A. L., KREEGER, R. E., SALEM, J. A., VARGAS, M. M. & DRABIAK, D. R. The adhesion strength of impact ice measured using a modified lap joint test. AIAA Aviation Forum, 2018.

WU, D., ZHANG, D., YE, Y., MA, L., MINHAS, B., LIU, B., TERRYN, H. A., MOL, J. M. C. & LI, X. 2019. Durable lubricant-infused anodic aluminum oxide surfaces with high-aspect-ratio nanochannels. *Chemical Engineering Journal,* 368**,** 138-147.

WU, S., DU, Y., ALSAID, Y., WU, D., HUA, M., YAN, Y., YAO, B., MA, Y., ZHU, X. & HE, X. 2020. Superhydrophobic photothermal icephobic surfaces based on candle soot. *Proceedings of the National Academy of Sciences,* 117**,** 11240-11246.

XIE, Q., HAO, T., WANG, C., KANG, Z., SHI, Z. & ZHANG, J. 2021. The Mechanical Mechanism and Influencing Factors of Ice Adhesion Strength on Ice-Phobic Coating. *Journal of Marine Science and Engineering,* 9**,** 315.

YAVAS, D., BASTAWROS, A., DAWOOD, B. & GIUFFRE, C. 2019. Characterization of Mode-II Interfacial Fracture Toughness of Ice/Metal Interfaces. SAE Technical Paper.

YEONG, Y. H., MILIONIS, A., LOTH, E. & SOKHEY, J. 2018. Self-lubricating icephobic elastomer coating (SLIC) for ultralow ice adhesion with enhanced durability. *Cold Regions Science and Technology*.

YIN, X., ZHANG, Y., WANG, D., LIU, Z., LIU, Y., PEI, X., YU, B. & ZHOU, F. 2015. Integration of Self-Lubrication and Near-Infrared Photothermogenesis for Excellent Anti-Icing/Deicing Performance. 25**,** 4237-4245.

YOUNG, T. 1805. III. An essay on the cohesion of fluids. *Philosophical Transactions of the Royal Society of London,* 95**,** 65-87.

YU, Y.-S., WANG, M.-C. & HUANG, X. 2017. Evaporative deposition of polystyrene microparticles on PDMS surface. *Scientific Reports,* 7**,** 14118.

YUE, X., LIU, W. & WANG, Y. 2018. Freezing delay, frost accumulation and droplets condensation properties of micro- or hierarchically-structured silicon surfaces. *International Journal of Heat and Mass Transfer,* 126**,** 442-451.

YUE, X., LIU, W. & WANG, Y. 2019. Freezing and melting of sessile droplet on micro- and hierarchically-structured silicon surfaces. *Applied Thermal Engineering,* 161**,** 114185.

ZHANG, H., LU, X., XIN, Z., ZHANG, W. & ZHOU, C. 2018. Preparation of superhydrophobic polybenzoxazine/SiO2 films with self-cleaning and ice delay properties. *Progress in Organic Coatings,* 123**,** 254-260.

ZHANG NEWBY, B.-M. & CHAUDHURY, M. K. 1997. Effect of Interfacial Slippage on Viscoelastic Adhesion. *Langmuir,* 13**,** 1805-1809.

ZHANG NEWBY, B.-M. & CHAUDHURY, M. K. 1998. Friction in Adhesion. *Langmuir,* 14**,** 4865-4872.

ZHANG, Y., KLITTICH, M. R., GAO, M. & DHINOJWALA, A. 2017. Delaying Frost Formation by Controlling Surface Chemistry of Carbon Nanotube-Coated Steel Surfaces. *ACS Applied Materials & Interfaces,* 9**,** 6512-6519.

ZHAO, X., BI, L., KHATIR, B., SERLES, P., FILLETER, T., WULFF, J. E. & GOLOVIN, K. 2022. Crosslinking inert liquidlike polydimethylsiloxane brushes using bis-diazirine chemical insertion for enhanced mechanical durability. *Chemical Engineering Journal,* 442**,** 136017.

ZHAO, X., KHATIR, B., MIRSHAHIDI, K., YU, K., KIZHAKKEDATHU, J. N. & GOLOVIN, K. 2021. Macroscopic Evidence of the Liquidlike Nature of Nanoscale Polydimethylsiloxane Brushes. *ACS Nano,* 15**,** 13559-13567.

ZHENG, H., LIU, G., NIENHAUS, B. B. & BUDDINGH, J. V. 2022. Ice-Shedding Polymer Coatings with High Hardness but Low Ice Adhesion. *ACS Applied Materials & Interfaces*.

ZHOU, L., LIU, A., ZHOU, L., LI, Y., KANG, J., TANG, J., HAN, Y. & LIU, H. 2022. Facilely Fabricated Self-Lubricated Photothermal Coating with Long-Term Durability and External-Replenishing Property for Anti-Icing/Deicing. *ACS Applied Materials & Interfaces,* 14**,** 8537-8548.

ZHU, L., XUE, J., WANG, Y., CHEN, Q., DING, J. & WANG, Q. 2013. Ice-phobic Coatings Based on Silicon-Oil-Infused Polydimethylsiloxane. *ACS Applied Materials & Interfaces,* 5**,** 4053-4062.

ZHUO, Y., HÅKONSEN, V., HE, Z., XIAO, S., HE, J. & ZHANG, Z. 2018. Enhancing the Mechanical Durability of Icephobic Surfaces by Introducing Autonomous Self-Healing Function. *ACS Applied Materials & Interfaces,* 10**,** 11972-11978.

ZHUO, Y., LI, T., WANG, F., HÅKONSEN, V., XIAO, S., HE, J. & ZHANG, Z. 2019. An ultra-durable icephobic coating by a molecular pulley. *Soft Matter,* 15**,** 3607-3611.

ZHUO, Y., XIAO, S., AMIRFAZLI, A., HE, J. & ZHANG, Z. 2021. Polysiloxane as icephobic materials – The past, present and the future. *Chemical Engineering Journal,* 405**,** 127088.

Appendix 1: Technical drawings of microtribometer fixtures

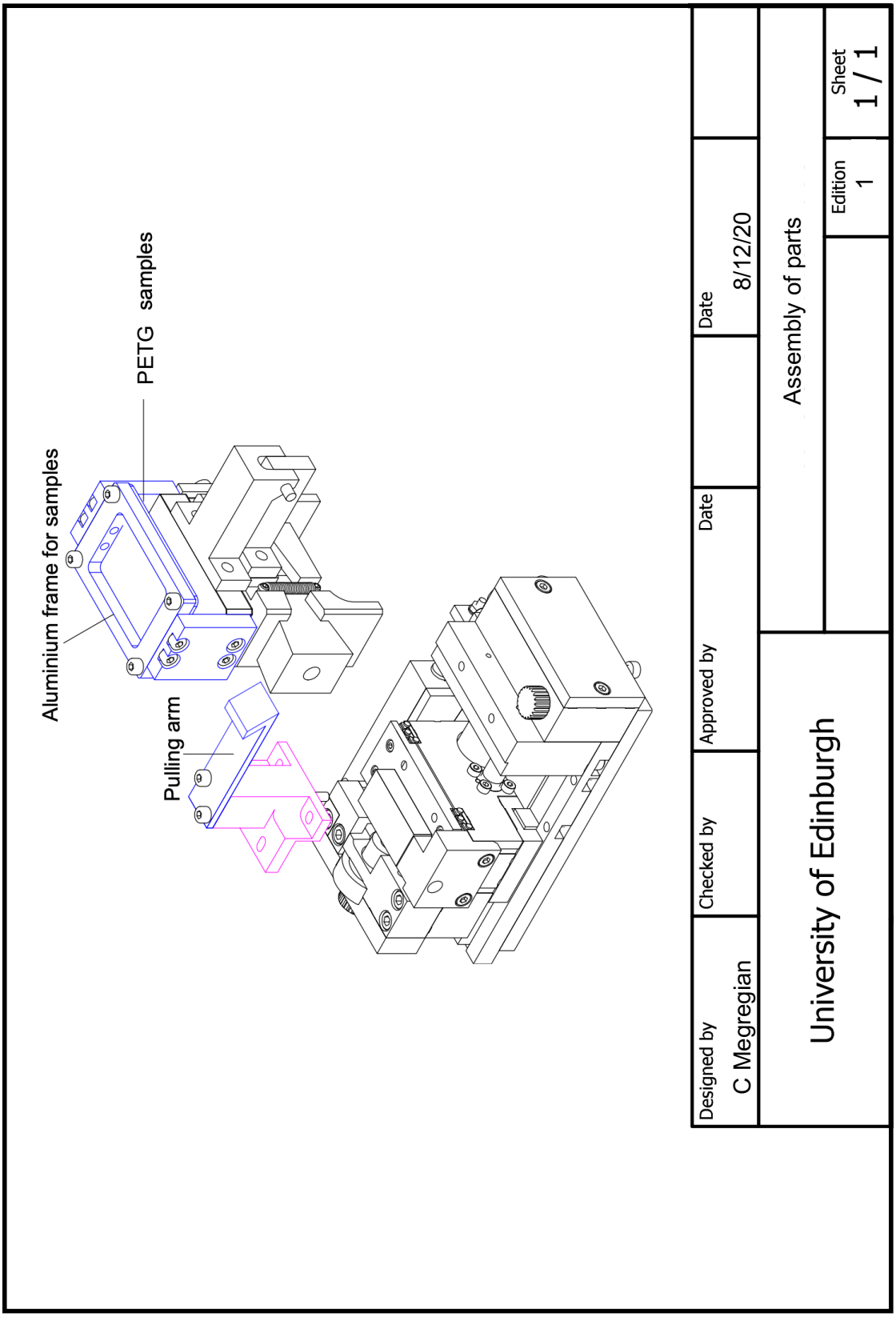

Appendix 1: Technical drawings of microtribometer fixtures

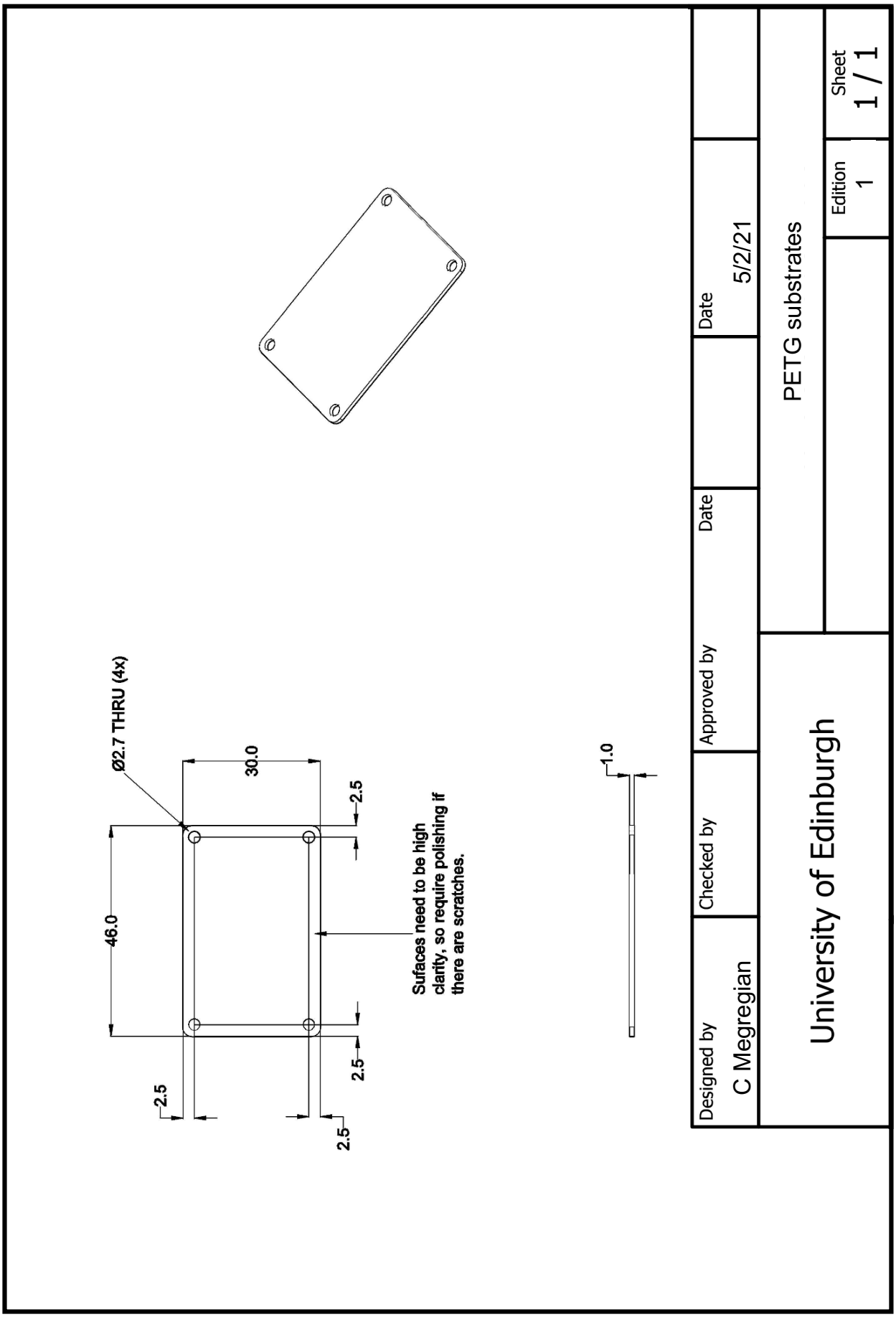

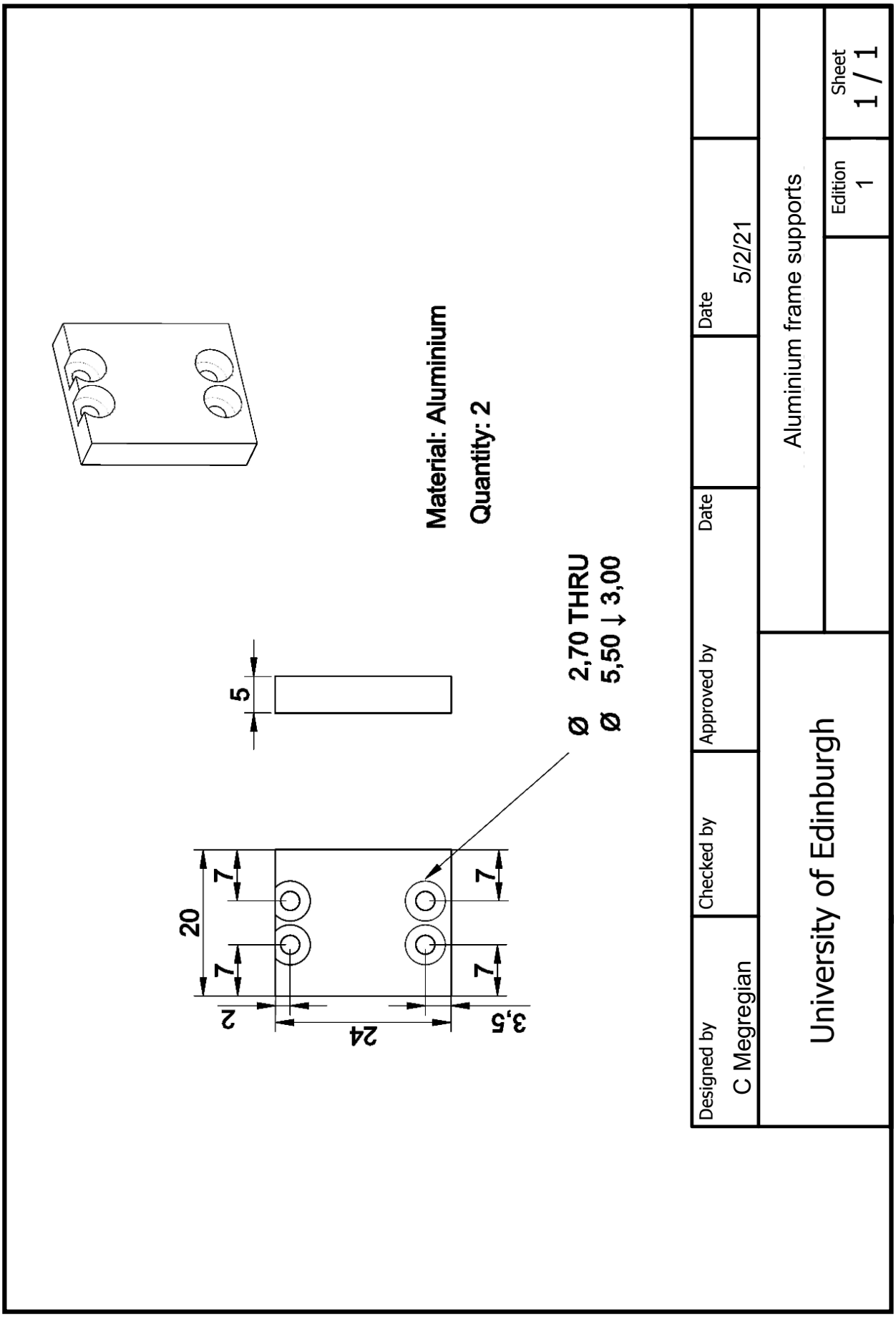
Material: Aluminium
Quantity: 2
Ø 2,70 THRU
Ø 5,50 ↓ 3,00
5
20
7
7
7
7
2
24
3,5
Designed by
C Megregian
Checked by
Approved by
Date
Date
5/2/21
Aluminium frame supports
University of Edinburgh
Edition
1
Sheet
1 / 1

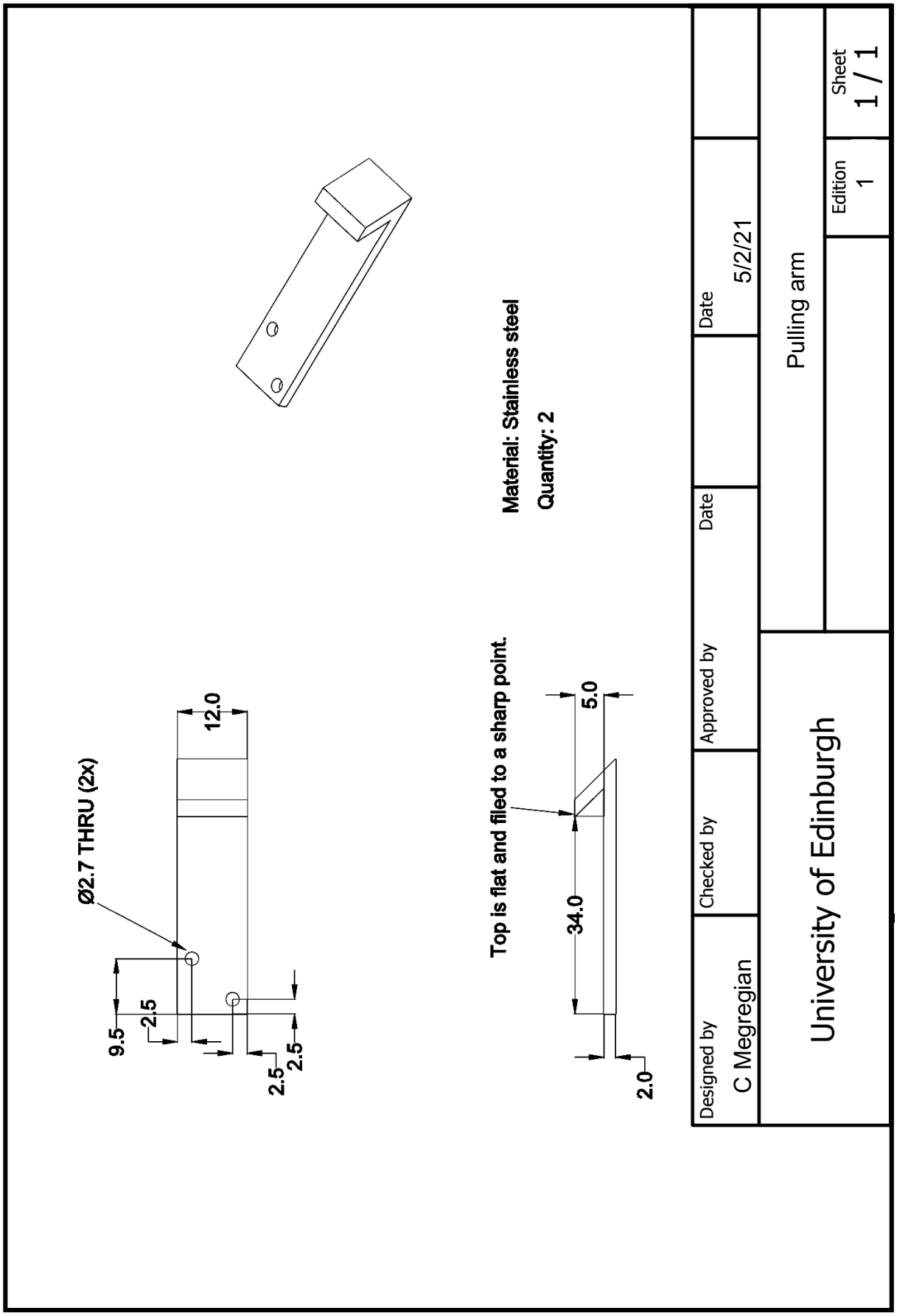
Ø2.7 THRU (2x)
12.0
9.5
2.5
2.5
2.5
Top is flat and filed to a sharp point.
5.0
34.0
2.0
Material: Stainless steel
Quantity: 2
Designed by
C Megregian
Checked by
Approved by
Date
Date
5/2/21
Pulling arm
Edition
1
Sheet
1 / 1
University of Edinburgh

Appendix 1: Technical drawings of microtribometer fixtures

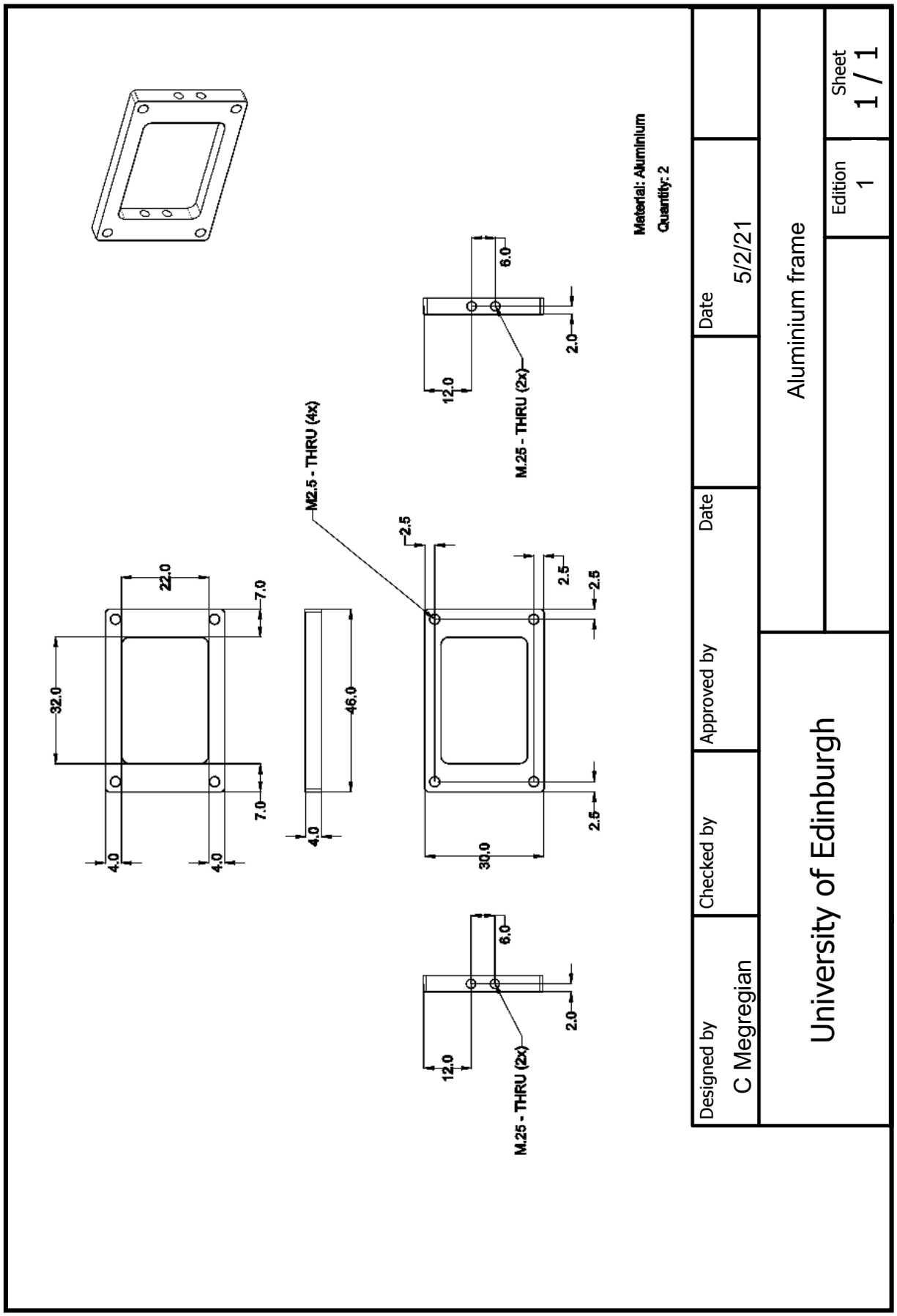

Appendix 2: Experimental protocols

Elastic modulus

1. Prepare coating formulations as described in Chapter 3.
2. Make 15 ml of silicone-based formulations, or 85 ml of NuSil R-2180.
3. Instead of pouring into mould, pour pre-polymer mixture into a petri dish of 9 mm diameter.
4. Cure thick film in the petri dish, using curing schedules in Chapter 3.
5. After curing, remove film from petri dish.
6. Using a biopsy punch, punch three 4 mm discs from the film.
7. Measure the thickness of the discs using a calliper.
8. Place disc between platens of mechanical tester (Instron 50 N).
9. Bring the top platen down so it is just in contact with the top of the specimen.
10. Compress the specimen at a rate of 20% strain/minute, up to 50% strain.
11. Convert force-displacement curves to stress-strain curves.
12. Determine elastic modulus by taking the gradient of the initial linear elastic region of the curve.
13. Repeat steps 8-12 twice. Coating elastic modulus is the average value of three specimens.

Contact angle

1. Using icephobicity specimens, place specimens on a flat surface.
2. Place a test 0.05 ml droplet of deionised water on the specimen.
3. Focus camera on droplet, keeping the centre of the camera lens at 90˚ horizontal from the droplet.
4. Place LED light source behind droplet to backlight droplets for better contrast with surroundings.
5. Remove droplet from surface by tilting specimen. Blot any remaining water using paper towel.
6. Return specimen to same position on flat surface.
7. Place a 0.05 ml droplet of deionised water on the specimen.
8. Check droplet is in focus, then take picture of the droplet.
9. Repeat steps 5-8 two more times for each specimen.
10. Using contact angle plug-in on ImageJ software, open each droplet picture and measure the contact angle of the droplet.
11. Place markers at the three-phase contact points, then around the edge of the droplet.
12. Use elliptical fit to determine thetaE, then subtract this value from 180˚ to calculate the contact angle.
13. Repeat steps 10-12 twice for each image and take the average value of the three measurements for each image.
14. Coating contact angle is the average value of both icephobicity specimens, which are the average of three images for each specimen, which are processed three times using contact angle measurement process (average of 18 angle measurements in total).

Coating thickness

1. Tape icephobicity specimen to foam block and place foam block on profilometer stage.
2. Bring stylus into contact with the specimen just outside of the coated area.
3. Run stylus profilometer (Mitutoyo SJ-410) over the specimen, starting on aluminium, passing over coated area and then falling back to the aluminium (lengthwise along specimen).
4. Stylus probe speed is 0.5 mm/s. Measurement resolution set to Auto. Measurement length is 25 mm.
5. Use profilometer step-measurement process to calculate the average thickness of the measurement.
6. Place first marker line along the substrate base, and second marker line along the lowest point on the surface of the coating (minimum coating thickness).
7. Use profilometer to calculate the difference between the substrate base depth, and the average height of the points above the minimum coating thickness.
8. Perform steps 1-7 five times along the width of the specimen, evenly spaced.
9. The average thickness of a coating is calculated from the measured thickness of all 10 traces across both icephobicity specimens

Coating roughness

1. Tape icephobicity specimen to foam block and place foam block on profilometer stage.
2. Bring stylus into contact with the specimen just inside of the coated area.
3. Run stylus profilometer (Mitutoyo SJ-410) across the specimen, remaining within the bounds of the coated area.
4. Stylus probe speed is 0.5 mm/s. Measurement resolution set to Auto. Measurement length is 15 mm.
5. Record measured value of R_a.
6. Perform steps 1-5 five times along the width of the coating and five times along the length of the coating, evenly spaced.
7. The average roughness of a coating is calculated from all 20 traces across both icephobicity specimens

Room temperature adhesion

1. Prepare coating formulations as described in Chapter 3.
2. Make 15 ml of silicone-based formulations, or 85 ml of NuSil R-2180.
3. Instead of pouring into mould, pour pre-polymer mixture into a petri dish of 9 mm diameter.
4. Cure thick film in the petri dish, using curing schedules in Chapter 3.
5. After curing, remove film from petri dish.
6. Using a biopsy punch, punch three 6 mm discs from the film.
7. Measure the thickness of the discs using a calliper.
8. Carefully roughen the discs using 400-grit paper.
9. Using cyanoacrylate glue (Loctite power gel super glue), glue disc to a 10 mm diameter steel disc (1 mm thickness), which is backed with strong adhesive tape.
10. Let glue cure for 30 minutes, then remove protective backing from adhesive tape and stick steel disc (with glued coating disc) to bottom platen of the mechanical tester (Instron 50 N).
11. Bring the top platen down so it is just in contact with the top of the specimen.
12. Compress specimen at a speed of 50 μm/s, up to 3% strain. Then immediately retract at the same speed, until force falls to 0 N and the platen detaches from the specimen.
13. Convert force-displacement curves to stress-strain curves.
14. The peak adhesive stress is determined as the lowest point on the curve.
15. Repeat steps 9-14 twice. Coating peak adhesive stress is the average value of three specimens.

Ice adhesion

1. Testing is performed inside a cold laboratory at –10ºC and 80% humidity.
2. Place icephobicity specimen on a flat surface and acrylic cylinder (10 mm internal diameter, 1 mm wall thickness, 2 cm height) on top of icephobicity specimen, in the middle.
3. Measuring with a thermocouple, chill deionised water to 1ºC and then fill cylinder with 1 ml of water.
4. Allow water to freeze overnight.
5. The following day, carefully bolt icephobicity specimen to ForceBoard™ base plate.
6. Use ForceBoard™ probe arm to detach the ice cylinder.
7. Set probe speed to 5 mm/s.
8. Convert force-time graphs to force-displacement graphs.
9. Take peak force value and convert to adhesion stress using contact area of ice cylinder.

Freezing delay

1. Testing is performed inside a cold laboratory at –10ºC and 80% humidity.
2. Place icephobicity specimen on flat surface, directly underneath the digital camera.
3. Measuring with a thermocouple, chill a beaker of deionised water to 8ºC.
4. Either a droplet was immediately placed onto the surface (ambient starting temperature), or the water was allowed to cool to the designated starting temperature.
5. Start video recording.
6. Deposit a 0.05 ml droplet of deionised water on the specimen and leave to freeze.
7. When the freezing front has reached the top of the droplet and there are no visual changes stop recording.
8. If nucleation had not occurred within 7 minutes terminate test.
9. Calculate the freezing delay time from the video recording by noting time from deposition to completion of freezing.

Damage

1. Damage to untested icephobicity tests is carried out by carefully abrading the surface with 400-grit paper manually or cutting the specimen with scalpel.
2. Scalpel cut is along the middle of the specimen, through the full depth, lengthwise.
3. Abrasion is performed by rubbing the grit paper back and forth over the entire surface, lengthwise until the surface appears cloudy and rough.

Surface repair

1. To repair damaged surfaces, prepare 2.2 ml of the pre-polymer mixtures, as described in Chapter 3 and leave for 30 minutes for bubbles to disperse.
2. Mix the pre-polymer mixture with 8.8 ml of hexane (ratio of 1:4 pre-polymer:hexane) and cover to prevent evaporation of hexane.
3. Dispense 0.2 ml of pre-polymer/hexane mixture into an airbrush.
4. Spray all 0.2 ml evenly over the surface of one damaged specimen.
5. Cure specimens as in Chapter 3.

Room temperature SEM

1. Tape icephobicity specimen to Hitachi TM4000 plus stage.
2. Mark a small box on centre of coating (approximately 3 mm x 3 mm) to keep consistent imaging area.
3. Insert stage into SEM.
4. Operate SEM with secondary electron imaging using a 5 kV accelerating voltage under a moderate vacuum.

Cryo-FIB/SEM

1. Prepare specimens in similar way to Chapter 3, with the following differences.
2. Use 10 mm steel SEM stubs and wrap with tape around the circumference to form a mould for the coating.
3. Place stubs in cold laboratory for 1 day.
4. Using the tip of a syringe, deposit small drops of deionised water on the surface. Make droplets as small as possible.
5. Freeze droplets for 1 hour, then transfer to a cryo-storage vessel for transport to the cryo-FIB/SEM facility.
6. Remove a specimen from the cryo-storage vessel, and mount into a shuttle while under a liquid nitrogen reservoir.
7. Plunge the shuttle and specimen into nitrogen slush and then into the antechamber of the cryo-FIB/SEM chamber (Zeiss Crossbeam 550).
8. Put specimen under vacuum and sputter coat with thin platinum covering then transfer into the SEM chamber.
9. Collect images of the droplet surface.
10. Coat the specimens with a second layer of platinum using a gas injection system. This second layer is approximately 1 μm thick.
11. Mill sections of the droplet-coating interface using the FIB, comprised of gallium ions, with a voltage of 30 kV and a current of 15 nA.
12. Mill and image 30 successive slices of 1 μm thickness.
13. Use a scanning beam voltage of 1.2 kV and a current of 100 pA.
14. Use both secondary electrons and back-scattered electrons to image the interface.

Interfacial slippage

1. Dilute microparticle suspension with deionised water by a factor of 2000, to lower microparticle concentration from 1% to 0.0005%.
2. Place 0.1 ml of 1% suspension in beaker and mix with 200 ml of deionised water.
3. Prepare specimens in similar way to Chapter 3, with following differences.
4. Using PETG substrates with protective film, peel off protective film and then prime. Do not clean with isopropanol and hexane before priming.
5. Tape substrates to baking tray to prevent curling during heat-curing.
6. Proceed with same method as Chapter 3, until 25% of curing time has elapsed.
7. Remove from oven and dispense 2 ml of fluorescent microparticles into mould on top of coating.
8. Return to oven and complete curing schedule.
9. Prepare 2.2 ml of the pre-polymer mixtures, as described in Chapter 3 and leave for 30 minutes for bubbles to disperse.
10. Mix the pre-polymer mixture with 8.8 ml of hexane (ratio of 1:4 pre-polymer:hexane) and cover to prevent evaporation of hexane.
11. Dispense 0.02 ml of pre-polymer/hexane mixture into an airbrush.
12. Spray all 0.02 ml evenly over the surface of one damaged specimen.
13. Cure specimens as in Chapter 3.
14. Bring specimens into cold room and leave for 1 day to acclimatise.
15. Bolt specimens into aluminium frame of Deben microtribometer (Appendix 1) with coated side facing away from frame and place on flat surface. Mark uncoated side and top of coating with ink.
16. Deposit a droplet of 0.1 ml of deionised water on the surface by syringe, above marks.
17. Leave to freeze on the surface for 1 hour then mount specimen upside-down on the microtribometer.
18. Place microtribometer and specimen underneath the microscope and record microscope feed.
19. Bring mark on uncoated side into focus, then bring microparticles into focus (using mark on top of coating to help), with fluorescent light filters in place.

20. Start test, with jaws opening at speed of 5 mm/min to bring the pulling arm into contact with the ice droplet, detaching and sliding the droplet along the surface.
21. Once the test is complete, bring the mark on the uncoated side into focus.
22. Using stills from the videos overlay starting and final positions of the particles and mark on uncoated side.
23. Using scale bar from microscope feed, measure distance moved by 5 particles and distance moved by mark on uncoated side at 5 points.
24. Take average of both sets of measurements and subtract average distance moved by mark from average distance moved by particles to get total particle displacement.

Appendix 3: Material specifications

Sylgard 184

Technical Data Sheet

SYLGARD™ 184 Silicone Elastomer

Transparent encapsulant with good flame resistance

FEATURES & BENEFITS

- Flowable
- Room temperature and heat cure
- Good dielectric properties
- Rapid, versatile cure processing controlled by temperature
- High transparency allows easy inspection of components

COMPOSITION

- Two-part
- 10 to 1 mix ratio
- Polydimethylsiloxane elastomer

APPLICATIONS

SYLGARD™ 184 Silicone Elastomer is suitable for:

- LED Lighting encapsulation
- Power supplies
- Connectors
- Sensors
- Industrial controls
- Transformers
- Amplifiers
- High voltage resistor packs
- Relays
- Adhesive/encapsulant for solar cells
- Adhesive handling beam lead integrated circuits during processing

TYPICAL PROPERTIES

Specification Writers: These values are not intended for use in preparing specifications.

Property	Unit	Result
One or Two Part		Two
Color		Colorless
Viscosity (Base)	cP	5100
	Pa-sec	5.1
Viscosity (Mixed)	cP	3500
	Pa-sec	3.5
Thermal Conductivity	btu/hr ft °F	0.15
	W/m °K	0.27
Specific Gravity (Cured)		1.03
Working Time at 25°C (Pot Life - Hours)	hours	1.5
Cure Time at 25°C	hours	48
Heat Cure Time at 100°C	minutes	35
Heat Cure Time at 125°C	minutes	20
Heat Cure Time at 150°C	minutes	10
Durometer Shore		43
Dielectric Strength	volts/mil	500
	kV/mm	19

TYPICAL PROPERTIES (Continued)

Property	Unit	Result
Volume Resistivity	ohm*cm	2.9E+14
Dissipation Factor at 100 Hz		0.00257
Dissipation Factor at 100kHz		0.00133
Dielectric Constant at 100 Hz		2.72
Dielectric Constant at 100 kHz		2.68
Linear CTE (by DMA)	ppm/°C	340
Tensile Strength	PSI	980
	MPa	6.7
	Kg/cm^2	69
Refractive Index	@ 589 nm	1.4118
Refractive Index	@ 632.8 nm	1.4225
Refractive Index	@1321 nm	1.4028
Refractive Index	@ 1554 nm	1.3997
UL RTI Rating	°C	150

DESCRIPTION

Dow silicone 10 to 1 encapsulants are supplied as two-part liquid component kits. When liquid components are thoroughly mixed, the mixture cures to a flexible elastomer, which is well suited for the protection of electrical/PCB system assembly applications. Dow silicone encapsulants cure without exotherm at a constant rate regardless of sectional thickness or degree of confinement.

Dow silicone elastomers require no post cure and can be placed in service immediately following the completion of the cure schedule. Standard silicone encapsulants require a surface treatment with a primer in addition to good cleaning for adhesion while primerless silicone encapsulants require only good cleaning.

APPLICATION METHODS

- Automated metered mixing and dispensing
- Manual mixing

MIXING AND DE-AIRING

The 10 to 1 mix ratio these products are supplied in gives one latitude to tune the modulus and hardness for specific application needs and production lines. In most cases de-airing is not required.

PREPARING SURFACES

In applications requiring adhesion, priming will be required for many of the silicone encapsulants. For best results, the primer should be applied in a very thin, uniform coating and then wiped off after application. After application, it should be thoroughly cured prior to application of the silicone elastomer. Additional instructions for primer usage can be found in the information sheets specific to the individual primers.

PROCESSING/CURING

Thoroughly mixed Dow silicone encapsulant may be poured/dispensed directly into the container in which it is to be cured. Care should be taken to minimize air entrapment. When practical, pouring/dispensing should be done under vacuum, particularly if the component being potted or encapsulated has many small voids. If this technique cannot be used, the unit should be evacuated after the silicone encapsulant has been poured/ dispensed. Dow silicone encapsulants may be either room temperature (25°C/77°F) or heat cured. Room temperature cure encapsulants may also be heat accelerated for faster cure. Ideal cure conditions for each product are given in the product selection table.

POT LIFE AND CURE RATE

Cure reaction begins with the mixing process. Initially, cure is evidenced by a gradual increase in viscosity, followed by gelation and conversion to a solid elastomer. Pot life is defined as the time required for viscosity to double after base and curing agent are mixed and is highly temperature and application dependent. Please refer to the data table.

USEFUL TEMPERATURE RANGES

For most uses, silicone elastomers should be operational over a temperature range of -45 to 200°C (-49 to 392°F) for long periods of

time. However, at both the low and high temperature ends of the spectrum, behavior of the materials and performance in particular applications can become more complex and require additional considerations and should be adequately tested for the particular end-use environment. For low-temperature performance, thermal cycling to conditions such as -55°C (-67°F) may be possible, but performance should be verified for your parts or assemblies. Factors that may influence performance are configuration and stress sensitivity of components, cooling rates and hold times, and prior temperature history. At the high-temperature end, the durability of the cured silicone elastomer is time and temperature dependent. As expected, the higher the temperature, the shorter the time the material will remain useable.

COMPATIBILITY

Certain materials, chemicals, curing agents and plasticizers can inhibit the cure of addition cure gels. Most notable of these include: Organotin and other organometallic compounds, silicone rubber containing organotin catalyst, sulfur, polysulfides, polysulfones or other sulfur containing materials, unsaturated hydrocarbon plasticizers, and some solder flux residues. If a substrate or material is questionable with respect to potentially causing inhibition of cure, it is recommended that a small scale compatibility test be run to ascertain suitability in a given application. The presence of liquid or uncured product at the interface between the questionable substrate and the cured gel indicates incompatibility and inhibition of cure.

REPAIRABILITY

In the manufacture of electrical devices and PCB system assemblies it is often desirable to salvage or reclaim damaged or defective units. With most non-silicone rigid potting/encapsulating materials, removal or entry is difficult or impossible without causing excessive damage to internal circuitry. Dow silicone encapsulants can be selectively removed with relative ease, depending on the chosen remove method and technique and repairs or changes accomplished, and the repaired area repotted in place with additional product. To remove silicone elastomers, simply cut with a sharp blade or knife and tear and remove unwanted material from the area to be repaired. Sections of the adhered elastomer are best removed from substrates and circuitry by mechanical action such as scraping or rubbing and can be assisted by applying DOWSIL™ OS Fluids to swell the elastomer. Before applying additional encapsulant to a repaired device, roughen the exposed surfaces of the cured encapsulant with an abrasive paper and rinse with a suitable solvent and dry. This will enhance adhesion and permit the repaired material to become an integral matrix with the existing encapsulant. Silicone prime coats are not recommended for adhering products to themselves.

PACKAGING INFORMATION

Multiple packaging sizes are available for this product.

USABLE LIFE AND STORAGE

Shelf life is indicated by the "Use Before" date found on the product label. Refer to the product label for storage temperature requirements. Special precautions must be taken to prevent moisture from contacting these materials. Containers should be kept tightly closed and head or air space minimized. Partially filled containers should be purged with dry air or other gases, such as nitrogen.

HANDLING PRECAUTIONS

PRODUCT SAFETY INFORMATION REQUIRED FOR SAFE USE IS NOT INCLUDED IN THIS DOCUMENT. BEFORE HANDLING, READ PRODUCT AND SAFETY DATA SHEETS AND CONTAINER LABELS FOR SAFE USE, PHYSICAL AND HEALTH HAZARD INFORMATION. THE SAFETY DATA SHEET IS AVAILABLE ON THE DOW WEBSITE AT WWW.CONSUMER.DOW.COM, OR FROM YOUR DOW SALES APPLICATION ENGINEER, OR DISTRIBUTOR, OR BY CALLING DOW CUSTOMER SERVICE.

LIMITATIONS

This product is neither tested nor represented as suitable for medical or pharmaceutical uses.

HEALTH AND ENVIRONMENTAL INFORMATION

To support customers in their product safety needs, Dow has an extensive Product Stewardship organization and a team of product safety and regulatory compliance specialists available in each area.

For further information, please see our website, www.consumer.dow.com or consult your local Dow representative.

LIMITED WARRANTY INFORMATION – PLEASE READ CAREFULLY

The information contained herein is offered in good faith and is believed to be accurate. However, because conditions and methods of use of our products are beyond our control, this information should not be used in substitution for customer's tests to ensure that our products are safe, effective, and fully satisfactory for the intended end use. Suggestions of use shall not be taken as inducements to infringe any patent.

Dow's sole warranty is that our products will meet the sales specifications in effect at the time of shipment.

Your exclusive remedy for breach of such warranty is limited to refund of purchase price or replacement of any product shown to be other than as warranted.

TO THE FULLEST EXTENT PERMITTED BY APPLICABLE LAW, DOW SPECIFICALLY DISCLAIMS ANY OTHER EXPRESS OR IMPLIED WARRANTY OF FITNESS FOR A PARTICULAR PURPOSE OR MERCHANTABILITY.

DOW DISCLAIMS LIABILITY FOR ANY INCIDENTAL OR CONSEQUENTIAL DAMAGES.

HOW CAN WE HELP YOU TODAY?

Tell us about your performance, design, and manufacturing challenges. Let us put our silicon-based materials expertise, application knowledge, and processing experience to work for you.

For more information about our materials and capabilities, visit **www.consumer.dow.com**.

To discuss how we could work together to meet your specific needs, go to **www.consumer.dow.com** for a contact close to your location. Dow has customer service teams, science and technology centers, application support teams, sales offices, and manufacturing sites around the globe.

www.sylgard.com

DOWSIL 1200 OS

Technical Data Sheet

DOWSIL™ 1200 OS Primer

Versatile, adhesion enhancing, clear primer dispersed in low molecular weight silicone fluid

Features & Benefits

- Useful for both moisture curing RTV and heat curing silicones
- Diluted in low molecular weight silicone fluid
- Meets many international regulations for low VOC content (including European Union)
- Similar to DOWSIL™ P5200 Adhesion Promoter
- Useful on most metals, glass, ceramics, masonry, wood, fabric and some plastics (including FR-4)

Applications

DOWSIL™ 1200 OS Primer enhances bonding/adhesion of RTV and heat cure silicones to many:

- Metals
- Ceramics
- Glass
- Wood
- Masonry
- Structural plastics

Typical Properties

Specification Writers: These values are not intended for use in preparing specifications.

Property	Unit	Result
Flash Point	°F	81
	°C	27
Volatile Organic Content (OS Fluid exempt)	grams/liter	112
Volatile Organic Content (OS Fluid non-exempt)	grams/liter	742
Shelf Life at 25°C	months	18

Description

Dow primers, prime coats and adhesion promoters are dilute solutions of silane coupling agents and other active ingredients. The surface reactive components typically must be applied in a very thin layer for best bonding. The solvents used in these products serve to deliver the active ingredients in a thin, uniform coating, enhance surface cleaning, and in some cases, aid in the penetration of the active ingredients into the bonding surface. Primers can be used to increase design flexibility, reduce total costs or increase performance reliability of PCB system assemblies. They do this by enabling adhesion to lower-cost substrates or lower temperature processes which reduce energy budgets, among other possibilities.

Form No. 11-1546-01 C

Application Methods

- Apply in a very light, even coat by:
  - Wiping
  - Dipping
  - Spraying
- Excess material should be wiped off to avoid over-application
- Diluting by a factor of 2 to 4 with additional solvent may avoid excessive build-up

How To Use

These products should be applied in a very light, even coat by wiping, dipping or spraying. Excess material should be wiped off to avoid overapplication, which generally appears as a white, chalky surface. When dip or spray coating, diluting by a factor of 2 to 4 with additional solvent may avoid excessive build-up. Apply additional cleaner/primer to the cloth every 3 to 5 minutes to ensure fresh material can react with the substrate.

Preparing Surfaces

The active ingredients must thoroughly wet-out and coat the bonding surfaces. Mild abrasion, solvent cleaning, plasma, corona discharge and other pre-treatments have been used to clean and enhance surface reactivity to bonding. In general, light surface abrasion is recommended whenever possible, because it promotes good cleaning and increases the surface area for bonding. Surfaces should be cleaned and/or degreased with Dow OS fluids, naphtha, mineral spirits, methyl ethyl ketone (MEK) or other suitable solvents that will remove oils and other contaminants that may be present. A final surface wipe with acetone or IPA may also be helpful. Different cleaning techniques may give better results than others.

Users should determine the best technique for their applications. For especially difficult-to-bond-to surfaces, it may be necessary to increase the surface reactivity by chemical etchants or oxidizers, or by exposing the surface to UV, corona, plasma or flame sources. Allow solvents to completely evaporate before applying the primer.

Processing/Curing

These products require moisture in the air to cure, and are generally cured at room temperature and in a range of 20 to 90 percent relative humidity for 1 to 2 hours. Low humidity and/or low temperature conditions require longer cure times. Mild heat acceleration of the cure rate may be possible but temperatures above 60°C (140°F) are not recommended. During application, the carrier solvent typically evaporates off quickly, allowing the active ingredients to begin to react with atmospheric moisture and bonding surfaces. For optimal bonding, different cure times may be required for different temperature and humidity conditions. Users should determine the best cure schedule and conditions for their applications. The desired silicone elastomer should be applied after the primer, prime coat or adhesion promoter has fully cured.

Handling Precautions

PRODUCT SAFETY INFORMATION REQUIRED FOR SAFE USE IS NOT INCLUDED IN THIS DOCUMENT. BEFORE HANDLING, READ PRODUCT AND SAFETY DATA SHEETS AND CONTAINER LABELS FOR SAFE USE, PHYSICAL AND HEALTH HAZARD INFORMATION. THE SAFETY DATA SHEET IS AVAILABLE ON THE DOW WEBSITE AT WWW.COMSUMER.DOW.COM, OR FROM YOUR DOW SALES APPLICATION ENGINEER, OR DISTRIBUTOR, OR BY CALLING DOW CUSTOMER SERVICE.

Usable Life And Storage

Shelf life is indicated by the “Use Before” date found on the product label. For best results, Dow primers, prime coats and adhesion promoters should be stored below 32°C (90°F).

Form No. 11-1546-01 C

Usable Life And Storage (Cont.)

Special precautions must be taken to prevent moisture from contacting these materials before use. Containers should be kept tightly closed and head or air space minimized. Partially filled containers should be purged with dry air or other gases such as nitrogen to maximize shelf life. Small amounts for immediate use should be poured into clean, dry containers and discarded when finished. Material should not be used once it takes on a milky appearance or a large amount of white precipitate is observed, indicating moisture contamination. Repeated opening of the container can cause a small amount of white precipitate to form inside the container cap area, which does not affect the bulk material.

Packaging Information

In general, Dow primers, prime coats and adhesion promoters are supplied in nominal 1 gallon (3.8 L) and 13.5 fl oz (400 mL) or 1 pint (473 mL) containers, net volume. Not all products may be available in all packages and some additional packages may be available for certain products.

Limitations

This product is neither tested nor represented as suitable for medical or pharmaceutical uses.

Health And Environmental Information

To support customers in their product safety needs, Dow has an extensive Product Stewardship organization and a team of product safety and regulatory compliance specialists available in each area.

For further information, please see our website, www.consumer.dow.com or consult your local Dow representative.

How Can We Help You Today?

Tell us about your performance, design, and manufacturing challenges. Let us put our silicon-based materials expertise, application knowledge, and processing experience to work for you.

For more information about our materials and capabilities, visit **www.consumer.dow.com**.

To discuss how we could work together to meet your specific needs, go to **www.consumer.dow.com** for a contact close to your location. Dow has customer service teams, science and technology centers, application support teams, sales offices, and manufacturing sites around the globe.

http://www.consumer.dow.com

LIMITED WARRANTY INFORMATION – PLEASE READ CAREFULLY

The information contained herein is offered in good faith and is believed to be accurate. However, because conditions and methods of use of our products are beyond our control, this information should not be used in substitution for customer's tests to ensure that our products are safe, effective, and fully satisfactory for the intended end use. Suggestions of use shall not be taken as inducements to infringe any patent.

Dow's sole warranty is that our products will meet the sales specifications in effect at the time of shipment.

Your exclusive remedy for breach of such warranty is limited to refund of purchase price or replacement of any product shown to be other than as warranted.

TO THE FULLEST EXTENT PERMITTED BY APPLICABLE LAW, DOW SPECIFICALLY DISCLAIMS ANY OTHER EXPRESS OR IMPLIED WARRANTY OF FITNESS FOR A PARTICULAR PURPOSE OR MERCHANTABILITY.

DOW DISCLAIMS LIABILITY FOR ANY INCIDENTAL OR CONSEQUENTIAL DAMAGES.

NuSil R-2180

ADVANCED ENGINEERING

R-2180

ICE PHOBIC COATING

DESCRIPTION

- Two-part silicone elastomer dispersed in xylene
- Two medium viscosity parts blend easily in a convenient 1:1 ratio (Part A:B)

APPLICATION

- For dip casting and heat-curing of thin elastomeric films
- For use as a coating to minimize ice adhesion[1]

PROPERTIES

TYPICAL PROPERTIES	AVERAGE RESULT	ASTM	NT-TM
Uncured:			
Appearance*	Transparent to translucent.	D2090	002
Viscosity*	3,075 cP (3,075 mPas)	D1084, D2196	001
Non-Volatile Content*	20%	D2288	004
Work Time	>72 hours	-	-
Cured: 30 minutes minimum @ ambient temp. and humidity, 45 minutes @ 75°C (167°F), and 135 minutes @ 150°C (302°F)			
(The given ramped cure schedule is suggested to remove solvent prior to elevated temperature cure)			
Refractive Index*	1.41	D1747, D1218	018
Durometer, Type A*	40	D2240	006
Tensile Strength*	1,700 psi (11.7 MPa)	D412	007
Elongation*	1,050%	D412	007
Tear Strength*	300 ppi (52.9 kN/m)	D624	009
Stress @ 100% Strain*	150 psi (1.03 MPa)	D412	007

*Properties tested on a lot-to-lot basis. Do not use the properties shown in this technical profile as a basis for preparing specifications. Please contact NuSil Technology for assistance and recommendations in establishing particular specifications.

[1] EM 1110-2-1612, Engineering and Design-Ice Engineering, U.S. Army Corps of Engineers, Department of the Army, September 2006, Chapter 20

INSTRUCTIONS FOR USE

Mixing

Thoroughly stir individual components prior to addition to ensure homogeneity. Mix in a 1:1 ratio by weight or volume. Exercise care to prevent solvent loss during deairing. Accomplish additional dilution for thin film applications by adding appropriate solvent.

Warning: Consult the MSDS for R-2180 prior to use as its solvent carrier is hazardous.

Vacuum Deaeration

Remove air entrapped during mixing by common vacuum deaeration procedure, observing all applicable safety precautions. Slowly apply full vacuum to a container rated for use and at least four times the volume of material being deaerated. Hold vacuum until bulk deaeration is complete.

Packaging

2 Pint Kit (910 g)
2 Gallon Kit (7.28 kg)
10 Gallon Kit (36.4 kg)
2 Drum Kit (360 kg)

Warranty

12 Months

Substrate Considerations

Cures in contact with most materials. Exceptions include: sulfur-cured organic rubbers, latex, chlorinated rubbers, some RTV silicones and unreacted residues of some curing agents.

HEAT AND LOW-TEMPERATURE RESISTANCE

In most applications, silicone may be heated from 180 to 200°C for a year, or even up to 450°C for short periods, without any appreciable effect on physical properties. Silicone also demonstrates flexibility at extreme low temperatures, with a stiffening temperature range of -50 to -70°C.

The operating temperature range of a silicone in any application is dependent on many variables, including but not limited to: temperature, time of exposure, type of atmosphere, exposure of the material's surface to the atmosphere, and mechanical stress. In addition, a material's physical properties will vary at both the high and low end of the operating temperature range. The user is responsible to verify performance of a material in a specific application.

RoHS AND REACh COMPLIANCE

R-2180 is compliant with the Restriction of the Use of Certain Hazardous Substances in Electrical and Electronic Equipment (RoHS) regulation contained in Article 4(1) of the European Parliament and Council's Directive 2002/95/EC. RoHS mandates that manufacturers restrict the use of lead, mercury, cadmium, hexavalent chromium, polybrominated biphenyls, polychlorinated biphenyls, and polybrominated diphenyl ethers in electrical and electronic equipment.

R-2180 is also compliant with the Registration, Evaluation, and Authorization of Chemicals (REACh) regulation (European Union 1907/2006). R-2180 does not contain any of the 16 chemicals identified as Substances of Very High Concern (SVHC) by the European Chemicals Agency (ECHA), which oversees REACh compliance.

Please contact NuSil Technology's Regulatory Compliance department with any questions or for further assistance.

SPECIFICATIONS

Do not use the properties shown in this technical profile as a basis for preparing specifications. Please contact NuSil Technology for assistance and recommendations in establishing particular specifications.

WARRANTY INFORMATION

The warranty period provided by NuSil Technology LLC (hereinafter "NuSil Technology") is 12 months from the date of shipment when stored below 40°C in original unopened containers. Unless NuSil Technology provides a specific written warranty of fitness for a particular use, NuSil Technology's sole warranty is that the product will meet NuSil Technology's then current specification. NuSil Technology specifically disclaims all other expressed or implied warranties, including, but not limited to, warranties of merchantability and fitness for use. The exclusive remedy and NuSil Technology's sole liability for breach of warranty is limited to refund of purchase price or replacement of any product shown to be other than as warranted. NuSil Technology expressly disclaims any liability for incidental or consequential damages.

WARNINGS ABOUT PRODUCT SAFETY

NuSil Technology believes, to the best of its knowledge, that the information and data contained herein are accurate and reliable. The user is responsible to determine the material's suitability and safety of use. NuSil Technology cannot know each application's specific requirements and hereby notifies the user that it has not tested or determined this material's suitability or safety for use in any application. The user is responsible to adequately test and determine the safety and suitability for their application and NuSil Technology makes no warranty concerning fitness for any use or purpose. NuSil Technology has completed no testing to establish safety of use in any medical application.

NuSil Technology has tested this material only to determine if the product meets the applicable specifications. (Please contact NuSil Technology for assistance and recommendations when establishing specifications.) When considering the use of NuSil Technology products in a particular application, review the latest Material Safety Data Sheet and contact NuSil Technology with any questions about product safety information.

Do not use any chemical in a food, drug, cosmetic, or medical application or process until having determined the safety and legality of the use. The user is responsible to meet the requirements of the U.S. Food and Drug Administration (FDA) and any other regulatory agencies. Before handling any other materials mentioned in the text, the user is advised to obtain available product safety information and take the necessary steps to ensure safety of use.

PATENT / INTELLECTUAL PROPERTY WARNING

NuSil Technology disclaims any expressed or implied warranty against the infringement of any domestic or international patent/intellectual property right. NuSil Technology does not warrant the use or sale of the products described herein will not infringe the claims of any domestic or international patent/intellectual property right covering the product itself, its use in combination with other products, or its use in the operation of any process.

NuSil SP-270

ADVANCED ENGINEERING

SP-270
SILICONE PRIMER

DESCRIPTION

- Specially formulated primer designed for use with platinum-cured systems where conventional silicone primers are insufficient
- One-component primer supplied in VM&P Naphtha requires no mixing
- Air-drying
- Convenient container sizes produce less waste

APPLICATION

- Improves the adhesion of addition-cured systems to iridite coated materials as well as other various substrates including: metals, glass, ceramics, some plastics, and other silicone material

PROPERTIES

TYPICAL PROPERTIES	AVERAGE RESULT	ASTM	NT-TM
Uncured:			
Appearance	Translucent	D2090	002
Percent Solids - Silicone Primers	15 %	D2369	047
Specific Gravity, Pycnometer	0.80	D891, D1475	022

Properties tested on a lot-to-lot basis. Do not use the properties shown in this technical profile as a basis for preparing specifications. Please contact NuSil Technology for assistance and recommendations in establishing particular specifications.

NuSil

SP-270 19 May 2014 Rev. A

INSTRUCTIONS FOR USE

Applying

Apply by brushing, wiping or dipping a uniform thin film onto the substrates. The following procedures are recommended for best bonding results:

1. Clean and degrease the surface being primed with an appropriate solvent and a coarse lint-free cloth.
2. Rinse the surface off with clean solvent.
3. When completely dry, apply a uniform thin coat by dipping, spraying or brushing. A camel hair brush may be used, or on smooth surfaces, a lint-free tissue. Dried primer coatings vary from being clear to having a slight haze. If dried to a whitish haze or chalky appearance, the coating is too thick. Clean and reapply.
4. Allow to dry for 30 minutes at room temperature and 50% relative humidity. This primer is actuated by atmospheric moisture, so lower levels of humidity require longer drying times.
5. Apply the appropriate NuSil Technology adhesive/sealant.

Packaging

0.5 Ounce (14 g)
1 Ounce Bottle
2 Ounce Bottle
4 Ounce Bottle
8 Ounce Bottle
16 Ounce Bottle (340 g)
1 Gallon (2.88 kg)
5 Gallon (14.4 kg)

Warranty

12 Months

Storage

Containers should remain sealed when not in use. This material hydrolyzes in the presence of atmospheric moisture and it is recommended that an inert gas, such as argon or nitrogen, be used to blanket the product before closing the container. Hydrolyzation is indicated by the appearance of a precipitate. The formation of moderate amounts of precipitate as a result of hydrolyzation is inherent in this material and will not adversely affect the performance of the material.

Note: NuSil Technology's primers are supplied in flammable hydrocarbon solvents. Keep away from heat and open flames. Use only with adequate ventilation.

RoHS AND REACh COMPLIANCE

SP-270 is compliant with the Restriction of the Use of Certain Hazardous Substances in Electrical and Electronic Equipment (RoHS) regulation contained in Article 4(1) of the European Parliament and Council's Directive 2002/95/EC. RoHS mandates that manufacturers restrict the use of lead, mercury, cadmium, hexavalent chromium, polybrominated biphenyls, polychlorinated biphenyls, and polybrominated diphenyl ethers in electrical and electronic equipment.

SP-270 is also compliant with the Registration, Evaluation, and Authorization of Chemicals (REACh) regulation (European Union 1907/2006). SP-270 does not contain any of the 16 chemicals identified as Substances of Very High Concern (SVHC) by the European Chemicals Agency (ECHA), which oversees REACh compliance.

Please contact NuSil Technology's Regulatory Compliance department with any questions or for further assistance.

SPECIFICATIONS

Do not use the properties shown in this technical profile as a basis for preparing specifications. Please contact NuSil Technology for assistance and recommendations in establishing particular specifications.

WARRANTY INFORMATION

The warranty period provided by NuSil Technology LLC (hereinafter "NuSil Technology") is 12 months from the date of shipment when stored below 40°C in original unopened containers. Unless NuSil Technology provides a specific written warranty of fitness for a particular use, NuSil Technology's sole warranty is that the product will meet NuSil Technology's then current specification. NuSil Technology specifically disclaims all other expressed or implied warranties, including, but not limited to, warranties of merchantability and fitness for use. The exclusive remedy and NuSil Technology's sole liability for breach of warranty is limited to refund of purchase price or replacement of any product shown to be other than as warranted. NuSil Technology expressly disclaims any liability for incidental or consequential damages.

WARNINGS ABOUT PRODUCT SAFETY

NuSil Technology believes, to the best of its knowledge, that the information and data contained herein are accurate and reliable. The user is responsible to determine the material's suitability and safety of use. NuSil Technology cannot know each application's specific requirements and hereby notifies the user that it has not tested or determined this material's suitability or safety for use in any application. The user is responsible to adequately test and determine the safety and suitability for their application and NuSil Technology makes no warranty concerning fitness for any use or purpose. NuSil Technology has completed no testing to establish safety of use in any medical application.

NuSil Technology has tested this material only to determine if the product meets the applicable specifications. (Please contact NuSil Technology for assistance and recommendations when establishing specifications.) When considering the use of NuSil Technology products in a particular application, review the latest Material Safety Data Sheet and contact NuSil Technology with any questions about product safety information.

Do not use any chemical in a food, drug, cosmetic, or medical application or process until having determined the safety and legality of the use. The user is responsible to meet the requirements of the U.S. Food and Drug Administration (FDA) and any other regulatory agencies. Before handling any other materials mentioned in the text, the user is advised to obtain available product safety information and take the necessary steps to ensure safety of use.

PATENT / INTELLECTUAL PROPERTY WARNING

NuSil Technology disclaims any expressed or implied warranty against the infringement of any domestic or international patent/intellectual property right. NuSil Technology does not warrant the use or sale of the products described herein will not infringe the claims of any domestic

or international patent/intellectual property right covering the product itself, its use in combination with other products, or its use in the operation of any process.